

University of St Andrews



Full metadata for this thesis is available in
St Andrews Research Repository
at:

<http://research-repository.st-andrews.ac.uk/>

This thesis is protected by original copyright

Electromagnetically Induced Transparency and Inversionless Gain in Doppler-broadened systems

A thesis presented by

James R. Boon, M.Sci

to the University of St. Andrews in application for the degree of
Doctor of Philosophy



J.F. Allen Physics Research Laboratories

School of Physics and Astronomy

University of St. Andrews

North Haugh

St. Andrews KY16 9SS

Scotland

August 1998



Th
D158

Declarations

I, James Robert Boon, hereby certify that this thesis, which is approximately 69,000 words in length, has been written by me, that it is the record of work carried out by me and that it has not been submitted in any previous application for a higher degree.

date 24/8/98 signature of candidate

I was admitted as a research student in September 1995 and as a candidate for the degree of Doctor of Philosophy in September 1996; the higher study for which this is a record was carried out in the University of St. Andrews between 1995 and 1998.

date 24/8/98 signature of candidate

I hereby certify that the candidate has fulfilled the conditions of the Resolution and Regulations appropriate for the degree of Doctor of Philosophy in the University of St. Andrews and that the candidate is qualified to submit this thesis in application for that degree.

date 24/8/98 signature of supervisor

In submitting this thesis to the University of St. Andrews I understand that I am giving permission for it to be made available for use in accordance with the regulations of the University Library for the time being in force, subject to any copyright vested in the work not being affected thereby. I also understand that the title and abstract will be published, and that a copy of the work may be made and supplied to any bona fide library or research worker.

date 24/8/98 signature of candidate

Abstract

Theoretical and experimental studies of electromagnetically induced transparency (EIT) have been carried out to critically examine the limitations of Doppler-broadening. In particular, the effects of changing the probe and coupling wavelengths have been explored to assess the potential of high frequency continuous wave (cw) inversionless lasers in Doppler-broadened media.

This thesis constitutes the first comprehensive treatment of the surprisingly complex interplay of processes that occur in Doppler-broadened systems. Insight is gained by looking at the contribution of the individual velocity groups to the overall process, both in terms of Autler-Townes splitting and coherence. Various energy level configurations have been studied and a distinct advantage for mismatched wavelengths has been identified in the Vee scheme. Results clearly indicate that, contrary to prevailing thought, atomic interference and coherence effects are not confined to matched wavelengths in Doppler-broadened media.

An extensive experimental investigation of a mismatched Doppler-broadened Vee scheme was carried out in rubidium vapour, in which the probe field frequency ($\lambda_p=422\text{nm}$) significantly exceeded that of the coupling field ($\lambda_c=780\text{nm}$). The results constitute an unambiguous observation of EIT for a high frequency probe despite Doppler effects. Furthermore, the comparison of experiment and theory demonstrated that the limiting factor on EIT was absorption of the driving field, not Doppler-broadening.

An authoritative review of experiments exhibiting inversionless gain and lasing sets the scene for a theoretical comparison of inversionless gain in matched and mismatched Doppler-broadened Vee schemes. The analysis predicted substantial gain in the mismatched ($\lambda_c > \lambda_p$) system for realistic steady state experimental conditions.

The role of Doppler effects in EIT has been elucidated, confirming that the restrictions of Doppler-broadening are significantly less stringent than previously supposed. Surprising possibilities for mismatched quantum interference effects have been highlighted, particularly for the Vee-type system. This work emphasises the potential of the Vee scheme as a means to create cw high frequency inversionless lasers in the presence of Doppler effects.

Acknowledgements

I would like to thank Professor Malcolm Dunn for his invaluable guidance and support. I greatly appreciate the opportunity to benefit from the insight of someone with a brain far larger than my own. I have also been fortunate to work, throughout the course of my research, in a group; so for the company, the support, the advice and the patience I thank Dr Sara Shepherd, Dr David Fulton, Litsa Zekou and David McGloin. Thanks are also due to the technical staff for building the apparatus that made blue transparency possible. I am grateful to Professor Stephen Harris for kick-starting research in this field and chuckling at my physics joke during my presentation at IQEC.

The day I started my PhD was also the day I met Suzanne Neilson. Her love and support over the last three years has been indispensable. I also acknowledge the support, wisdom, and grammatical advice of my parents, as well as the encouragement I received from them and the Neilson family.

I would like to take this opportunity to express my gratitude to Tom Edwards for abandoning the shampooing of Highland cattle and returning to St. Andrews. My Granddad has a firm belief that one always finds the right kind of people, and I would like to thank Tom, Colin, Ian, the Grahams and the Davids for being those people. For the times I wandered beyond the confines of the physics building I would also like to thank Ian, Jason, and Corrina for looking after me. Ian and Jason were also good enough to beat me at squash when the physics got too much.

I would like to thank Sensei Paul Dempsey for his tuition and guidance in karate which has proved useful, albeit in a non-violent way, in the pursuit of a PhD. Thanks also to Moira Mackenzie, who not only provided me with gainful employment in the library but also offered much needed common sense when physics clouded my brain. Credit must be placed with Herbie Hancock, J. J. Cale, Neil Young and various other artists for providing the soundtrack to this thesis.

Finally, undoubted thanks go to 2π for being such an important factor in this work, I'm glad to say that it didn't get left out - this time...

TABLE OF CONTENTS

Declarations

Abstract

Acknowledgements

Table of Contents

Dedication

Chapter 1: EIT and the Light-Matter Interaction

| | |
|--|-----------|
| 1.1 Introduction | 1 |
| 1.2 Brief History of EIT | 4 |
| 1.3 Physical Interpretation of EIT | 9 |
| 1.3.1 Basic Concepts | 9 |
| 1.3.2 Two Route Interference | 10 |
| 1.3.3 State Amplitude Model | 13 |
| 1.4 Thesis Objectives | 16 |
| 1.5 Related Effects and Applications of EIT | 18 |
| 1.5.1 The Autler-Townes Effect | 18 |
| 1.5.2 Dressed State Analysis | 19 |
| 1.5.3 Nonlinear Enhancement | 20 |
| 1.5.4 Quantum Coherence and OPOs | 21 |
| 1.5.5 Phaseonium | 24 |
| 1.5.6 Electromagnetically Induced Focusing | 26 |
| 1.5.7 Inversionless Lasing | 28 |
| 1.5.8 Progress in Quantum Coherence | 29 |
| 1.6 The Role of Doppler-broadening in EIT | 32 |
| 1.6.1 Previous Work at St. Andrews | 33 |
| 1.6.2 Current Work at St. Andrews | 34 |
| 1.6.3 Other Work on the Role of Doppler-broadening | 36 |

| | |
|--|-----------|
| 1.7 Thesis Overview | 38 |
| References | 40 |
| Chapter 2: Theoretical Modelling of Quantum Coherence | |
| Effects | |
| 2.1 Introduction | 47 |
| 2.2 Semiclassical Density Matrix Formulation of Quantum | |
| Mechanics | 48 |
| 2.2.1 Population Decay Rates | 51 |
| 2.2.2 Coherence Dephasing Rates | 52 |
| 2.2.3 Incoherent Pumping Rates | 53 |
| 2.3 Employment of the Density Matrix Model | 55 |
| 2.4 Nuances of the Density Matrix Model | 61 |
| 2.4.1 Temperature | 61 |
| 2.4.2 Dephasing | 62 |
| 2.4.3 Rabi Frequency | 65 |
| 2.4.4 Spontaneous Decay | 66 |
| 2.4.5 Velocity Range | 68 |
| 2.4.6 Relative Populations | 70 |
| 2.5 The Three Schemes for EIT | 72 |
| 2.5.1 The Cascade Scheme | 73 |
| 2.5.2 The Lambda Scheme | 76 |
| 2.5.3 The Vee Scheme | 78 |
| 2.6 Three-dimensional Modelling | 81 |
| 2.7 Moseley's N Level Rules | 84 |
| References | 85 |
| Chapter 3: Experimental Apparatus and Materials | |
| 3.1 Introduction | 86 |
| 3.2 Laser Systems | 87 |
| 3.2.1 Pump Lasers | 87 |

| | |
|---|------------|
| 3.2.2 Schwartz Titanium Sapphire Laser (750 - 820nm) | 88 |
| 3.2.3 Microlase MBR 110 Titanium Sapphire Laser (700-1060nm) | 88 |
| 3.2.4 Spectra Physics 380D Dye Laser | 89 |
| 3.2.5 Experimental Applications | 90 |
| 3.3 Diagnostic and Ancillary Equipment | 92 |
| 3.3.1 Diagnostics | 92 |
| 3.3.2 Signal Detection | 92 |
| 3.4 Frequency Doubling System | 96 |
| 3.4.1 Potassium Niobate | 97 |
| 3.4.2 Thermoelectric Cooler and Mount | 100 |
| 3.4.3 Creating a Dry Environment | 103 |
| 3.5 Incoherent Excitation | 107 |
| 3.5.1 Destroying Phase Coherence | 108 |
| 3.6 Rubidium Atomic Vapour | 111 |
| 3.6.1 Fine Structure | 112 |
| 3.6.2 Hyperfine Structure | 114 |
| 3.6.3 Rubidium Vapour Cell | 119 |
| 3.6.4 Einstein A Coefficients | 121 |
| References | 122 |

Chapter 4: Comparison of Wavelength Dependence in Cascade, Lambda, and Vee-type Schemes for Electromagnetically Induced Transparency

| | |
|-------------------------------------|------------|
| 4.1 Introduction | 125 |
| 4.2 Basis of Comparison | 127 |
| 4.3 The Autler-Townes Effect | 129 |
| 4.4 Theoretical Results | 136 |
| 4.4.1 The Cascade Scheme | 137 |
| 4.4.2 The Lambda Scheme | 141 |

| | |
|--|------------|
| 4.4.3 The Vee Scheme | 145 |
| 4.5 Discussion | 157 |
| 4.5.1 Further Theoretical Considerations | 165 |
| 4.6 The Role of Coherence | 169 |
| 4.7 Conclusion | 176 |
| References | 177 |
| | |
| Chapter 5: Experimental Observation of Electromagnetically Induced Transparency on a Blue Probe in a Doppler-broadened Mismatched Vee-type System | |
| 5.1 Introduction | 180 |
| 5.2 Theoretical Analysis | 184 |
| 5.3 Optical Pumping | 188 |
| 5.4 Experimental Results | 192 |
| 5.4.1 Power | 195 |
| 5.4.2 Detuning | 208 |
| 5.4.3 Fluorescence | 217 |
| 5.5 Discussion | 220 |
| References | 222 |
| | |
| Chapter 6: Review of Inversionless Lasing and Gain Experiments Carried Out to Date | |
| 6.1 Introduction | 224 |
| 6.2 Historical Development | 226 |
| 6.2.1 Gain and Lasing Without Inversion by Quantum Coherence | 227 |
| 6.3 Experimental Amplification Without Inversion | 230 |
| 6.3.1 Gao <i>et al</i> , June 1992 | 230 |
| 6.3.2 Nottlemann <i>et al</i> , March 1993 | 232 |

| | |
|--|------------|
| 6.3.3 van der Veer <i>et al</i> , May 1993 | 234 |
| 6.3.4 Fry <i>et al</i> , May 1993 | 236 |
| 6.3.5 Kleinfeld and Streater, June 1994 | 239 |
| 6.3.6 Zibrov <i>et al</i> , May-June 1995 | 241 |
| 6.3.7 Zhu and Lin, March 1996 | 243 |
| 6.3.8 Fort <i>et al</i> , June 1997 | 245 |
| 6.3.9 Durrant <i>et al</i> , May 1998 | 247 |
| 6.4 Experimental Lasing Without Inversion | 250 |
| 6.4.1 Zibrov <i>et al</i> , August 1995 | 250 |
| 6.4.2 Peters and Lange, 1996 | 251 |
| 6.4.3 Padmabandu <i>et al</i> , March 1996 | 253 |
| 6.4.4 Sellin <i>et al</i> , September 1996 | 256 |
| 6.4.5 Jong <i>et al</i> , June 1998 | 258 |
| 6.5 Conclusions and a View of the Future | 260 |
| References | 261 |
| | |
| Chapter 7: Theoretical Analysis of Mismatched Gain in Doppler-broadened Media | |
| 7.1 Introduction | 267 |
| 7.2 Comparison of Matched and Mismatched Systems | 270 |
| 7.3 Absorption and Gain Measurements | 273 |
| 7.3.1 Simple Two Level Theory | 273 |
| 7.3.2 Calculation of Absorption Based on Density Matrix Analysis | 275 |
| 7.4 Theoretical Results | 281 |
| 7.5 Discussion | 292 |
| 7.6 Further Practical Considerations | 305 |
| 7.7 Conclusion | 309 |
| References | 310 |

Chapter 8: Conclusions and Future Work

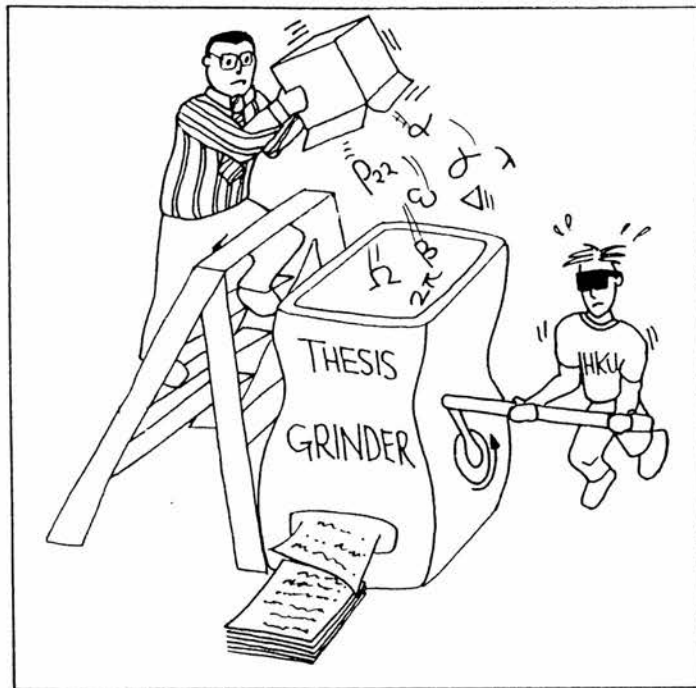
| | |
|--------------------------------|------------|
| 8.1 Conclusions | 312 |
| 8.2 Future Work | 316 |
| 8.2.1 Near Ultra-Violet Scheme | 317 |
| 8.2.2 Radio Frequency Scheme | 319 |
| References | 322 |

Appendices

| | |
|---|------------|
| A. Solving the Density Matrix with Mathematica | 323 |
| B. Coherent Excitation Scheme | 327 |
| C. Role of Coherence Model | 329 |
| D. Publications, Presentations, and Awards | 330 |

To Mum and Dad

Thanks



JBoon '98

CHAPTER 1

EIT and the Light-Matter Interaction

“And God said, ‘Let there be light,’ and there was light.”

Genesis 1 vs.3

1.1 Introduction

Identifying the importance of light goes beyond simply trying to imagine what life would be like without it. Light is not only essential to the way we perceive the world visually, but also through photosynthesis it forms the foundation of all life.

Scientists have studied the relationship between light and matter seeking to understand, and where possible harness, this fundamental interaction. At the very beginning of this century these studies became inextricably linked to the discovery and development of quantum mechanics. On the 10th of December 1900 Max Planck delivered a lecture in which he assumed the emission and absorption of radiation always took place in discrete portions of energy - quantum theory was born [1].

Later, Rutherford, through work on atomic alpha particle scattering, shed more light on the nature of the atom. He described the atom as consisting of a central charge surrounded by a sphere, of well defined radius, containing an evenly distributed electric charge of equal magnitude and opposite sign to that in the centre of the atom [2]. The experimental evidence did not conclusively show whether the central charge was positive or negative, but Rutherford did go as far as suggesting that the outer charge may be located in a number of rotating electrons rather than uniformly distributed in a sphere.

Thirteen years later, in 1913, Niels Bohr began to synthesise the ideas of Rutherford and Planck [3]. He modelled the atom as a central nucleus of positive charge Ze , surrounded by Z negatively charged electrons. The electrons all carried the same magnitude of charge e and moved according to the laws of classical mechanics. In addition, Bohr introduced the concept of stationary states and the idea that the atom may pass from one such state to another, resulting in the absorption or emission of radiation at a specific frequency. He was thus able to explain the existence of spectral lines, and verify the Balmer formula that was derived empirically by the observation of the hydrogen spectrum.

In 1917 Albert Einstein discussed the interaction of light and matter in terms of transition probabilities in an atom subject to broadband radiation [4]. This led to the first explanation of why atoms might pass from one state to another and predicted the likelihood of them doing so. Einstein highlighted three processes that may occur: stimulated absorption, spontaneous emission, and stimulated emission. A stimulated process occurs as a result of the interaction of a light field with a transition between states,

while a spontaneous process occurs when an atom in a high energy state independently relaxes to a lower energy level emitting the excess energy as light.

This body of work formed the foundation upon which modern quantum mechanics was developed [5]. More than forty years later, in 1958, Schawlow and Townes proposed an extension of the maser concept into the optical frequency region [6] which led to the realisation of the laser - *light amplification by the stimulated emission of radiation* [7]. Einstein's picture of the light-matter interaction is now widely used to provide a phenomenological model for the study of laser action in atoms [8]. Ironically, the invention of the laser identified a shortfall in Einstein's picture; namely, that it does not account for the interaction of atoms with radiation of a monochromatic or narrowband nature. We now know, for example, that a narrowband coherent radiation field will cause an electron to 'Rabi flop' between atomic states. Rather than occupying a stationary state, the atom switches between the upper and lower levels of a transition at a frequency determined by the intensity of the narrowband radiation field and the strength of interaction between that field and the atomic transition in question. A semiclassical or fully quantum picture is required to model such a phenomenon.

The research presented in this thesis is based on a semiclassical perspective of the light-matter interaction obtained through density matrix formalism. We describe the atom quantum mechanically, but the radiation is still treated as a classical electric field. By virtue of this perspective a greater insight into the nature of the interaction of light and matter can be achieved. One can go further and adopt a fully quantum picture in which both light and matter are treated quantum mechanically. This 'dressed state analysis' will be discussed briefly in Section 1.5.2.

The precise nature of this study is concerned with the interaction of coherent narrowband optical fields with a well characterised atomic vapour. In addition to the three processes discussed by Einstein, quantum coherence effects are found to occur as a result of the narrowband nature of the light fields applied to the medium and the coherence they impart on the atomic states therein. Under certain conditions the atomic medium may be rendered transparent at a specific frequency. An account of electromagnetically induced transparency (EIT), as this phenomenon is now called, was first presented in 1989 by

Stephen Harris [9]. This initial work led to the growth of a new field of research in quantum optics.

A wealth of experimental and theoretical studies have been carried out on EIT and related effects [10,11,12]; so much so, that over the course of writing this thesis EIT has made its way into a text book [13]. The main focus of research has been the production of lasing in the absence of a population inversion [14]. This concept runs contrary to the model of laser action based on Einstein's early hypothesis [8], yet it has recently been demonstrated experimentally [15].

This first chapter presents a chronological review of the work carried out in this field. A brief history of EIT will be followed by a qualitative exposition of related effects and applications. The intent of this chapter is to provide a broad overview of this field in a contemporary context, setting the scene for the work presented in the chapters that follow.

1.2 Brief History of EIT

In 1961 Fano published the results of an early study of quantum interference [16]. Fano reported the observation of characteristically asymmetric peaks in excitation spectra that occurred due to the presence of a discrete auto-ionised state within the continuum. An auto-ionised state is a virtual, transitory state with an energy value greater than the ionisation energy of the atom. Such a state may occur in an atom that has two electrons in its outer shell - these electrons may simultaneously occupy a loosely bound state whose energy is greater than the ionisation energy of a single electron. Its presence provides an alternative route for ionisation which may occur directly from the continuum or via the auto-ionised state. The two possible routes to ionisation in Fano's system are shown in Fig. 1.1.

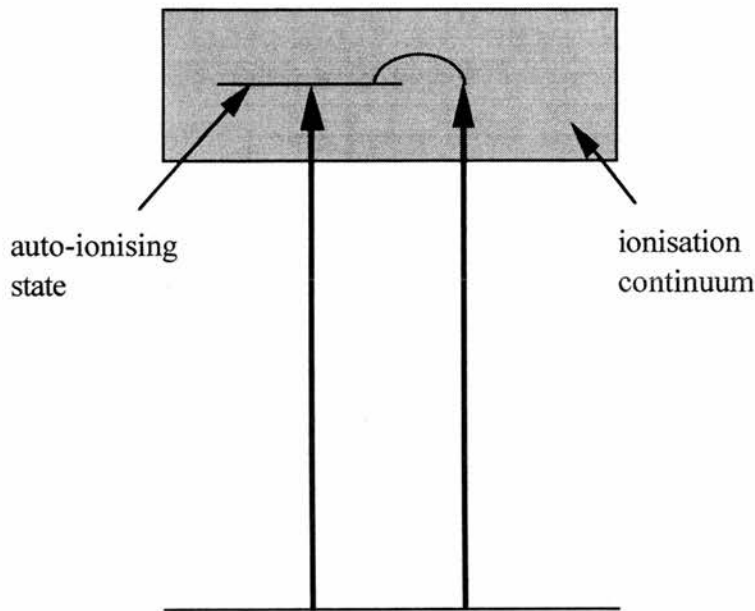


Figure 1.1: *The direct and indirect routes to ionisation in Fano interference.*

Fano established the concept of phase interaction between the discrete auto-ionised state and the continuum. This phase relationship varied through the linewidth of the state producing the asymmetrical absorption curves. An example of such a curve is shown in Fig. 1.2.

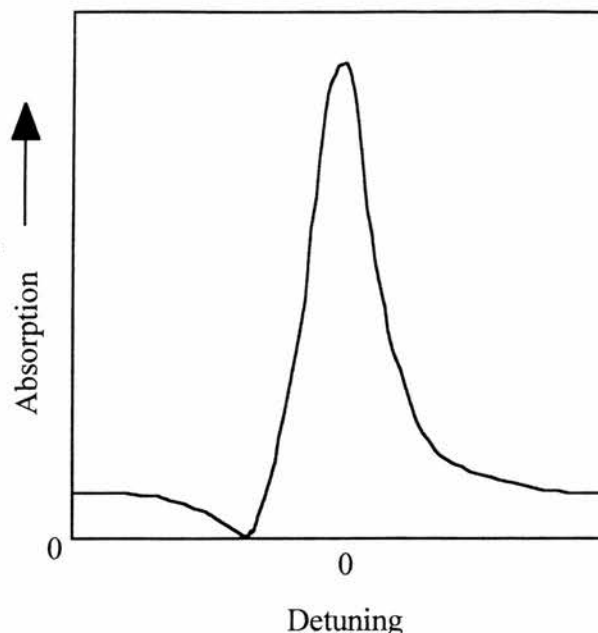


Figure 1.2: *An asymmetrical natural lineshape created by Fano interference.*

The asymmetrical curves include a point at which absorption is reduced to zero. Although not emphasised at the time, this was an early observation of the effect now called electromagnetically induced transparency. A physical interpretation of this phenomenon involves the interference of two possible routes, in this case to ionisation. When the phase relationship between the state and the continuum is such that the two routes shown in Fig. 1.1 cancel each other out, there is a resulting zero point in the absorption spectrum.

In 1976 Arimondo and Orriols described a similar interference effect occurring in a three level system [17] in what has become known as the ‘Pisa experiment’. The folded energy level configuration employed in this work is called a Lambda scheme, and it is depicted schematically in Fig. 1.3. This study into optical pumping utilised a single laser beam operating with two coherent modes. When the frequency separation between the laser modes was equal to the splitting between the two hyperfine levels of the ground state, the two coherent laser modes effectively acted as two separate light fields. This provided two distinct absorption routes from the hyperfine split ground state to level $|3\rangle$. These routes interfered to cancel out absorption between the ground state and the upper level, resulting in the disappearance of fluorescence produced by radiative decay from level $|3\rangle$.

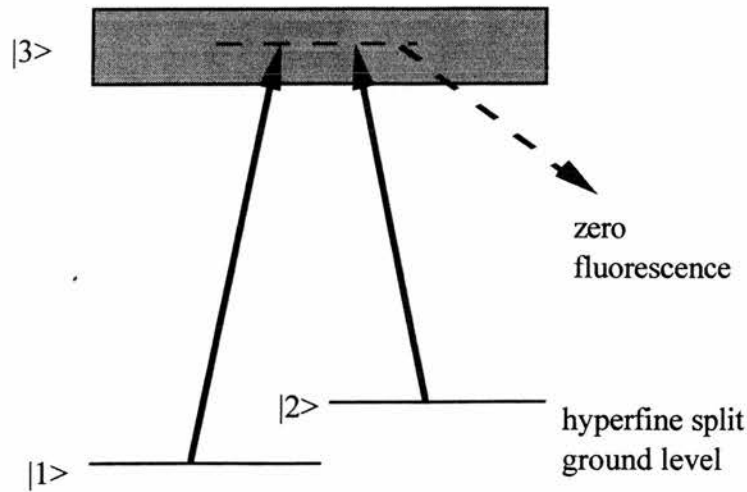


Figure 1.3: Closed three level scheme employed in the Pisa experiment.

Other work published in 1978 by Gray, Whitley and Stroud gave rise to the concept of coherent population trapping [18]. In this scheme the atomic population was coherently trapped in low lying states, preventing absorption or excitation. The authors considered this to be a problem because it prevented efficient excitation; however, they stated that it could be overcome by utilising lasers with linewidths greater than the linewidth of the transition. The sharp interference feature that results from the population trapping described by Gray *et al* is shown in Fig. 1.4. Where σ_{22} is the excited state population and δ_b is the normalised frequency separation between the laser modes.

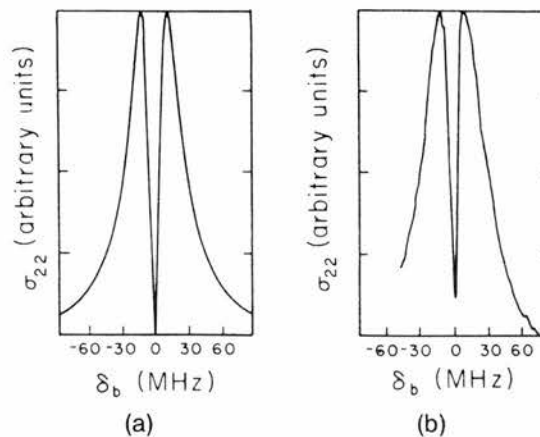


Figure 1.4: (a) Theoretical and (b) Experimental curves showing the excited state population σ_{22} as a function of the normalised frequency separation, δ_b , between laser modes.

With the benefit of hindsight we can clearly see that these early experiments describe exactly the type quantum coherence effect that is considered in this thesis. However, none of the researchers involved had recognised these phenomena as potentially useful effects. This important breakthrough was made by Stephen Harris in 1989 [9]. The significance of Harris' contribution was his recognition of the potential of EIT to revolutionise modern laser technology. At the time, contemporary theory suggested that laser action could only be achieved by inverting the population on the lasing transition. In Siegman's definitive book on lasers he states that "for laser action to occur, the pumping process must produce not merely excited atoms, but a condition of *population inversion*, in which more atoms are excited into some higher quantum energy level than are in some lower energy level in the laser medium" [8]. In a theoretical paper published in 1989 Harris demonstrated that the interference in absorption routes that led to the creation of a transparency had no reciprocal effect in the emission profile [9]. The requirement for a population inversion to induce laser action arises from the competition between stimulated emission and absorption. In a medium in which absorption has been turned off, stimulated emission becomes dominant even in the absence of a population inversion. Gain and subsequent laser action can be achieved with almost all of the population still in the lower laser level.

Harris published an experimental observation of electromagnetically induced transparency in 1991 [19]. A Lambda scheme in strontium vapour, similar to that employed in the Pisa experiment, was used for this pioneering work. The energy level structure of this configuration is shown in Fig. 1.5 where level $|3\rangle$ is an auto-ionised state within the continuum. The experimental scheme employed pulsed laser sources and a significant transparency was observed.

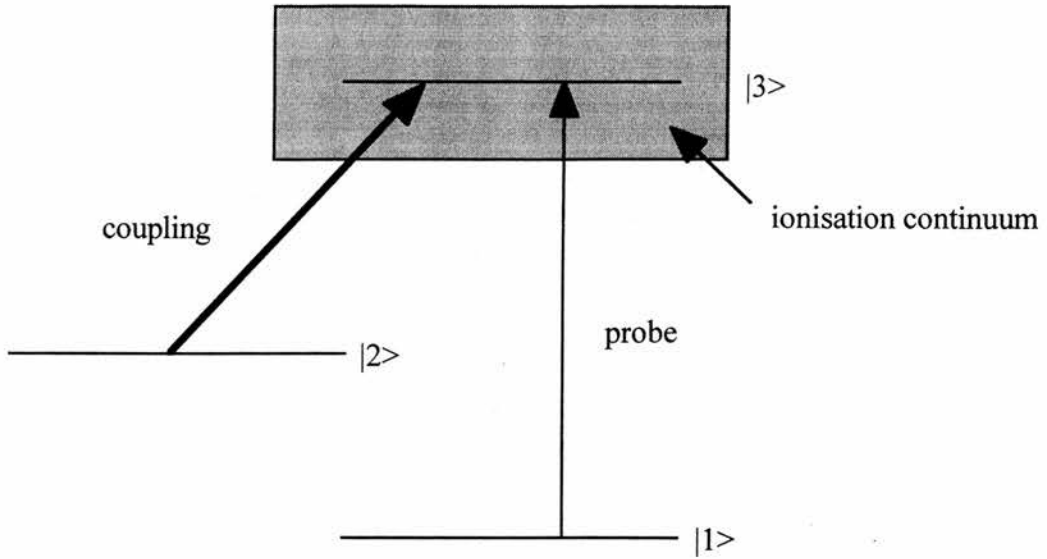


Figure 1.5: Schematic of Lambda configuration employed in the first experimental observation of EIT by Harris.

Despite differences in the atomic level structures, the effect observed by Harris *et al* [19] was of the same nature as the one previously detected by Fano [16]; Arimondo and Orriols [17]; and Gray, Whitley and Stroud [18]. The important step Harris made was recognising the potential of EIT as a useful phenomenon.

1.3 Physical Interpretation of EIT

We now consider two alternative methods of explaining EIT. ‘Two Route Interference’ is the easiest to grasp on an intuitive level, while the ‘State Amplitude Model’ takes a more quantitative approach, occupying the mathematical high ground. The density matrix analysis (described in Chapter 2) that forms the basis of the theoretical modelling in this thesis is an extension of the state amplitude model, dealing with an ensemble rather than a single atom. Before considering each specific approach some basic concepts are presented that will prove relevant to the subsequent discussion of EIT.

1.3.1 Basic Concepts

Electromagnetically induced transparency involves an intense ‘coupling’ laser rendering a medium transparent at a specific frequency. The strong coupling field turns off the absorption on a transition between energy levels in the medium. This transition is monitored by a weak ‘probe’ laser. Note that the presence of this laser field is necessary for the effect to occur.

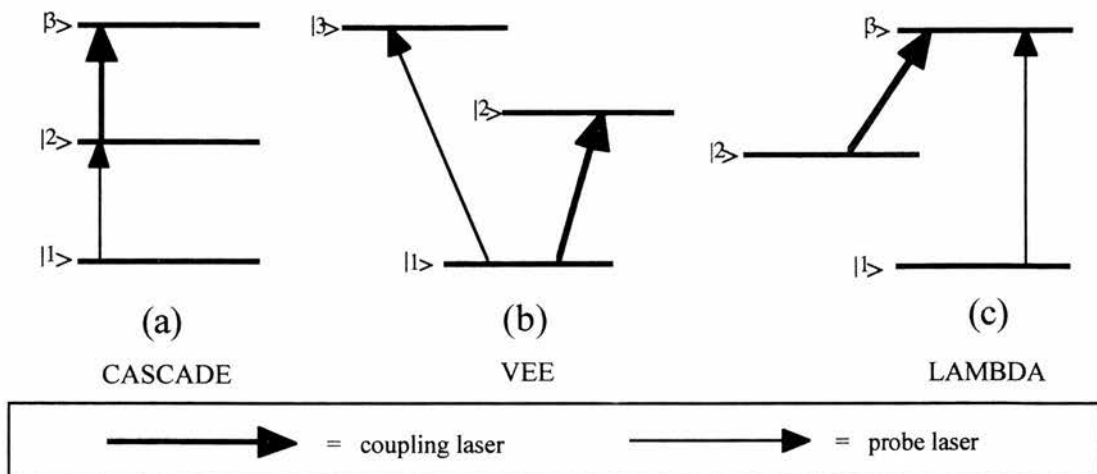


Figure 1.6: Three atomic configurations for EIT: (a) Cascade, (b) Vee, and (c) Lambda. These schemes are depicted in their simplest form and may have more complex level structure in real atomic systems.

Three basic schemes for EIT are shown in Figure 1.6. In each case a strong coupling laser induces the transparency and a probe laser scans the transition upon which the transparency is induced. The medium becomes virtually 100% transmitting at the frequency corresponding to the probe laser transition.

Figure 1.7 shows line profile traces produced by scanning the probe laser frequency across the probe transition. We see a straightforward Doppler-broadened absorption profile in Fig. 1.7 (a). Absorption reaches a maximum at line centre which corresponds to resonance with the probe transition. Figure 1.7 (b) depicts the transparency window created at line centre when the coupling laser field is applied.

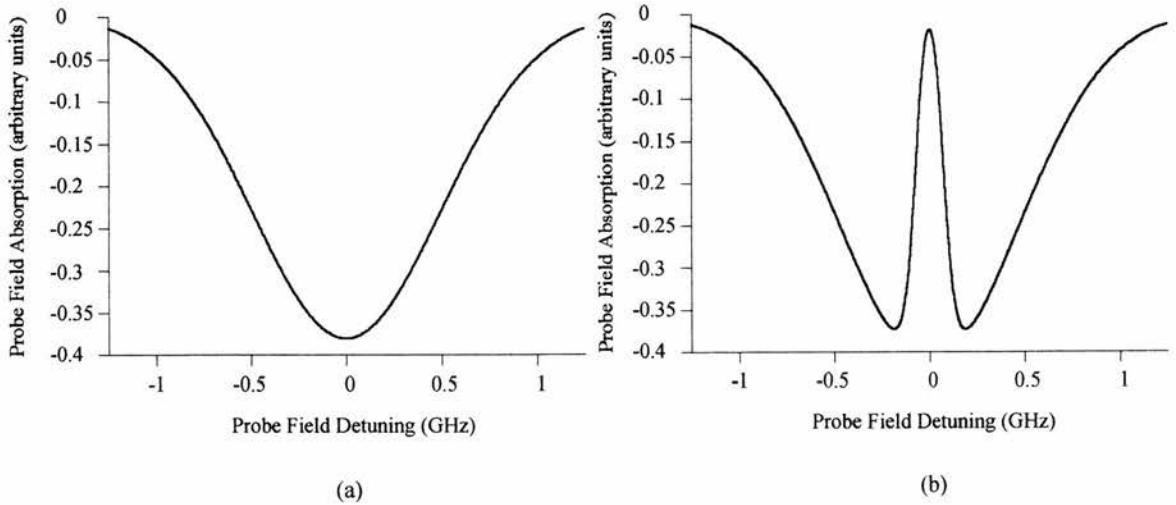


Figure 1.7: *Probe field absorption is plotted as a function of the probe field detuning from line centre (a) in the absence of the coupling field, and (b) in the presence of the coupling field. Probe field absorption is defined as the appropriate off-diagonal density matrix element that is proportional to the probe absorption coefficient.*

1.3.2 Two Route Interference

EIT can be explained by the creation of two possible routes to absorption on a single transition. These routes interfere destructively to cancel each other out.

Let us consider the Cascade scheme of Fig. 1.6 (a). The coupling laser turns off the absorption between the ground state and level $|2\rangle$ by offering an alternative pathway for absorptive movement of the atomic population. This transparency occurs when the

system is in two-photon resonance. Two-photon absorption takes place when an electron in the ground state absorbs energy from a photon of each laser and is excited into level $|3\rangle$. Although the use of the word photon implies a quantum mechanical treatment of light it is not necessary to model the interaction of light and matter in this way. As we shall see, quantum coherence effects can be predicted with a semiclassical model in which the light is treated as a classical electric field. In this case the two routes to absorption still exist and lead to the creation of a transparency; however, it is easier to envisage the two distinct absorption routes by using the photon description of light and the photon picture is employed here for that reason alone.

The coupling laser also facilitates the movement of population from level $|3\rangle$ into level $|2\rangle$. This ‘two-photon’ absorption route will interfere with the traditional route where an electron in the ground state is excited directly into level $|2\rangle$ by a probe laser photon. The two absorption routes, for all three schemes, are shown in Figure 1.8.

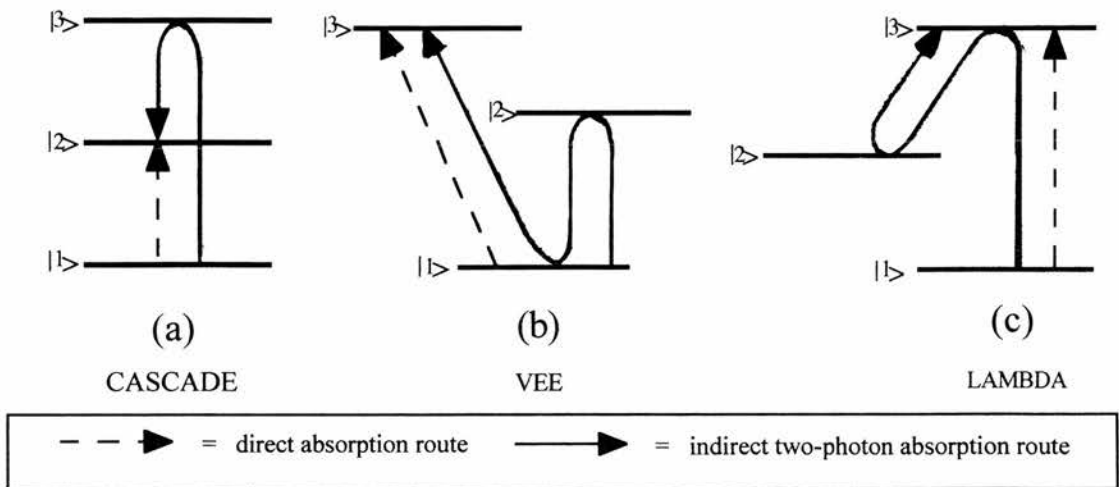


Figure 1.8: Two routes to absorption in the three EIT schemes: (a) Cascade, (b) Vee, and (c) Lambda.

The interference between these routes is of a quantum nature, but it can be understood by drawing a classical analogy with the interference of waves created in water. If the two absorption routes are out of phase they will interfere destructively. Referring back to Figure 1.7 (b) the EIT window can clearly be seen in the centre of the absorption feature. This is the region for which two-photon and single photon resonance coincides, resulting in a sharp decrease in the amount of light absorbed. The role of two-photon

absorption can be seen more clearly by detuning the coupling laser and hence altering the probe frequency for which two-photon resonance occurs.

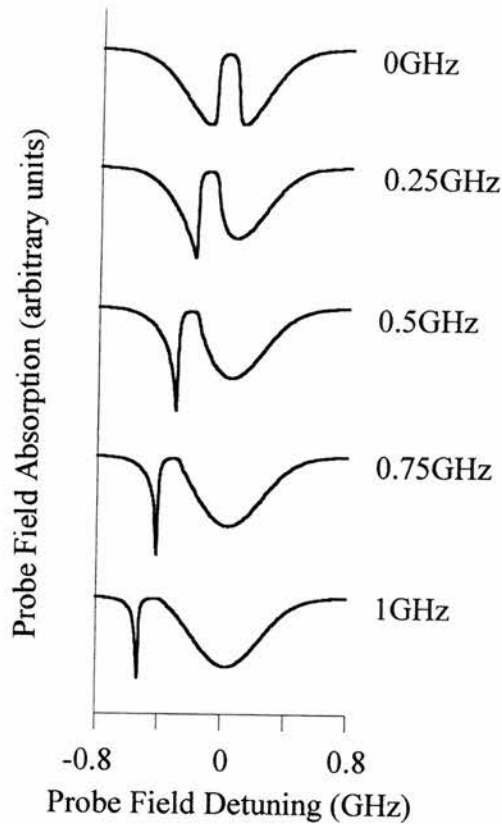


Figure 1.9: *Theoretical traces produced from the density matrix model of a Doppler-broadened Cascade scheme. Absorption (ρ^i_{12} in arbitrary units) is depicted as a function of probe field detuning. The detuning of the coupling laser is indicated to the right of each trace.*

The sharp two-photon absorption feature is completely resolved from the Doppler-broadened absorption profile when the coupling laser is significantly detuned from resonance, as shown in Fig. 1.9. In this case, the single photon absorption is maximum at line centre, as we would expect. It is evident, as the coupling laser is tuned onto resonance, that the EIT window develops as the two-photon feature moves onto the centre of the single photon absorption. Hence, we can think of these two absorption routes interfering destructively to create the transparency.

In conclusion, EIT is the interference of absorption routes, made possible by the presence of the coupling laser, that leads to a transparency at the probe laser frequency.

The interference of alternative pathways to absorption is also manifested in the trapping of the atomic population in certain states. It is possible to describe the mechanism of EIT in terms of coherent population trapping. While there are subtle distinctions between electromagnetically induced transparency and coherent population trapping, these terms describe the same general phenomenon.

1.3.3 State Amplitude Model

The state amplitude model can be employed to describe the time evolution of the state amplitudes in an atom subject to one or more radiation fields. Probability densities may be deduced, from the state amplitudes, which allow us to gain an insight into the relative magnitude of the state populations and the polarisations associated with absorption, gain and dispersion. This makes the model a useful tool in the exploration of EIT [20].

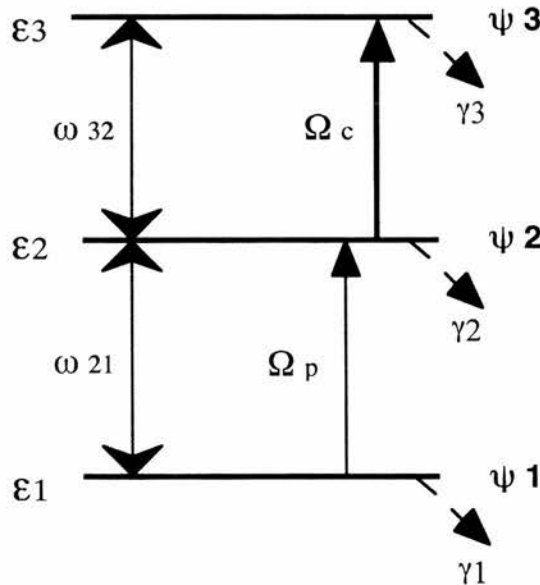


Figure 1.10: *Three level atom with two applied radiation fields in the Cascade configuration. Where Ω_c and Ω_p are the coupling and probe field Rabi frequencies respectively.*

If we consider a simple Cascade scheme in a three level atom we can apply the state amplitude model and examine the condition for creating EIT. Figure 1.10 depicts the

energy scheme of such an atom, subject to two coherent radiation fields. Note that the nomenclature in this case differs from that employed in the density matrix model and elsewhere in this thesis.

The three levels have energy ε_1 , ε_2 , and ε_3 ; associated state eigenfunctions ψ_1 , ψ_2 , and ψ_3 ; and associated decay rates γ_1 , γ_2 , and γ_3 which decay to levels outside the system that are not explicitly considered in this model. The Rabi frequencies induced by the applied fields are: Ω_c for the coupling field (between states $|2\rangle$ and $|3\rangle$) and Ω_p for the probe field (between states $|1\rangle$ and $|2\rangle$).

The starting point of this model is the time dependent Schrödinger equation:

$$H\Psi(r,t) = i\hbar \frac{\partial \Psi(r,t)}{\partial t} \quad (1.1)$$

where $\Psi(r,t)$ is the overall wavefunction of the atom and H is the Hamiltonian of the system. The Hamiltonian is made up of two parts: that associated with the isolated atom, including the damping effect of population decay, and that describing the effect of the interaction of the atom and the two optical fields. The latter is treated in terms of the electric dipole approximation. The Hamiltonian is given by:

$$H = H_0 + exE_p \cos(\omega_p t) + exE_c \cos(\omega_c t) \quad (1.2)$$

where ω_p , ω_c and E_p , E_c are the angular frequencies and the electric field amplitudes of the probe and coupling fields respectively; e is the electronic charge; and x is the relative displacement of the electron from the nucleus in the dipole approximation.

In the state amplitude model we write the wavefunction of the atomic system, which is the solution to Eq. (1.1), in terms of the unperturbed eigenfunctions with time dependent coefficients. These coefficients are the state amplitudes:

$$\Psi(r,t) = a_1(t)\psi_1 + a_2(t)\psi_2 \exp(-i\omega_{21}t) + a_3(t)\psi_3 \exp(-i\omega_{32}t) \quad (1.3)$$

where ω_{21} and ω_{32} are the angular frequencies of the resonant transitions. Substituting the Hamiltonian, Eq. (1.2), and the wavefunction, Eq. (1.3), into the time dependent Schrödinger equation, Eq. (1.1), allows us to derive three coupled equations that describe the evolution of the state amplitudes. In so doing, we assume that the two radiation fields are in exact resonance with the appropriate transition: $\omega_p = \omega_{21}$ and $\omega_c = \omega_{32}$ and that the

rotating wave approximation holds, which implies that the effect of high frequency terms may be ignored.

$$\dot{a}_1 = -i\Omega_p a_2 - \gamma_1 a_1 \quad (1.4a)$$

$$\dot{a}_2 = -i\Omega_p a_1 - i\Omega_c a_3 - i\gamma_2 a_2 \quad (1.4b)$$

$$\dot{a}_3 = -i\Omega_c a_2 - \gamma_3 a_3 \quad (1.4c)$$

These equations describe the evolution of the state amplitudes with respect to time. If we ignore the effects of damping and set the rate of change of the state amplitudes to zero we can simplify these coupled equations to describe an undamped steady state situation:

$$\dot{a}_1 = -i\Omega_p a_2 = 0 \quad (1.5a)$$

$$\dot{a}_2 = -i\Omega_p a_1 - i\Omega_c a_3 = 0 \quad (1.5b)$$

$$\dot{a}_3 = -i\Omega_c a_2 = 0 \quad (1.5c)$$

By rearranging Eqs. (1.5a) to (1.5c) we can derive two conditions for EIT:

$$a_2 = 0 \quad (1.6)$$

$$-\frac{a_1}{a_3} = \frac{\Omega_c}{\Omega_p} \quad (1.7)$$

In order that the state amplitudes become time independent we require the atomic system to satisfy Eq. (1.6). In this case, the atomic population will be trapped in levels $|1\rangle$ and $|3\rangle$, and the rate of change of the state amplitudes will be zero. Thus, there will be no absorption between states $|1\rangle$ and $|2\rangle$. Equation (1.7) describes the relationship between the state amplitudes and the Rabi frequencies induced by the incident optical fields for the case in which the state amplitude of level $|2\rangle$ is time independent. This relationship can be construed as the ratio of field strengths and state populations necessary to induce transparency.

1.4 Thesis Objectives

So far we have considered the initial discovery of EIT and its physical interpretation from the perspective of both interfering absorption routes and the state amplitude model. The remainder of this chapter provides a selective overview of the work carried out in the field of EIT, while the current section briefly outlines the specific objectives of this thesis.

The research undertaken by the group at the University of St. Andrews has exclusively utilised continuous wave laser sources. The work presented herein explores the limitations of Doppler-broadening in EIT and highlights some surprising possibilities that remain for practical inversionless lasing in a gaseous medium, despite the presence of Doppler effects. A fuller understanding of the consequences of Doppler-broadening for EIT is achieved through both theoretical and experimental study. Chapters 4 to 7 describe a theoretical comparison of the wavelength dependence of all three EIT schemes, the experimental realisation of EIT on a blue transition controlled by an infrared field (in the presence of Doppler-broadening), and the prediction of inversionless gain in a mismatched (different probe and coupling wavelengths) Vee-type system.

The importance attributed to exploring EIT in configurations for which the wavelengths of the probe and coupling fields differ arises from the application of inversionless lasing. The primary goal of lasing without inversion is to access difficult high frequency transitions beyond the capabilities of conventional laser technology. Optimistically, this would include what Marlan Scully described as the “Holy Grail” of laser physics research: table-top X-ray and gamma-ray lasers [21]. If EIT is to provide the means of achieving this goal it is obvious that it must be possible to induce transparency at a probe frequency significantly higher than the frequency of the coupling field. The main thrust of this thesis is that, contrary to prevailing opinion [22], such mismatched systems are realisable in the presence of Doppler-broadening at continuous wave laser powers. The research presented herein provides theoretical and experimental evidence to back up this claim. Figure 1.11 shows a schematic map of the work contained within this thesis.

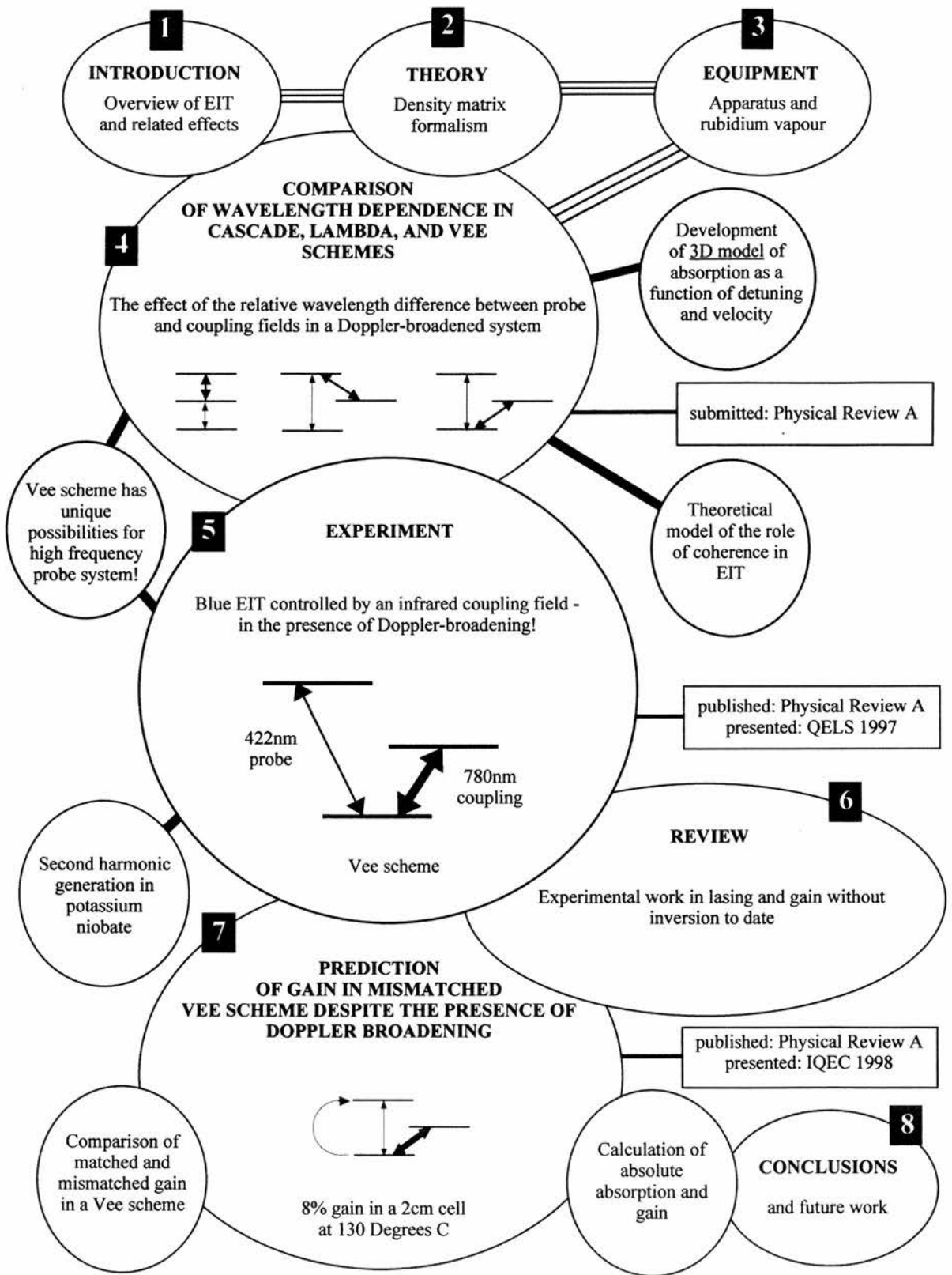


Figure 1.11: A schematic map of the work presented in this thesis.

1.5 Related Effects and Applications of EIT

The following presents a cross-section of the research carried out in the field of EIT and quantum coherence. These various strains of research are treated in a qualitative fashion due to the restrictions of space. Areas of study that are directly relevant to the work in this thesis will be treated in more detail.

1.5.1 The Autler-Townes Effect

The transparency window created in EIT occurs in association with Autler-Townes splitting. Research at the University of St. Andrews has shown that there is an important interplay between Autler-Townes splitting and EIT [23].

The Autler-Townes effect is named after the scientists that reported its discovery in 1955 [24]. It is also called the ac, or dynamic, Stark effect since it is the high frequency analogue of the dc Stark effect.

Upon the application of a laser beam the levels at each end of an atomic transition split into two components separated by Ω_{obs} , given in Eq. (1.8):

$$\Omega_{\text{obs}} = \sqrt{\Delta^2 + \Omega^2} \quad (1.8)$$

The observed splitting is made up of Δ , the detuning of the laser from resonance with the transition; and Ω , the Rabi frequency induced by the applied field. The Rabi frequency is defined, in angular terms, as:

$$\Omega_{ij} = \frac{\mu_{ij} E}{\hbar} \quad (1.9)$$

and will be further discussed in Chapter 2. In a phenomenological sense, the Rabi frequency can be regarded as a parameter which indicates the strength of the interaction between the atom and the incident radiation. It corresponds to the rate at which the population would flop back and forth between the levels of an undamped system.

The absorption lineshape for transitions to a level showing an Autler-Townes doublet is simply the addition of the two split sub-components of that level. The splitting induced on the coupling transition is shown schematically in Fig. 1.12 for the on-resonance case. A fuller treatment of Autler-Townes splitting, including the detuned case, will be considered in Section 4.3. The lineshape shown previously in Fig. 1.7 (b) shows the EIT

transparency window falling between the absorption peaks of the two sub-levels. The position of the transparency window is determined by the two-photon resonance condition; its width by the coupling field Rabi frequency; and its depth by the nature of the driving coherence controlled by the ratio of field strengths, the atomic decay rates and the dephasing on the specific transition in question. However, according to both the theory and experiment described in this thesis, we see that these conditions are only true in a Doppler free system. Moreover, in the presence of Doppler-broadening, Autler-Townes splitting can be an important determining factor in both the width and the depth of the induced transparency.

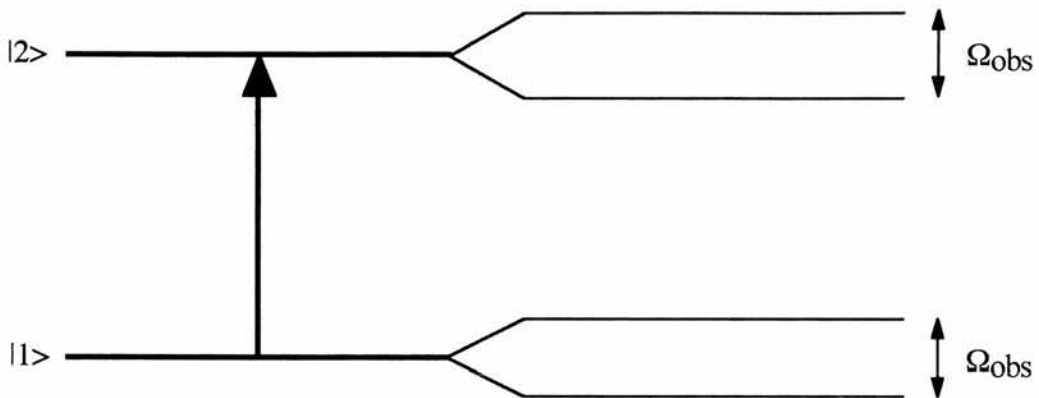


Figure 1.12: *Autler-Townes splitting on a transition by the application of a coherent laser field, inducing a Rabi frequency of Ω . The observed splitting, Ω_{obs} , is given by Eq. (1.8).*

1.5.2 Dressed State Analysis

Dressed state analysis is an alternative viewpoint in which an altered form of the Hamiltonian [25-28] leads to a new basis set of levels, referred to as ‘dressed states’. The Hamiltonian of the system is taken as the sum of the isolated atom Hamiltonian, the field Hamiltonian and the interaction Hamiltonian. This approach leads, intrinsically, to the inclusion of Autler-Townes split levels in the basis set. In this analysis, EIT is the manifestation of an interference between the pair of closely spaced dressed states (Autler-Townes split by the applied field Rabi frequency) coupled by their lifetime broadening [29]. The described picture is the semiclassical dressed state model. It is also possible to

adopt a fully quantum dressed state picture by quantising the radiation field, via the photon creation and annihilation operators [25,30], as well as the atom. The dressed state model has been used, in one form or another, in various research concerning quantum coherence [31,32].

The work presented in this thesis takes the semiclassical approach of density matrix formalism (described in Chapter 2). This method describes the interaction of light and matter in terms of a quantised atom and a classical electric field. The density matrix model is a well established means of studying the interaction of light and matter [33] that has been widely applied to experiments in this field [34-36].

1.5.3 Nonlinear Enhancement

The presence of a transparency at line centre has fortuitous consequences for nonlinear optics. Nonlinear effects are enhanced if a light field is tuned closer to resonance with a transition. A rapid increase in high order susceptibilities occurs as an optical field tunes onto resonance. One would therefore expect an enhancement of nonlinear optical processes such as second harmonic generation. However, at line centre the generated wave would suffer greatest re-absorption in the medium. The application of EIT, with its ability to create a transparency on resonance, removes the detrimental effect of re-absorption at the negligible expense of an additional laser source.

A theoretical paper published by Harris *et al* in 1990 predicted improvements in conversion efficiency for a four wave sum frequency mixing process [37]. The first experimental demonstration of nonlinear enhancement also came in 1990 [38]. The next year Hakuta, Marmet and Stoicheff used a dc electric field rather than an optical coupling field to induce a transparency, resulting in the reduction of second harmonic re-absorption in hydrogen [39]. EIT can also be used to reduce the absorption of the input wave causing a similar enhancement of a nonlinear process [40]. Zhang *et al* have recently demonstrated the nonlinear generation of extreme-ultraviolet radiation, enhanced due to EIT, in hydrogen [41], while a four wave mixing scheme was employed by Dorman *et al* to generate vacuum ultraviolet in krypton [42]. In the latter case an enhancement of conversion efficiency, due to EIT, of greater than 10^2 was estimated.

Other applications for nonlinear optical processes include the use of EIT to control phase matching and dispersion in four wave mixing processes [43,44], the generation of bright squeezed light [45], and the reduction of noise fluctuations in the probe beam [46,47]. In addition, gain without population inversion has been predicted for a coherently driven two-level atom interacting with a broadband squeezed vacuum [48].

1.5.4 Quantum Coherence and OPOs

A fairly recent development for quantum coherence in the field of nonlinear optics has been the proposal of an optical parametric oscillator (OPO) pumped by coherently trapped atoms [49]. By virtue of quantum coherence effects this OPO has a projected bandwidth that is of the order of the centre frequency (the frequency at the signal and idler waves are degenerate).

OPOs have been around for a long time [50] and are now well documented devices [51,52] with a plethora of useful applications [53,54]. The energy level diagram describing a standard OPO is shown in Fig. 1.13. Although this is not normally the picture used to characterise an OPO, it is useful when considering the role of quantum coherence in the particular device proposed by Harris [49].

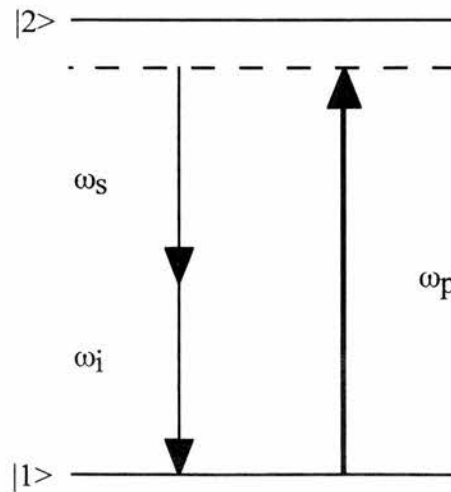


Figure 1.13: Energy level scheme for a simple optical parametric oscillator.

The operation of an OPO is based on the idea of splitting a pump photon into two separate parts, corresponding to the output signal and idler photons. This nonlinear process must obey the law of energy conservation:

$$\omega_p = \omega_s + \omega_i \quad (1.10)$$

where ω_p , ω_s , and ω_i are the angular frequencies of the pump, signal, and idler photons respectively. The pump photon must also split in such a way as to conserve momentum. This condition is expressed in Eq. (1.11):

$$\Delta k = k_p - k_s - k_i \quad (1.11)$$

where k_p , k_s , and k_i are the wavevectors of the pump, signal, and idler fields respectively. Equation (1.11) can be re-written in terms of the angular frequency:

$$\Delta k = \frac{1}{c} (n_p \omega_p - n_s \omega_s - n_i \omega_i) \quad (1.12)$$

These two conditions are not satisfied for all ratios of signal and idler frequency because the refractive index, n , experienced by each light field in the medium, is dependent on frequency. Equation (1.12) is referred to as the phase matching condition, and it is only satisfied when the phases of the light fields propagating through the medium are matched. This condition is normally only fulfilled for a specific ratio of signal and idler frequencies in a given system.

The OPO proposed by Harris in lead vapour is driven by quantum coherence rather than a straight forward pumping field. Figure 1.14 shows the energy level scheme which depicts a simple Lambda configuration where the signal and idler photons are produced on the unlinked transition between levels $|1\rangle$ and $|2\rangle$.

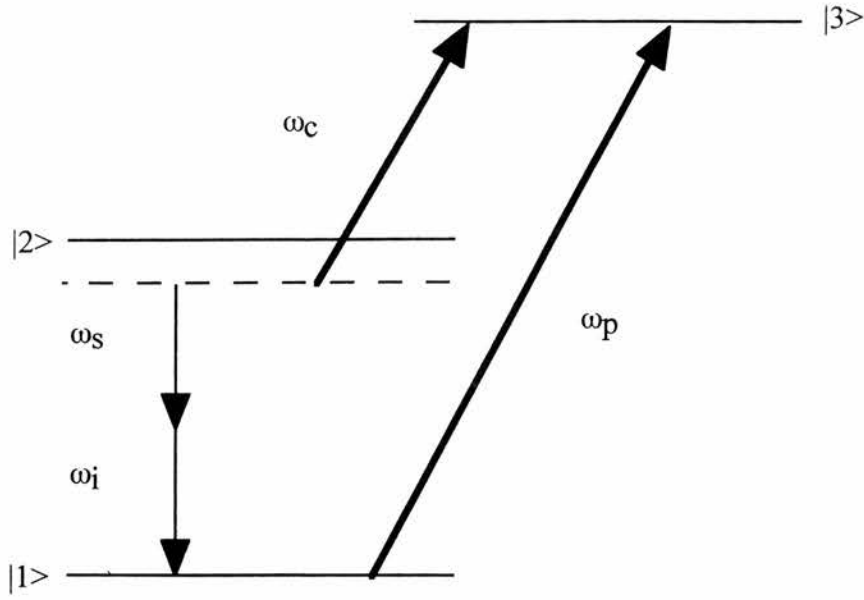


Figure 1.14: Schematic of quantum coherence OPO configuration proposed by Harris.

In an EIT experiment we would be looking for transparency on the probe transition, level $|1\rangle$ to level $|3\rangle$; however, here we are concerned with the novel phase matching properties on the unlinked transition. The OPO is driven, in effect, by the trapped populations in states $|1\rangle$ and $|2\rangle$. Both the coupling and probe fields employed are strong and drive the unlinked transition to a point of maximum coherence which equalises the populations in states $|1\rangle$ and $|2\rangle$ and reduces the population in state $|3\rangle$ to zero. With the populations thus trapped the effects of dispersion are compensated to the extent that the phase matching condition holds across a bandwidth spanning the entire transition. Phase matching is thus maintained for any ratio of the signal and idler frequencies that satisfy energy conservation. In this system the energy conservation is given by:

$$\omega_s + \omega_i = \omega_p - \omega_c \quad (1.13)$$

and the phase matching condition becomes:

$$\Delta k = \delta k - k_s - k_i \quad (1.14)$$

where δk is related to the phase variation of the coherence on the unlinked transition [49].

1.5.5 Phaseonium

The initial description of EIT has been concerned exclusively with its effect on the optical property of absorption. However, there is a second optical property that is significantly affected by the induced transparency, that of refractive index. The latter is directly related to the absorption in such a way that the window in the absorption profile generated by EIT has a corresponding feature in the refractive index profile. This relationship can be seen in Figure 1.15. The presence of an anomalously high refractive index in a medium that is virtually transparent was first recognised by Scully in 1991 [55]. Scully classed this medium as an entirely new type of matter called ‘phaseonium’. This is justified by the fact that normal materials exhibiting a high refractive index also suffer from an inherently high absorption.

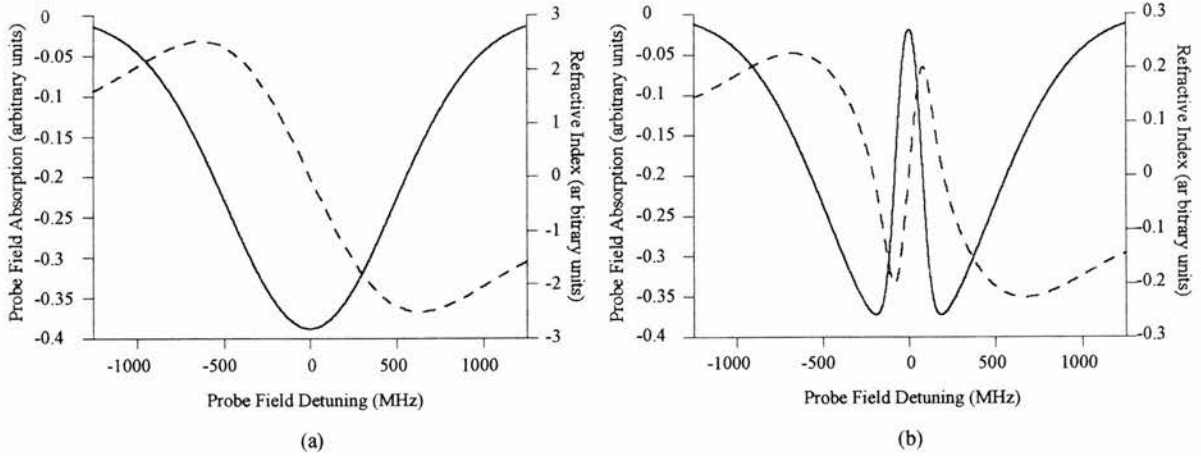


Figure 1.15: Absorption, ρ_{12}^i in arbitrary units, (solid line) and refractive index (dashed line) profiles (a) in the absence of the coupling laser and (b) in the presence of the coupling laser. The latter case depicts EIT.

Figure 1.16 displays the absorption and refractive index profiles for the specific case of a phaseonium type medium. Phaseonium is arranged such that a maximum in refractive index is coincident with the frequency for which the absorption is zero. The only restriction on the refractive index therefore becomes the particle density that can be achieved in the medium.

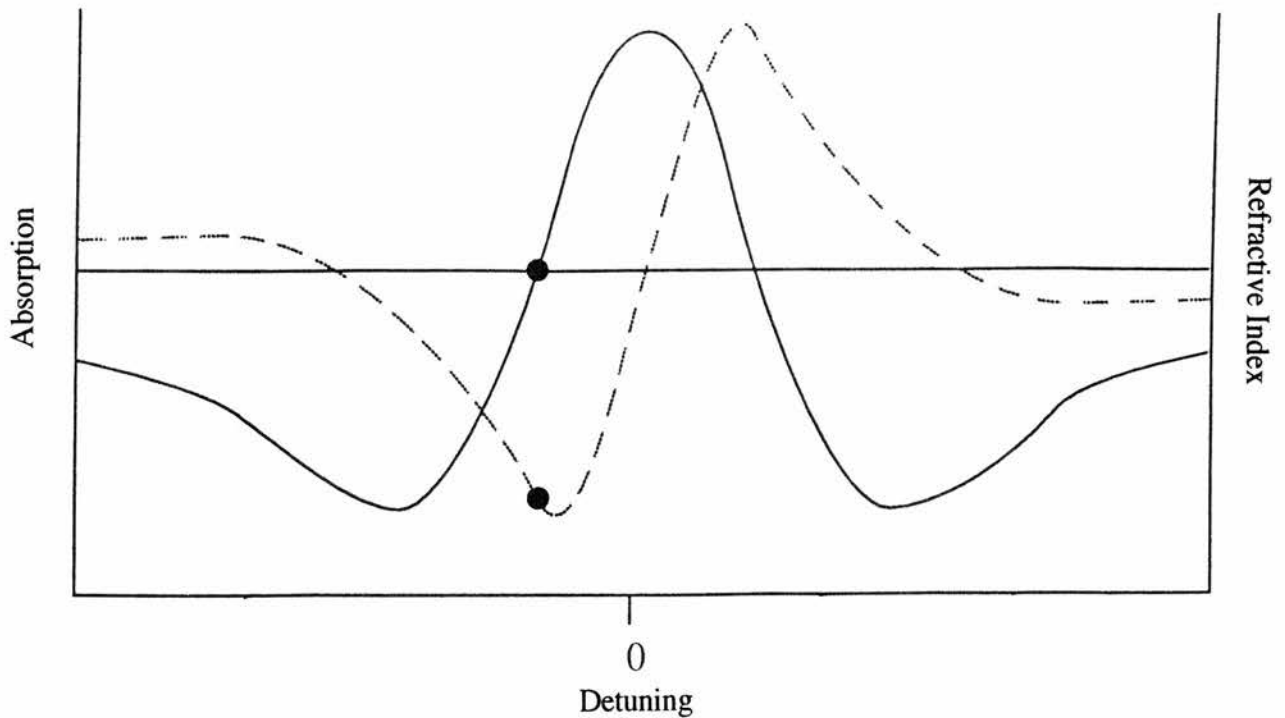


Figure 1.16: *Absorption (solid line) and refractive index (dashed line) profiles required in a medium to create the properties of phaseonium. The marked points on the profiles indicate the coincidence of a zero in absorption and a maximum in refractive index.*

There are many applications for phaseonium, the most straightforward of which is its potential to enhance the performance of microscopes. The resolution attainable with a microscope is limited by the refractive index of the immersing medium. The use of a medium with a higher refractive index will augment the microscope's resolution; however, it also increases its absorptive loss which is detrimental to the microscope's performance. The advent of phaseonium removes this constraint, allowing a high refractive index to be employed without a high absorption. Another important application, which has been discussed by Fleischhauer and Scully [56], is the fabrication of highly sensitive magnetometers based on atomic phase coherence.

Other work concerning the effect of EIT on dispersion has been carried out by various research groups [57-59]. One such study led to the discovery of electromagnetically induced focusing.

1.5.6 Electromagnetically Induced Focusing

In January 1995 the University of St. Andrews' research group published a paper detailing the observation of an entirely new effect occurring within EIT [60]. Moseley *et al* provided experimental evidence that the coupling laser induced a variable lens in the gain medium in addition to rendering the medium transparent. This effect was named electromagnetically induced focusing (EIF).

The dependence of refractive index on absorption has been established. It follows that in the EIT regime the refractive index depends on the level of the induced transparency set by the intensity of the coupling laser. The refractive index in a medium subject to EIT is therefore controlled by the coupling laser intensity.

A normal lens is made from a material of constant refractive index with a thickness that is varied so that an incident light beam will experience differing path lengths through the material. The lens creates a variation in the velocity of light across the profile of the beam. This result is effectively the same as inserting a medium of constant thickness and varying refractive index.

The intensity of a laser beam is greatest in the centre, decreasing radially outwards. The spatial variation in the intensity of the coupling laser results in a spatial variation in the refractive index of the active medium. The probe beam experiences this varying refractive index which has an effect equivalent to that of a regular lens. Experiments have shown that the induced lens can cause both focusing and defocusing effects by tuning the probe laser frequency through the EIT window.

In addition, the region of transparency created in the cell acts like an aperture in the path of the propagating probe beam. This diffraction effect is inextricably linked to the lens-like behaviour of the medium and observed effects are a combination of these phenomena. The spectacular nature of these effects is demonstrated in Figs. 1.17 and 1.18 [61].

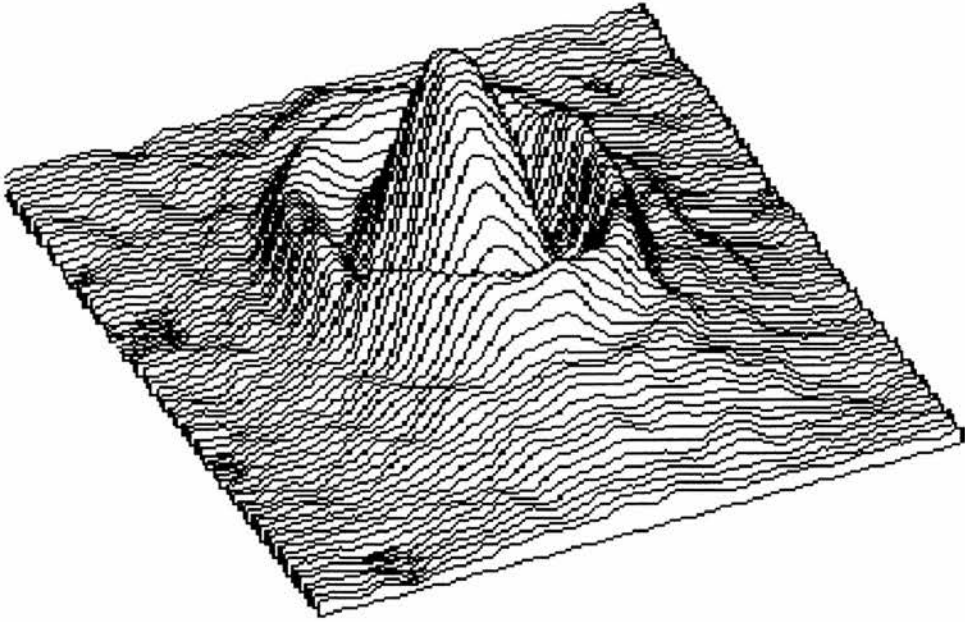


Figure 1.17: *Three-dimensional plot of the probe beam cross-section with the coupling laser focused within the probe beam waist. In this configuration the coupling beam induces a small circular transparency within the gain medium, smaller than the probe waist, that acts like an aperture producing an Airy disc diffraction pattern. This image was obtained using a CCD camera.*

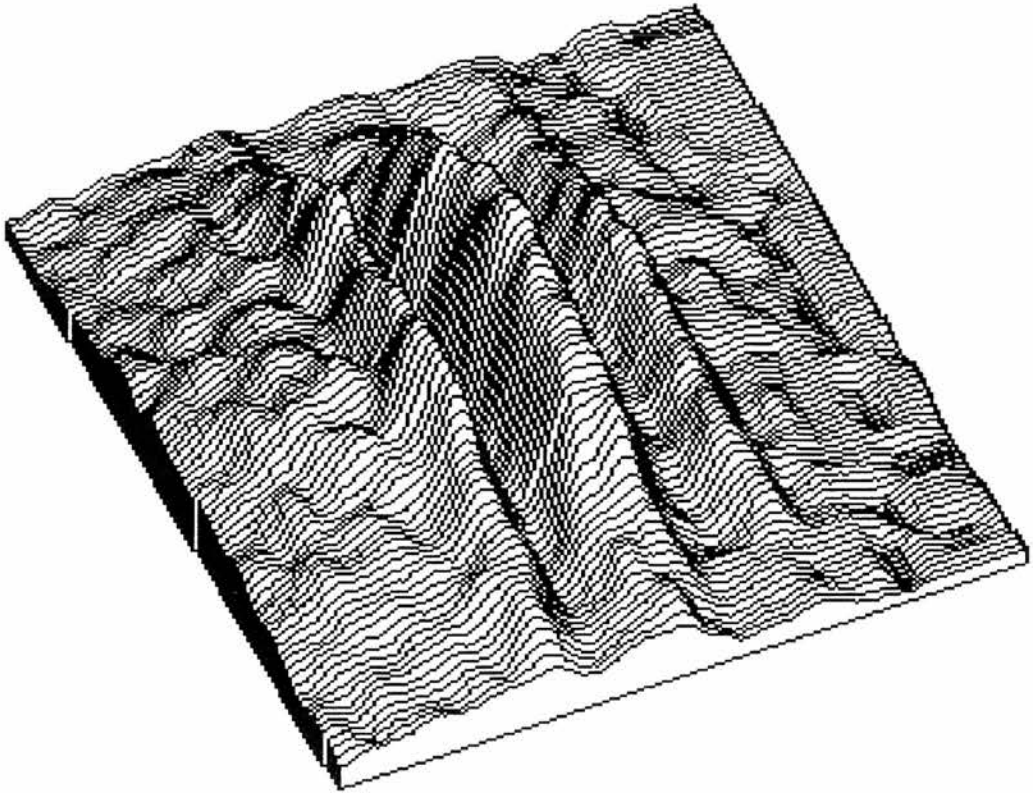


Figure 1.18: *Three-dimensional plot of the probe beam cross-section created by placing a cylindrical lens in the coupling beam. This instrument acts to induce a slit like transparency in the gaseous gain medium that produces the observed interference fringes.*

The probe experiences two unusual effects due to EIT: a medium that should attenuate it becomes transparent and the same medium acts like a lens. The discovery of EIF is important both for the applications it offers and the implications it holds for the further study of EIT.

1.5.7 Inversionless Lasing

Lasing without inversion has undoubtedly been the central focus of EIT research. A plethora of theoretical studies has been published and the first experimental evidence was supplied by Zibrov *et al* in August 1995 [15]. However, this was a proof of principle experiment and no commercially viable system has yet been developed.

The theory of lasing without inversion follows quickly on the heels of EIT. Having induced a transparency, a population inversion is no longer required to consummate laser action. In the absence of absorption, theory indicates that we only need a small fraction of population in the upper laser level to achieve gain. This modest excited state population can be accomplished with a weak incoherent pump; however, inversionless lasing is not so easily conceived in practice. This is chiefly due to the difficulty of isolating a real atomic system to match the ideal three level schemes associated with EIT. In reality, atomic systems are far more complex and the experimenter faces problems such as optical pumping and the breakdown of EIT due to the presence of additional coherent fields.

This experimental reality begs the question - why pursue inversionless lasing? Its implementation requires an additional coupling laser and traditional laser systems are already practically realisable. However, existing laser technology cannot access high frequency transitions because they inherently decay at rapid rates. The pumping requirements are impractically high because the population falls out of the upper level as soon as it is introduced. Although lasing without inversion may be problematic, it provides potential access to these higher frequency transitions as only a modest upper laser level population would be necessary rather than a complete inversion. This new breed of high frequency lasers could include X-ray and gamma ray systems.

Chapter 6 of this thesis will provide a comprehensive review of all the experimental work on inversionless amplification and lasing that has been carried out to date.

1.5.8 Progress in Quantum Coherence

From small beginnings, research into quantum coherence effects, such as EIT, has mushroomed. Contemporary work now involves such topics as EIT in solids, coherence effects controlled by microwave or RF fields, and EIT and lasing without inversion (LWI) in Doppler-free environments. 100% transparency due to EIT has been demonstrated in a rare earth doped crystal [62], and studies have been carried out in Australia characterising the absorption and dispersion profiles obtained through quantum coherence in the nitrogen vacancy centre in diamond [63]. Various research has also been carried out in semiconductor materials [64-66], and the enhancement of nonlinear effects, due to EIT, has been demonstrated in a spectral hole-burning crystal [67]. In addition, studies concerning

the possibility of semiconductor lasers without inversion have been carried out [68], including one scheme in which the coherence is controlled by a dc field [69]. Clearly, the field of quantum coherence is by no means confined to gaseous media.

One of the recent experiments carried out in a solid also demonstrates the realisation of transparency induced by a microwave field [70]. However, some doubt has been cast as to the validity of these results, particularly to what degree optical pumping is responsible for the observed decrease in absorption. The idea of controlling an optical field with a radio frequency (RF) field is not new, and various studies have been carried out on lasing without inversion in such a configuration [71-73]. Interestingly, a group in India have theoretically demonstrated the use of an additional RF field to achieve Doppler-free absorption within an EIT transparency window [74].

The use of a Doppler free environment allows us to pick out the sharp spectral features of EIT at very low powers. To this end, EIT has been demonstrated experimentally in laser cooled rubidium in a magneto-optical trap [75], and independently by another group who attributed the observed absorption and dispersion effects solely to Autler-Townes splitting [76]. In the latter case, the presented curves are clearly an excellent example of EIT [76]. More recently, Kitching presented experimental results of inversionless gain achieved for rubidium atoms in a magneto-optical trap [77]. In such a configuration, a low population density of cooled atoms can be probed to obtain a virtually Doppler-free absorption profile. EIT has also been studied in cold free atoms where the medium is probed immediately after the magneto-optical trapping fields are switched off [78]. A group at the University of Florence has reported the use of EIT to actually trap atoms in a novel type of dark spontaneous-force optical trap [79]. Conversely, the application of a strong coupling field has also been shown to switch off radiation trapping [80].

Another method of obtaining virtually Doppler-free measurements is to observe the atomic medium in a collimated beam where the transverse velocity component of the individual atoms is minimised so that a probe laser beam perpendicular to the atomic beam will encounter a very small Doppler width. Laser oscillation without population inversion has been observed in a sodium atomic beam [81], and both theoretical and experimental

studies of the temporal evolution of coherent population trapping have been carried out [82].

Other interesting developments include the prospect of inversionless lasing in molecules [83], the use of EIT in a scheme to enhance spectral resolution [84], lossless channelling in waveguides [85], and applications of quantum coherence to optical data storage [86] and optical NOT gates [87].

1.6 The Role of Doppler-broadening in EIT

Early experiments in EIT were carried out in gaseous media [19,88,89] which are inherently subject to the effects of Doppler-broadening. While some experiments are now being carried out in solids [62,63,67] the majority still take place in a gas.

Doppler-broadening is a form of inhomogeneous broadening in which the absorption profile of a gaseous medium is spread out in frequency due to the random spread of atomic velocities. A given velocity, of an atom relative to the laser source, will result in a Doppler shift in the laser frequency. Generally speaking, we can assume a Maxwellian distribution of atomic velocities in a gas. Consequently, there will be a similar spread of frequencies at which absorption of the incident narrowband laser radiation can occur. The problem with this, in terms of quantum interference, is that it is only possible to resolve such effects when the lower level of the probe transition is Autler-Townes split beyond the Doppler width. In practical terms, this means we require a coupling laser of a sufficient power to split the Autler-Townes absorption components so that they can be resolved outside the Doppler-broadened profile. At least, this has been the position taken by most researchers in the field [22].

This fundamental power requirement for the observation of EIT in a Doppler-broadened medium is no problem for pulsed laser sources [19]. Continuous wave (cw) lasers, however, cannot readily reach the powers necessary to achieve such large splittings. Nevertheless, the use of continuous wave lasers is still desirable since observed effects are easier to understand in the steady state regime. The philosophy of researchers seeking to observe quantum coherence effects in gases has been to reduce the effects of Doppler-broadening. There are several methods by which this can be achieved, such as utilising an atomic beam [81] or trap [75]. Another widely employed method is to ‘match’ the wavelengths of the probe and coupling fields. The proper choice of co- or counter-propagating beams can then render the medium virtually Doppler free for any of the three EIT schemes. For example, in the Cascade scheme counter propagating probe and coupling beams of the same wavelength will ensure that the two-photon process is Doppler-free. This result occurs because the Doppler shifts associated with each radiation field will be of the same magnitude and opposite sign. The net Doppler shift associated with the two-photon process will therefore be zero. This method has been employed in many cw

quantum coherence experiments [88,89], including the first observation of inversionless lasing [15]. Indeed, rubidium has been chosen for many such experiments because of the presence of infrared transitions closely matched in frequency [90].

1.6.1 Previous Work at St. Andrews

Contrary to this view of continuous wave EIT in the presence of Doppler-broadening, recent study has shown that the interplay between the Autler-Townes effect and EIT creates a situation in which the induced transparency is still significant for mismatched wavelengths [23,91]. The surprising result of the work carried out at the University of St. Andrews [23] was that the best EIT is achieved for coupling wavelengths less than that of the probe in the Cascade configuration. Figure 1.19 shows the level of theoretically calculated transparency as a function of wavelength mismatch in a Cascade scheme. Experimental points are also presented, verifying the original theoretical predictions.

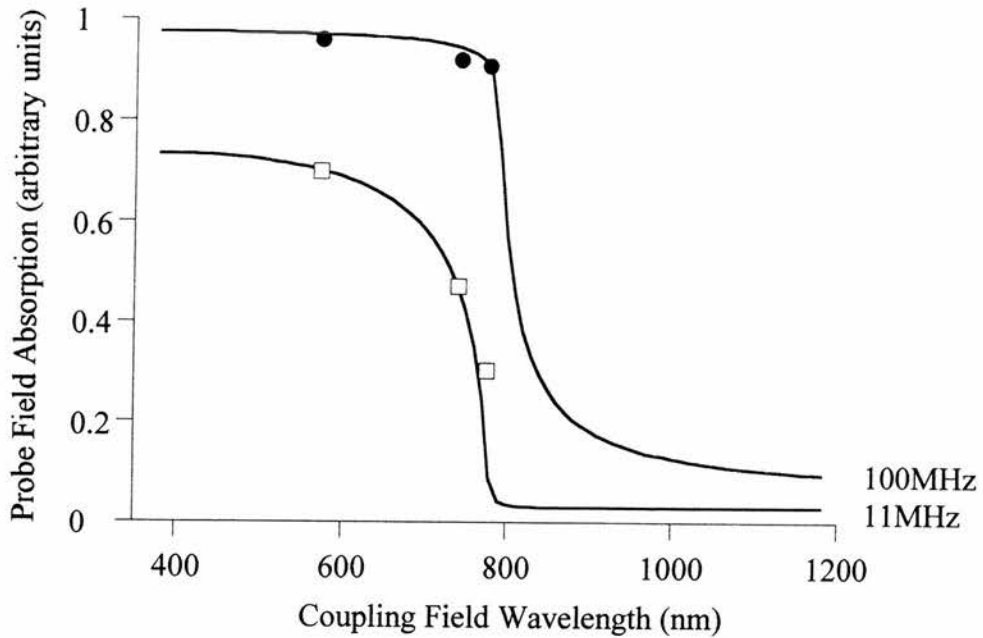


Figure 1.19: *Experimental and theoretical data demonstrating the relationship between the level of transparency (ρ^i_{12} in arbitrary units) and wavelength mismatch in a Cascade scheme. The probe wavelength is 780nm and the coupling wavelength is varied. The solid circles represent experimental measurements taken with a laser power that induced a linear Rabi frequency of approximately 100MHz, and the hollow squares represent experimental measurements taken with a laser power that induced a Rabi frequency of 11MHz.*

1.6.2 Current Work at St. Andrews

While a description of the roles played by Autler-Townes splitting and EIT in the production of an experimental transparency feature was supplied by Shepherd for the Cascade scheme [23], this explanation has been updated and extended to the case of all three energy level configurations that may be employed for EIT (see Chapter 4).

Importantly, further research presented in this thesis predicts that EIT in a Vee scheme is relatively insensitive to the mismatch of the probe and coupling wavelengths. Figure 1.20 shows the effects of wavelength mismatch in each of the EIT schemes.

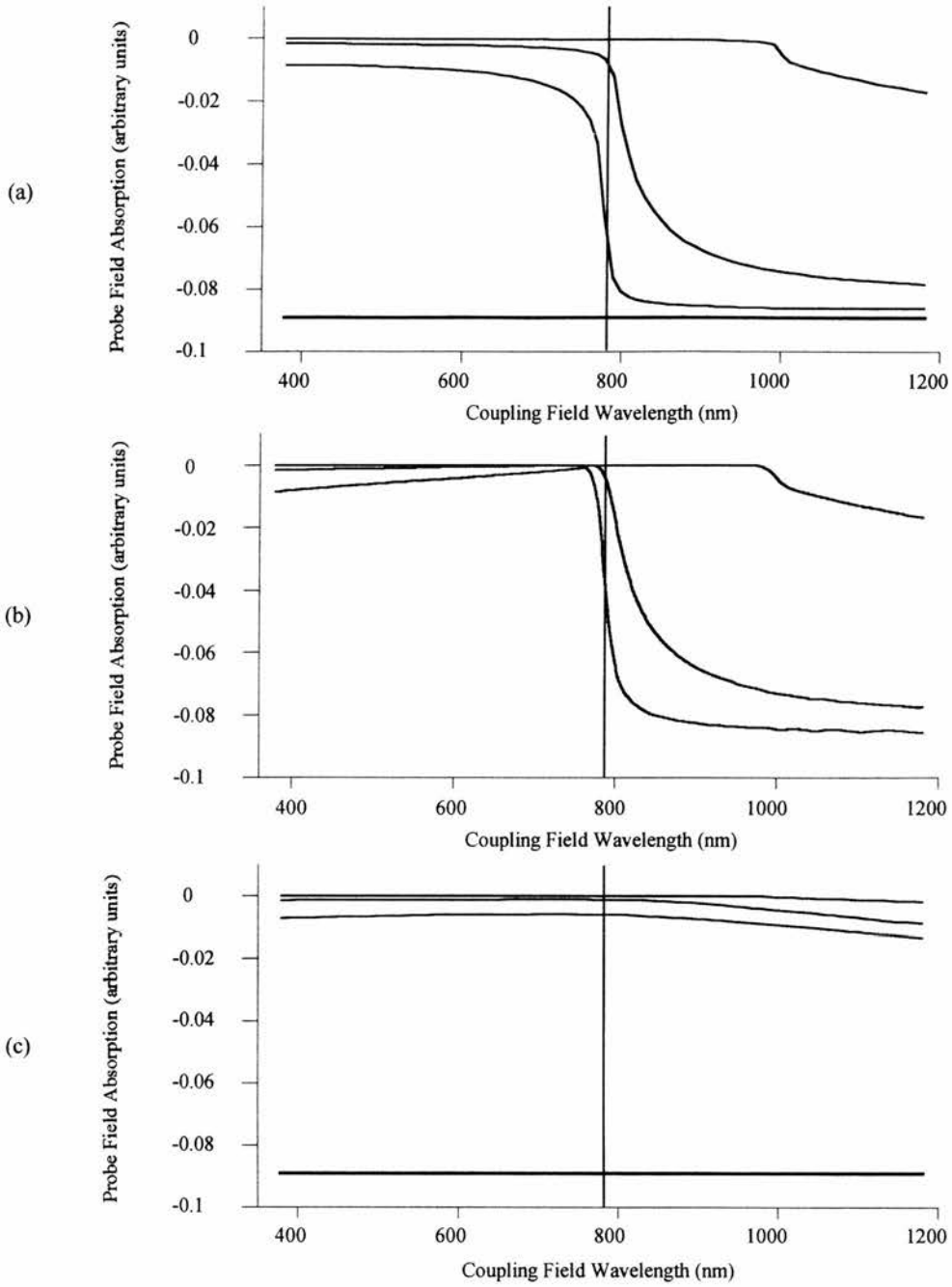


Figure 1.20: The probe field wavelength is 780nm and the coupling field wavelength is varied between 380nm and 1180nm. The solid vertical line indicates matched wavelengths. The solid horizontal line in (a) and (c) indicates the maximum absorption predicted in the absence of the coupling field. The on-resonance Probe field absorption, ρ_{12}^i in arbitrary units, (increasing vertically downwards) is plotted for (a) the Cascade scheme, (b) the Lambda scheme, and (c) the Vee scheme.

Figure 1.20 predicts that mismatched EIT is observable in a gas despite the effects of Doppler-broadening. This discovery heralds a great step forward in inversionless lasing research since it opens access to high frequency transitions in Vee-type schemes. Using Shepherd's research as a starting point this thesis attempts to approach the study of EIT with a new philosophy. *Rather than attempting to reduce the effects of Doppler-broadening, we accept them and investigate the extent to which EIT can still be used to produce practical high frequency laser sources.*

1.6.3 Other Work on the Role of Doppler-broadening

Several research groups have paid close attention to the effects of Doppler-broadening in steady state quantum coherence experiments. A group in Arkansas published a theoretical and experimental study of EIT in a Cascade scheme subject to inhomogeneous broadening [91]. While they did state that a deeper transparency was possible for coupling wavelengths less than that of the probe, they focused on the case of matched frequencies. As has already been discussed, the Doppler shifts associated with the probe and coupling fields cancel so that the two-photon resonance is essentially Doppler-free. In a more recent paper the same group further scrutinises the frequency matching effect [92], showing that the coherence is dominated by the two-photon process and the medium is only transparent to those probe frequencies that satisfy the two-photon resonance condition.

Two separate studies have been undertaken into the effects of Doppler-broadening in cw inversionless laser systems [93,94]. Both studies focused on the choice of co- or counter-propagating beams in a Cascade or Ladder scheme [93] and a Vee scheme [94]. The conclusions emphasise that in a matched wavelength situation the appropriate choice of beam geometry can lead to Doppler cancellation. In a Cascade scheme the two-photon Doppler shifts will cancel if the beams are counter-propagating, and in a Vee or Lambda scheme this result can be achieved for co-propagating beams.

One of these groups also reported work on sub-Doppler resolution in inhomogeneous media [95,96]. Their findings have general relevance in the field of quantum optics and involve resolving a component of the probe absorption broadened by its natural lineshape. The realisation of this effect relies on the Doppler cancellation achieved through

matching the probe and coupling wavelengths. As the coupling field is detuned from resonance, in a Cascade or Lambda scheme, EIT is destroyed and the two-photon absorption is separated spectrally from the single photon absorption profile because the two-photon resonance point, unlike the single photon absorption, is dependent on the coupling laser frequency. The separate resolution of single and two-photon absorptions has been demonstrated experimentally [97], and used in the realisation of a matched wavelength inversionless gain scheme in rubidium [98]. This effect was also characterised both theoretically and experimentally in an earlier paper by Moseley *et al* [99], and it was discussed in Section 1.3.2 of this chapter in the context of two route interference leading to EIT. This effect is certainly of interest, but since it relies on matched wavelengths it is not useful in producing inversionless lasers in the high frequency regime.

Finally, Zhu has shown that up-conversion is possible in four level systems modelled in the absence of Doppler-broadening. He predicts that the strength of the effects predicted should make it possible to realise such a scheme in a real system at cw laser powers [100].

The approach taken in this thesis is markedly different to that employed in other research groups. While it is acknowledged that Doppler-broadening does make it difficult to achieve high frequency laser systems, the outlook is not as bleak as is generally believed. Studies have shown that inversionless gain is feasible in a Doppler-broadened system in which the wavelengths of the probe and coupling fields are markedly different. Indeed, in some cases the Doppler effect actually helps us to overcome the broadening with which it is associated.

1.7 Thesis Overview

This first chapter has taken a broad look at quantum coherence effects, providing a general insight into this field of study. The scene has been set for a detailed examination of atomic coherence against the background of the interaction of light and matter. The work to which this thesis pertains represents a small piece in a very large jigsaw, allowing us to gain a greater understanding of this fundamental interaction.

Chapter 2 is devoted to an exposition of the theoretical methods of analysis employed in this work. Much attention is devoted to the semiclassical density matrix formalism of quantum mechanics, the merits of this approach, and some examples of its application.

The apparatus and materials used in subsequent experimental work are presented in Chapter 3. Details and relevant attributes of the laser systems employed are given along with the specifications of all ancillary equipment. Importantly, an overview of rubidium atomic vapour, the medium in which atomic coherence effects are studied, is provided. Particular attention is given to any equipment designed or purchased specifically for the work in this thesis.

Chapter 4, describes a study into the effects of varying the coupling wavelength in the Cascade, Lambda and Vee-type EIT schemes when the probe wavelength is kept constant. This chapter contains the central argument of my thesis upon which the subsequent experiment and theory relies. We see that transparency can be induced in all three schemes despite Doppler effects and that a significantly improved reduction in absorption is obtained by increasing the frequency of the coupling field. Crucially, it is also possible to realise a scheme for which the probe frequency is well in excess of the coupling field frequency. This goal can be accomplished in all energy level schemes if we Autler-Townes split beyond the Doppler width, but only in the Vee-type configuration for sub-Doppler width driving Rabi frequencies.

Chapter 5 describes the successful creation of transparency at a blue wavelength, induced by an infrared coupling field, in a Doppler-broadened medium. The significance of this work lies in the fact that it represents the first experimental realisation of cw mismatched transparency in a medium subject to the effects of Doppler-broadening. Indeed, until recently it was thought impossible to achieve EIT in such a way without

relying on the high power of pulsed laser systems. The theoretical explanation of this system is presented along with detailed experimental results.

The subsequent chapter, Chapter 6, provides an authoritative review of experimental inversionless lasing and gain to date. The different methods of obtaining lasing in the absence of inversion are discussed, focusing on the use of quantum coherence to drive the initial transparency that makes lasing without inversion (LWI) possible. This chapter sets the scene for the ensuing study of mismatched inversionless gain.

Chapter 7 discusses the theoretical analysis of taking the mismatched transparency one step further to produce gain. A general theory is considered with a view to proposing an alternative method of producing gain in mismatched Doppler-broadened systems; thus, obviating the need to move into Doppler-free regimes by the employment of atomic beams or traps. A comparison of matched and mismatched gain systems is explored within a hypothetical atomic system based on rubidium vapour. The resulting theory is applied to a realistic experimental situation. A theoretical means of calculating the absolute absorption or gain is developed and applied to the considered experimental scheme so that our mismatched system may be directly compared to those discussed in Chapter 6.

This thesis concludes with suggestions for possible further work in this area. The future of gain in Doppler-broadened media is assessed in the context of the practical realisation of robust mismatched systems. Over the past three years the possibility of inversionless lasing within inhomogeneously broadened Doppler media has been resurrected, leaving the future of lasing without inversion wide open.

References

- [1] M. Planck, Verhandlungen der Deutschen physikalischen Gesellschaft, Dec 14, 237, (1900).
- [2] E. Rutherford, Phil. Mag. 2I (sixth series), 699, (1911).
- [3] N. Bohr, Phil. Mag. 26, 27, 29, and 30, (1913, 1914, and 1915).
- [4] A. Einstein, Phys. Zs. **18**, 121, (1917).
- [5] B. L. Van der Waerden, *Sources of Quantum Mechanics*, (North-Holland publishing company, (1967)).
- [6] A. L. Schawlow, and C. H. Townes, Phys. Rev. **112**, 1940, (1958).
- [7] T. H. Maiman, Phys. Rev. Lett. **4**, 564, (1960).
- [8] A. E. Siegman, *Lasers*, (University Science Books, (1986)).
- [9] S. E. Harris, Phys. Rev. Lett. **62**, 1033, (1989).
- [10] S. E. Harris, Phys. Today. July, (1997).
- [11] R. Moseley, and M. Dunn, Phys. World. January, (1995).
- [12] J. H. Marangos, J. of Mod. Opt. **45**, 471-503, (1998).
- [13] M. O. Scully, and S. Zubairy, *Quantum Optics*, (Cambridge University Press, (1997)).
- [14] B. G. Levi, Phys. Today. September, (1995).

- [15] A. S. Zibrov *et al*, Phys. Rev. Lett. **75**, 8, (1995).
- [16] U. Fano, Phys. Rev. **124**, 1866, (1961).
- [17] E. Arimondo, G. Orriols, Lettere Al Nuovo Cimento. **17**, 10, (1976).
- [18] H. R. Gray, R. M. Whitley, and C. R. Stroud, Opt. Lett. **3**, 6, (1978).
- [19] K. J. Boller, A. Imamoglu, and S. Harris, Phys. Rev. Lett. **66**, 2593, (1991).
- [20] M. H. Dunn, *Laser Sources and Applications*, Scottish Universities Summer School in Physics, 47th, 1995, St. Andrews, Scotland, (IoP, (1996)).
- [21] M. O. Scully, and M. Fleischhauer, Science. **263**, 21 Jan, (1994).
- [22] M. D. Lukin *et al*, Laser Phys. **6**, 3, 436-447, (1996).
- [23] S. Shepherd *et al*, Phys. Rev. A. **54**, 6, 5394, (1996).
- [24] S. H. Autler and C. H. Townes, Phys. Rev. **100**, 703, (1955).
- [25] B. W. Shore, *The Theory of Coherent Atomic Excitation*, (Wiley, New York, (1990)).
- [26] C. Cohen-Tannoudji, and S. Reynaud, J. Phys. B: At. Mol. Phys. **10**, 345, (1977).
- [27] C. Cohen-Tannoudji, and S. Reynaud, J. Phys. B: At. Mol. Phys. **10**, 365, (1977).
- [28] P. R. Berman, and R. Salomaa, Phys. Rev. A. **25**, 2667, (1982).
- [29] A. Imamoglu and S. E. Harris, Opt. Lett. **14**, 1344, (1989).

- [30] R. Loudon, *The Quantum Theory of Light*, (Oxford University Press, (1991)).
- [31] M. Löffler *et al*, Phys. Rev. A. **56**, 6, 5014, (1997).
- [32] G. S. Agarwal, Phys. Rev. A. **44**, 1, R28, (1991).
- [33] J. Vanier, *Basic theory of Lasers and Masers*, (Gordon and Breach, London, (1971)).
- [34] A. Imamoglu, J. E. Field, and S. E. Harris, Phys. Rev. Lett. **66**, 9, 1154, (1991).
- [35] R. Moseley *et al*, Phys. Rev. A. **50**, 5, 4339, (1994).
- [36] Y. Li, and M. Xiao, Phys. Rev. A. **51**, 4, R2703, (1995).
- [37] S. Harris, J. Field and A. Imamoglu, Phys. Rev. Lett. **64**, 1107, (1990).
- [38] K. H. Hahn, D. A. King and S. Harris, Phys. Rev. Lett. **65**, 2777, (1990).
- [39] K. Hakuta, L. Marmet and B. P. Stoicheff, Phys. Rev. Lett. **66**, 596, (1991).
- [40] R. Moseley, *Sum Frequency Mixing and Quantum Interference in Three Level Atoms*, (unpublished PhD thesis, University of St Andrews, (1994)).
- [41] G. Z. Zhang *et al*, Phys. Rev. A. **56**, 1, 813, (1997).
- [42] C. Dorman, J. P. Marangos, and J. C. Petch, J. of Mod. Opt. **45**, 6, 1123-1135, (1998).
- [43] S. P. Tewari, and G. S. Agarwal, Phys. Rev. Lett. **56**, 1811 (1986).
- [44] M. Jain, G. Y. Yin, J. E. Field, and S. Harris, Opt. Lett. **18**, 998, (1993).
- [45] K. M. Gheri, and D. F. Walls, Phys. Rev. A **45**, 6675, (1992).

- [46] G. S. Agarwal, Phys. Rev. Lett. **67**, 980, (1991).
- [47] M. Orszag, S. Y. Zhu, J. Bergou, and M. O. Scully, Phys. Rev. A. **45**, 4872, (1992).
- [48] P. Zhou, and S. Swain, Phys. Rev. A. **55**, 1, 772, (1997).
- [49] S. E. Harris, and M. Jain, Opt. Lett. **22**, 9, 636, (1997).
- [50] M. K. Oshman, and S. E. Harris, IEEE J. of Quan. Elect. **4**, 8, (1968).
- [51] D. L. Weinberg, Laser Focus. Apr, (1969).
- [52] R. E. Wallace, and S. E. Harris, Laser Focus. Nov, (1970).
- [53] C. L. Tang *et al*, Laser Focus World. Sept, (1990).
- [54] J. Hecht, Laser Focus World. Sept, (1993).
- [55] M. O. Scully, Phys. Rev. Lett. **67**, 1855, (1991).
- [56] M. Fleischhauer, and M. O. Scully, Phys. Rev. A. **49**, 3, 1973, (1994).
- [57] S. E. Harris, J. E. Field, and A. Kasapi, Phys. Rev. A. **46**, 1, R29, (1992).
- [58] C. Szymanowski, and C. H. Keitel, J. Phys. B: At. Mol. Opt. Phys. **27**, 5795-5812, (1994).
- [59] S. Sultana, and M. S. Zubairy, Phys. Rev. A. **49**, 1, 438, (1994).
- [60] R. Moseley *et al* , Phys. Rev. Lett. **74**, 5, (1995).

- [61] R. Moseley *et al*, Phys. Rev. A. **53**, 1, 408, (1996).
- [62] B. S. Ham, P. R. Hemmer, and M. S. Shahriar, Opt. Com. **144**, 227, (1997).
- [63] C. Wei, N. B. Manson, and J. P. D. Martin, Phys. Rev. A. **51**, 2, 1438, (1995).
- [64] W. Potz, Phys. Rev. Lett. **79**, 17, 3262, (1997).
- [65] Y. Zhao, D. Huang, and C. Wu, Opt. Lett. **19**, 11, 816, (1994).
- [66] H. Schmidt *et al*, Appl. Phys. Lett. **70**, 25, 23, 3455, (1997).
- [67] B. S. Ham, M. S. Shahriar, and P. R. Hemmer, Opt. Lett. **22**, 15, 1138, (1997).
- [68] A. Imamoglu, and R. J. Ram, Opt. Lett. **19**, 21, 1744, (1994).
- [69] Y. Zhao, D. Huang, and C. Wu, J. Opt. Soc. Am. B. **13**, 7, 1614, (1996).
- [70] Y. Zhao *et al*, Phys. Rev. Lett. **79**, 4, 641, (1997).
- [71] H. Fearn *et al*, Opt. Com. **87**, 3223-330, (1992).
- [72] V. R. Blok, and G. M. Krochik, Opt. Com. **82**, 3, 309, (1991).
- [73] K. Zaheer, Phys. Rev. A. **49**, 4, 2914, (1994).
- [74] S. N. Sandhya, and K. K. Sharma, Phys. Rev. A. **55**, 3, 2155, (1997).
- [75] S. A. Hopkins *et al*, Opt. Com. **138**, 185-192, (1997).

- [76] T. Van der Veldt *et al*, *Opt. Com.* **137**, 420-426, (1997).
- [77] J. Kitching, and L. Hollberg, *Electromagnetically induced transparency in cold atoms*, (presented IQEC, (1998)).
- [78] F. S. Cataliotti *et al*, *Phys. Rev. A.* **56**, 3, 2221, (1997).
- [79] C. Fort *et al*, *Opt. Lett.* **22**, 14, 1107, (1997).
- [80] L. Fini, and M. Mazzoni, *Opt. Comm.* **142**, 299-307, (1997).
- [81] G. G. Padmabandu *et al*, *Phys. Rev. Lett.* **76**, 12, 2053, (1996).
- [82] E. A. Korsunsky *et al*, *Phys. Rev. A.* **56**, 5, 3908, (1997).
- [83] L. Adhya *et al*, *Phys. Rev. A.* **52**, 5, 4078, (1995).
- [84] M. O. Scully *et al*, *Opt. Com.* **136**, 39-43, (1997).
- [85] J. T. Manassah, and B. Gross, *Laser Phys.* **6**, 1, 10-21, (1996).
- [86] B. S. Ham *et al*, *Opt. Lett.* **22**, 24, 1849, (1997).
- [87] T. Gantsog *et al*, *Opt. Com.* **124**, 579-594, (1996).
- [88] D. J. Fulton *et al*, *Phys. Rev. A.* **52**, 3, 2302, (1995).
- [89] Y-q. Li *et al*, *Phys. Rev. A.* **51**, R1754, (1995).
Y-q. Li, and M. Xiao, *Phys. Rev. A.* **51**, 4, R2703, (1995).

- [90] A. Weiss *et al*, IEEE Technical Digest, Fifth European Quantum Electronics Conference 1994 (Optical Society of America, Washington DC, (1994)) p. 252.
- [91] J. Gea-Banacloche *et al*, Phys. Rev. A. **51**, 1, 576, (1995).
- [92] B. Lu *et al*, Opt. Comm. **141**, 269-272, (1997).
- [93] G. Vemuri, and G. S. Agarwal, Phys. Rev. A. **53**, 2, 1060, (1996).
- [94] D-Z. Wang, and J-Y. Gao, Phys. Rev. A. **52**, 4, 3201, (1995).
- [95] G. Vemuri *et al*, Phys. Rev. A. **53**, 4, 2842, (1996).
- [96] G. Vemuri *et al*, Phys. Rev. A. **54**, 4, 3695, (1996).
- [97] Y. Zhu, and T. N. Wasserlauf, Phys. Rev. A. **54**, 4, 3653, (1996).
- [98] Y. Zhu, and J. Lin, Phys. Rev. A. **53**, 3, 1767, (1996).
- [99] R. Moseley *et al*, Opt. Com. **119**, 61-68, (1995).
- [100] Y. Zhu, J. Opt. Soc. Am. B. **11**, 5, 943, (1994).

CHAPTER 2

Theoretical Modelling of Quantum Coherence Effects

“...I think I can safely say that nobody understands quantum mechanics”

Richard Feynman

2.1 Introduction

The main body of theoretical work in this thesis is concerned with modelling the interaction of light and matter. A given atomic system is considered via the simple energy level picture; wherein, each discrete state has a defined energy, and a transition occurs between two states separated by a specific frequency. An applied optical field, of a defined frequency, may interact with a transition and is said to be on resonance when the field frequency exactly matches that of the transition. The consequences of such an interaction involve the movement of population between atomic states, refraction, and attenuation or amplification of the applied field. These phenomena are all accounted for in the density matrix model. In addition, the density matrix approach is an extension of the state amplitude model, discussed in Section 1.3.3, and as such describes an ensemble rather than an isolated atom. For this reason the density matrix is a more realistic approximation to a real experimental system.

This chapter deals initially with density matrix formalism. A general introduction is followed by a worked through derivation for a simple two level atomic system interacting with a single optical field. The theoretical modelling of this system is considered in some depth. Examples are then given of the three basic configurations for EIT: the Cascade, Lambda and Vee schemes. Three-dimensional modelling of the velocity groups within a Doppler-broadened absorption profile will be introduced in this chapter, while further theoretical methods will be discussed where they are most relevant in the remainder of this thesis. Moseley's N level rules [1], which have proved most useful in the derivation of the more complicated density matrices, will be mentioned briefly.

2.2 Semiclassical Density Matrix Formalism of Quantum Mechanics

Experiments are primarily concerned with the evolution of an atom's excited state populations when it is subject to an incident light field as well as the feedback onto the field. If the incident radiation is broadband or incoherent, rate equations can be successfully employed, using the Einstein coefficients, to accurately model the response of the atomic system [2]. However, in the case of narrowband, coherent light the time independent transition probabilities that constitute the Einstein coefficients no longer apply. The resulting strong signal processes, such as Rabi flopping, require a more complex approach. The analysis presented here uses semiclassical theory to treat the interaction of coherent light fields with the medium, while incoherent processes such as population decay are still characterised by the time independent transition probabilities. In the semiclassical theory the radiation field is treated as a classical wave with well defined amplitude and phase, and the atom is considered quantum mechanically whereby each atomic state has an associated wavefunction that follows the time dependent Schrödinger equation.

Unlike the state amplitude model, discussed in Section 1.3.3, we consider an ensemble or group of atoms excited at different times. We employ the density matrix method in which the radiation field is classical and the medium is described by density matrix elements defined as the ensemble average of the probability amplitudes. These may be on-diagonal or off-diagonal elements, relating to the atomic state populations and the atomic coherences respectively. The evolution of the density matrix elements with respect to time is described by the Liouville equation which is derived directly from the Schrödinger equation. In the density matrix model the radiation interacts with matter through perturbation in the energy Hamiltonian and the feedback of the macroscopic polarisation onto the field.

A brief account of the approach employed to obtain the density matrix for an experimental system now follows. For a more detailed exposition on the subject refer to one of the referenced texts [2-5].

The atomic wavefunction is defined as a superposition of a basis set, $\psi_n(\mathbf{r},t)$, weighted by the probability amplitudes of each element of the basis set, $a_n(t)$:

$$\Psi(\mathbf{r}, t) = \sum_n a_n(t) \psi_n(\mathbf{r}, t) \quad (2.1)$$

In general, the constituent elements of this basis correspond to the unperturbed states of an isolated atom. The density matrix is constructed of elements, ρ_{ij} , defined by the bilinear combinations of these probability amplitudes:

$$\rho_{ij} = \overline{a_j^* a_i} \quad (2.2)$$

Importantly, the above definition is an ensemble average of the combined probability amplitudes designated by the bar. It also follows from Eq. (2.2) that $\rho_{ij} = \rho_{ji}^*$ and hence, that the density matrix is Hermitian. We also have the trace normalisation condition:

$$\text{tr}(\rho) \equiv \sum_k \rho_{kk} = \sum_k a_k^* a_k = 1 \quad (2.3)$$

which follows directly from the normalisation condition of $\Psi(\mathbf{r}, t)$, in Eq. (2.1).

The wavefunction of each system in the ensemble must satisfy the time dependent Schrödinger equation. This is the starting point in the derivation of the Liouville equation [4], which describes the evolution with time of the density matrix elements:

$$\begin{aligned} \frac{\partial \rho_{ij}}{\partial t} &= -\frac{i}{\hbar} [\hat{H}, \rho]_{ij} \\ &= -\frac{i}{\hbar} \sum_{k=1}^n (H_{ik} \rho_{kj} - \rho_{ik} H_{kj}) \end{aligned} \quad (2.4)$$

In the analysis of the atom interacting with light, the Hamiltonian \hat{H} includes an interaction term, \hat{H}_I , which accounts for electric dipole interactions induced in the atom by the applied optical fields. In Eq. (2.4) the Hamiltonian is defined in the following way:

$$\hat{H} = \hat{H}^{(0)} + \hat{H}_I \quad (2.5a)$$

$$H_{ij} = H_{ij}^{(0)} - \mu_{ij} E(z, t) \quad (2.5b)$$

where, for Eq. (2.5b) the dipole matrix elements are defined by $\mu_{ij} = \int \psi_i^* H_I \psi_j dV$. If $i = j$ in Eq. (2.5b) we assume there is no permanent dipole and $H_{ij} = H_{ij}^{(0)}$. In the case for which $i \neq j$, $H_{ij}^{(0)}$ is set to zero because there is no time independent perturbation of the isolated atom Hamiltonian, and $H_{ij} = -\mu_{ij} E(z, t)$.

The elements, ρ_{ij} , comprising the density matrix characterise particular observables. The diagonal elements, ρ_{ii} , relate to the relative population of the atomic states by yielding the average probability of finding an atom, within the ensemble, in state i . The off-diagonal elements relate to the atomic coherences that arise as a result of the applied optical fields. These coherences drive the radiating electric dipoles of the ensemble. Thus, the induced polarisation, $P(t)$, can be given in terms of the off-diagonal density matrix elements:

$$P(t) = N\mu_{ij}\rho_{ij} \quad (2.6)$$

where the ensemble consists of N atoms per unit volume. From the alternative macroscopic perspective the polarisation of a medium is related to the electric field via the susceptibility, χ :

$$\begin{aligned} P(t) &= \epsilon_0 \chi E \\ &= \epsilon_0 (\chi' - i\chi'')E \end{aligned} \quad (2.7)$$

where ϵ_0 is the permittivity of free space. It is well established that the real part of the susceptibility, χ' , is proportional to the refractive index, while the imaginary part, χ'' , is related to the absorption (or gain) experienced by the electric field. The overall result of this atomic polarisation is both to change the phase delay experienced by the electric field [2], per unit length, from k to $k + \Delta k$, where:

$$\Delta k = \frac{k\chi'(\omega)}{2n^2} \quad (2.8)$$

as well as to cause the amplitude to vary exponentially with distance [2] according to $\exp[(\gamma/2)z]$ where z is the distance propagated and:

$$\gamma(\omega) = -\frac{k\chi''(\omega)}{n^2} \quad (2.9)$$

where n is the index of refraction far from resonance.

Equating (2.6) and (2.7) relates the density matrix element to the susceptibility such that the real and imaginary elements can be given as:

$$\chi'(\omega) = \frac{N\mu_{ij}^2 \operatorname{Re}(\rho_{ij})}{2\epsilon_0 \hbar \Omega_R} \quad (2.10a)$$

and

$$\chi''(\omega) = -\frac{N\mu_{ij}^2 \operatorname{Im}(\rho_{ij})}{2\epsilon_0 \hbar \Omega_R} \quad (2.10b)$$

where the angular Rabi frequency induced by the optical field is defined as:

$$\Omega_R = \frac{\mu_{ij}E}{2\hbar} \quad (2.11)$$

It should be noted that this definition of Rabi frequency is actually half of the definition employed by most authors [4]. This alteration is made as it simplifies the form of the derived density matrices. In the associated numerical models, the input Rabi frequency can subsequently be doubled to restore the consistency between experiment and theory.

The experimental work under consideration involves, exclusively, the use of continuous wave (cw) lasers to study coherence effects in atoms. We are therefore concerned with the application of the density matrix model to the analysis of steady state conditions. Previous theoretical analysis of atomic systems by Brewer and Hahn [6], utilised an analytical approach and consequently led to very complex solutions. These solutions did not take into account the effects of Doppler broadening which must be added numerically. Until recently, systems considered at St. Andrews were solved entirely by numerical means, incorporating Doppler broadening by integrating over the velocity profile [1]. The modelling carried out over the course of this work utilised Mathematica to solve the matrix analytically and perform a numerical integration over the velocity profile to incorporate the effects of Doppler-broadening. The details of this approach will be discussed in Section 2.3.

A simple example will be explored in order to further illuminate the density matrix approach. Before proceeding, some of the relevant attributes of an atomic system will be considered. The way in which these atomic parameters are incorporated with the density matrix model is discussed.

2.2.1 Population Decay Rates

One advantage of density matrix formalism is the ability to add phenomenological terms to the Liouville equation in a straightforward fashion. Such terms are introduced to account for decay, dephasing, and incoherent pumping, as appropriate to the specific system under consideration. The decay term, Γ_{ji} , denotes the spontaneous movement of population between the levels j and i , arising from the tendency of the atomic population of

each state to revert to its thermal equilibrium value. Decay phenomena are taken into account by appending a term, of the form $-\Gamma_{ji} \rho_{jj}$, to the appropriate diagonal element of the matrix. This term represents the movement of population, as a result of spontaneous decay, out of level j . A corresponding positive term, $+\Gamma_{ji} \rho_{jj}$, is then added to the receiving level i , if that level lies within the system of study. In general we have:

$$\frac{\partial \rho_{jj}}{\partial t} = -\frac{i}{\hbar} [\hat{H}, \rho]_{jj} - \sum_k \Gamma_{jk} \rho_{jj} + \sum_l \Gamma_{lj} \rho_{ll} \quad (2.12)$$

where k denotes all the levels below j into which population may decay ($k < j$), and l denotes all the levels above j from which population may decay into level j ($l > j$). Corresponding terms will be added and subtracted to the Liouville equations for the k and l states respectively.

2.2.2 Coherence Dephasing Rates

The off-diagonal density matrix elements, that relate to atomic coherence, are also subject to decay towards their thermal equilibrium values at rates given by:

$$\gamma_{ij} = \frac{1}{2} \left(\sum_k \Gamma_{ik} + \sum_l \Gamma_{jl} \right) + \gamma_{\text{deph}} \quad (2.13)$$

where k denotes all the levels into which population may decay from level i ($k < i$), and l denotes all the levels into which population may decay from level j ($l < j$). The bulk of this dephasing is a direct consequence of the population decay from the levels of the transition on which the coherence is being considered. In addition, the term γ_{deph} takes into account the macroscopic dephasing due to collisions acting on the system without causing significant population decay. The rule of thumb for establishing the decay terms is that any spontaneous population decay rate that removes population from either level i or j contributes half its value to the coherence dephasing rate γ_{ij} on that particular transition. Decay rates that add to the population in either level i or j have no contribution to the coherence dephasing rate γ_{ij} . With these terms in mind, the dephasing on an atomic transition is taken into account by appending the correct form of Eq. (2.13) to the appropriate Liouville equation. In general, for an off-diagonal density matrix element, we have:

$$\frac{\partial \rho_{ij}}{\partial t} = -\frac{i}{\hbar} [\hat{H}, \rho]_{ij} - \gamma_{ij} \rho_{ij} \quad (2.14)$$

2.2.3 Incoherent Pumping Rates

Incoherent pumping can also be incorporated into the density matrix model by adding appropriate terms to the Liouville equation. These terms are usually employed in the study of inversionless lasing systems, since they require a small amount of population to be excited into the upper lasing level. Conceptually, it is simpler to envisage an incoherent pumping source rather than a coherent one. In addition, incoherent pumping provides a more practical method, since the employment of a coherent source unbalances the important quantum coherences already present in the system. Here we consider the case for which incoherent pumping is incorporated by applying a broadband light source to a specific transition (this method is described in Section 3.5). In addition to exciting the population from the lower to the upper level, transitions will also be stimulated in the other direction. Incoherent pumping is modelled by adding terms to the Liouville equation in exactly the same way as in the case of population decay, except that this pumping process is reversible. The rate of pumping in each direction is identical, as this will depend in both cases on the Einstein B coefficient. If, for example, we consider the incoherent excitation of population from level $|1\rangle$ to level $|2\rangle$, the related Liouville equations must be altered such that:

$$\frac{\partial \rho_{11}}{\partial t} = -\frac{i}{\hbar} [\hat{H}, \rho]_{11} + \Pi_{12} (\rho_{22} - \rho_{11}) \quad (2.15a)$$

$$\frac{\partial \rho_{22}}{\partial t} = -\frac{i}{\hbar} [\hat{H}, \rho]_{22} - \Pi_{12} (\rho_{22} - \rho_{11}) \quad (2.15b)$$

where Π_{12} is the incoherent pumping rate.

Note that the dephasing between the levels is increased by the introduction of incoherent pumping. To account for this, an additional $\Pi_{12}/2$ term must be added to the coherence dephasing rates corresponding to any transition linked to either of the levels of the pumped transition. In general, a transition is dephased when population is removed from one or both of the levels that constitute the transition. In this instance, because the

pumping is reversible, population is removed from both the upper and lower levels of the pumped transition.

2.3 Employment of the Density Matrix Model

The derivation of the density matrix for a simple two level atomic system is now considered. Figure 2.1 presents a schematic of the atomic system, which is closed with regard to the atomic basis set; that is, the lifetime broadening occurs by radiative decay to other states within the same system. A single optical field, at angular frequency ω_1 , is near resonant with the transition of angular frequency ω_{12} .

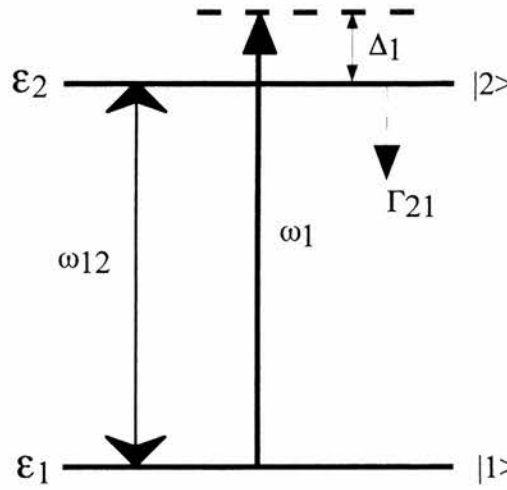


Figure 2.1: Schematic of a closed two level atom.

Level $|2\rangle$ decays at a rate Γ_{21} to level $|1\rangle$. The derivation employed here assumes that the Rabi frequency involved is much smaller than the corresponding laser frequency.

ASIDE: In a more complex system, involving a number of connected transitions, it would be necessary to consider atomic selection rules and ascertain which transitions were dipole allowed and which were dipole forbidden [1,4].

We can define a classical electric field, in general, as:

$$E_j(z,t) = \frac{E_j^0}{2} \left\{ \exp[i(\omega_j t - k_j z)] + \text{c.c.} \right\} \quad \text{here } j=1 \quad (2.16)$$

and the angular Rabi frequency is given, as before, by:

$$\Omega_{12} = \frac{\mu_{12} E_1^0}{2\hbar} \quad (2.17)$$

The applied optical field frequency, ω_1 , has an exact detuning from atomic resonance given by:

$$\Delta_1 = \omega_1 - \omega_{12} - k_1 V_z \quad (2.18)$$

where $k_1 V_z$ is the Doppler shift contribution to the detuning, caused by an atom moving with a z-component of velocity V_z , and k_1 is the wavevector defined as $2\pi n/\lambda_1$.

The Liouville equation, Eq. (2.4), is employed to evaluate the rate of change of each density matrix element. The first step is to expand the summation in the Liouville equation, appending the relevant decay or dephasing terms as described in Section 2.2. Equation (2.5b) is then substituted for the Hamiltonian and terms that do not correspond to the system under consideration are removed. Substitutions are then made for the electric field, Eq. (2.16), which allows the Rabi frequency to be resolved according to Eq. (2.17). The time dependent and independent terms are separated by substituting the following equation for the off-diagonal density matrix element ρ_{12} :

$$\rho_{12} = \tilde{\rho}_{12} \exp[i(\omega_1 t - k_1 z)] \quad (2.19)$$

The rotating wave approximation is invoked to remove high frequency components of the remaining expressions. Terms oscillating rapidly at around $2\omega_1$ are removed since they average out to zero for an integration time of anything over a few optical cycles. Thus, the solutions for the two level system are:

$$\dot{\rho}_{11} = i\Omega_{12}(\tilde{\rho}_{21} - \tilde{\rho}_{12}) + \Gamma_{21}\rho_{22} \quad (2.20a)$$

$$\dot{\rho}_{22} = i\Omega_{12}(\tilde{\rho}_{12} - \tilde{\rho}_{21}) - \Gamma_{21}\rho_{22} \quad (2.20b)$$

$$\dot{\tilde{\rho}}_{12} = -i(\Delta_1 - i\gamma_{12})\tilde{\rho}_{12} + i\Omega_{12}(\rho_{22} - \rho_{11}) \quad (2.20c)$$

These three equations, along with the complex conjugate of Eq. (2.20c), completely describe the final state of the density matrix. However, for ease of calculation it is convenient to convert these complex equations into four real simultaneous equations by separating the real and imaginary parts using the following definitions:

$$\tilde{\rho}_{ij} = \rho_{ij}^r + i\rho_{ij}^i \quad (2.21a)$$

$$\tilde{\rho}_{ij}^* = \rho_{ij}^r - i\rho_{ij}^i \quad (2.21b)$$

where $\rho_{ij}^r = \text{Re}(\tilde{\rho}_{ij})$ and $\rho_{ij}^i = \text{Im}(\tilde{\rho}_{ij})$. The calculation can be further simplified since population conservation implies the trace normalisation:

$$\rho_{11} + \rho_{22} = 1 \quad (2.22)$$

Equation (2.22) removes one degree of freedom, leaving three equations which fully describe the system:

$$\dot{\rho}_{22} = -\Gamma_{21}\rho_{22} - 2\Omega_{12}\dot{\rho}_{12}^i \quad (2.23a)$$

$$\dot{\rho}_{12}^i = -2\Omega_{12}\rho_{22} + \Delta_1\rho_{12}^r + \gamma_{12}\rho_{12}^i + \Omega_{12} \quad (2.23b)$$

$$\dot{\rho}_{12}^r = \gamma_{12}\rho_{12}^r - \Delta_1\rho_{12}^i \quad (2.23c)$$

Hence, in the steady state, with all the time derivatives set equal to zero, the system can be represented in matrix form, $\mathbf{Ax} = \mathbf{b}$:

Matrix 2.1: *A closed two level system.*

$$\begin{bmatrix} -\Gamma_{21} & 0 & -2\Omega_{12} \\ 0 & \gamma_{12} & -\Delta_1 \\ -2\Omega_{12} & \Delta_1 & \gamma_{12} \end{bmatrix} \begin{bmatrix} \rho_{22} \\ \rho_{12}^r \\ \rho_{12}^i \end{bmatrix} = \begin{bmatrix} 0 \\ 0 \\ -\Omega_{12} \end{bmatrix}$$

To render solutions without taking the effects of Doppler-broadening into account, we can simply remove the factor $k_1 V_z$ from the definition of detuning, Eq. (2.18), and solve Matrix 2.1 for each density matrix element. If we consider, for example, the off-diagonal element, ρ_{12}^i , and solve the matrix for a range of probe field detunings we can produce a simple absorption profile, as shown in Fig. 2.2 (a) where the off-diagonal density matrix element, ρ_{12}^i , (proportional to the absorption coefficient) is plotted as a function of probe field detuning. Figure 2.2 (b) depicts the off-diagonal element, ρ_{12}^r , (proportional to refractive index) as a function of probe field detuning. It is useful to carry out Doppler free modelling of systems because the matrix can be solved very quickly to gain initial insight into a particular configuration. However, Doppler-broadening has a significant impact on the light-matter interaction and must be taken into account to accurately simulate a real experimental situation in which the Doppler effect is known to occur.

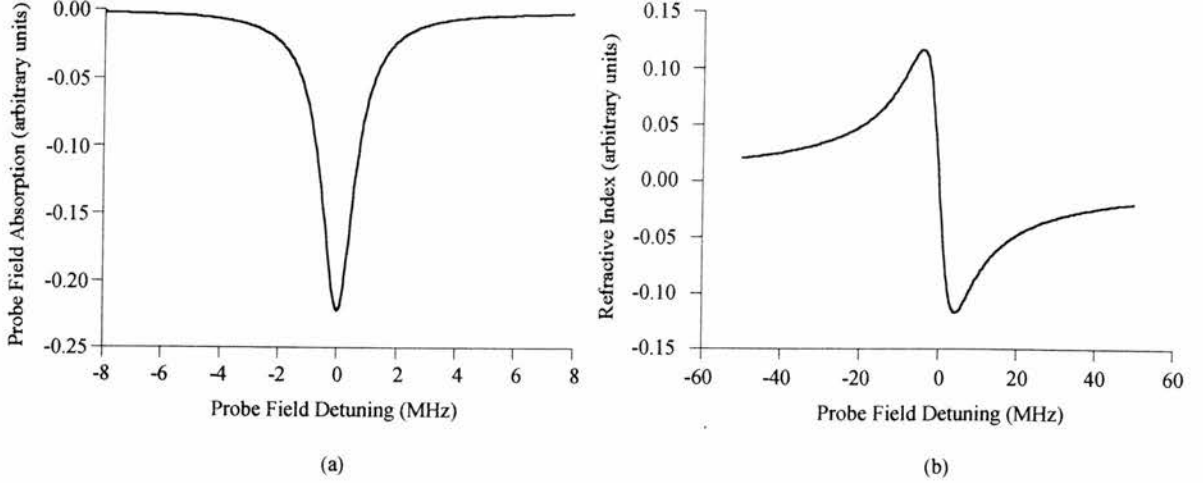


Figure 2.2: (a) Absorption trace (ρ^i_{12} in arbitrary units) and (b) refractive index trace (ρ^r_{12} in arbitrary units) produced with the two level density matrix model, using a probe field Rabi frequency of 320kHz. Doppler-broadening was not taken into account.

The detunings experienced by an atom are altered by the Doppler shift associated with its motion with respect to the relevant optical field. A Maxwellian distribution of velocities is assumed, giving the fraction of atoms whose z component of the velocity lies between V_z and $V_z + dV_z$ as:

$$f(V_z) = \frac{\exp\left(-\left(\frac{V_z}{u}\right)^2\right)}{\sqrt{\pi}} \frac{dV_z}{u} \quad (2.24)$$

where u is the average atom velocity, given by:

$$u = \sqrt{\frac{2k_B T}{M}} \quad (2.25)$$

k_B is Boltzmann's constant, T is the temperature in Kelvin, and M is the atomic mass. To yield a final solution for each density matrix element we must integrate over the velocity distribution via:

$$\bar{\rho}_{ij} = \int_{-\infty}^{\infty} f(V_z) \rho_{ij}(V_z) dV_z \quad (2.26)$$

Figure 2.3 shows absorption and refractive index profiles (ρ^i_{12} and ρ^r_{12} in arbitrary units) created by solving the density matrix for a range of probe field detunings while incorporating the effects of Doppler-broadening. These curves were calculated for exactly

the same conditions as those shown in Fig. 2.2 with the addition of Doppler-broadening. Figure 2.3 (a) shows that the absorption is reduced in peak magnitude and spread out over a larger range of probe detuning.

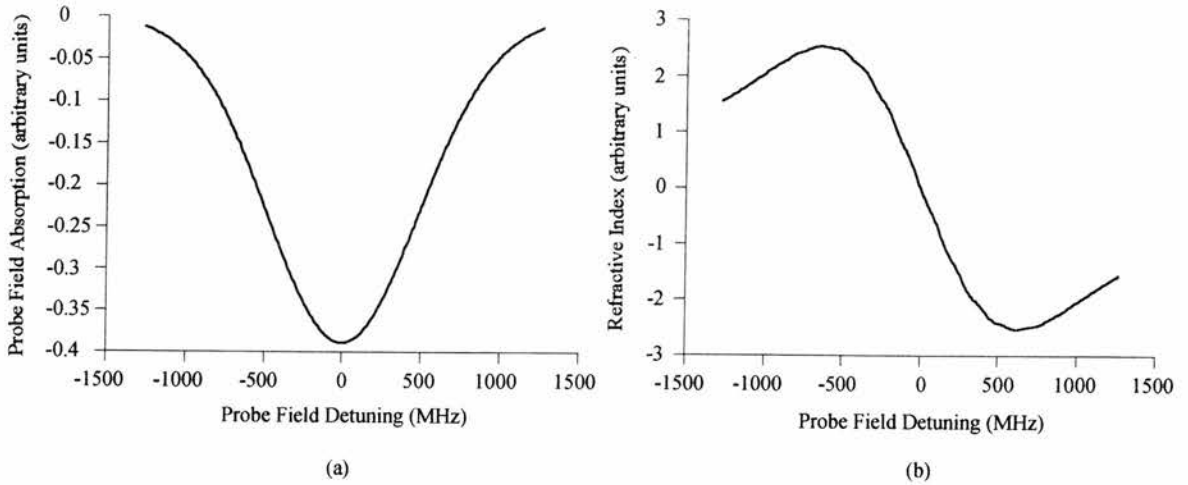


Figure 2.3: *Theoretical curves showing (a) the probe field absorption (ρ^i_{12} in arbitrary units) and (b) the refractive index (ρ^r_{12} in arbitrary units) as a function of the probe field detuning. The effects of Doppler-broadening have been taken into account by integrating over the range of atomic velocities.*

The model can also be used to calculate the relative populations in each of the atomic states. In this case all the population resides in the lower energy level because the probe field is very weak.

Incorporating Doppler-broadening in this way makes the calculation lengthy, particularly for systems of greater complexity. Previous work in this field at the University of St. Andrews relied on C and FORTRAN programming languages to carry out these density matrix calculations. However, more recent work has utilised Mathematica [7] to decrease the running times of the density matrix models. The Mathematica system allows numerical, symbolic and graphical calculations to be carried out. It is the symbolic capability that provides the key to dramatically reducing the running time of a density matrix calculation. The solution algorithm can be simplified with respect to those previously employed, resulting in an enhanced processing speed. This improvement is achieved because the iterative step involving LU factorisation, which was previously

calculated at every numerical velocity value v , is effectively replaced with a single step which involves one inversion of a matrix. The velocity, v , can be retained as an algebraic term within the optical field detunings. The effects of various parameters within the program are considered in the following section.

2.4 Nuances of the Density Matrix Model

Theoretical analysis is presented to characterise the effect of changing the parameters that describe an atomic system on the diagonal and off-diagonal elements that comprise the matrix. The effects of temperature, dephasing, spontaneous decay, Rabi frequency and velocity range are considered for the simple two level model of an atom probed by a single optical field. Appendix A describes the Mathematica program used to solve the density matrix that describes such a system (Matrix 2.1). The wavelength of the probe beam is that of the $5S_{1/2} - 6P_{1/2}$ transition in rubidium, approximately 422nm. The model is capable of providing us with information concerning the absorption of the probe (ρ^i_{12}), the refractive index experienced by the probe (ρ^r_{12}) and the population in the excited state (ρ_{22}). The latter value also indicates the fraction of the population that resides in the ground state via the normalisation condition given in Eq. (2.22). Here we look specifically at the dependence of the density matrix element, ρ^i_{12} , on certain parameters of a real atomic system.

2.4.1 Temperature

The principle effect of temperature is to determine the particle density in the vapour. However, this effect is not included within the density matrix, but can be taken into account in the subsequent calculation of absorption or gain as described in Section 7.3. Temperature still affects the density matrix model due to Doppler-broadening. At higher temperatures the spread of atomic velocities in the vapour will be greater with the effect of increasing the inhomogeneous broadening and reducing the peak magnitude of the absorption at line centre. Figure 2.4 shows the ‘on-resonance’ probe field absorption (ρ^i_{12} , which is proportional to the absorption coefficient) decreasing with increasing cell temperature.

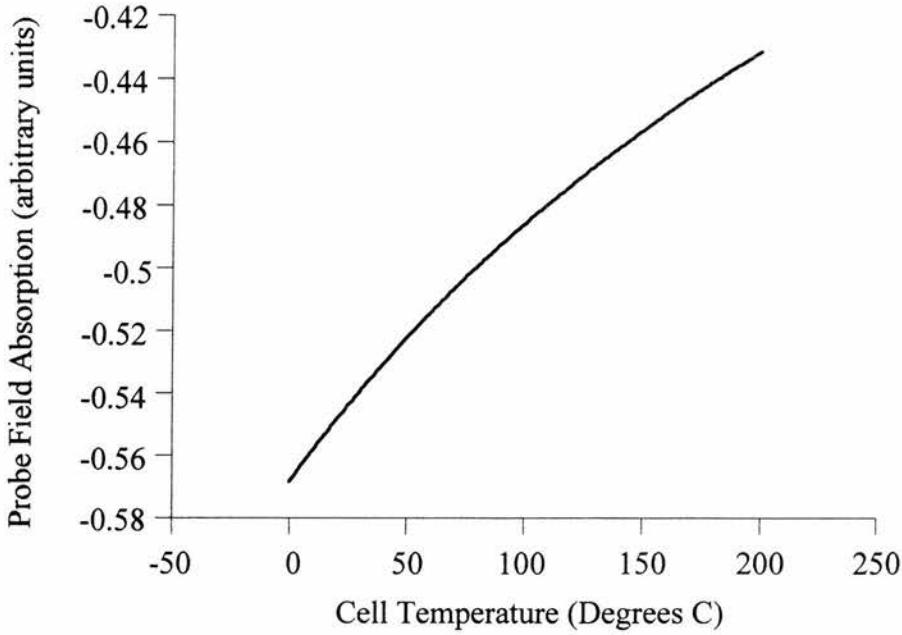


Figure 2.4: The peak 'on-resonance' absorption (ρ^i_{12} in arbitrary units) is plotted as a function of the cell temperature. This data is produced by the two level density matrix model, solved for a range of temperatures.

2.4.2 Dephasing

In general, dephasing acts to destroy the coherence that builds up due to the presence of driving optical fields. The principal provocateur in this action, as already discussed, is the spontaneous decay of population from atomic states. The relaxation of population is detrimental to the coherence because the latter is maintained by trapping the population in certain levels. In a real atomic system, dephasing will always be greater than zero and tends to reduce the magnitude of observed quantum coherence effects.

In a two level model where absorption alone is considered, an increase in dephasing (γ_{12}) will affect the absorption through the associated increase in the medium's homogeneous linewidth. In a practical system dephasing may increase as a result of collisions that do not move population. Figure 2.5 shows a monochromatic laser source, of frequency ω_0 , interacting with the total atomic population which is spread out in frequency due to the inhomogeneous effects of Doppler-broadening.

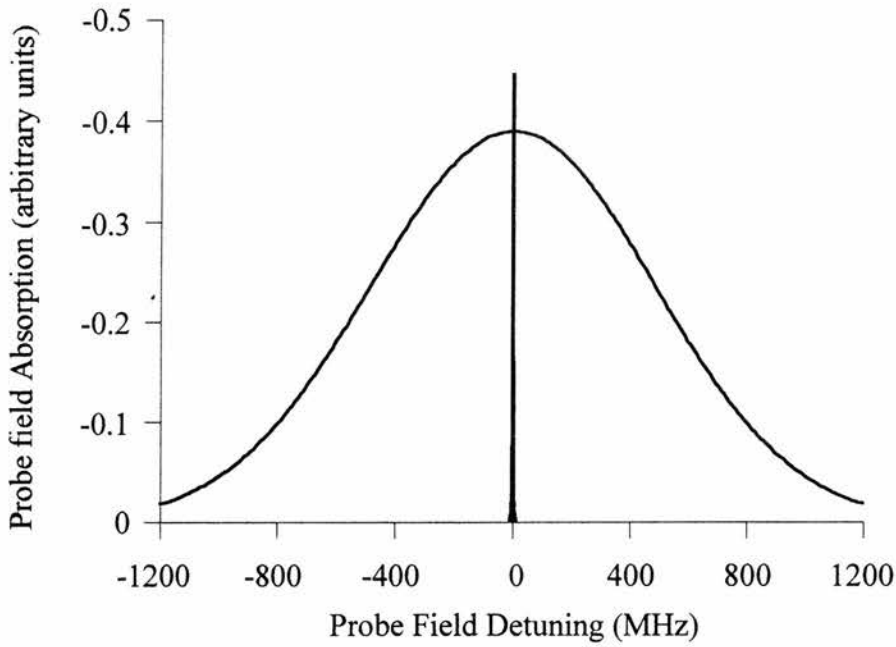


Figure 2.5: *The Doppler-broadened absorption profile superimposed with the homogeneous lineshape of the medium. The area of overlap indicates the atoms that will contribute to absorption at line centre. The relative heights of these profiles are arbitrary.*

The interaction of the monochromatic field, in Fig. 2.5, is represented by a Lorentzian function determined by the homogeneous broadening of the transition in question. A monochromatic light field interacts most strongly with the atoms within one homogeneous linewidth centred on ω_0 , the resonant frequency. The strength of interaction falls off in a manner prescribed by the Lorentzian function. The homogeneous linewidth is defined as the distance over which the strength of interaction falls to one half of its peak value. The homogeneous lineshape function corresponding to the purely radiative decay of $4 \times 10^6 \text{ s}^{-1}$ is shown separately in Fig. 2.6 (a).

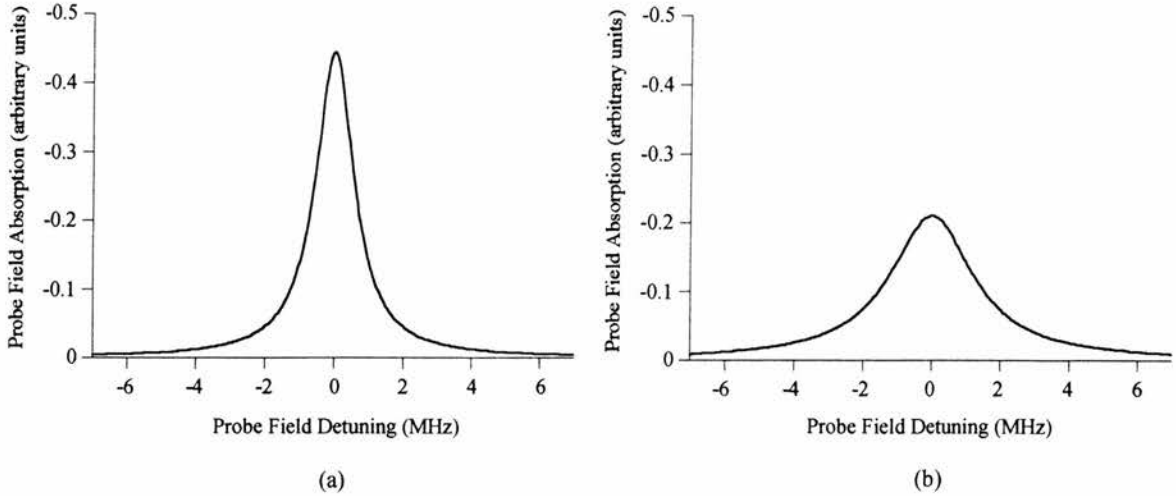


Figure 2.6: *Homogeneous lineshape of the medium with (a) the dephasing associated with the radiative decay of the upper level, $4 \times 10^6 \text{ s}^{-1}$, and (b) an increased dephasing, $9 \times 10^6 \text{ s}^{-1}$, exhibiting a greater homogeneous linewidth.*

When the homogeneous linewidth is increased by dephasing, the peak ‘on-resonance’ absorption reduces as the width of the homogeneous lineshape function increases. Figure 2.6 (b) shows an example of an increased homogeneous linewidth caused by a dephasing of $9 \times 10^6 \text{ s}^{-1}$. The total number of atoms that contribute to absorption on line centre is affected both by the change in width and the change in height of the homogeneous lineshape function, and to an extent these effects are compensatory. However, with increasing dephasing the wings of the homogeneous linewidth will gradually increase beyond the Doppler-width causing a modest reduction in absorption at line centre.

Figure 2.7 shows the change in the peak ‘on-resonance’ absorption for a wide range of dephasings. Note also that the ‘on-resonance’ absorption is affected by the choice of Rabi frequency for low dephasing rates. For a medium in which dephasing is close to the radiative limit ($4 \times 10^6 \text{ s}^{-1}$), the homogeneous linewidth is narrow and the small velocity range of atoms that the incident field couples into may become saturated for a relatively low field strength; thus, the absorption is decreased due to saturation for higher Rabi frequencies.

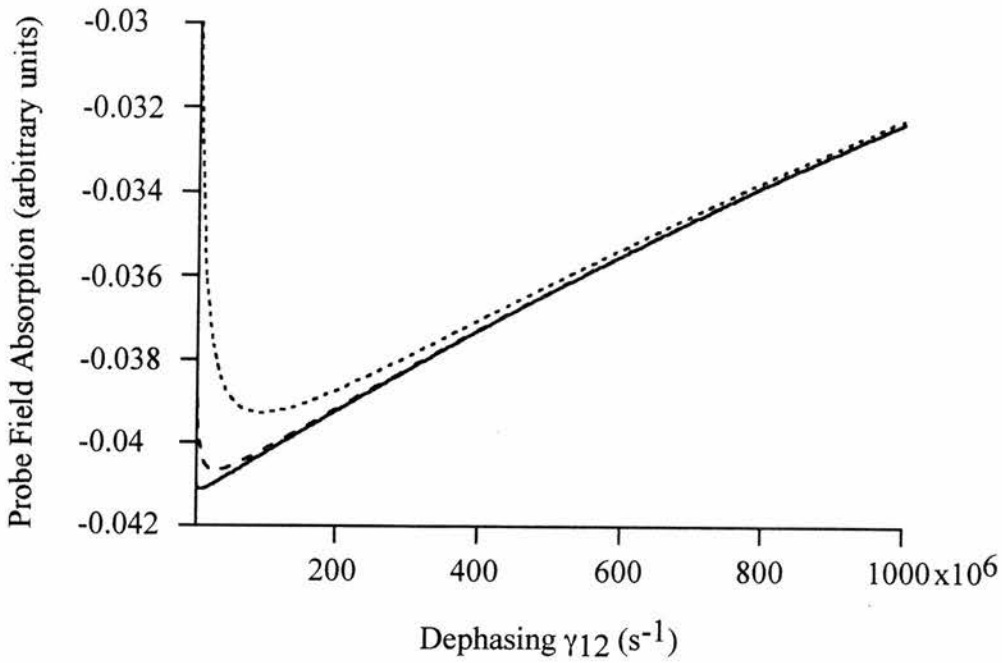


Figure 2.7: *The on-resonance probe field absorption (ρ^i_{12} in arbitrary units) as a function of the dephasing in the two level atomic system for linear Rabi frequencies of 0.1MHz (solid line), 0.3MHz (dashed line), and 1MHz (dotted line).*

2.4.3 Rabi Frequency

The Rabi frequencies induced by the two fields in an EIT experiment have different effects on the overall system. It is normally assumed that the probe field is weak, to the extent that it does not significantly move population out of the lower level of the probe transition. This assumption is referred to as the weak probe limit. We consider the off-diagonal coherence element as a function of the probe field Rabi frequency (Ω_{12}) in the simple two level model. Figure 2.8 shows that for low values of Rabi frequency, the ratio of the imaginary part of the coherence and the Rabi frequency - on the vertical axis - is constant. The imaginary part of the off-diagonal coherence is divided by the Rabi frequency because this ratio is directly proportional to the absorption for the whole range of Rabi frequencies considered. The constant region defines the range of Rabi frequencies over which the weak probe limit is valid.

As the Rabi frequency increases beyond this range the probe begins to move a significant amount of the lower level population into the excited state. The absorption is thus reduced because less lower state population remains to be absorbed. Note that as

dephasing is increased the region of constant absorption persists for higher Rabi frequencies. As discussed in the previous section, this is because the homogeneous linewidth is increased and the field may couple into a greater number of atoms. In the case of $4 \times 10^6 \text{ s}^{-1}$ dephasing, the probe field saturates the transition for Rabi frequencies greater than about 10 MHz, the populations in the upper and lower levels are equalised and no further absorption may take place.

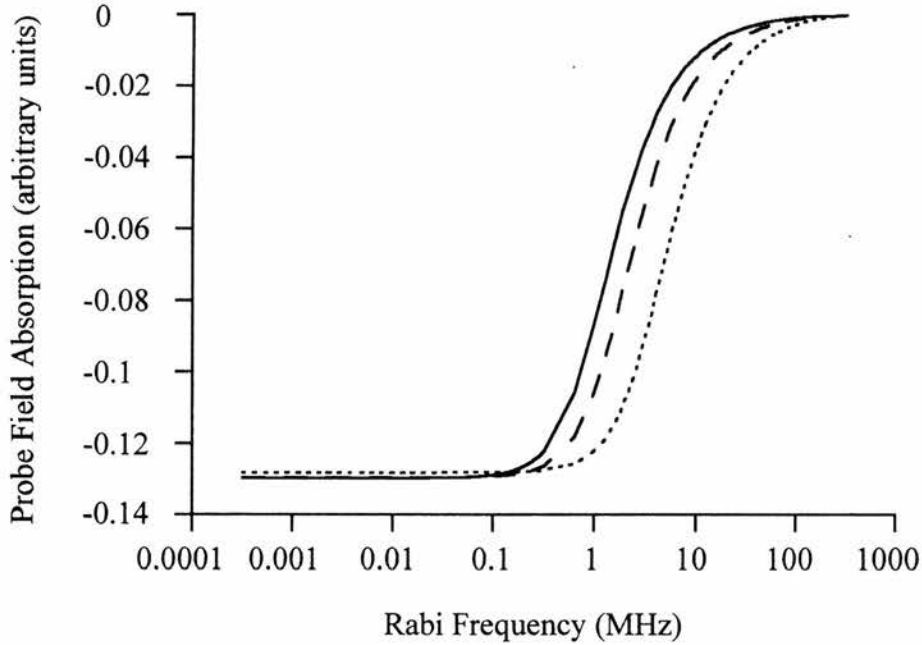


Figure 2.8: *The on-resonance probe field absorption (ρ^i_{12} in arbitrary units) as a function of the logarithm of the Rabi frequency induced by the incident light field for dephasings of $4 \times 10^6 \text{ s}^{-1}$ (solid line), $10 \times 10^6 \text{ s}^{-1}$ (dashed line), and $50 \times 10^6 \text{ s}^{-1}$ (dotted line).*

The effects of Rabi frequency on an EIT experiment will be considered in Chapters 5 and 7.

2.4.4 Spontaneous Decay

The decay rates in an atomic system are important determining factors in quantum coherence effects. Here we consider the effect the decay rate (Γ_{21}) has on straightforward absorption in a two level atom. The population decay is made up of the relaxation of population from state $|2\rangle$ to state $|1\rangle$, radiative decay from level $|2\rangle$ to any other level, and

collisions that result in a movement of population. The radiative decay from state $|2\rangle$ to state $|1\rangle$ is fixed by the Einstein A coefficient. Changing this would not only alter the decay rate, but also the Rabi frequency induced for a given laser field power. When we vary the decay rate, Γ_{21} , in the model, we are effectively changing the contribution that arises due to collisions since the Rabi frequency is unaltered. Alternatively, we could envisage increasing the A coefficient and compensating by altering the incident laser power to maintain a constant Rabi frequency.

Increasing the decay rate in this manner has two potential effects. The first is to more efficiently recycle the upper state population, and the second is to increase the dephasing which is defined as half the decay rate. The former effect only comes into play when the radiation field is strong enough to saturate the transition by equalising the population in levels $|1\rangle$ and $|2\rangle$. Saturating the transition prevents further absorption, but a faster decay rate will mean that the upper state population will relax back into the lower level more promptly, allowing further absorption to occur.

Figure 2.9 shows the change in absorption as the decay rate is increased for a probe Rabi frequency of 0.3MHz. We observe the same general shape as previously seen in Fig. 2.7, but we can see that the reduction in the absorption is about half of that in the case of directly increasing the dephasing; this is because the dephasing is defined as one half of the decay rate in Eq. (2.13).

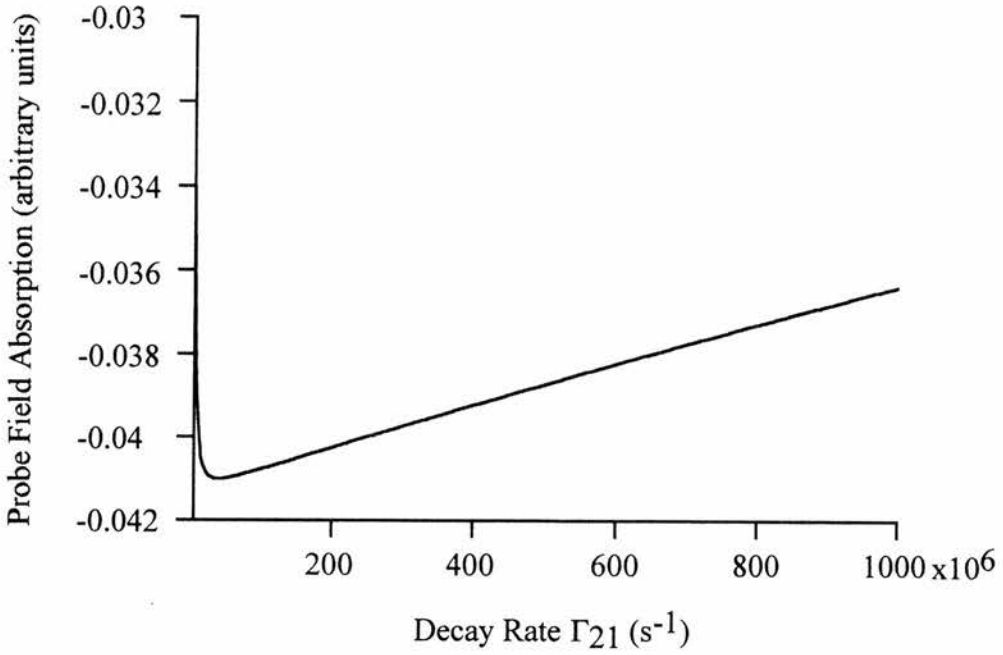


Figure 2.9: *The on-resonance probe field absorption (ρ_{12}^i in arbitrary units) as a function of the decay from the upper state in the two level atomic system. The probe Rabi frequency is approximately 0.3MHz.*

2.4.5 Velocity Range

The width of the velocity distribution function is determined by the range of velocities over which Simpson's rule is carried out in the model. As a rough guide the maximum extent of the velocity range can be taken as the average thermal velocity given previously in Eq. 2.25. This is an absolute minimum value as it effectively considers a range of velocities equal to double the full width half maximum of the velocity distribution function. This function is depicted in Fig. 2.10. Taking a smaller velocity range effectively discards the contribution of the higher velocity atoms. The consequences of this are demonstrated in Fig. 2.11, in which the absorption profile is calculated for various ranges of atomic velocity. If the range selected is correct the velocity function should normalise to one, as should the total relative atomic state population, ρ_{11} and ρ_{22} .

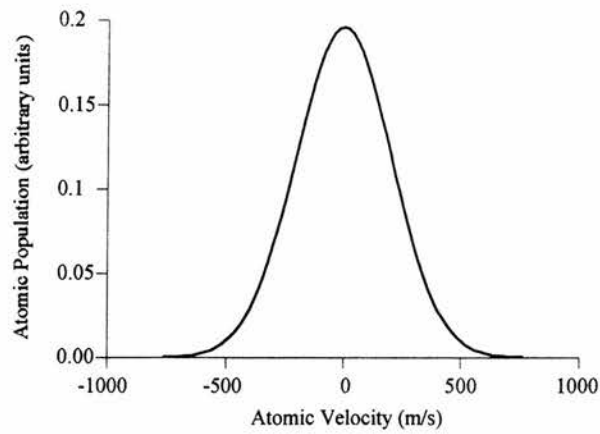


Figure 2.10: Fraction of the atomic population as a function of the atom velocity in the vapour.

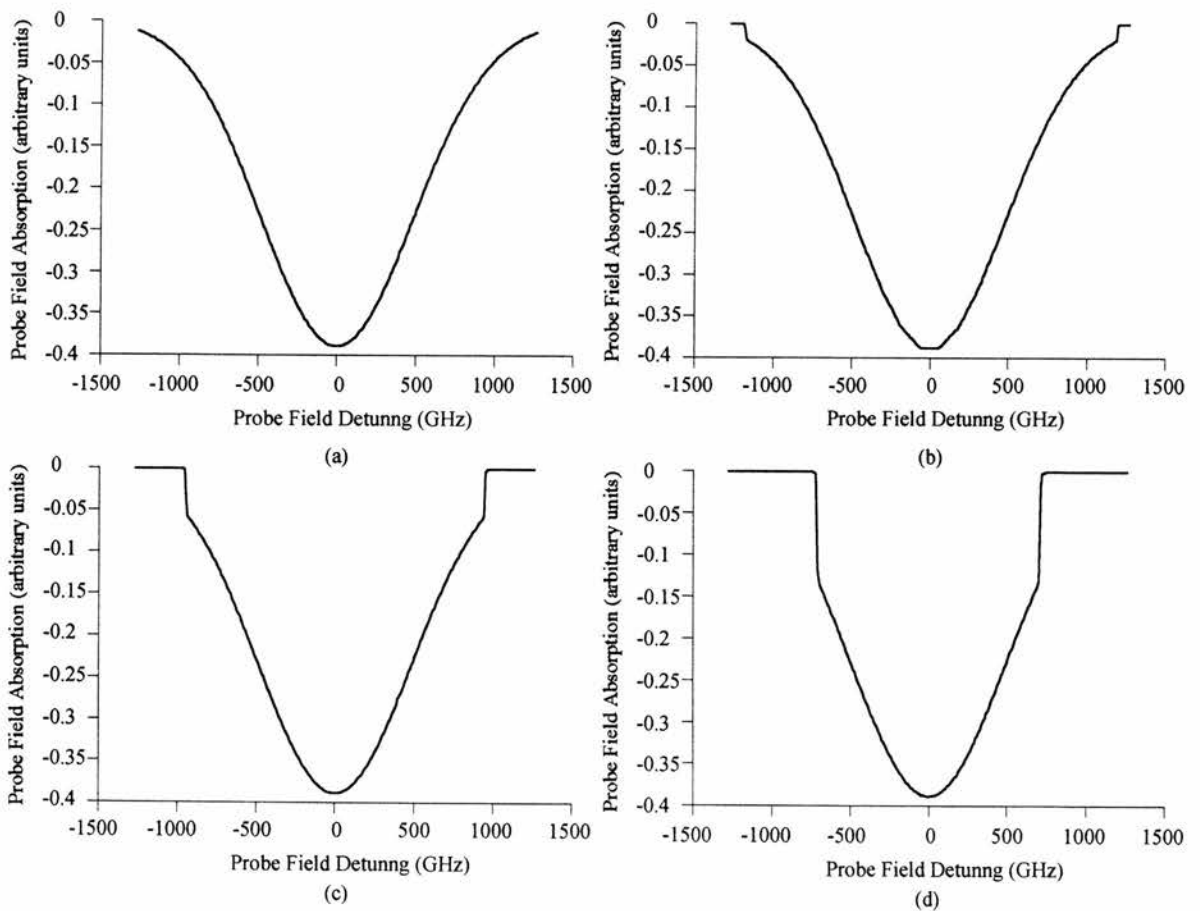


Figure 2.11: Probe field absorption (ρ_{12}^i in arbitrary units) as a function of the probe field detuning for velocity ranges of (a) 600, (b) 500, (c) 400, and (d) 300ms^{-1} .

2.4.6 Relative Populations

We now examine the populations (ρ_{11} and ρ_{22}) in the two state atom. First we consider the Doppler free case. Figure 2.12 shows the on-diagonal density matrix elements ρ_{22} and ρ_{11} which indicate the relative populations in the upper and lower states respectively. In a Doppler free system the field will couple into all the atomic population at resonance and transfer of population will occur for a sufficiently strong field. In Fig. 2.12 we see that the upper and lower populations are nearly equalised due to the action of the probe field. As the applied field is detuned the fraction of population excited into the upper level falls off rapidly.

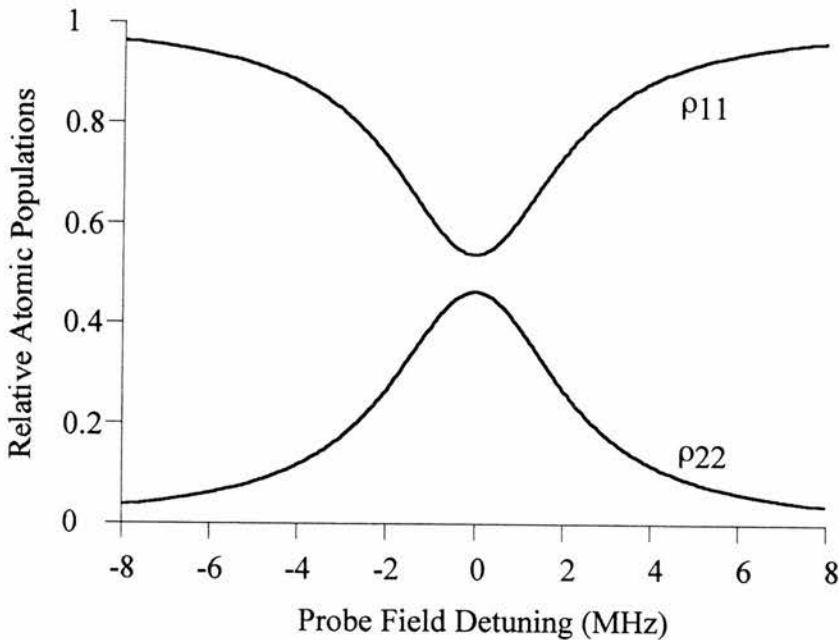


Figure 2.12: *Relative atomic populations in a two level Doppler free system, for a probe Rabi frequency of 6.4MHz.*

In a Doppler-broadened system the distribution of population is different. We saw in Section 2.4.5 that the atomic population has a Maxwellian distribution of velocities. Consequently, detuning the probe field from resonance with the zero velocity group moves the field onto resonance with another velocity group. While each velocity group will have a different total fraction of the atomic population, the ratio of the upper to the lower level population for each velocity group will be the same. Figure 2.13 shows the relative populations as a function of probe field detuning and atomic velocity for the velocities resonant with the corresponding probe detuning. We see that in all cases the ratio of ρ_{22}

and ρ_{11} is the same, and the total population varies according to the Maxwellian function, as described in Fig. 2.10. The populations quoted throughout this thesis refer to the relevant on diagonal density matrix element integrated over the considered velocity range.

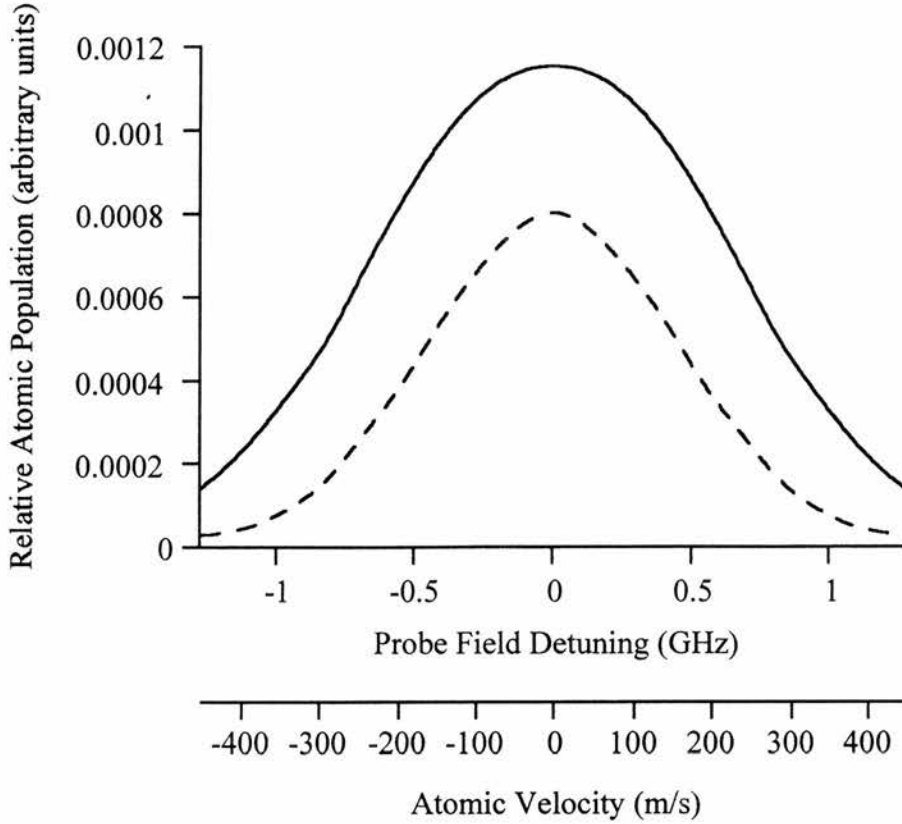


Figure 2.13: *Relative atomic populations in a Doppler-broadened two level atom subject to a single applied field. The lower state population, ρ_{11} , is indicated by a solid line and the upper state population, ρ_{22} , is indicated by a dashed line.*

2.5 The Three Schemes for EIT

The three schemes that may be employed to produce EIT have already been introduced in Chapter 1. The work presented in this thesis primarily involves the Vee scheme in which a fundamental difference in the mechanism for EIT can be exploited. The nature and consequence of the Vee scheme's uniqueness will be discussed in Chapter 4. Now we briefly look at the density matrix model for each scheme and some simple theoretical results that may be obtained in the presence of Doppler-broadening to characterise absorption, refractive index, and the atomic state populations.

For each of the considered schemes a real atomic system is chosen in rubidium vapour. An energy level scheme is provided along with the density matrix describing the atomic system that was derived using the method described in Section 2.3. The nomenclature employed is identical to that used previously for the two level scheme in Fig. 2.1 and the indices refer to the levels labelled in the appropriate diagram.

In all schemes the density matrix is solved for a probe Rabi frequency of 320kHz and a coupling Rabi frequency of 40MHz. These values were chosen both to ensure that the models satisfy the weak probe limit and that the coupling field power necessary to induce the Rabi frequency is well within the capabilities of cw lasers. Calculations are based on a cell temperature of 47°C.

2.5.1 The Cascade Scheme

Figure 2.14 shows a detailed schematic of the energy level configuration for a Cascade scheme. The relevant density matrix is shown in Matrix 2.2. The probe wavelength is approximately 794nm, with a coupling wavelength of 727nm, corresponding to the $5S_{1/2} - 5P_{1/2}$ and $5P_{1/2} - 7S_{1/2}$ transitions in rubidium vapour respectively [8]. The decay rates for these transitions are $40 \times 10^6 \text{s}^{-1}$ (Γ_{21}) and $6 \times 10^6 \text{s}^{-1}$ (Γ_{32}). Figure 2.15 shows the variation of (a) absorption and (b) refractive index with probe field detuning, and Fig. 2.15 (c) shows the relative populations in each of the atomic states.

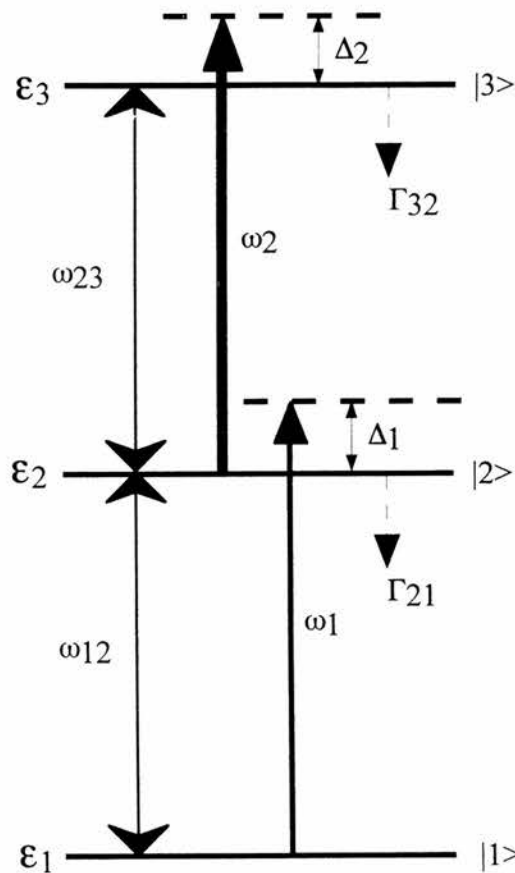


Figure 2.14: Schematic of the energy level configuration for a Cascade EIT system. The probe field is shown between states $|1\rangle$ and $|2\rangle$ with the coupling field applied to the transition between states $|2\rangle$ and $|3\rangle$.

Matrix 2.2: *Three level Cascade system.*

$$\begin{bmatrix}
 -\Gamma_{21} & \Gamma_{32} & 0 & 0 & 0 & -2 \times \Omega_{12} & 0 & 2 \times \Omega_{23} \\
 0 & -\Gamma_{32} & 0 & 0 & 0 & 0 & 0 & -2 \times \Omega_{23} \\
 0 & 0 & \gamma_{12} & 0 & 0 & -\Delta_{12} & -\Omega_{23} & 0 \\
 0 & 0 & 0 & \gamma_{13} & 0 & -\Omega_{23} & (-\Delta_{12} - \Delta_{23}) & \Omega_{12} \\
 0 & 0 & 0 & 0 & \gamma_{23} & 0 & \Omega_{12} & -\Delta_{23} \\
 -2 \times \Omega_{12} & -\Omega_{12} & \Delta_{12} & \Omega_{23} & 0 & \gamma_{12} & 0 & 0 \\
 0 & 0 & \Omega_{23} & (\Delta_{12} + \Delta_{23}) & -\Omega_{12} & 0 & \gamma_{13} & 0 \\
 \Omega_{23} & -\Omega_{23} & 0 & -\Omega_{12} & \Delta_{23} & 0 & 0 & \gamma_{23}
 \end{bmatrix}
 \begin{bmatrix}
 \rho_{22} \\
 \rho_{33} \\
 \rho_{12}^r \\
 \rho_{13}^r \\
 \rho_{23}^r \\
 \rho_{12}^i \\
 \rho_{13}^i \\
 \rho_{23}^i
 \end{bmatrix}
 =
 \begin{bmatrix}
 0 \\
 0 \\
 0 \\
 0 \\
 0 \\
 -\Omega_{12} \\
 0 \\
 0
 \end{bmatrix}$$

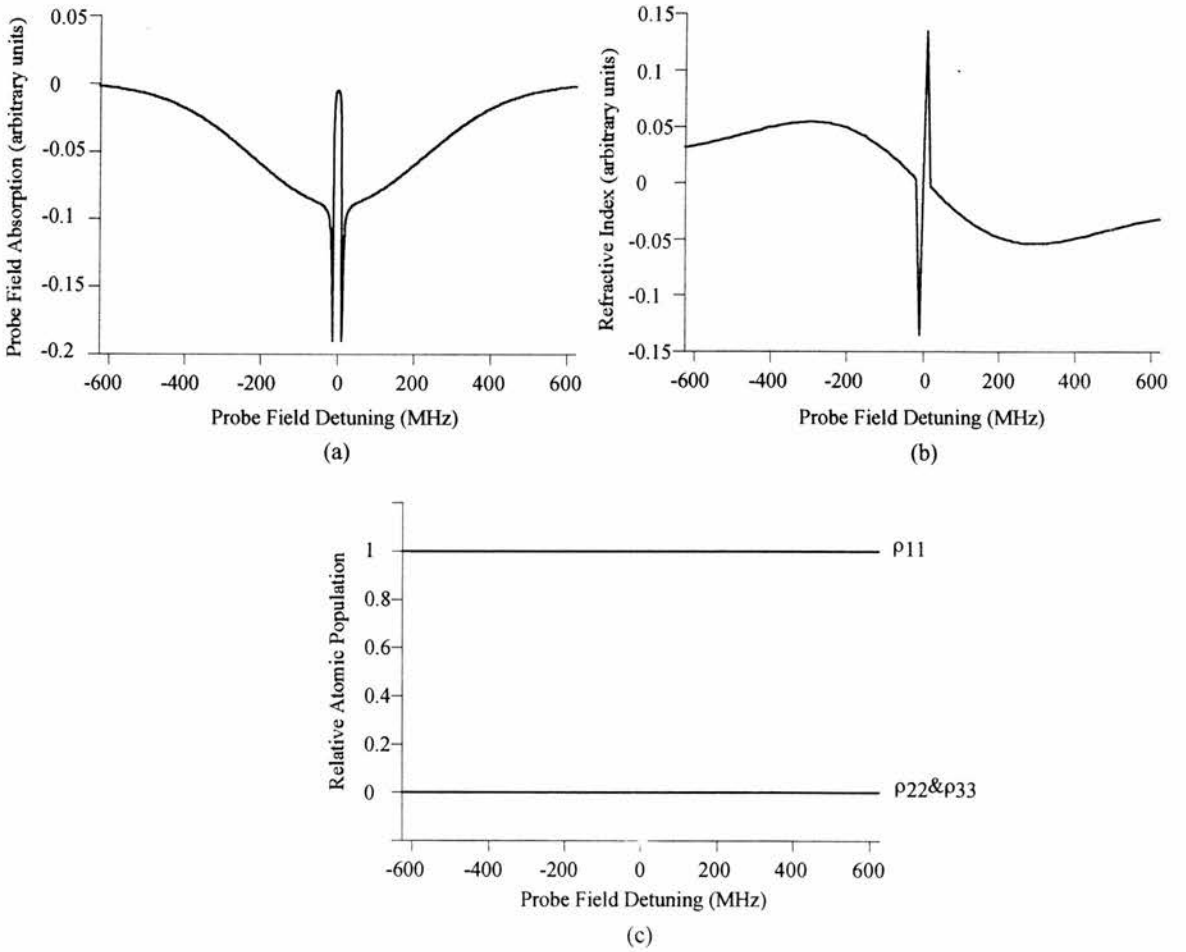


Figure 2.15: Shows (a) absorption, (b) refractive index, and (c) the relative atomic populations as a function of probe field detuning for a simple three level Cascade scheme in rubidium vapour. The labelled density matrix elements in (c), ρ_{11} , ρ_{22} , and ρ_{33} correspond to the population in states $|1\rangle$, $|2\rangle$, and $|3\rangle$ respectively.

In Fig. 2.15 (a) two sharp peaks in absorption are observed either side of line centre in addition to the expected transparency on resonance. The dephasing of the unlinked $|1\rangle - |3\rangle$ transition is $3 \times 10^6 \text{ s}^{-1}$ (determined by half the sum of the radiative decay from levels $|1\rangle$ and $|3\rangle$). Given the relatively small dephasing of the coherence, the ratio of the decays on the probe and coupling transitions, and the near matching of the probe and coupling wavelengths (reducing the Doppler-broadening for the two-photon absorption process), we are able to resolve the enhancement of absorption corresponding to resonance with the zero velocity position of the Autler-Townes sub-levels of the intermediate state. Such features are not observed in an experimental scheme because the linewidth is greater than that calculated from the radiative decay alone, due to collisions occurring in the medium that are not taken into account in the model employed here.

2.5.2 The Lambda Scheme

Figure 2.16 depicts the energy level configuration employed in a Lambda type system. The relevant density matrix can be found in Matrix 2.3. The probe and coupling wavelengths are both approximately 794nm corresponding to the $5S_{1/2} - 5P_{1/2}$ transition in rubidium vapour [8]. The optical fields are resonant with two distinct sub-levels of the $5S_{1/2}$ ground state. These sub-levels correspond to the hyperfine states, $F=2$ and $F=3$, which are separated by approximately 3GHz in ^{85}Rb . The decay rates for this configuration are both $40 \times 10^6 \text{ s}^{-1}$ (Γ_{31} and Γ_{32}). Figure 2.17 depicts (a) the absorption, (b) the refractive index, and (c) the relative atomic populations.

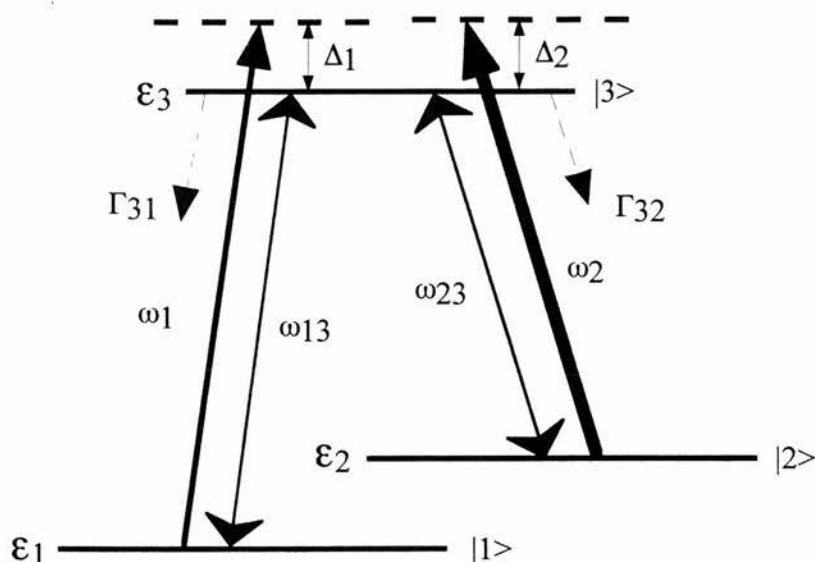


Figure 2.16: Schematic of the energy level configuration for a Lambda EIT system. The probe field is shown between states $|1\rangle$ and $|3\rangle$, with the coupling field applied to the transition between states $|2\rangle$ and $|3\rangle$. In a Lambda scheme the positions of the probe and coupling field are interchangeable.

Matrix 2.3: *Three level Lambda system.*

$$\begin{bmatrix}
 0 & \Gamma_{32} & 0 & 0 & 0 & 0 & 0 & 2 \times \Omega_{23} \\
 0 & (-\Gamma_{32} - \Gamma_{31}) & 0 & 0 & 0 & 0 & -2 \times \Omega_{13} & -2 \times \Omega_{23} \\
 0 & 0 & \gamma_{12} & 0 & 0 & (\Delta_{23} - \Delta_{13}) & -\Omega_{23} & -\Omega_{13} \\
 0 & 0 & 0 & \gamma_{13} & 0 & -\Omega_{23} & -\Delta_{13} & 0 \\
 0 & 0 & 0 & 0 & \gamma_{23} & \Omega_{13} & 0 & -\Delta_{23} \\
 0 & 0 & (\Delta_{13} - \Delta_{23}) & \Omega_{23} & -\Omega_{13} & \gamma_{12} & 0 & 0 \\
 -\Omega_{13} & 2 \times \Omega_{13} & \Omega_{23} & \Delta_{13} & 0 & 0 & \gamma_{13} & 0 \\
 \Omega_{23} & -\Omega_{23} & \Omega_{13} & 0 & \Delta_{23} & 0 & 0 & \gamma_{23}
 \end{bmatrix}
 \begin{bmatrix}
 \rho_{22} \\
 \rho_{33} \\
 \rho_{12}^r \\
 \rho_{13}^r \\
 \rho_{23}^r \\
 \rho_{12}^i \\
 \rho_{13}^i \\
 \rho_{23}^i
 \end{bmatrix}
 =
 \begin{bmatrix}
 0 \\
 0 \\
 0 \\
 0 \\
 0 \\
 0 \\
 -\Omega_{13} \\
 0
 \end{bmatrix}$$

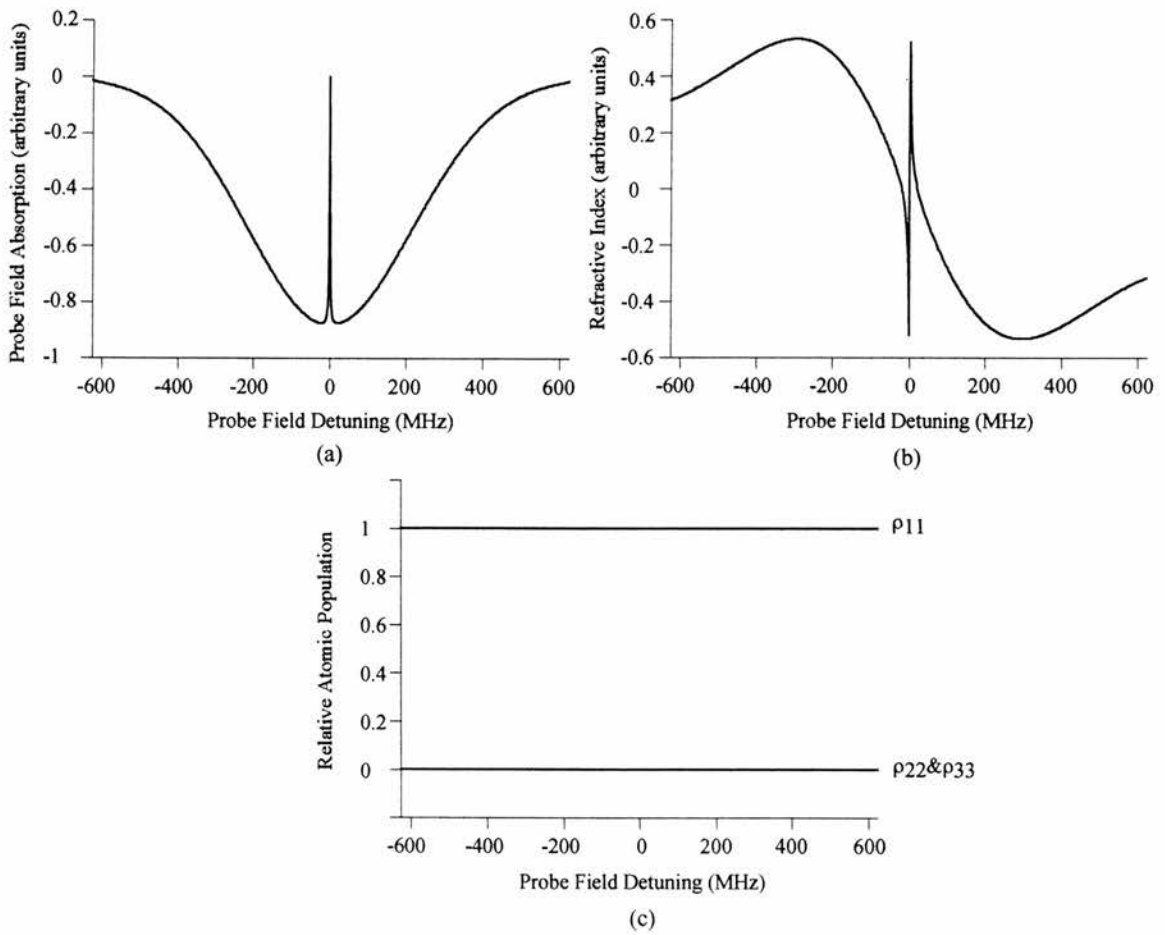


Figure 2.17: Shows (a) absorption, (b) refractive index, and (c) the relative atomic populations as a function of probe field detuning for a simple three level Lambda scheme in rubidium vapour. The labelled density matrix elements in (c), ρ_{11} , ρ_{22} , and ρ_{33} , correspond to the population in states $|1\rangle$, $|2\rangle$, and $|3\rangle$ respectively.

2.5.3 The Vee Scheme

Figure 2.18 depicts the energy level configuration employed in a Vee-type scheme. The relevant density matrix is shown in Matrix 2.4. The probe and coupling wavelengths are approximately 794nm and 780nm, corresponding to the $5S_{1/2} - 5P_{1/2}$ and $5S_{1/2} - 5P_{3/2}$ transitions in rubidium vapour respectively [8]. The decay rates are $40 \times 10^6 \text{ s}^{-1}$ (Γ_{31}) and $40 \times 10^6 \text{ s}^{-1}$ (Γ_{21}). Figure 2.19 shows (a) the absorption, (b) the refractive index, and (c) the relative populations in each of the atomic states.

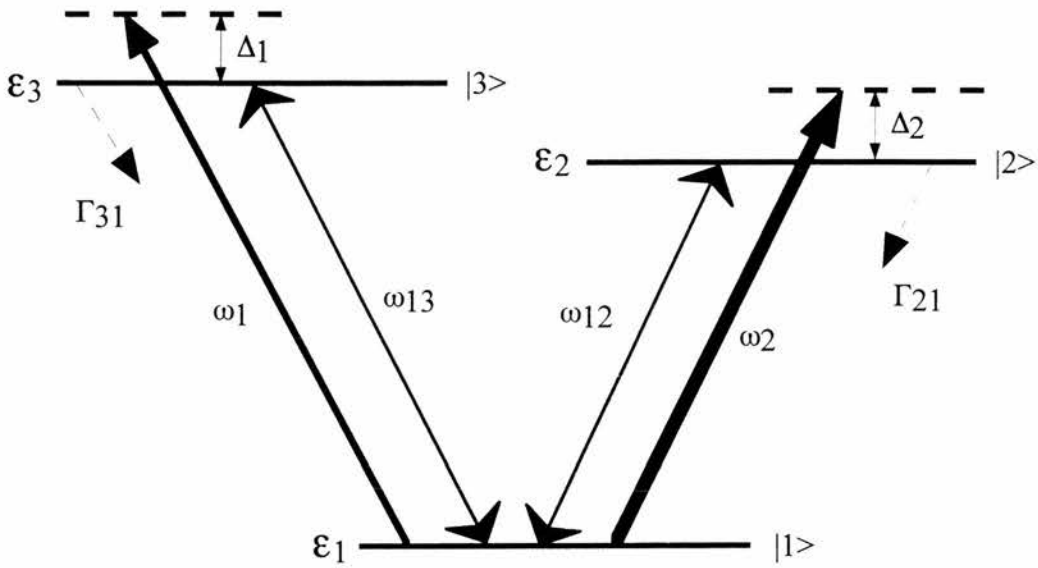


Figure 2.18: Schematic of the energy level configuration for a Vee EIT system. The probe field is shown between states $|1\rangle$ and $|3\rangle$, with the coupling field applied to the transition between states $|1\rangle$ and $|2\rangle$. In a Vee scheme the positions of the probe and coupling field are interchangeable.

Matrix 2.4: *Three level Vee system.*

$$\begin{bmatrix}
 \Gamma_{21} & 0 & 0 & 0 & 0 & 2 \times \Omega_{12} & 0 & 0 \\
 0 & \Gamma_{31} & 0 & 0 & 0 & 0 & 2 \times \Omega_{13} & 0 \\
 0 & 0 & \gamma_{12} & 0 & 0 & -\Delta_{12} & 0 & -\Omega_{13} \\
 0 & 0 & 0 & \gamma_{13} & 0 & 0 & -\Delta_{13} & \Omega_{12} \\
 0 & 0 & 0 & 0 & \gamma_{23} & \Omega_{13} & \Omega_{12} & -(\Delta_{13} - \Delta_{12}) \\
 -2 \times \Omega_{12} & -\Omega_{12} & \Delta_{12} & 0 & -\Omega_{13} & \gamma_{12} & 0 & 0 \\
 -\Omega_{13} & -2 \times \Omega_{13} & 0 & \Delta_{13} & -\Omega_{12} & 0 & \gamma_{13} & 0 \\
 0 & 0 & \Omega_{13} & -\Omega_{12} & (\Delta_{13} - \Delta_{12}) & 0 & 0 & \gamma_{23}
 \end{bmatrix}
 \begin{bmatrix}
 \rho_{22} \\
 \rho_{33} \\
 \rho_{12}^r \\
 \rho_{13}^r \\
 \rho_{23}^r \\
 \rho_{12}^i \\
 \rho_{13}^i \\
 \rho_{23}^i
 \end{bmatrix}
 =
 \begin{bmatrix}
 0 \\
 0 \\
 0 \\
 0 \\
 0 \\
 -\Omega_{12} \\
 -\Omega_{13} \\
 0
 \end{bmatrix}$$

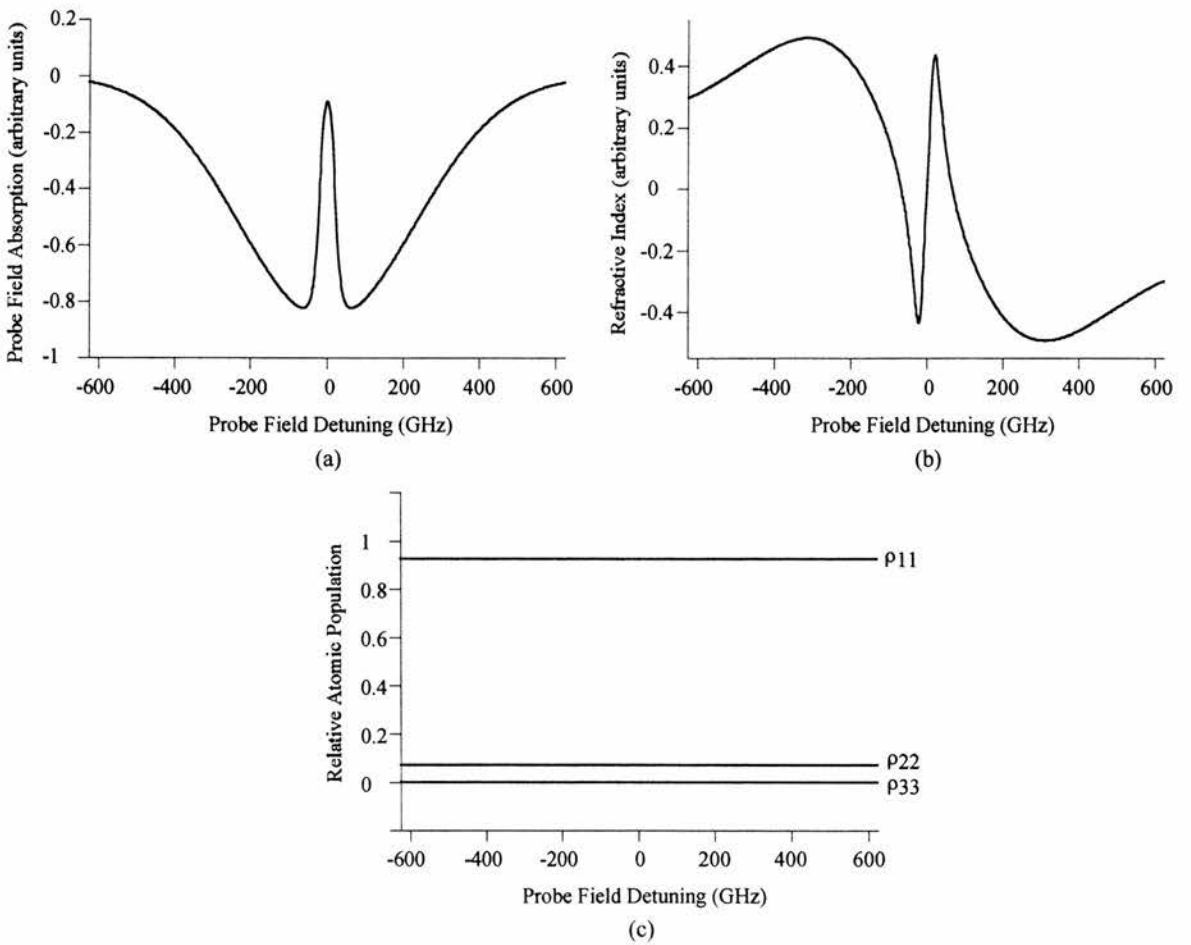


Figure 2.19: Shows (a) absorption, (b) refractive index, and (c) the relative atomic populations as a function of probe field detuning for a simple three level Vee scheme in rubidium vapour. The labelled density matrix elements in (c), ρ_{11} , ρ_{22} , and ρ_{33} , correspond to the population in states $|1\rangle$, $|2\rangle$, and $|3\rangle$ respectively.

Aside from the sharp peaks in absorption that are predicted in the Cascade scheme the biggest differences between the profiles generated for each atomic energy level configuration are the spectral width of the absorption and refractive index features that appear as a result of quantum coherence. The width of these features is controlled by the dephasing on the unlinked transition in the employed atomic system. The features are sharpest in the Lambda scheme because the unlinked transition is not dephased by radiative decay. In the Cascade scheme the dephasing is very small at only $3 \times 10^6 \text{ s}^{-1}$, and the features predicted are correspondingly narrow. The dephasing of the unlinked transition in the Vee scheme is significantly larger at $40 \times 10^6 \text{ s}^{-1}$, and the predicted coherently induced changes in the absorption and refractive index, consequently, have a much broader lineshape. In an experimental situation the features observed would be broader still, due to additional dephasing mechanisms that have not been taken into account in our idealised models.

2.6 Three-dimensional Modelling

To achieve a better understanding of the effects of Doppler-broadening and the interplay of Autler-Townes splitting and coherence, a three-dimensional model of EIT was created. This is based on the density matrix model, but rather than integrating over the atomic velocities, the density matrix elements are plotted as a function of both the probe field detuning and the atomic velocity. This allows us to assess the contribution of each velocity group to the overall absorption. A picture is thus gained, of exactly how the Autler-Townes absorptions overlap at line centre. As we shall see in Chapter 4 the ability to model a system in this way allows us to differentiate between the wavelength dependence of the transparency in the three EIT schemes.

Figure 2.20 shows a three-dimensional plot of the absorption experienced in a two level atom subject to a single optical field. The probe absorption (ρ_{12}^i in arbitrary units) is calculated for a finite number of discrete atomic velocities within the Doppler-broadened profile. The 'net' absorption profile can be constructed by integrating over all such atomic velocities. In Fig. 2.20 we can see the shape of the Doppler-broadened absorption profile traced out by the peak absorptions of each velocity group. The zero velocity group has the strongest absorption because there are more atoms at rest than there are at any other specific non-zero velocity. If we consider the non-zero velocities, the magnitude of the absorption diminishes because the number of atoms available to absorb decreases with increasing velocity.

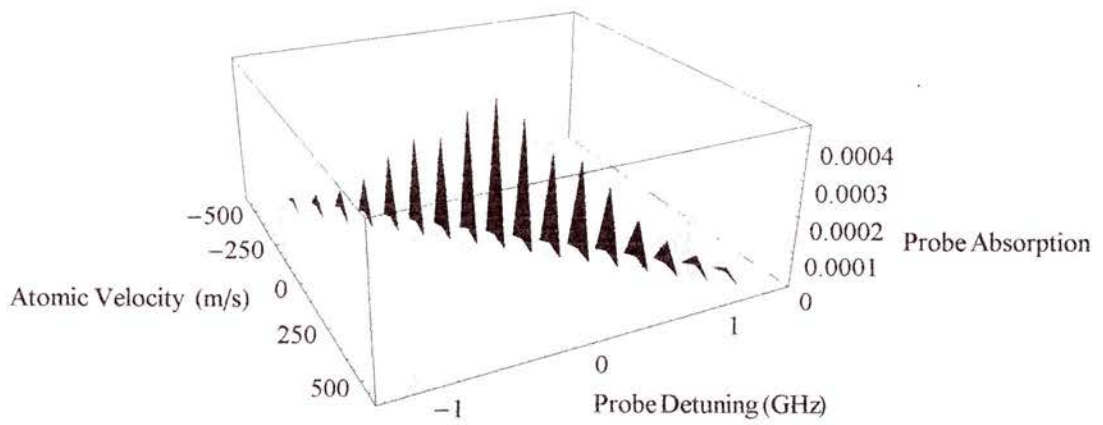


Figure 2.20: Three-dimensional plot of the probe field absorption (ρ_{12}^i in arbitrary units) as a function of atomic velocity and probe field detuning. The absorption is calculated for a finite number of discrete atomic velocities within the Doppler-broadened profile.

Figure 2.21 shows three absorption profiles for individual velocity groups which correspond exactly to the relevant peaks in the three dimensional plot (Fig. 2.20).

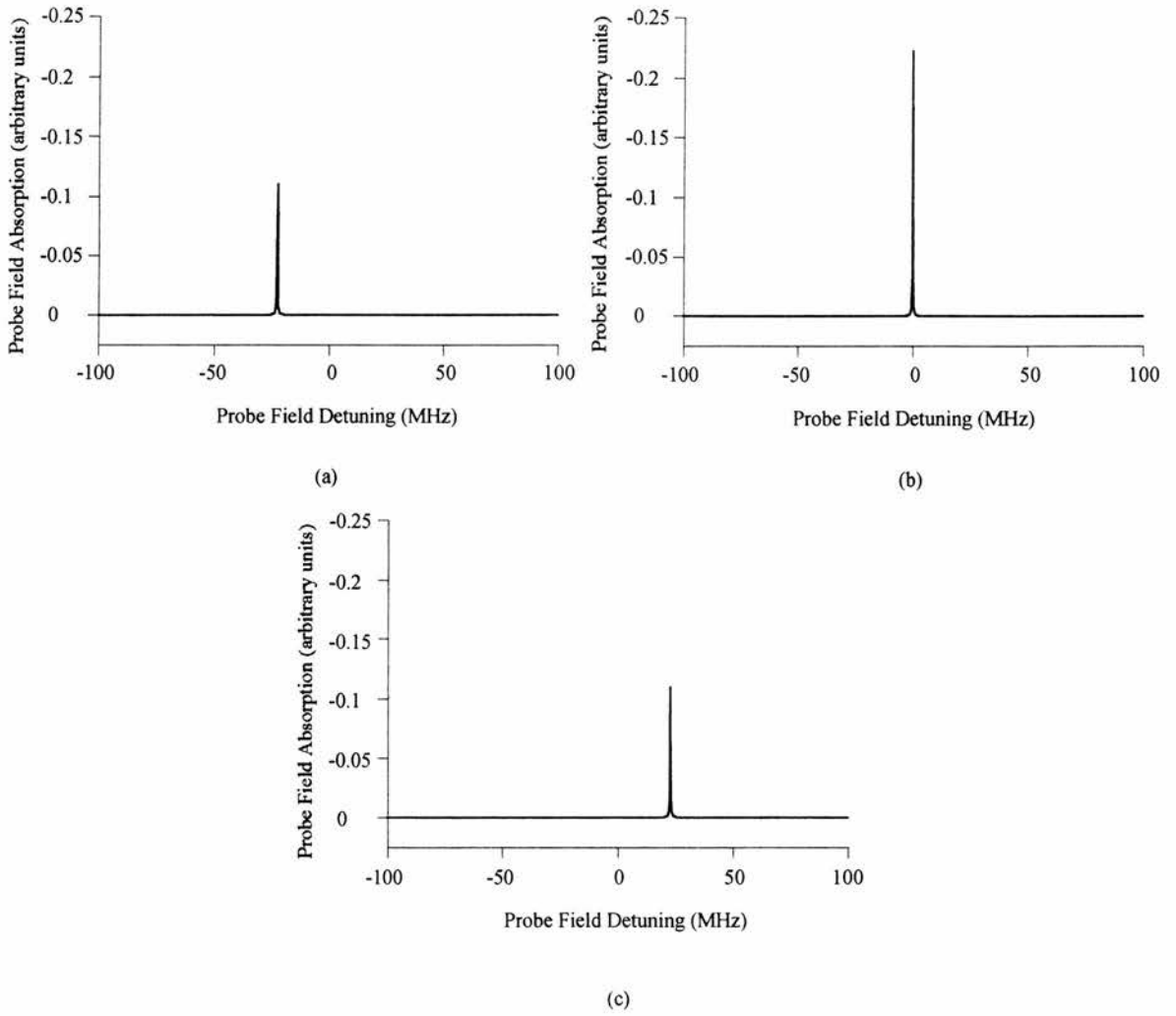


Figure 2.21: Three absorption profiles for the atomic velocities (a) -60 , (b) 0 , and (c) 60ms^{-1} .

2.7 Moseley's N Level Rules

During the course of his PhD, Richard Moseley developed a set of rules that may be used to derive the density matrix quickly for a given system [1]. These rules are based on the patterns that occur within the density matrices, dividing the matrix into key areas associated with particular aspects of the light-matter interaction. For example, the top left hand corner of the matrix contains the population decay terms and any incoherent pumping rates or mixing terms that may have been added to the system. Employing these rules allows a system matrix to be written down directly, without reference to the original Liouville equation, and thus bypasses the bulk of the time-consuming derivation that would otherwise be necessary. Moseley's N level rules allow the construction of the $N^2 - 1$ real simultaneous equations which describe the steady state of an arbitrary N level atom subjected to a number of coherent electromagnetic fields (up to a maximum of $N - 1$), while implicitly employing the rotating wave approximation. The full potential of these rules can only be realised if they are used with care and an appreciation of the full derivation process from first principles. However, with this understanding in place these rules serve as a very useful and elegant way of deriving a particular system's density matrix. Moreover, the rules provide a useful method of verifying a matrix derived by the traditional method described in Section 2.3.

References

- [1] R. R. Moseley, *Sum Frequency Mixing and Quantum Interference in three level Atoms*, (unpublished PhD thesis, St. Andrews, (1994)).
- [2] A. Yariv, *Quantum Electronics*, (Wiley, New York, 3rd edition, (1989)).
- [3] R. Tolman, *The Principles of Statistical Mechanics*, (Clarendon Press, Oxford, (1939)).
- [4] B. Shore, *The Theory of Coherent Atomic Excitation*, (John Wiley & Sons, New York, (1990)).
- [5] J. Vanier, *Basic Theory of Lasers and Masers*, (Gordon and Breach, London, (1971)).
- [6] R. G. Brewer and E. L. Hahn, *Phys. Rev. A* **11**, 1641, (1975).
- [7] S. Wolfram, *Mathematica: A System for Doing Mathematics by Computer*, (Addison-Wesley, Reading, 2nd edition, (1993)).
- [8] C. E. Moore, *Atomic Energy Levels - As derived From the Analyses of Optical Spectra*, (Circular of the National Bureau of Standards 467, (1952)).

CHAPTER 3

Experimental Apparatus and Materials

“The thing with high-tech is that you always end up using
scissors.”

David Hockney

3.1 Introduction

Experimental studies of coherence effects require multiple laser sources and a variety of diagnostic equipment. This chapter looks at the laser systems employed in these studies at St. Andrews along with the diagnostic and detection apparatus. The equipment includes items purchased commercially, modified systems, and apparatus designed specifically for the study of EIT. Special attention is devoted to the system utilised for the production of blue light (experiment, Chapter 5) as well as a possible method for providing the incoherent excitation required to produce gain. The final section of this chapter deals with the interaction medium, rubidium vapour, employed experimentally. Understanding the atomic structure and properties of rubidium is essential to the interpretation of the reported experimental results.

3.2 Laser Systems

There are several constraints on the optical fields required to produce electromagnetically induced transparency, as implied by previous discussion. For quantum interference effects to take place it is necessary for the applied coupling field to be coherent and of a narrow spectral width. The latter condition is satisfied by the employment of a laser field. Although it is not essential for the probe field to meet these criteria [1] the theoretical modelling discussed in Chapter 2 assumed as much and a coherent narrowband laser is used for all the work in this thesis. Furthermore, the theory developed in Chapter 2 was strongly dependent on the premise that experiments would take place under steady state conditions. This assumption was based on the utilisation of continuous wave laser systems. In addition, spectroscopic work of this nature requires systems that are tuneable over specific wavelength ranges. In our case, we seek to access selected transitions in rubidium vapour. The atomic structure of rubidium involves several closely matched near infrared (750 - 850nm) transitions which correspond to the spectral range of Ti:sapphire lasers. In addition, the 422nm, $5S_{1/2} - 6P_{1/2}$, transition conveniently falls within the frequency doubled range of Ti:sapphire. It is also essential for the probe laser to lock and scan a transition over a frequency range of approximately 10GHz. The precise combination of laser systems for an experiment will depend on the specific requirements of that study. This section gives an overview of the systems relevant to the work presented in this thesis.

3.2.1 Pump Lasers

The Ti:sapphire laser systems used in this work were optically pumped by continuous wave, argon-ion lasers, which are themselves pumped by an electrical discharge. A Spectra Physics 2030 pumps a Schwartz Ti:sapphire laser and a Spectra Physics 2080 with BeamLock™ pumps a Microlase Ti:sapphire. The argon-ion lasers are run at 10W and 8W respectively.

The BeamLock™ system uses feedback control to adjust the position of one of the argon-ion cavity mirrors. This adjustment is designed to keep the laser output stable while the system warms up.

3.2.2 Schwartz Titanium Sapphire Laser (750 - 820nm)

This system is comprised of a modified Schwartz Electro Optics Titan-cw laser, and it is described in detail by Shepherd [2]. Figure 3.1 shows a schematic of the travelling wave bow-tie cavity of the modified Schwartz laser. The birefringent filter coarsely tunes wavelength while finer tuning can be obtained by using the solid etalon which mode hops the output between cavity modes, separated by 250MHz. Brewster plates can also be added to the cavity to tune the frequency between cavity modes in order to find resonance with a desired atomic transition. The Brewster plates are not usually required and the addition of the extra optical element reduces the available output power. No commercial scanning or stabilisation system is included, but a free running linewidth of $< 5\text{MHz}$ has been measured [3], and a stabilisation and scanning system was designed by Shepherd [2]. The system is capable of producing 1.3W of single frequency light at approximately 800nm.

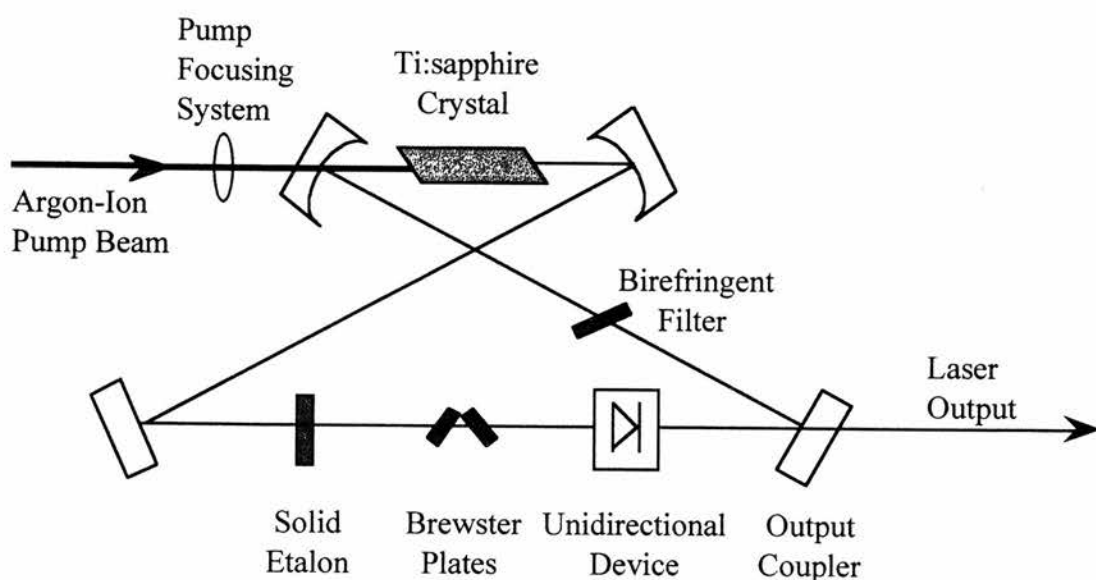


Figure 3.1: Schematic of Schwartz Ti:sapphire laser.

3.2.3 Microlase MBR 110 Titanium Sapphire Laser (700-1060nm)

The schematic in Fig. 3.2 shows a similar bow-tie cavity to the Schwartz laser. However, the Microlase incorporates a frequency stabilisation system via side of fringe locking to an external, temperature controlled, confocal reference cavity. This stabilisation technique results in specified linewidths of less than 200kHz. In addition, the frequency may be smoothly scanned over a specified range of up to 30 GHz by the servo locking of

the single solid etalon. Good passive stability is maintained by housing the cavity in a monolithic block. Single frequency output powers of 2W may be achieved at 780nm. However, typical day to day figures are approximately 500mW output at a single frequency with a scanning range of up to 10GHz. The quoted range of wavelength operation, 700-1060nm, is achieved with six mirror sets.

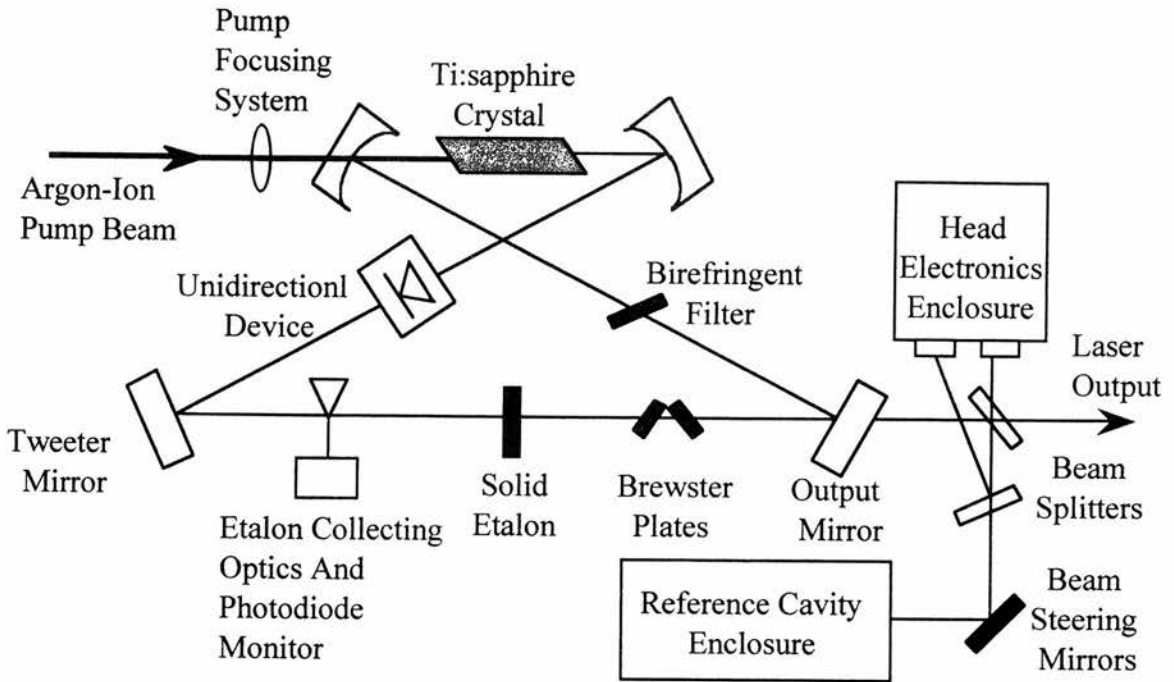


Figure 3.2: Schematic of Microlase Ti:sapphire laser.

3.2.4 Spectra Physics 380D Dye Laser

The Dye laser was originally employed to provide tuneable radiation for experiments in sodium [4,5]. Wavelength of operation is dependent on the choice of dye and regions of the spectrum beyond the range of Ti:sapphire lasers are possible. The Dye laser has therefore remained useful for accessing some transitions in rubidium that are unobtainable with Ti:sapphire based laser systems; specifically, the 572nm transition between the $5P_{3/2}$ and $7D_{5/2}$ excited states. In addition, some of the proposed inversionless lasing experiments require the application of more than two lasers. The Dye laser is a continuous wave, frequency stabilised source with a linewidth of approximately 1MHz that is scanable over 30GHz under the manufacturer's electronic control. The employed gain medium was rhodamine 6G dissolved in ethylene glycol which has an

operating lifetime of approximately 6 weeks. Pumped by the Spectra Physics 2030 argon-ion laser, 250mW can be reliably produced at 572nm. A schematic is provided in Fig. 3.3.

The Dye laser was utilised to obtain some of the experimental points verifying the theoretical prediction that mismatched EIT was achievable in a Doppler-broadened Cascade system [6]. This work was briefly summarised in Section 1.6.1.

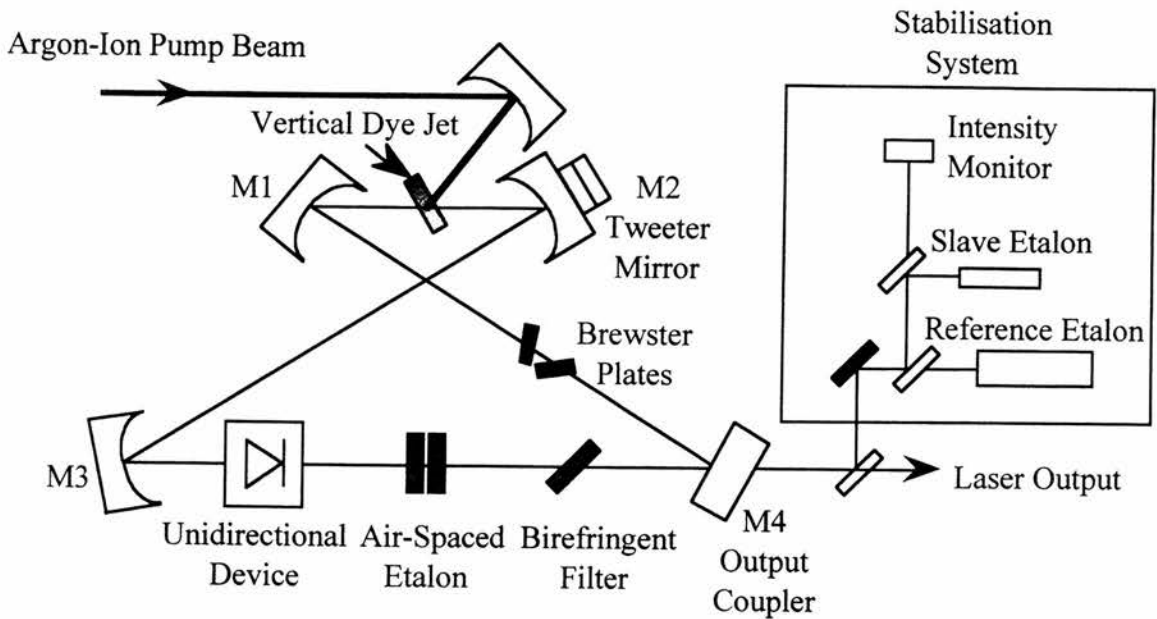


Figure 3.3: Schematic of Dye laser.

3.2.5 Experimental Applications

The experiment presented in Chapter 5 utilised the Schwartz and Microlase systems in the configuration shown in Fig. 3.4. The Dye laser was used to provide experimental verification of the theory developed by Shepherd [6], as shown previously in Fig. 1.19. Other laser systems, not described here, were developed to be used as pump sources both in the removal of optical pumping and the creation of optical gain. Optical pumping, as it transpired, was not present in our experimental scheme precluding the use of an additional pump source. An experimental investigation of inversionless gain is ongoing.

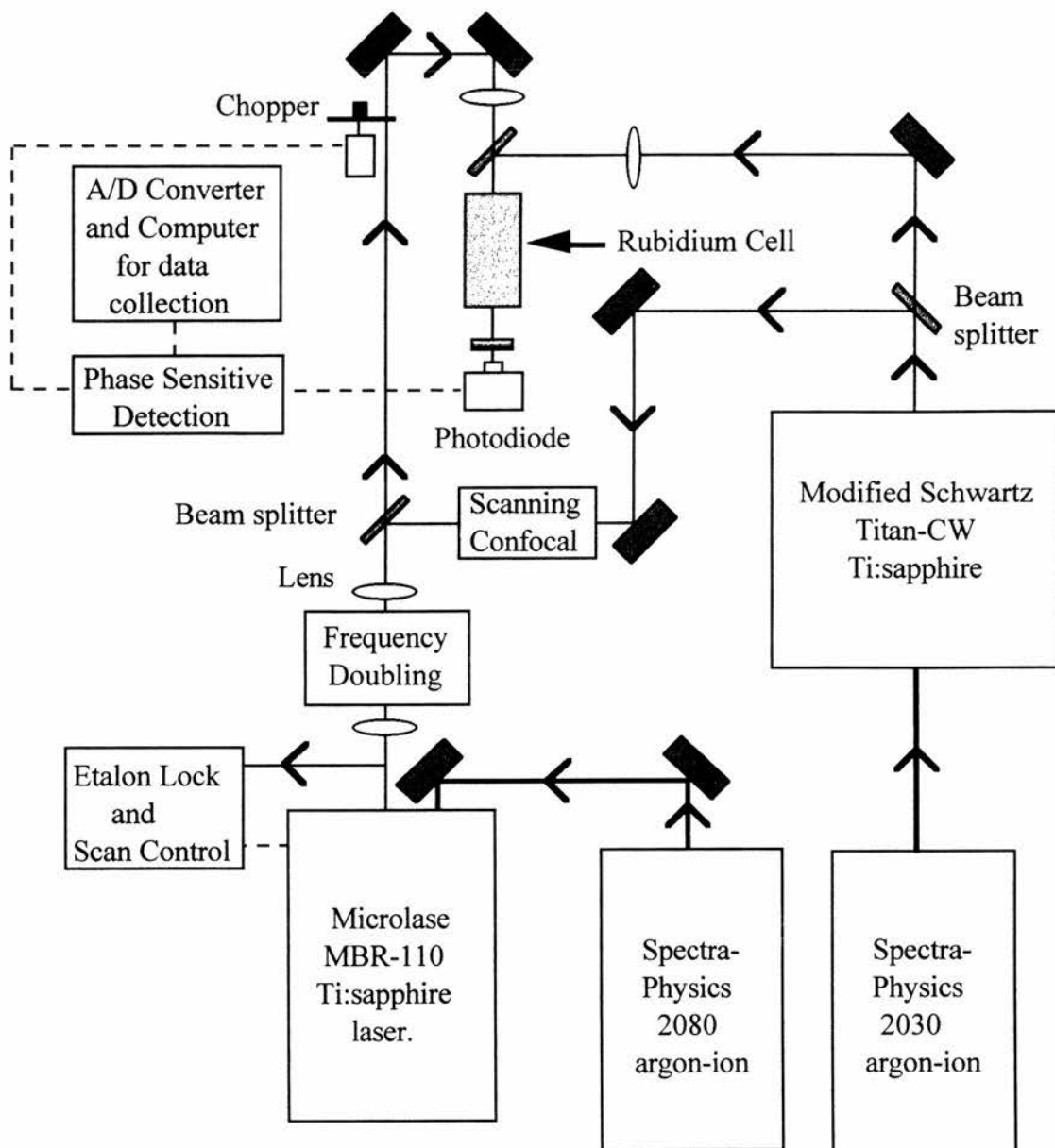


Figure 3.4: Schematic of set up employed in the experiment reported in Chapter 5. The probe beam (frequency doubled *Microlase Ti:sapphire*) and the coupling beam (*Schwartz Ti:sapphire*) co-propagate through the rubidium vapour cell.

3.3 Diagnostics and Ancillary Equipment

3.3.1 Diagnostics

A scanning confocal interferometer monitors the longitudinal mode operation of the lasers. The Fabry Perot interferometer, with a spectral range of 1.5GHz, is ramped by a piezo mirror and is thus able to detect single or multi-mode laser operation. The output of the etalon is viewed on an oscilloscope, and it can be used to monitor frequency stability as well as single mode operation.

A low finesse, fixed etalon provides a frequency marker for recorded scans of the Microlase Ti:sapphire. The etalon's free spectral range of 300MHz affords a useful frequency reference when analysing results. This value is based on $c/4L$ where L is the length of the etalon and assumes the etalon is not perfectly mode matched. The etalon is aligned experimentally so that mode matching does not occur. The mode matched free spectral range would be $c/2L$. When the confocal frequency marker was used in conjunction with the doubling system (Section 3.4) the frequency of the confocal marker was itself doubled to 600MHz.

The various employed Ti:sapphire laser wavelengths are measured using a Kowalski-style travelling wavemeter. This system is accurate to 1 part in 10^6 , employing a double Michelson interferometer arrangement with a scanning arm. The wavelength of incident light is measured by comparison with the wavelength of a polarisation-stabilised helium-neon laser at 473611.1GHz (633.43nm). The range of wavelength operation is very wide as a result of aluminium coated reflective optics. The accuracy of this system is sufficient to place the lasers within a single etalon mode of the desired atomic transition (to within a few GHz). A more detailed description of this apparatus is given by Kane [7].

Fluorescence from the rubidium cell can be measured, as an additional diagnostic, with a photomultiplier tube operating at the appropriate wavelength. The fluorescence results from the radiative decay of population excited by an incident laser beam.

3.3.2 Signal Detection

Powers of up to 100mW are measured with a Newport 835 Optical Power Meter. For greater powers either a Coherent 210 or a Spectra Physics 407A Power Meter is

utilised. Photomultiplier tubes, appropriate to the wavelength in question, are employed to detect weaker fluorescence signals. Measurements of the probe power transmitted through the rubidium cell are achieved with a reverse biased, wide-area photodiode in conjunction with a simple amplifier circuit. Optical filters are used to block the Ti:sapphire and argon-ion light, where appropriate.

In experiments in which more than one laser beam propagates through the cell, it is important to utilise the appropriate focusing optics. Lenses are selected on the basis of the specific experiment's requirements. Figure 3.5 shows typical beam waist measurements of the probe and coupling laser in a standard EIT Cascade experiment. The measurements were taken with a translational beam profiler. The important aspect is that the probe laser lies within the width of the coupling laser as the beams propagate through the vapour region in the cell. This configuration was based on a 20cm lens focusing the probe beam and a 40cm lens focusing the coupling beam through a 2cm cell.

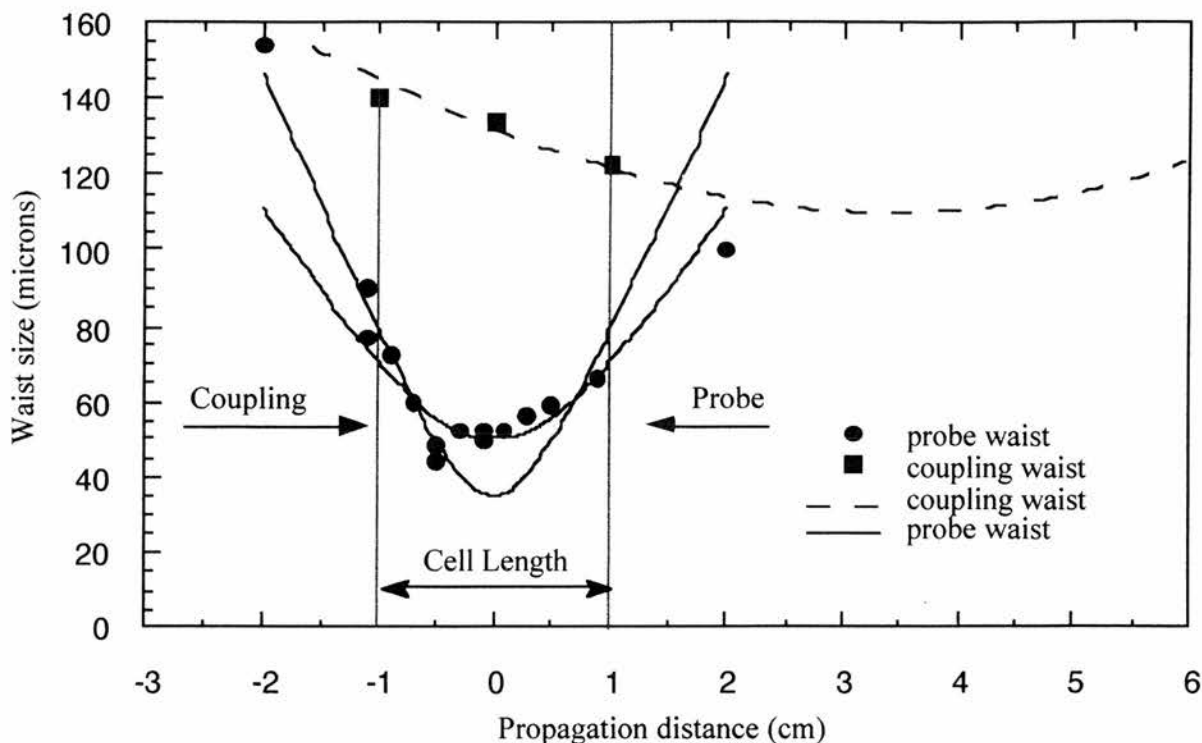


Figure 3.5: Measured waist sizes of the probe and coupling lasers inside the vapour cell. The solid squares and circles correspond to experimentally measured values of the coupling and probe waists respectively; the two solid lines represent theoretical beam waist values for the probe laser, corresponding to focused waist sizes of 35 and 50 μm ; and the dashed line represents theoretical beam waist values for a coupling beam of focused waist size 110 μm .

Input beam powers can be controlled with neutral density filters; allowing the power of the beam to be changed without affecting its transverse mode quality.

To obtain a useful measurement of the probe signal it is necessary to employ phase sensitive detection to remove unwanted background noise. The probe beam incident to the cell is chopped at a frequency of a few hundred Hertz. The end signal, fed into an oscilloscope from the lock-in amplifier, will be comprised only of light modulated at the chopper frequency. The un-chopped background light is thus discarded.

A digital Techtronix TDS 20 oscilloscope is used to monitor the level of transmitted probe signal after phase sensitive detection. This signal is sent via an analogue to digital converter to a PC along with the Microlase scan ramp and the frequency marker from the

fixed etalon. Figure 3.6 provides an example of such a trace as seen on the PC. This case corresponds to the absorption of a blue 422nm probe field on the $5S_{1/2} - 6P_{1/2}$ transition in ^{85}Rb and ^{87}Rb .

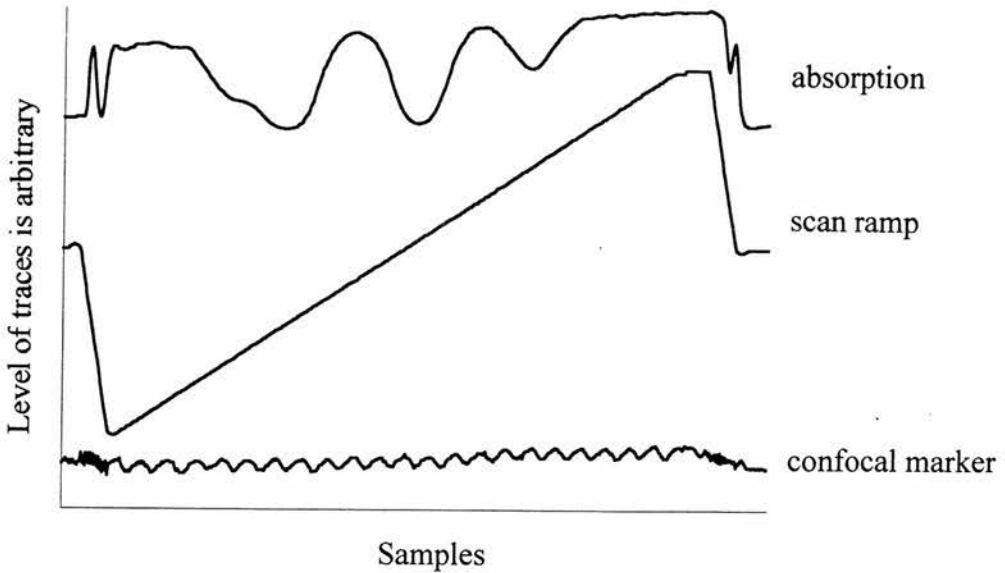


Figure 3.6: *Traces taken from a single scan of the Microlase Ti:sapphire. The top trace is the level of probe light transmitted through the rubidium cell. The middle trace corresponds to the scan ramp from the Microlase and the bottom trace is the confocal marker, in which one cycle represents 600MHz.*

3.4 Frequency Doubling System

The main thrust of experimental effort has been concentrated on breaking into the mismatched wavelength regime, while remaining within Doppler-broadened systems. This research has led to the realisation of EIT in visible light. We selected a Vee scheme for reasons that will become clear in Chapter 4. The probe transition lies between the $5S_{1/2}$ and $6P_{1/2}$ states of rubidium vapour, corresponding to a wavelength of approximately 422nm. It was therefore necessary to develop a blue laser source, at this wavelength, that satisfied all the normal requirements of a probe beam, i.e. an output power of the order of tens of microwatts, a stable single frequency, and a scanning range of approximately 10GHz.

Three methods were considered for the production of the blue probe field. The first system employed a grating tuned diode at 844nm that would be frequency doubled by potassium niobate in an external resonant cavity. Such a system already exists at the National Physics Laboratory, and an independently developed system became commercially available from Technolas in early 1997.

Diode lasers are now a viable alternative to Ti:sapphire lasers for many applications [8] and grating tuned diodes are a well documented means of producing narrow linewidth, tuneable light from a compact, relatively inexpensive, diode source [9].

In order to achieve high conversion efficiencies with the nonlinear crystal, it must be placed in a region of high fundamental field intensity. Such a region exists within the laser cavity itself; however, this poses certain problems. For instance, the thermal effects in the crystal degrade the frequency stability of the laser output and the addition of an extra birefringent element makes cavity alignment more critical, upsetting tuning and unidirectional behaviour. For an intra-cavity system, simultaneous optimisation of the internal field at both the fundamental and harmonic wavelengths would be required.

A possible solution to these problems is to place the doubling crystal in a separate external resonant cavity which has an internal field optimised at the harmonic wavelength. Similar work has been carried out to produce an ultraviolet source by frequency doubling a Ti:sapphire laser in an external resonant cavity [10]. Figure 3.7 depicts a schematic picture of a grating tuned diode system.

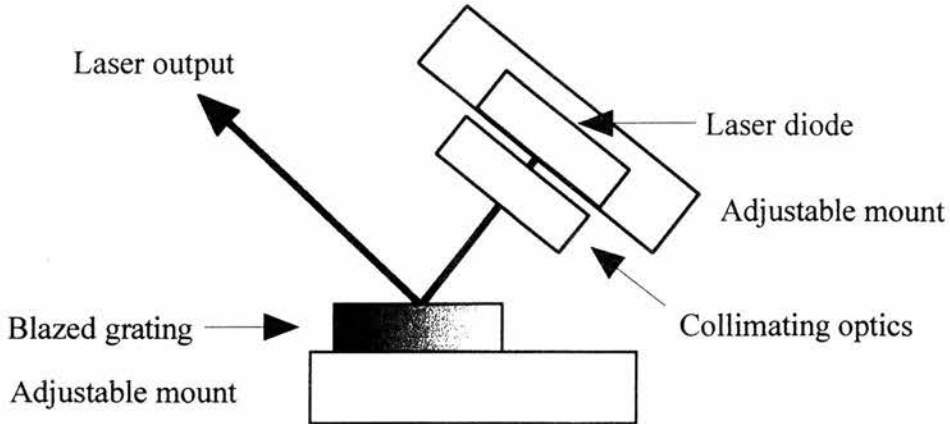


Figure 3.7: *Schematic of grating tuned laser diode system.*

Although this system is practically realisable, its construction was deemed too costly and time-consuming, given the more straightforward alternative. A second option was the possibility of frequency doubling the Technolas ‘turn key’ tuneable diode system with a single pass through potassium niobate. Single pass conversion will provide significantly less second harmonic power for a given pump level, but such a system may be adequate due to the low power requirements of a probe laser source. The experiment reported herein relied on a single pass doubling scheme but utilised the Microlase Ti:sapphire laser as a pump rather than a diode based system. This method was chosen chiefly for economic reasons.

Initial experiments at room temperature with a non-critical phase-matched (NCPM) KNbO_3 crystal showed that with a pump power of 150mW at 860nm, an output power of up to 150 μ W could be achieved at 430nm for optimised focusing in a crystal length of 10mm. Therefore, the output power required can be easily obtained by this method. An additional advantage of employing the Microlase as a pumping source is that the blue light, thus produced, would inherit the frequency stability and control of the Microlase.

3.4.1 Potassium Niobate

The choice of crystal is largely governed by its phase matching range and nonlinear coefficients. Additional factors that come into play include the optical damage limit, thermal properties and characteristics such as solubility in cleaning solvents like methanol.

A crystal's physical hardness may also limit the working of the crystal and the ease of applying anti-reflection coatings.

Potassium niobate was chosen for this work due to its favourable nonlinear coefficient and temperature tuned phase matching in a NCPM geometry. The low optical damage threshold is not an important consideration in this case, due to the low probe laser power requirements.

Potassium niobate is a type $mm2$ negative biaxial crystal, and hence has more than one phase matching possibility. Angle tuning can take place in the three crystal planes of potassium niobate achieving a wavelength range at room temperature of 857 - 4800nm. This entire range can be covered in the c-a plane (type I, o - o - e). At the lowest phase-matched wavelength (857nm) the effective nonlinear coefficient is 20.8pm/V. The other phase matching mechanism is achieved by temperature tuning the potassium niobate crystal. This alternative tuning method allows a single crystal to access a variety of wavelengths, within an NCPM geometry, beyond the room temperature range stated above.

The $5S_{1/2} - 6P_{1/2}$ transition we wish to probe in rubidium vapour has a wavelength of 421.55nm [11]. This transition requires a fundamental wavelength of approximately 843nm, outside the room temperature range of potassium niobate. We must therefore rely on temperature tuning to provide the required phase matching. The crystal is cut for propagation along the a axis as shown in Fig. 3.8. The principle and crystal axes are coincident and NCPM is therefore achieved for a room temperature wavelength of approximately 860nm ($n_x > n_y > n_z$). The fundamental Ti:sapphire light is horizontally polarised along the b axis by virtue of the Brewster plates in the laser cavity, and the second harmonic is vertically polarised as shown in Fig. 3.8. Note that it is necessary to place the crystal slightly off normal incidence to prevent feedback into the Ti:sapphire laser cavity. Consequently, some degree of walk-off will occur in the crystal; however, this effect will be small and of no great concern since the power requirement is not particularly demanding for this application.

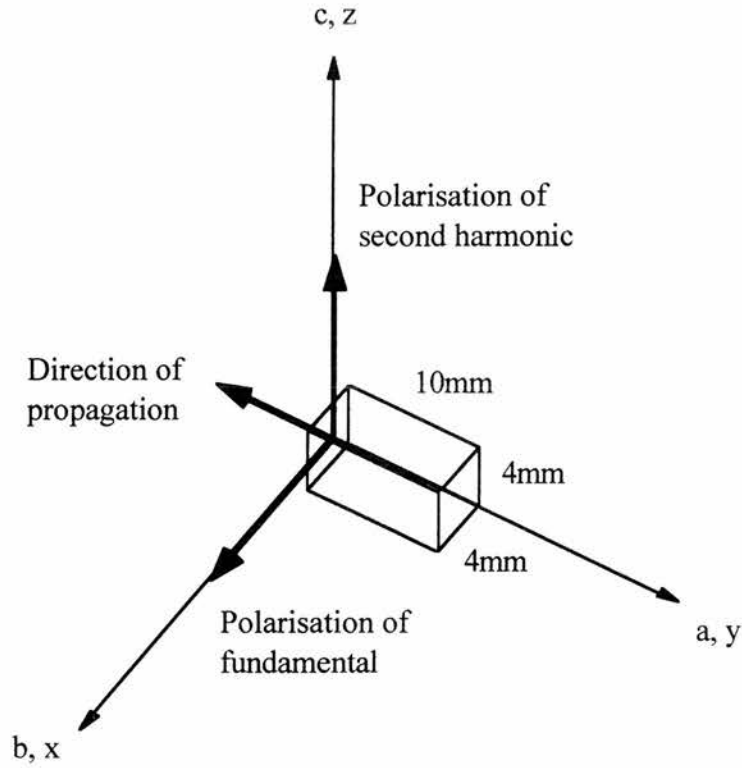


Figure 3.8: *Crystal and principle axes in potassium niobate along with polarisations of fundamental and second harmonic fields and the direction of propagation. The dimensions of the employed crystal are also indicated.*

Biaggio *et al* [12] proposed a temperature dependence for the phase matched wavelength which is a second degree polynomial, fitting the results from seven sources to give the following expression:

$$\lambda_{\text{pm}}(\text{nm}) = 850.4 + 0.294(T) + 1.234 \times 10^{-3}(T^2) \quad (3.1)$$

where T is the temperature in $^{\circ}\text{C}$. This expression, verified experimentally by Shepherd [2], is plotted in Fig. 3.9.

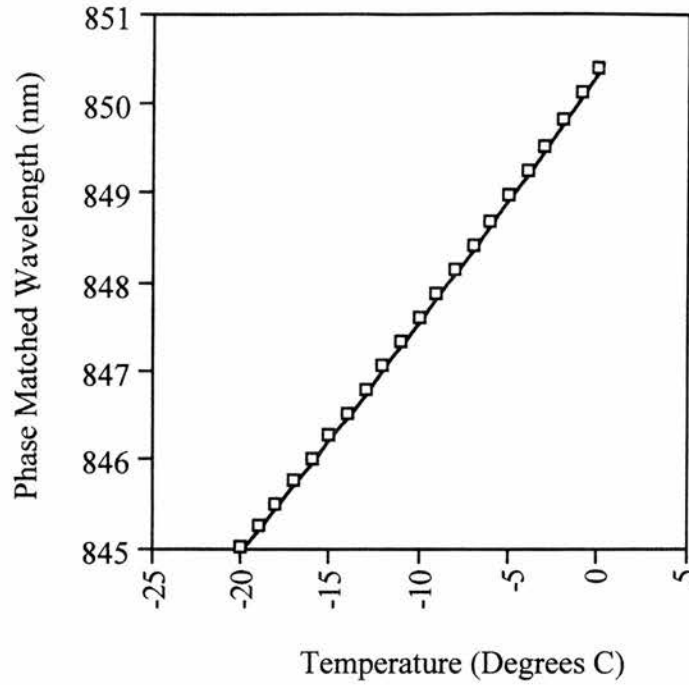


Figure 3.9: *Theoretical graph based on Eq. (3.1), showing the relationship between crystal temperature and phase matched wavelength.*

Figure 3.9 demonstrates that the potassium niobate crystal must be stabilised at approximately -15°C . This temperature was achieved and maintained with a thermoelectric cooler mounted in a specially designed oven.

3.4.2 Thermoelectric Cooler and Mount

Thermoelectric coolers (TECs) are small heat pumps that work by the same law of thermodynamics that governs the conventional refrigerator. The principal difference is that TECs are solidstate devices. Such a device is advantageous in this application since it provides localised cooling and precision temperature control in a small package. After testing the performance of several modules, our system uses a Marlow DT 12-4-LS thermoelectric cooler. The single stage thermoelectric cooler is made up of a matrix of thermoelectric couples, an example of which is shown schematically in Fig. 3.10.

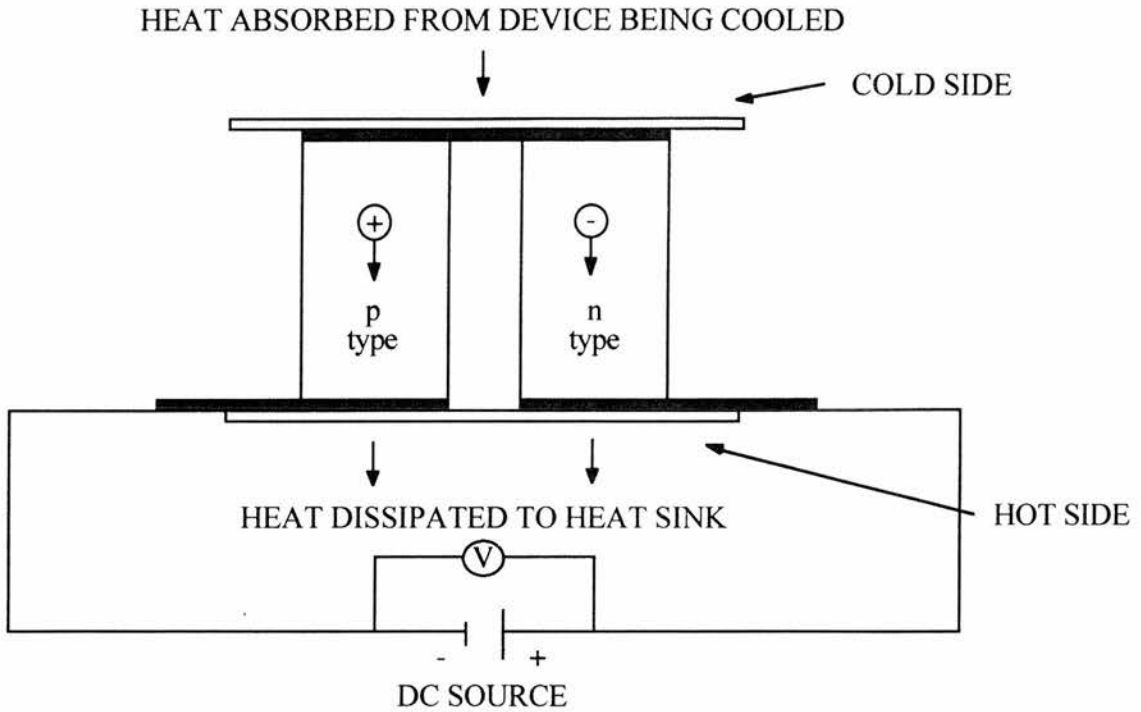


Figure 3.10: *Thermoelectric cooler (TEC).*

When a positive dc voltage is applied to the n-type thermoelement, electrons pass from p-type to n-type, and the cold side temperature begins to decrease as heat is absorbed. The heat absorption, or cooling, is proportional to the current and the number of thermoelectric couples. This process occurs when electrons pass from a low energy level in the p-type thermoelement to a higher energy level in the n-type thermoelement. The heat is then conducted through the hot side and liberated as the electrons return to a lower energy level.

It is necessary to remove the liberated heat energy from the system, and water cooling was employed to do so by pumping low pressure water through the brass cooling block that forms the base of the unit. Experience demonstrated that this cooling was essential to the successful operation of the device.

The potassium niobate crystal must be carefully mounted in thermal contact with the cold side of the TEC. Design must take into account the fact that potassium niobate is compression sensitive and mildly hygroscopic. An expanded view of the mount designed for this purpose is displayed in Fig. 3.11. Note that the mount is made from brass with a PTFE insulating jacket (not shown in Fig. 3.11).

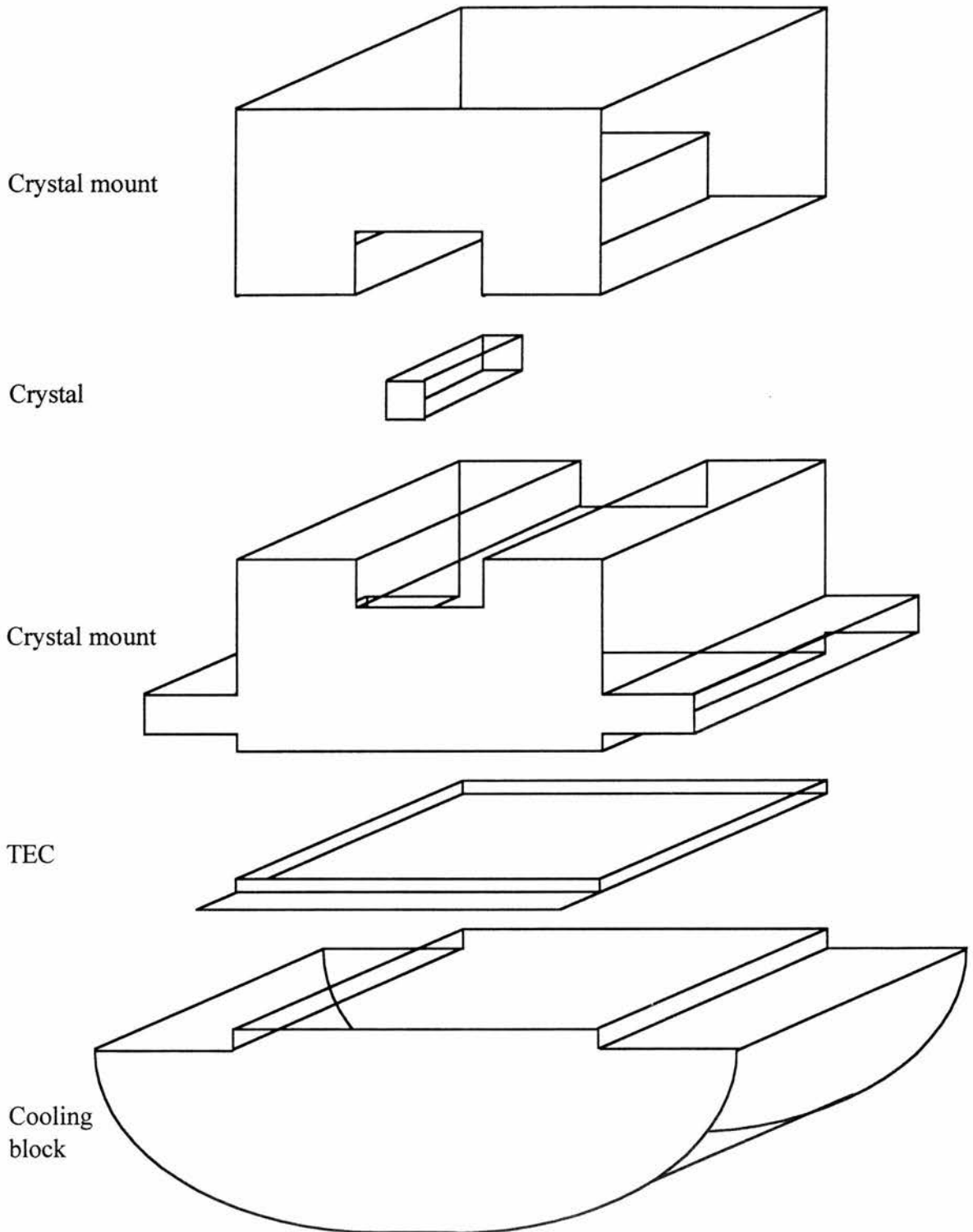


Figure 3.11: Cooling mount designed to stabilise the temperature of the potassium niobate crystal.

Care is taken to ensure that no thermal contact occurs between the hot and cold sides of the TEC by holding the module in place with nylon screws. The current driving the TEC is controlled by a Newport Model 325 Temperature Controller which allows the temperature to be stabilised at a specified value to an accuracy of 0.01°C with the help of an integrated circuit temperature sensor. This sensor stabilises the temperature to that of the brass mount rather than the crystal itself. An offset is therefore required to achieve the correct crystal temperature. An experimental calibration curve is shown in Fig. 3.12.

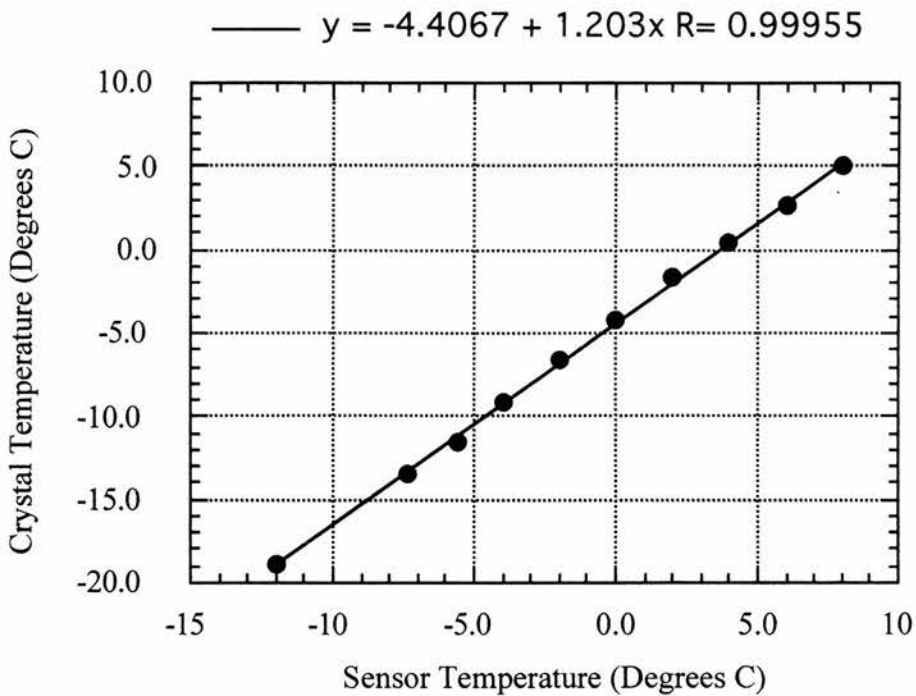


Figure 3.12: Calibration graph yielding the sensor temperature required to set the temperature of the crystal.

3.4.3 Creating a Dry Environment

When the potassium niobate crystal cools to -15°C condensation forms on both the crystal and crystal mount. Droplets of water on the crystal's surface increase the risk of optical damage occurring as a result of the incident laser radiation. The crystal itself is also hygroscopic, and high condensation levels will reduce the fundamental power falling on the crystal surface. It is therefore necessary to hermetically seal the crystal inside a perspex box as shown in Fig. 3.13.

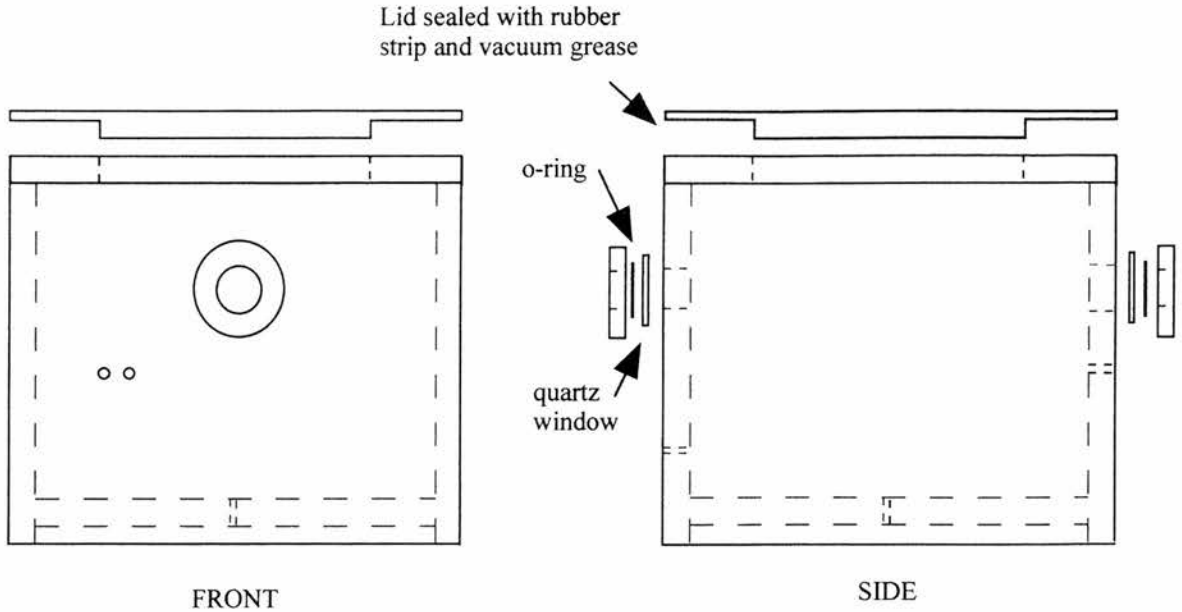


Figure 3.13: Schematic of sealed perspex box used to create dry environment for potassium niobate crystal.

Water cooling pipes pass through one wall of the box via rubber grommets and the integrity of these seals is improved with the liberal application of vacuum grease. The same approach is employed to pass electrical connections into the box. The lid of the box is securely fastened against a rubber seal (also greased), and it can be removed to allow angular and rotational adjustments of the crystal at room temperature. The box was designed so that the crystal would be at the correct height for the Ti:sapphire laser to pass through it. Quartz windows allow the light to pass through the box. These windows are Araldited in place with rubber o-rings to provide a good seal. It was found in practice that the seal in the box was not sufficient to prevent condensation without the addition of a modest but continual flow of dry nitrogen through the system. The nitrogen fills the box, maintaining a steady flow and, therefore, a slight positive pressure that prevents air and hence water vapour from re-entering the box.

The complete system can be seen in plate 3.1. A lens of focal length 10cm focuses the fundamental light into the crystal, and a second lens of focal length 10cm recollimates the beam after it leaves the box. This system can produce powers in excess of those required for the probe laser (up to $300\mu\text{W}$). Figure 3.14 shows an absorption profile

obtained by scanning the frequency of the probe field across the absorption lines of the two rubidium isotopes.

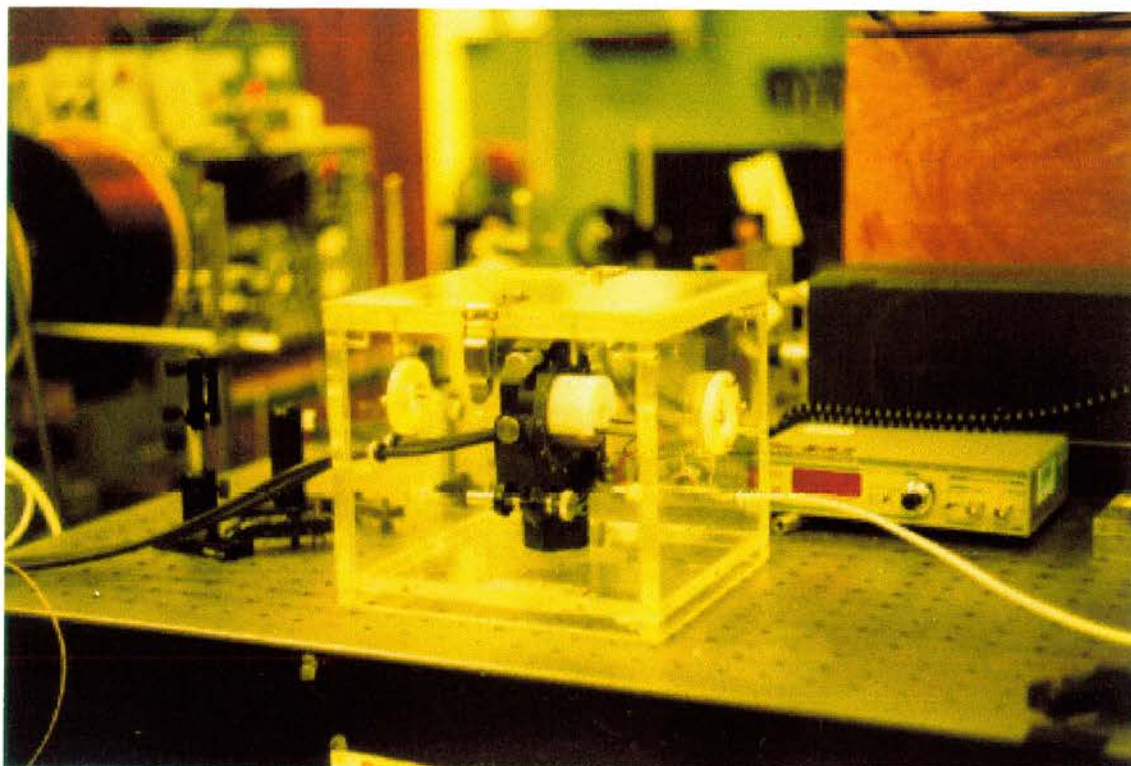


Plate 3.1: *The complete frequency doubling system.*

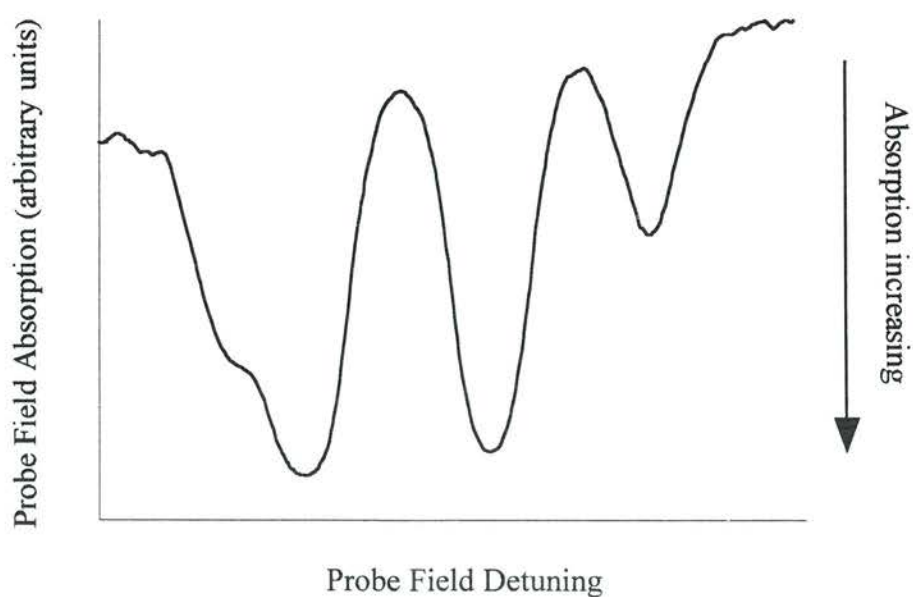
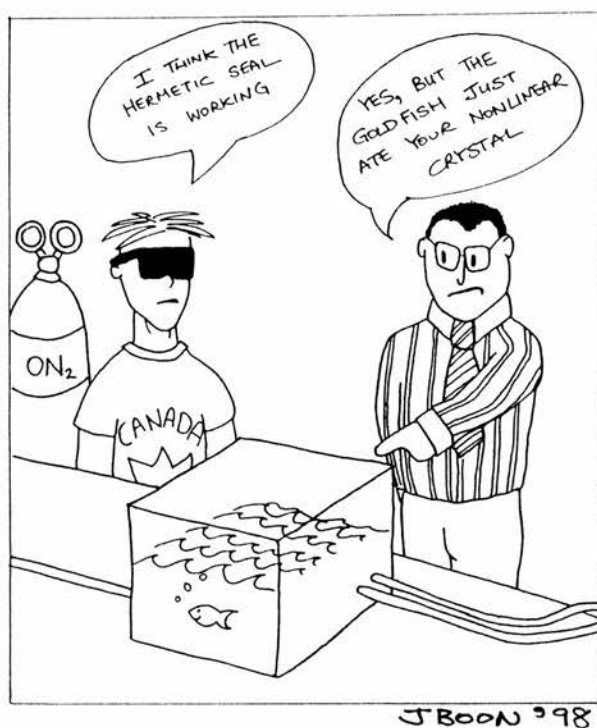


Figure 3.14: *Experimental absorption trace of blue 422nm probe field in atomic rubidium vapour.*



3.5 Incoherent Excitation

To facilitate the production of inversionless gain, it is necessary to excite a fraction of the atomic population into the upper level of the probe transition. The important distinction between inversionless and traditional laser action is that in the former case the fraction of population that must be excited is less than the fraction of the population that remains in the lower level of the lasing transition. As a result, the excitation requirement in an inversionless scheme is less demanding than in a standard laser system.

The complication in an inversionless lasing scheme is that the application of an additional coherent laser source upsets the delicate balance of the coherence that drives EIT. Disturbing the transparency in this way complicates inversionless lasing. Figure 3.15 demonstrates the absorption profile in an EIT experiment before and after the application of an additional pump laser. The transparency on-resonance (depicted by the dashed line) is destroyed upon the application of the coherent pump source. The atomic level scheme and density matrix describing this system is given in Appendix B.

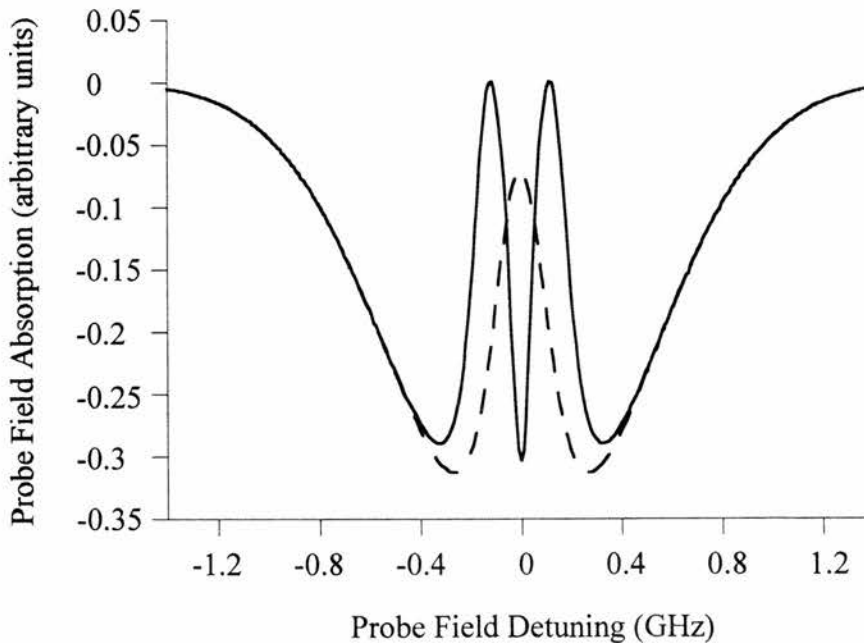


Figure 3.15: Probe field absorption (ρ_{12}^i in arbitrary units) as a function of probe detuning in the absence (dashed line) and presence (solid line) of a coherent pump field.

To circumvent this problem, we must either destroy the phase coherence of the pump source or select an inherently incoherent method of pumping. We will now look at

one method that was developed to destroy phase coherence so that a laser may be used as a pump in quantum coherence experiments.

3.5.1 Destroying Phase Coherence

Acousto-optic modulators have several applications [13], one of which is to shift the frequency of an incident laser beam by an amount equal to the frequency of the acoustic wave travelling through the modulator. As well as being frequency shifted, the beam is also deflected by an angle that is dependent on the frequency of the acoustic wave. A schematic of such a system, in which the acoustic wave is driven by a transducer, is shown in Fig. 3.16.

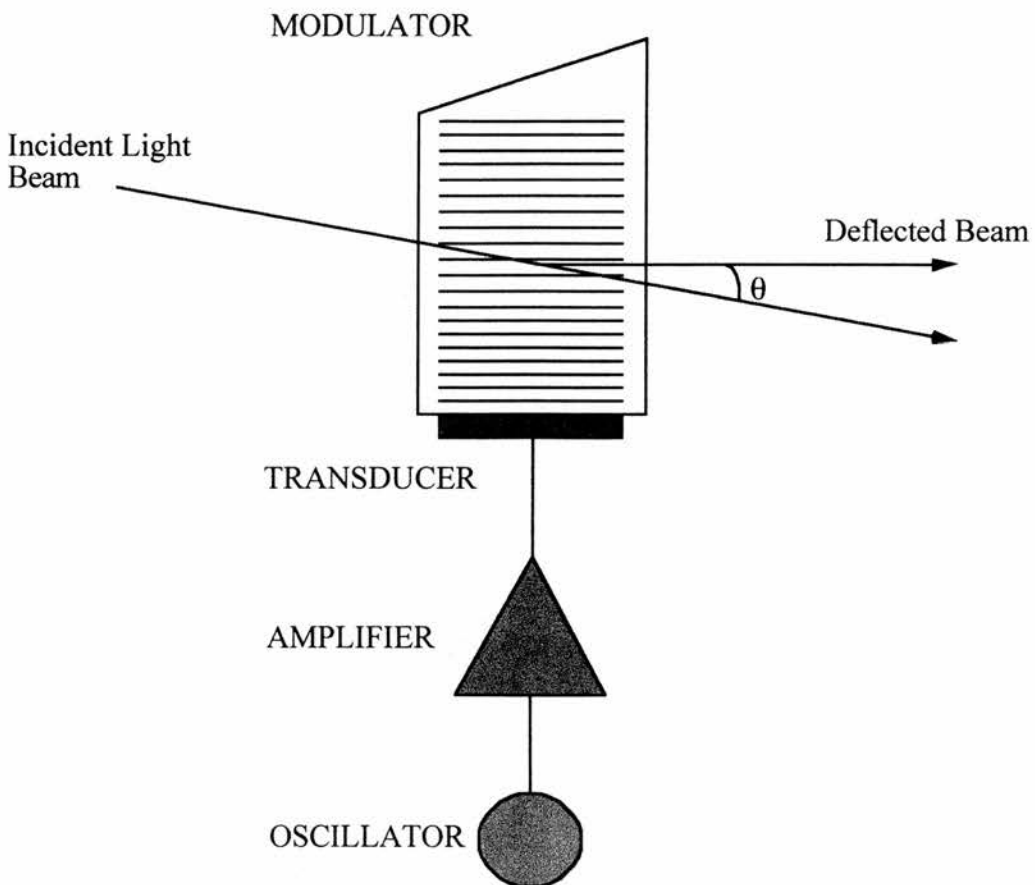


Figure 3.16: *Acousto-optic modulator shifts the frequency of the incident beam by the frequency of the acoustic wave.*

To render a laser source incoherent, it is necessary to increase its linewidth beyond the homogeneous linewidth of the transition under consideration. For the sake of example we will take a value of 40MHz. This broadening of the laser's spectral width can be

achieved by driving the transducer in the acousto-optic modulator with an RF noise generator. Rather than produce an acoustic wave of a single continuous frequency, the modulator will drive an acoustic wave at a range of randomly varying frequencies within a specified bandwidth. This bandwidth could be from 50 to 90 MHz, and it would set up an acoustic wave in the modulator with a randomly varying frequency between these values. The modulator must be carefully chosen so that its transducer is capable of producing these frequencies. The acoustic wave will impose a frequency shift on the light beam passing through the modulator that varies randomly between 50 and 90 MHz. The frequency of the light is effectively shifted by an amount centred on 70 MHz with a 40MHz bandwidth. The phase coherence of the laser is thus destroyed.

However, since the frequency of the acoustic wave is varying, so will the angle at which the beam is deflected. This deflection results in the undesirable breakdown of the laser beam's spatial coherence. The solution is to employ a double-pass geometry, the most straightforward version of which is shown in Fig. 3.17. This approach requires the acousto-optic modulator to have an aperture of at least 2mm. Double passing the laser beam means that the frequency shift is effectively doubled. An acoustic wave frequency of 70MHz will produce an overall shift of 140MHz. To produce a bandwidth of 40MHz, an acoustic wave with a range of 60 to 80MHz will therefore suffice.

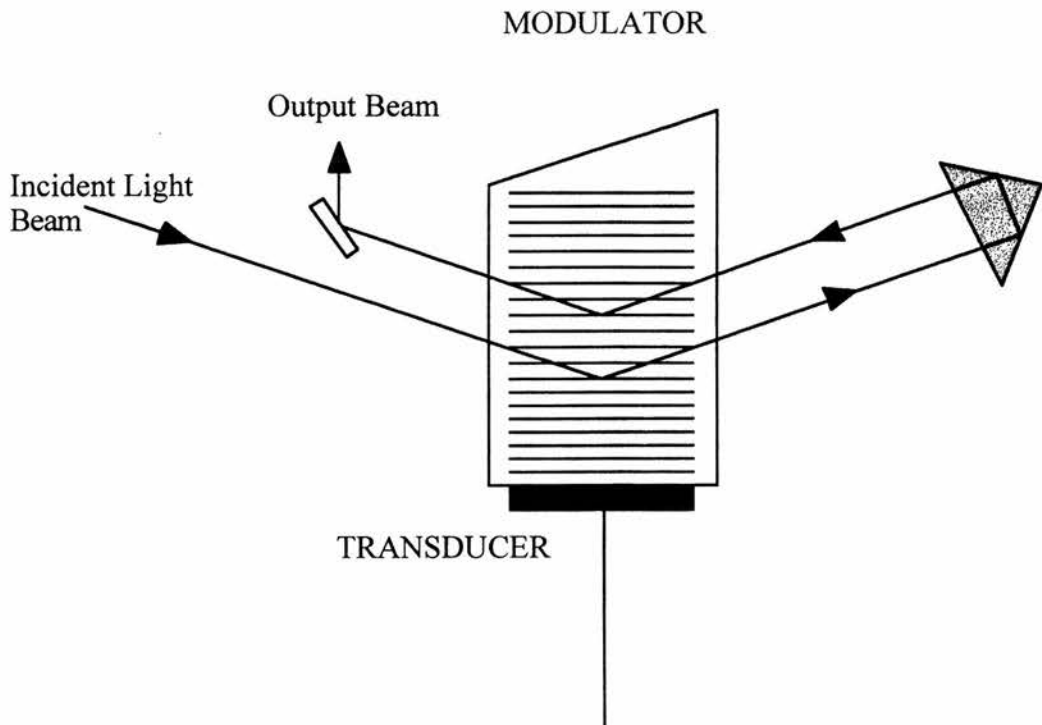


Figure 3.17: *Acousto-optic modulator in double pass configuration.*

3.6 Rubidium Atomic Vapour

Rubidium was discovered in 1861 by R. W. Bunsen and G. R. Kirchoff in Heidelberg, Germany by way of the spectroscope. Bunsen first prepared free rubidium metal that same year by an electrolytic method. Rubidium, atomic number 37, is an alkali metal in group Ia of the periodic table, and as such it has one valence electron determining its reactive properties. Fortuitously, the fact that rubidium has a single valence electron makes it amenable to the type of theoretical studies described in Chapter 2. This medium was selected for experimental study due to the presence of several transitions in the infrared, easily accessible to Ti:sapphire and diode laser sources.

The name rubidium comes from the Latin - *rubidius* - meaning deepest red. This name was chosen as a consequence of the strong infrared spectral lines associated with rubidium's discovery. It is a silver-white, very soft, highly reactive element that tarnishes instantly on exposure to air, igniting to form an oxide, and reacts vigorously with water to form a hydroxide solution and hydrogen gas. Rubidium exists as two natural isotopes, ^{85}Rb and ^{87}Rb , of which the latter is unstable with respect to Beta decay into ^{87}Sr ($t_{1/2}=5\times 10^{10}$ years). There are eight other known radioactive isotopes of rubidium, all with comparatively short half-lives. Ordinary rubidium is sufficiently radioactive to expose a photographic film in about 30 to 60 days [14]. Although rare, rubidium is widely distributed throughout nature in small amounts, with its abundance in the earth's crust being 310 parts per million (ranked 34th of the elements contained therein) and in seawater 0.2 parts per million (ranked 18th). The latter equates to roughly 570 tons per cubic mile of sea water [15]. Small quantities of rubidium can also be found in certain foods, including coffee, tea, tobacco, and several other plants. There is evidence indicating that trace quantities of the element are required by living organisms. The main source of rubidium is through the electrolysis of carnallite, the hydrate chloride of magnesium and potassium.

The uses of rubidium are fairly limited due to its rarity and hazardous nature [16]. However, rubidium metal is utilised in the manufacture of electron tubes; rubidium salts in glass and ceramic production; and rubidium compounds in the treatment of goitre and syphilis [15]. Portable rubidium atomic clocks were introduced by the U.S. army in 1963. Weighing as little as 20kg, they occupied a volume of approximately one cubic foot. The military applications of atomic clocks include synchronising radar nets, assisting in the

accurate tracking of missiles and satellites, and setting precise radio broadcasting frequencies [15]. Due to its electropositivity, rubidium has also been proposed as a working fluid in plasma propulsion for deep-space probes [17]. Interestingly, one estimate of the age of the solar system, as 4,500,000,000 years, is based on the ratio of ^{87}Rb to ^{87}Sr in a stony meteorite. Some of the physical and atomic properties of rubidium are listed below in Table 3.I:

| Property | Value |
|--------------------------|--------------------------|
| Atomic Number | 37 |
| Atomic Weight | 85.4678 a.m.u. |
| Crystal Structure | Body Centred Cubic |
| Valence | 1 |
| Electronic Configuration | (Kr) $5s^1$ |
| Melting Point | 38.89 ° C |
| Boiling Point | 686 ° C |
| Specific Gravity | 1.53 (20 ° C) |
| Density @ 20 ° C | 1.532 g cm ⁻³ |
| Natural Isotope Mass No. | % |
| 85 | 72.17 |
| 87 | 27.83 |

Table 3.I: *Atomic and physical properties of rubidium.*

The main disadvantage of employing rubidium to study atomic coherence effects is the fact that its energy levels are not single levels but are in fact complicated combinations of many fine and hyperfine sub-levels. An authoritative treatment of the creation of fine and hyperfine structure can be found in many texts [18-21]; therefore, only a brief summary of the most relevant characteristics is provided below.

3.6.1 Fine Structure

The fine structure within an atom is the result of the interaction of the intrinsic spin of an electron with the magnetic moment arising from its own orbital angular momentum

about the nucleus. The electron's spin and orbital angular momentum are represented by the atomic quantum numbers S and L respectively. Fine structure effects, or spin orbit coupling as they are commonly known, are strongest in the lowest orbital angular momentum states, L , since these orbits keep the electron, on average, in closer proximity to the nucleus. The notable exception is that of the lowest energy orbital angular state, $L = 0$, for which there is no spin orbit coupling effect.

The two angular momentum quantum numbers, L and S , couple together to produce the spin orbit interaction quantum numbers, J and m_J . Each angular momentum state, L , is split by the spin-orbit coupling into a number of J states ranging from $L+S$ to $|L-S|$. Each of these J states is again composed of a number of sub-levels, categorised by the m_J number, which ranges from J to $-J$ (in integer steps). In rubidium, where $S = 1/2$, the orbital angular momentum states (L) are each split into two by the spin, except in the lowest state, where $L=0$. Since spin orbit coupling effects are inversely proportional to the average radial distance of the electron from the nucleus, its effects produce significant fine structure splitting on the P and D states of rubidium while it becomes much less significant in higher orbital angular momentum states. In one electron systems the $J = L-S$ and $J = L+S$ states are separated by ΔE_F where ΔE_F is related to the fine structure constant, ξ_F , by [21]:

$$\Delta E_F = \frac{\xi_F}{2} (2L + 1) \quad (3.2)$$

Some of the fine structure constants for rubidium, relevant to this thesis, are presented in Table 3.II along with the corresponding fine level energy separations [11]. Negative values indicate an inversion of the fine states such that the lower value $J = L-S$ state actually occurs at a higher energy than the $J = L+S$ state.

| Level | ξ_F / GHz | ΔE_F / GHz |
|-------|---------------|--------------------|
| 5P | 4748.8 | 7123.2 |
| 4D | -5.3 | -13.2 |
| 6P | 1549.0 | 2323.5 |
| 5D | 35.5 | 88.7 |
| 7P | 701.3 | 1052.0 |
| 6D | 27.1 | 67.8 |
| 5F | -0.09 | -0.3 |
| 8P | 376.9 | 565.4 |
| 7D | 18.1 | 45.3 |

Table 3.II: *Fine level structure constants for rubidium along with corresponding energy separations.*

3.6.2 Hyperfine Structure

Hyperfine structure can be explained in terms of the properties of the angular momentum of the nucleus. In 1924 Pauli suggested that a nucleus has a total angular momentum, which is labelled by the quantum number I . This quantum number may have integral or half-integral values, like the total angular momentum quantum number J . The reason for this is that a nucleus is a compound structure of nucleons, protons and neutrons, each of which have intrinsic spin $1/2$ and may take part in orbital motion within the nucleus. For atomic rubidium, the nuclear spin varies between the two isotopes: $I = 5/2$ for ^{85}Rb and $I = 3/2$ for ^{87}Rb . Also attributed to the nucleus, in addition to its spin, are electromagnetic multipole moments of higher order than electric monopole. The interaction between these moments and the electromagnetic field produced at the nucleus by the orbiting electrons is responsible for hyperfine structure.

The quantum number $F = I+J$ describes the total angular momentum of the atom. A corresponding splitting occurs, analogous to fine splitting, into a number of hyperfine levels labelled by F , which have $m_F = (2F+1)$ degenerate sub-levels. In the lowest level, $L = 0$ and $J = 1/2$, there is no spin-orbit coupling, and the hyperfine structure effectively

replaces fine structure. The mathematics are directly analogous with the substitutions of $J \rightarrow F$, $L \rightarrow J$ and $S \rightarrow I$ [18]. For states where there is spin-orbit coupling ($L \geq 1$), the hyperfine structure provides further structure but on a smaller scale to that previously discussed.

For $J = 1/2$ states the two hyperfine structure states, $F = I + 1/2$ and $F = I - 1/2$, are displaced by ΔE_{HF} which is related to the hyperfine dipole constant, ξ_{HF} , by [18]:

$$\Delta E_{\text{HF}} = \frac{\xi_{\text{HF}}}{2} [F(F+1) - I(I+1) - J(J+1)] \quad (3.3)$$

When $J > 1/2$ the effects of electric quadrupole interactions must be taken into account such that the structure also depends on the quadrupole hyperfine constant, Q_{HF} , which is defined as [18]:

$$\Delta E_{\text{HF}} = \frac{\xi_{\text{HF}}}{2} \kappa + \frac{Q_{\text{HF}}}{4} \frac{\frac{3}{2} \kappa(\kappa+1) - 2I(I+1)J(J+1)}{I(2I-1)J(2J-1)} \quad (3.4)$$

where:

$$\kappa = F(F+1) - J(J+1) - I(I+1) \quad (3.5)$$

A review of the measurements of the hyperfine structure of free, naturally occurring, alkali atoms has been carried out by E. Arimondo *et al.* [22]. Some of these values for rubidium have been tabulated below in Table 3.III. Negative values of ξ_{HF} indicate an inversion of the F states such that lower value F states occur at higher energies than the higher value F states.

| Isotope | ⁸⁵ Rb | | ⁸⁷ Rb | |
|-------------------|--------------------------------|------------------------------|--------------------------------|------------------------------|
| | $\xi_{\text{HF}} / \text{MHz}$ | $Q_{\text{HF}} / \text{MHz}$ | $\xi_{\text{HF}} / \text{MHz}$ | $Q_{\text{HF}} / \text{MHz}$ |
| 5S _{1/2} | 1011.9 | | 3417.3 | |
| 5P _{1/2} | 120.7 | | 406.2 | |
| 5P _{3/2} | 25.0 | 25.9 | 84.8 | 12.5 |
| 5D _{3/2} | 4.18 | <5 | 14.4 | 3.5 |
| 5D _{5/2} | -2.12 | No value | -7.4 | <5 |
| 6S _{1/2} | 239.3 | | 809.1 | |
| 6P _{1/2} | 39.1 | | 132.6 | |
| 6P _{3/2} | 8.2 | 8.2 | 27.7 | 4.0 |

Table 3.III: Some hyperfine structure constants for rubidium.

In Fig. 3.18 a schematic energy level diagram is presented that shows the fine structure of rubidium from the 5S_{1/2} ground state up to the 7D_{5/2} excited state. Also included are some of the optical wavelengths which can be generated by the laser sources described in Section 3.2.

The fact that rubidium has an intrinsic nuclear spin results in complex sub-level structure. Since two separate isotopes exist naturally, each having its own values for I , ξ_{HF} and Q_{HF} , the splitting of the sub-level structure differs significantly. Figure 3.19 presents a second schematic energy level diagram of rubidium which again shows the 5S_{1/2} ground state and the two excited states, 6P_{1/2} and 5P_{3/2}, utilised in the experiment described in Chapter 5. Note that the hyperfine and magnetic hyperfine levels are now included. It is obvious from this second diagram that when the effects of nuclear spin are taken into account, the structure of rubidium becomes very complex.

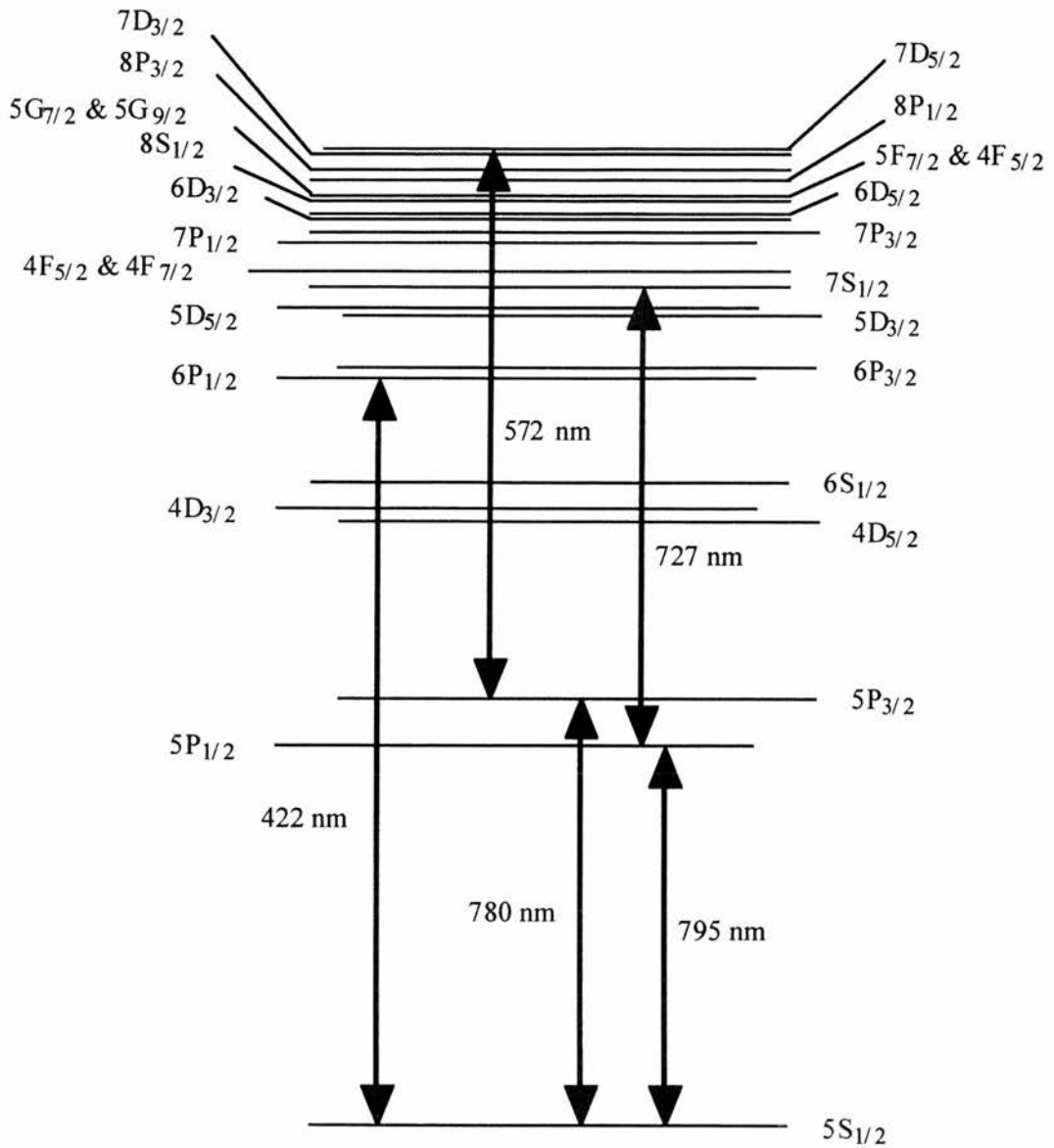


Figure 3.18: Schematic of the fine structure of atomic rubidium from the ground state to the $7D_{5/2}$ excited level. Transitions utilised in the three EIT schemes of Chapter 2 are shown along with the 422nm blue transition employed in the experiment presented in Chapter 5, and the 572nm Dye laser transition.

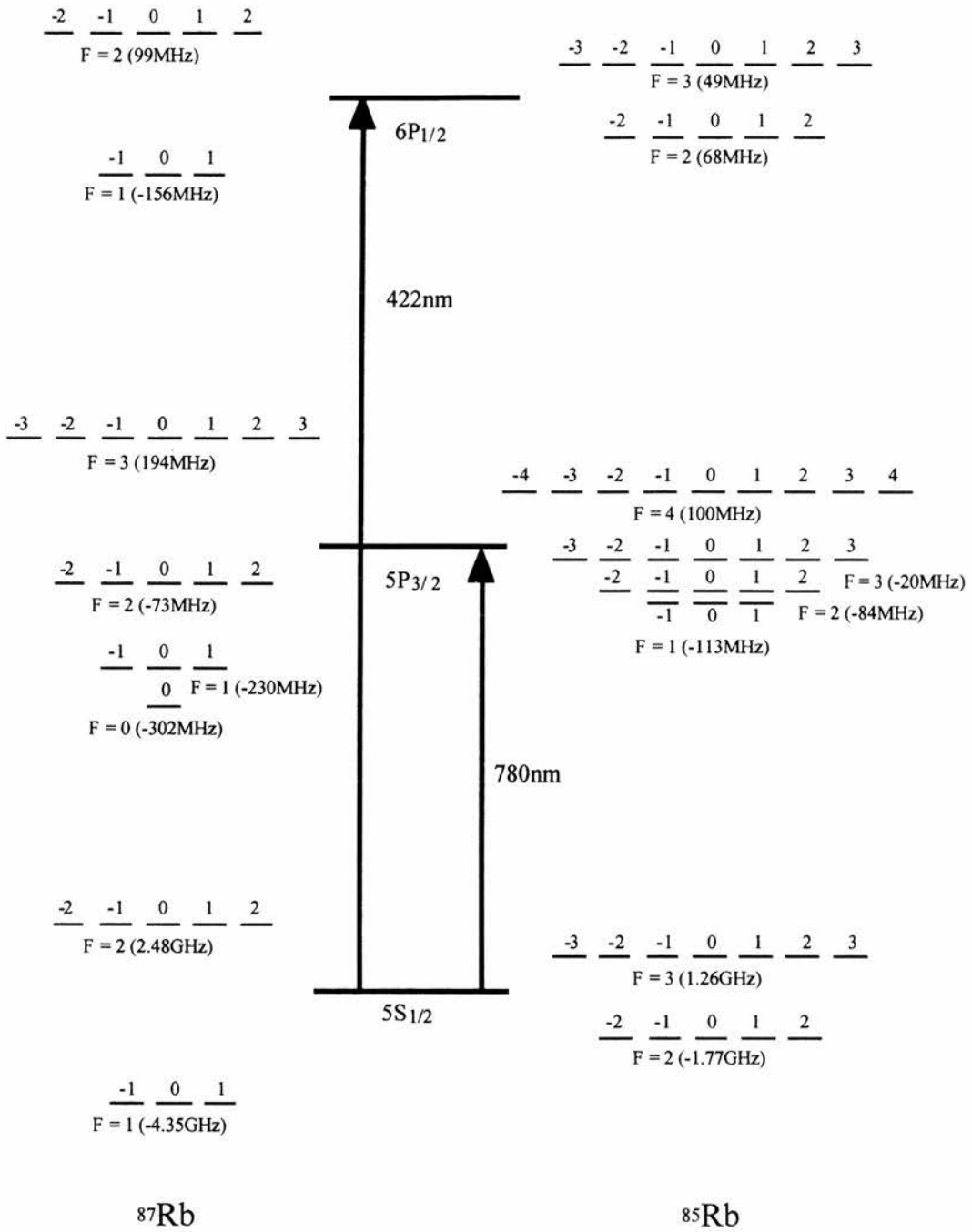


Figure 3.19: Schematic of the hyperfine structure of atomic rubidium for the ground state $5S_{1/2}$ and the excited states $5P_{3/2}$ and $6P_{1/2}$. Values of hyperfine splitting are calculated substituting the hyperfine constants quoted in Table 3.III into Eqs. (3.3) and (3.4).

3.6.3 Rubidium Vapour Cell

For the duration of the experiment, the rubidium vapour is contained within a quartz cell, obtained from Opthos Instruments, of length 2cm and diameter 1.5cm. The cell is evacuated to 10^{-6} Torr, filled with rubidium vapour and sealed. It is important that care is taken due to the reactivity of rubidium in air. The cell is heated by passing a current from the mains supply via a Variac transformer, through heating tape woven into a glass jacket that is secured around the length of the cell. The temperature of the cell controls the particle density in the vapour. Calculations of vapour particle density are made according to Thompson and Xu [23]. The vapour pressure, P , is worked out utilising Eq. (3.6), and it is then converted into a particle density using the ideal gas law, $N=P/kT$.

$$\log_{10} P = 10.875 - \frac{4420.4}{T} \quad (3.6)$$

where P is in units of mTorr and the temperature, T , is in Kelvin. Large discrepancies exist between published calculations of particle density in rubidium. Table 3.IV shows the different values of particle density that may be obtained using various sources identified by the first author in each case. The decision to rely on Thompson's formula was based on the fit with experimental measurements of absorption, and the fact that this formula provides the most conservative estimate of the gain that may be achieved in experiment.

| Temp (°C) | N(m ⁻³) | | | | | | | |
|--------------|-----------------------|-----------------------|-----------------------|-----------------------|-----------------------|-----------------------|-----------------------|--|
| | Nesmeyanov [24] | Miles [25] | Honig [26] | Ewing [27] | Hultgren [28] | Thompson [23]* | Piacente [29] | |
| 110 | 9.01×10 ¹⁸ | 1.03×10 ¹⁹ | | 1.02×10 ¹⁹ | | 5.48×10 ¹⁸ | 1.53×10 ¹⁹ | |
| 120 | 1.65×10 ¹⁹ | 1.85×10 ¹⁹ | | 1.86×10 ¹⁹ | | 1.05×10 ¹⁹ | 2.78×10 ¹⁹ | |
| 130 | 2.92×10 ¹⁹ | 3.21×10 ¹⁹ | 2.39×10 ¹⁹ | 3.29×10 ¹⁹ | 2.89×10 ¹⁹ | 1.92×10 ¹⁹ | 4.91×10 ¹⁹ | |
| 140 | 5.02×10 ¹⁹ | 5.42×10 ¹⁹ | | 5.61×10 ¹⁹ | | 3.47×10 ¹⁹ | 8.40×10 ¹⁹ | |
| 150 | 8.40×10 ¹⁹ | 8.92×10 ¹⁹ | | 9.36×10 ¹⁹ | | 6.08×10 ¹⁹ | 1.40×10 ²⁰ | |

Table 3.IV: Published values of particle density in rubidium atomic vapour for a range of temperatures.

Sources are indicated by the first author. The source used in this work is marked with an asterix.

3.6.4 Einstein A Coefficients

While there is reasonable agreement in the published values of the A coefficient for the infrared $5S_{1/2} - 5P_{3/2}$ transition, significant discrepancies exist in the literature for the blue $5S_{1/2} - 6P_{1/2}$ transition. The Einstein A coefficient is an important parameter in both the density matrix model and the calculation of absorption or gain. Table 3.V shows various published values for the Einstein A coefficient of the $5P_{3/2}$ and $6P_{1/2}$ excited states. The value taken from Theodosiou [30] of $8 \times 10^6 \text{ s}^{-1}$ relates to the total decay rate from the $6P_{1/2}$ level rather than that associated with the specific transition with the ground state. This higher value is used in the density matrix model as this is concerned primarily with the movement of population; whereas, the lower value of $1.5 \times 10^6 \text{ s}^{-1}$, according to Wiese [31], is utilised in the calculation of absorption and gain specific to the $5S_{1/2} - 6P_{1/2}$ transition. This choice of Einstein coefficient provides the best fit to experimental data and the most conservative estimate of gain.

| Transition | A(s ⁻¹) | | | | |
|---------------------|------------------------------|--------------------|---------------------|--------------------|---------------------|
| | $\lambda(\text{nm})$ [11] | Heavens [32] | Lingard [33] | Wiese* [31] | Theodosiou* [30] |
| $5P_{3/2}-5S_{1/2}$ | 780 | 37.5×10^6 | 37.73×10^6 | 37.0×10^6 | 38.9×10^6 |
| $6P_{1/2}-5S_{1/2}$ | 420 | 2.43×10^6 | 3.346×10^6 | 1.5×10^6 | 8×10^6 |

Table 3.V: Published values of the Einstein A coefficient for the two transitions in rubidium corresponding to the EIT experiment in Chapter 5. Sources are indicated by the first author. The asterix denotes the sources used for this work.

References

- [1] K. J. Boller, A. Imamoglu and S. Harris, *Phys. Rev. Lett.* **66**, 2593, (1991).
- [2] S. Shepherd, *Use and Development of a cw Titanium Sapphire Laser for Non-linear Optics*, (unpublished PhD thesis, University of St. Andrews, (1993)).
- [3] Titan-CW Series Preliminary Operator's Manual, Schwartz Electro-Optics.
- [4] S. Shepherd *et al*, *Phys. Rev. A.* **49**, 4, 3002, (1994).
- [5] R. R. Moseley *et al*, *Phys. Rev. A.* **50**, 5, 4339, (1994).
- [6] S. Shepherd, D. J. Fulton, and M. H. Dunn, *Phys. Rev. A.* **54**, 6, 5394, (1996).
- [7] D. M. Kane, *Atomic Spectroscopy in the UV and Visible*, (unpublished PhD thesis, University of St. Andrews, (1983)).
- [8] C. E. Wieman, and L. Holberg, *Rev. Sci. Instrum.* **62**, 1, (1991).
- [9] K. B. MacAdam, A. Steinbach, and C. Wieman, *Am. J. Phys.* **60**, 12, (1992).
- [10] C. S. Adams, and A. I. Ferguson, *Opt. Comm.* **90**, 89-94, (1992).
- [11] C. E. Moore, *Atomic Energy Levels - As derived From the Analyses of Optical Spectra*, (Circular of the National Bureau of Standards 467, (1952)).
- [12] Baiggio *et al*, *Opt. Soc. Am. B.* **9**, 4, (1992).
- [13] C. C. Davis, *Lasers and Electro-Optics - Fundamentals and Engineering*, (Cambridge University Press, (1996)).

- [14] R. C. Weast, *Handbook of Chemistry and Physics*, (CRC Press, 57th edition, (1976)).
- [15] D. M. Considine, and G. D. Considine, *Van Nostrand's Scientific Encyclopedia*, (Van Nostrand Reinhold, New York, 7th edition, (1989)).
- [16] N. I. Sax, *Dangerous Properties of Industrial Materials*, (Reinhold, New York, 2nd edition, (1963)).
- [17] *The New Encyclopaedia Britannica*, (Encyclopaedia Britannica Inc., (1982)).
- [18] G. K. Woodgate, *Elementary Atomic Structure*, (Clarendon Press, Oxford, 2nd edition, (1980)).
- [19] M. Weissbluth, *Atoms And Molecules*, (Academic Press Inc., London, Student edition, (1978)).
- [20] B. W. Shore, *The Theory Of Coherent Atomic Excitation*, (Wiley, New York, (1990)).
- [21] E. U. Condon and G. H. Shortley, *The Theory Of Atomic Spectra*, (University Press, Cambridge, (1953)).
- [22] E. Arimondo, M. Inguscio, and P. Violino, *Rev. Mod. Phys.* **49**, 31, (1977).
- [23] D. C. Thompson, and G-X. Xu, *Can. J. Phys.* **60**, 1496, (1982).
- [24] A. N. Nesmeyanov, *Vapor-Pressure of the elements*, (New York: Academic, (1963)).
- [25] R. B. Miles, and S. Harris, *IEEE J. Quantum Electron.* QE-9, 470, (1973).
- [26] R. E. Honig, *RCA Rev.* **23**, 567, (1967).

- [27] C. T. Ewing *et al*, J. Chem. Eng. Data. **14**, 210, (1969).
- [28] R. Hultgren *et al*, *Selected Values of the Thermodynamical Properties of the Elements*, (American Society for metals, Metals Park, Ohio, (1973)).
- [29] V. Piacente, G. Bardi, and L. Malaspina, J. Chem. Thermodyn. **5**, 219, (1973).
- [30] C. E. Theodosiou, Phys. Rev. A. **30**, 6, 2881, (1984).
- [31] W. L. Wiese, and G. A. Martin, *A Physicist's Desk Reference*, (American Institute of Physics, (1989)).
- [32] O. S. Heavens, J. Opt. Soc. Am. **51**, 10, 1058, (1961).
- [33] A. Lingard, and S. E. Neilsen, *Atomic Data and Nuclear Data Tables*, (Academic Press, New York and London, (1977)).

CHAPTER 4

Comparison of Wavelength Dependence in Cascade, Lambda, and Vee-type Schemes for Electromagnetically Induced Transparency

“As far as the laws of mathematics refer to reality, they are not certain; and as far as they are certain, they do not refer to reality.”

Albert Einstein

4.1 Introduction

In this chapter we consider the effects of changing the probe and coupling wavelengths on each of the three basic energy level configurations that can be employed to realise EIT. This theoretical study provides a foundation for the research presented in this thesis. We explore the limitations of three level systems subject to Doppler-broadening. Subsequent chapters seek to exploit the findings presented here, first by realising an experimental mismatched Vee system (Chapter 5), and then by predicting gain in such a system for which the probe frequency is far in excess of the coupling field frequency (Chapter 7).

Amplification and lasing without inversion (AWI and LWI) has recently been the subject of much experimental work [1-14]. This research culminated in the first observation of continuous wave inversionless lasing by Zibrov and co-workers in 1995 [10]. The Zibrov scheme utilised matched (equal probe and coupling) wavelengths in a gaseous medium subject to the effects of Doppler-broadening. While it has been thought that mismatched (unequal probe and coupling) wavelength systems subject to Doppler-broadening can only be realised for high coupling field powers [15], such mismatched schemes will be necessary to achieve the goal of high frequency inversionless laser systems. Indeed, the impetus for studying lasing in the absence of inversion is to create lasing on problematic high frequency transitions that cannot be accessed by conventional means due to the requirement of a population inversion. Now that the principle of LWI has been demonstrated it is pertinent to consider the regime for which the employed optical fields are unequal in wavelength. In this context, we study the phenomenon of EIT that creates the underlying reduction in absorption upon which LWI is based.

This chapter considers the effects of mismatching the probe and coupling wavelengths on the transparency that may be created through EIT in the Cascade, Lambda and Vee-type schemes. Three wavelength regimes are considered: mismatched wavelengths for which the coupling frequency is greater than the probe frequency, matched wavelengths for which the coupling and probe frequencies are equal, and mismatched wavelengths for which the probe frequency is greater than the coupling frequency. The transparency that may be induced in these regimes is compared for the Cascade, Lambda and Vee-type systems that were introduced in Section 2.5. In the first mismatched regime ($\lambda_c < \lambda_p$), EIT

is possible in all schemes and it is in fact stronger than in the matched case. It is also demonstrated that for the second mismatched regime ($\lambda_c > \lambda_p$), EIT can be realised most readily in the Vee-type configuration in the presence of Doppler-broadening. This is an important result for the study of EIT and LWI and is explained in terms of the ‘many pathways to absorption’ description of EIT, considering the absorption as a function of atomic velocity as well as probe field detuning. We see how mismatching the wavelengths in each scheme affects the position of the Autler-Townes components and the single and two-photon absorption resonances. These are the determining factors in EIT, along with the magnitude of the Autler-Townes components as a function of frequency.

Previous work characterising the effects of Doppler-broadening has shown that matching the probe and coupling frequencies [16] allows the EIT feature to be resolved despite such effects, and that this is dependent on selecting the proper geometry of either co- or counter-propagating beams [17]. The presented analysis concurs with these earlier studies and extends to the case of EIT realised with mismatched wavelengths. In addition, early work on wavelength dependence at St. Andrews (see Section 1.6.1) [18] demonstrated that EIT is more pronounced in Cascade systems for which the coupling frequency is greater than the probe frequency rather than for a matched Cascade scheme. The research presented here widens the study to include all three possible energy level configurations for EIT and both directions of relative wavelength mismatch.

The following section outlines the basis of the comparison that will be made, in terms of defining a set of hypothetical energy level schemes, so that all atomic parameters can be made equal except the wavelengths of the probe and coupling fields. A full account of the Autler-Townes effect will then be given, including the detuned case, along with derived equations that can be used to calculate the positions of the Autler-Townes components and the absorption resonances for all three energy level schemes. Subsequently, we consider both the absorption profiles generated for each system and the three-dimensional model of absorption as a function of detuning and velocity. Finally, the results will be collated and discussed, highlighting the possibilities for mismatched quantum coherence in Doppler-broadened systems.

4.2 Basis of Comparison

A valid comparison of the wavelength dependence in the three EIT schemes is impossible without creating hypothetical energy level structures. In this way a comparison can be made solely on the basis of the type of scheme and the relative mismatch of the probe and coupling wavelengths while all other parameters are kept constant. This would not be feasible if we based the study on real atomic systems. A comparison of real Cascade, Lambda, and Vee-type schemes was carried out in Section 2.5 and more fully by Fulton [19], in both cases, however, only closely matched wavelengths were considered.

Here we assume closed three level systems as shown in Fig. 4.1 for (a) the Cascade, (b) the Lambda, and (c) the Vee-type configurations. All decay rates, shown in Fig. 4.1, are set to $40 \times 10^6 \text{ s}^{-1}$ and the dephasing on the unlinked transition is also set to $40 \times 10^6 \text{ s}^{-1}$ for every system. The latter value corresponds to the maximum dephasing that would naturally occur due to level lifetime effects given the selected decay rates.

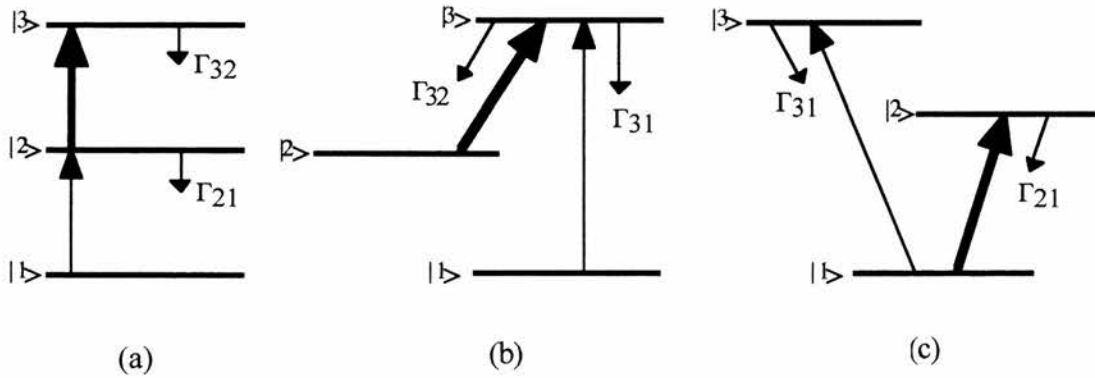


Figure 4.1: Schematic energy level diagrams for the (a) Cascade, (b) Lambda, and (c) Vee-type systems. The coupling and probe fields are indicated by the thick and thin arrowed lines respectively. The decay rates shown are all set to $40 \times 10^6 \text{ s}^{-1}$.

In order to make a direct comparison of the absorption profiles, the wavelength of the probe transition is kept constant while three values are selected for the coupling field. The probe wavelength was taken to be 800nm with three coupling wavelengths of 400, 800, and 1600nm that lead to a total of nine considered systems, i.e. three wavelength

regimes ($\lambda_c < \lambda_p$, $\lambda_c = \lambda_p$, and $\lambda_c > \lambda_p$) for each of the three energy level schemes. We ensure that the chosen probe Rabi frequency, 100kHz, does not significantly populate the upper level of the probe transition and choose a coupling field Rabi frequency (250MHz) that is approximately half the probe Doppler width (500MHz). The Doppler width is based on rubidium at a temperature of 40°C, for which significant absorption on the infrared rubidium transitions occurs (80m^{-1}). Rubidium vapour has been utilised in a wide range of EIT amplification and lasing without inversion experiments [6,7,9,10].

The analysis of these systems is carried out utilising the semiclassical density matrix formalism [20] discussed at length in Chapter 2. The density matrices describing the atomic systems under consideration were presented in Section 2.5.

4.3 The Autler-Townes Effect

The Autler-Townes effect [21] has already been introduced briefly in Section 1.5.1. Here we look more closely at the effects of detuning the applied optical field and the consequences of Doppler-broadening. First, we consider the case of a Vee-type scheme in which the coupling laser Autler-Townes splits the upper and lower levels of the coupling transition and the probe laser scans the lower split level, connecting it to some other arbitrary excited state. Ignoring the quantum coherence effect of EIT, we look solely at the consequences of the coupling field Autler-Townes splitting the lower level which is common to both fields. The simple on-resonance case, which was considered previously, is shown in Fig. 4.2 (a) and the detuned case is depicted in Fig. 4.2 (b). Initially we assume a Doppler free system in which the detuning is caused solely by a manual change in the coupling laser frequency in the lab frame.

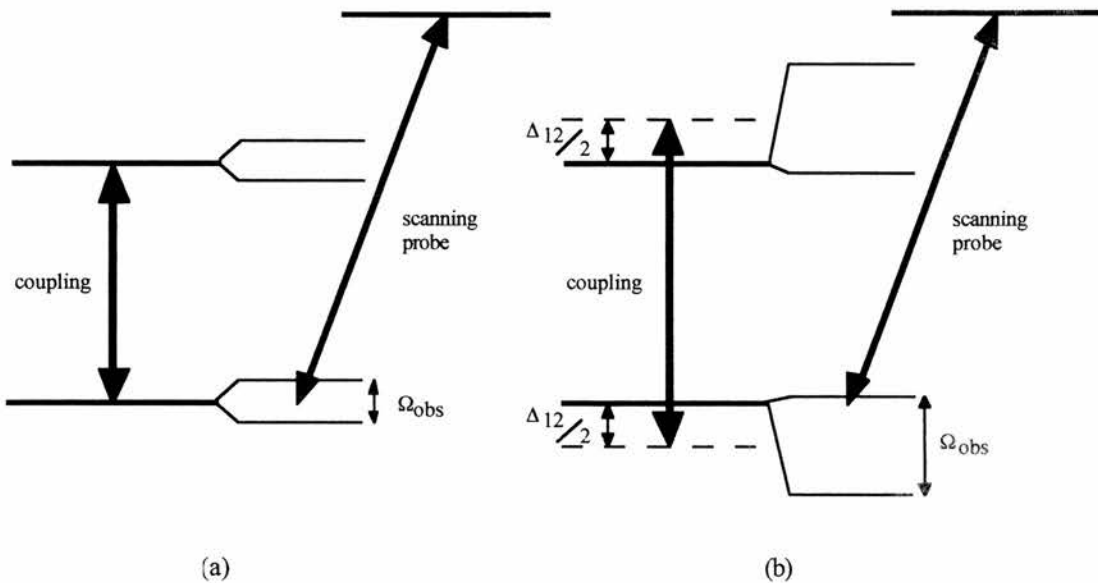


Figure 4.2: Schematic energy level representation of (a) the on-resonance and (b) the detuned Autler-Townes effect. Δ_{12} is the manual coupling field detuning and Ω_{obs} is the observed Autler-Townes splitting given in Eq. (4.1).

In the absence of the coupling field (and Doppler effects) the probe will scan across the lower level of the coupling transition producing a straightforward homogeneously

broadened absorption profile. When the coupling field is applied exactly on resonance with the transition as shown in Fig. 4.2 (a), the absorption profile will be split into two peaks of equal magnitude placed symmetrically about line centre. The magnitude of the splitting between the peaks can be calculated, as before, from the following equation:

$$\Omega_{\text{obs}} = \sqrt{(\Omega_c^2 + \Delta_{12}^2)} \quad (4.1)$$

where Ω_{obs} is the magnitude of the observed Autler-Townes splitting, Ω_c is the coupling field Rabi frequency, and Δ_{12} is the detuning of the coupling field. In this 'on-resonance' case the detuning will be zero and the magnitude of the Autler-Townes splitting is equal to the coupling field Rabi frequency.

If we detune the coupling field from resonance by an amount Δ_{12} , as shown in Fig 4.2 (b), the magnitude of the splitting increases as described by Eq. (4.1), and the Autler-Townes peaks can be found symmetrically placed about the detuned position of the coupling field, which is marked with a dashed line in Fig. 4.2 (b). The absorption profile will also change because the magnitude of the absorption that takes place between each of the Autler-Townes split levels and the upper level of the probe transition will no longer be equal. The peak which corresponds to the Autler-Townes sub-level, shown in Fig. 4.2 (b), that lies closest to the position of the single level that would exist in the absence of the coupling field is preferentially enhanced. If the detuning of the coupling laser is steadily increased this Autler-Townes sub-level will move closer to the original position of the state; hence, the associated peak will increase in magnitude while the other peak diminishes.

For this non-Doppler case, the positions of the Autler-Townes peaks can be given in terms of the probe field detuning in the following manner:

$$\Delta_{13} = \frac{\Delta_{12}}{2} \pm \frac{\Omega_{\text{obs}}}{2} \quad (4.2)$$

where Δ_{13} and Δ_{12} are the probe and coupling field detunings respectively, and Ω_{obs} is the magnitude of the Autler-Townes splitting as defined in Eq. (4.1). Before continuing onto the Doppler-broadened case we note that while this is true for the Vee and Lambda schemes it does not hold for the Cascade system. This difference arises because, unlike the Lambda and Vee configurations, the Cascade system has the probe and coupling fields orientated in the opposite sense. That is, if the coupling frequency is increased then the

probe frequency must be decreased for the fields to remain coincident in a Cascade scheme. Consequently, Eq. (4.2) becomes the following, for the Cascade system:

$$\Delta_{12} = -\frac{\Delta_{23}}{2} \mp \frac{\Omega_{\text{obs}}}{2} \quad (4.3)$$

where Δ_{12} and Δ_{23} are the probe and coupling field detunings respectively. The nomenclature is otherwise as before.

If we now include the effects of Doppler-broadening, the situation becomes more complex because both the probe and the coupling frequencies are shifted by an amount dependent on the velocity of the atoms the fields interact with. As a result, zero detuning of the probe laser in the lab frame no longer necessarily corresponds to resonance with the probe transition, and the Autler-Townes sub-levels are detuned from resonance by a different amount for each specific atomic velocity - even when the coupling laser is on resonance in the lab frame. We define the total detuning for the probe and coupling lasers in a Vee scheme as follows:

$$\Delta_{13} = \Delta_{\text{probe}} - k_1 V_z \quad (4.4a)$$

$$\Delta_{12} = \Delta_{\text{coupling}} - k_2 V_z \quad (4.4b)$$

where Δ_{13} and Δ_{12} are the total probe and coupling field detunings respectively, Δ_{probe} and Δ_{coupling} are the zero velocity detunings in the lab frame, and $k_1 V_z$ and $k_2 V_z$ are the Doppler shifts in the probe and coupling field frequency respectively. The total detuning is made up of any manual detuning imposed in the lab frame and the contribution of the Doppler shift which will vary according to the atomic velocity. The medium as a whole will exhibit a spread of detunings which causes the characteristic Doppler-broadening of the absorption profile. Equations (4.4a) and (4.4b) represent the case of co-propagating beams (Vee and Lambda schemes). In the Cascade scheme, because the fields are orientated in the opposite sense, the beams are counter-propagated [17,19,22]. In this case, Eqs. (4.4a) and (4.4b) become:

$$\Delta_{12} = \Delta_{\text{probe}} - k_1 V_z \quad (4.5a)$$

$$\Delta_{23} = \Delta_{\text{coupling}} + k_2 V_z \quad (4.5b)$$

We now derive an expression for the positions of the Autler-Townes components in a Doppler-broadened system by substituting Eqs. (4.4) and (4.5) into Eqs. (4.2) and

(4.3) respectively. The positions of the Autler-Townes components, in terms of the manual detuning of the probe field, are given for the Lambda and Vee schemes, and the Cascade system in the two following equations respectively:

$$\Delta_{\text{probe}} = k_1 V_z - \frac{1}{2}(\Delta_{\text{coupling}} + k_2 V_z) \mp \frac{1}{2} \left(\sqrt{\Omega_c^2 + (\Delta_{\text{coupling}} + k_2 V_z)^2} \right) \quad (4.6a)$$

$$\Delta_{\text{probe}} = k_1 V_z + \frac{1}{2}(\Delta_{\text{coupling}} - k_2 V_z) \pm \frac{1}{2} \left(\sqrt{\Omega_c^2 + (\Delta_{\text{coupling}} - k_2 V_z)^2} \right) \quad (4.6b)$$

In the case of zero manual detuning of the coupling laser in the lab frame, these equations simplify to a single formula which holds for all three energy level configurations:

$$\Delta_{\text{probe}} = k_1 V_z - \frac{1}{2}(k_2 V_z) \mp \frac{1}{2} \left(\sqrt{\Omega_c^2 + (k_2 V_z)^2} \right) \quad (4.7)$$

This equation describes the effect of detuning on the Autler-Townes positions, that is due solely to the Doppler shifts of the probe and coupling fields. Note that the magnitude of the observed splitting will also be affected by Doppler-broadening, as we see by substituting Eq. (4.4b) into Eq. (4.1):

$$\Omega_{\text{obs}} = \sqrt{\left(\Omega_c^2 + (\Delta_{\text{coupling}} - k_2 V_z)^2 \right)} \quad (4.8)$$

When Δ_{coupling} is equal to zero this equation will be the same for all three schemes. Having derived an expression for the Autler-Townes positions it is useful to consider the positions of the absorption resonances. There are two reasons for this: firstly, EIT is created by the interference of the two pathways to absorption; and secondly, when the Autler-Townes components are detuned they are preferentially enhanced by the absorption resonance that lies closest to them. The latter phenomenon was described in relation to the Doppler-free detuned case in Fig. 4.2 (b).

In all three schemes the single photon absorption resonance is derived simply by setting the total detuning in Eq. (4.4a) or (4.5a) equal to zero and rearranging for Δ_{probe} :

$$\Delta_{\text{probe}} = k_1 V_z \quad (4.9)$$

Figure 4.3 shows the Lambda and Vee-type systems in detuned two-photon resonance, which occurs for $\Delta_{13} = \Delta_{12}$ in a Vee scheme and similarly $\Delta_{13} = \Delta_{23}$ in a Lambda system. An expression for the two-photon resonance position is derived by substituting Eqs. (4.4a) and (4.4b) into this relation:

$$\Delta_{\text{probe}} = k_1 V_z - k_2 V_z + \Delta_{\text{coupling}} \tag{4.10}$$

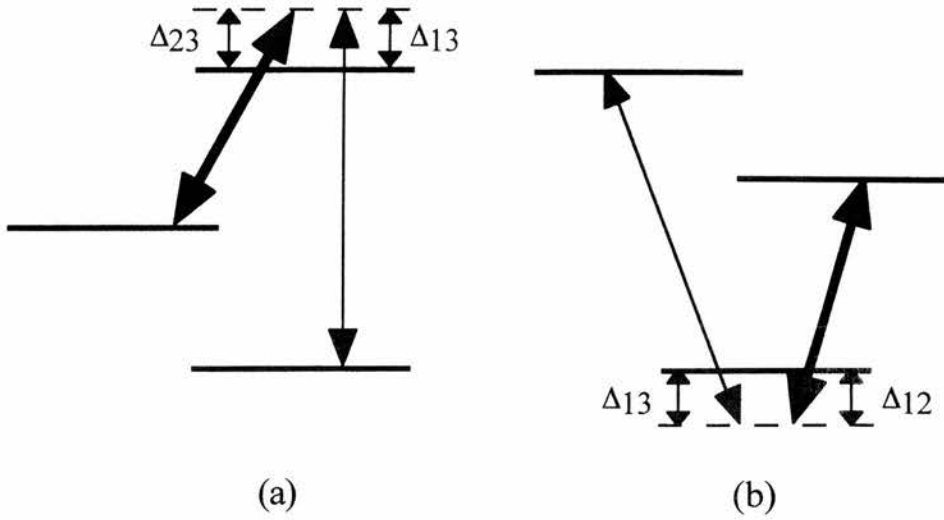


Figure 4.3: (a) The Lambda and (b) the Vee energy level diagrams depicted in detuned two-photon resonance.

For the Cascade scheme two-photon resonance occurs for $\Delta_{12} = -\Delta_{23}$, as shown in Fig. 4.4. By substituting Eqs. (4.5a) and (4.5b) we obtain:

$$\Delta_{\text{probe}} = k_1 V_z - k_2 V_z - \Delta_{\text{coupling}} \tag{4.11}$$

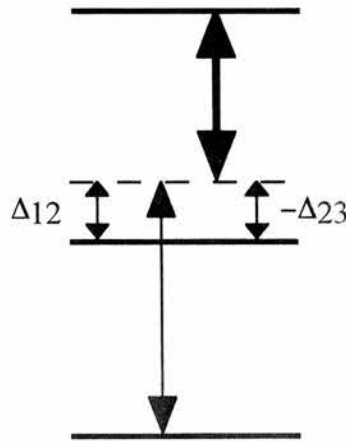


Figure 4.4: The Cascade energy level scheme depicted in detuned two-photon resonance.

For the case of zero manual detuning of the coupling laser in the lab frame, we see that the two-photon resonance position will be the same for all three energy level configurations. Equations (4.10) and (4.11) reduce to:

$$\Delta_{\text{probe}} = k_1 V_z - k_2 V_z \quad (4.12)$$

We now have three equations (Eqs. (4.7), (4.9) and (4.12)) that fully describe the positions of the Autler-Townes components and the single and two-photon resonances for all three schemes when the manual zero velocity detuning of the coupling is zero ($\Delta_{\text{coupling}} = 0$). Figure 4.5 shows the positions of the Autler-Townes components and absorption resonances for the three wavelength regimes described in Section 4.2. These diagrams apply to all three schemes and show that as we change the coupling field wavelength, the position of the two-photon resonance changes along with the associated Autler-Townes components. The single photon resonance position is indicated by a dashed line, the two-photon resonance by a dotted line, and the Autler-Townes components by solid lines. These diagrams will be discussed in detail in Section 4.5.

For the purposes of subsequent discussion we identify two types of Autler-Townes components for any given system. As we tune the probe away from the zero velocity atoms, the Autler-Townes components split further apart. If we consider increasing velocity either positively or negatively we see that one set of Autler-Townes components follows the position of the single photon resonance while the other follows the position of the two-photon resonance. We refer to the former as the primary Autler-Townes components and the latter as the secondary Autler-Townes components. These are indicated on Fig. 4.5 for each wavelength regime. Note that while the position of the primary components does not change, the secondary Autler-Townes components move when the coupling wavelength is altered. Before proceeding with this discussion we consider the density matrix analysis of each system.

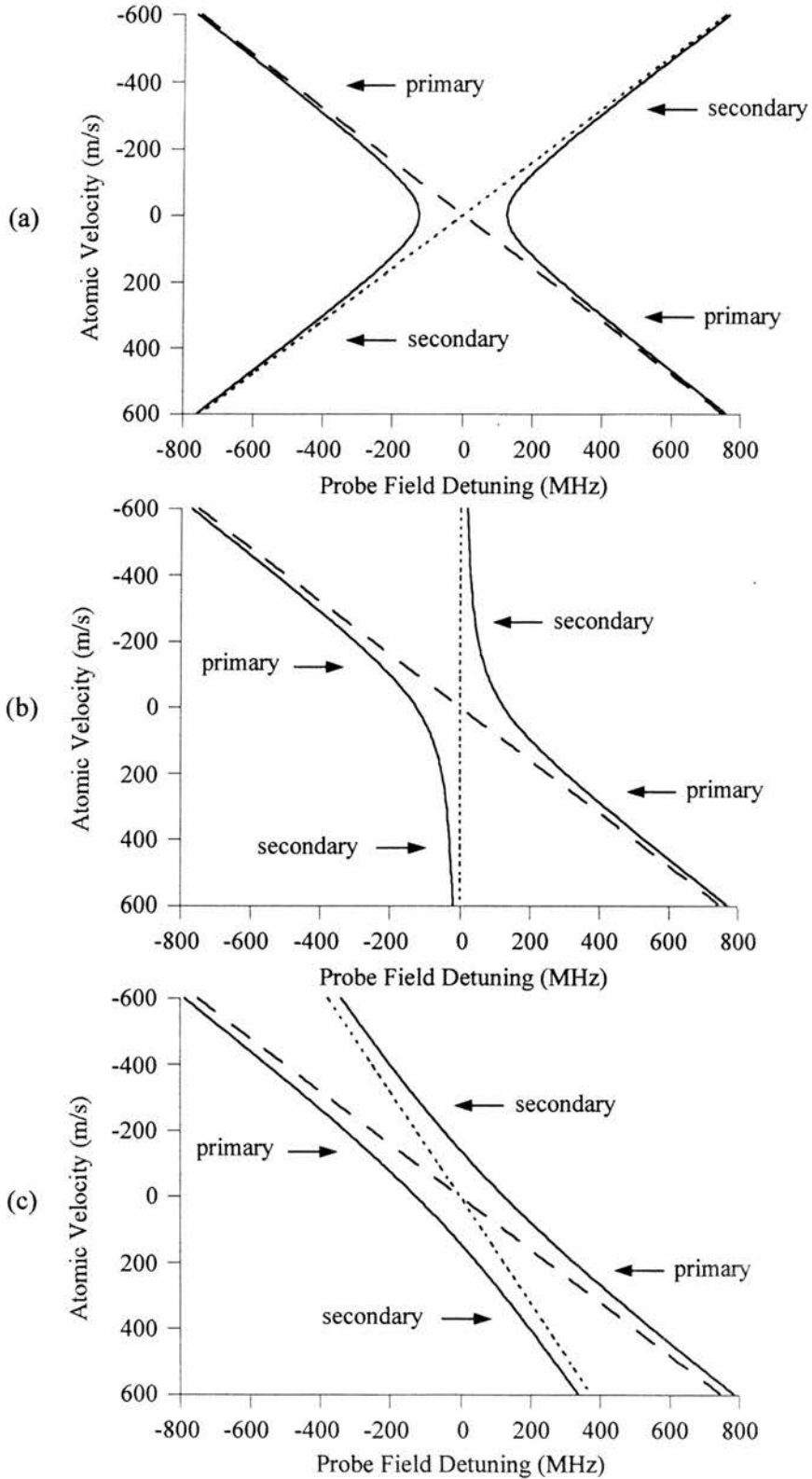


Figure 4.5: The Autler-Townes and absorption resonance positions as a function of atomic velocity and probe field detuning for the three wavelength regimes: (a) $\lambda_c < \lambda_p$, (b) $\lambda_c = \lambda_p$, and (c) $\lambda_c > \lambda_p$. These figures apply to all three energy level schemes with Δ_{coupling} set to zero.

4.4 Theoretical Results

In this section we analyse each of the nine systems that consist of three wavelength regimes for each of the three energy level configurations. For each scheme, density matrix analysis has been carried out to produce profiles of the probe field absorption as a function of probe field detuning. In addition, we consider three-dimensional absorption profiles plotted as a function of probe field detuning and atomic velocity. The density matrices used to model all of these systems have already been introduced in Section 2.5 which compared ‘real’ Cascade, Lambda, and Vee-type schemes. Having considered each system in this way, the information from this section and the previous one will be presented in a single set of nine figures which will form the basis for subsequent discussion.

4.4.1 The Cascade Scheme

4.4.1.a Mismatched wavelengths ($\lambda_c < \lambda_p$)

In this wavelength regime the coupling frequency is twice that of the probe field. Figure 4.6 shows the probe field absorption as a function of linear probe field detuning. A significant transparency window is observed at line centre. Figure 4.7 depicts the absorption as a function of both velocity and detuning for a discrete number of velocities.

4.4.1.b Matched wavelengths ($\lambda_c = \lambda_p$)

In this regime the wavelengths of the probe and coupling fields are equal. Figure 4.8 shows the probe field absorption as a function of linear probe field detuning. A significant transparency window is observed at line centre that is narrower than that predicted in the mismatched ($\lambda_c < \lambda_p$) case. Figure 4.9 depicts the absorption as a function of both velocity and detuning for a discrete number of velocities.

4.4.1.c Mismatched wavelengths ($\lambda_c > \lambda_p$)

In this wavelength regime the probe frequency is twice that of the coupling field. Figure 4.10 shows the probe field absorption as a function of linear probe field detuning. No transparency window is observed at line centre. Figure 4.11 depicts the absorption as a function of both velocity and detuning for a discrete number of velocities.

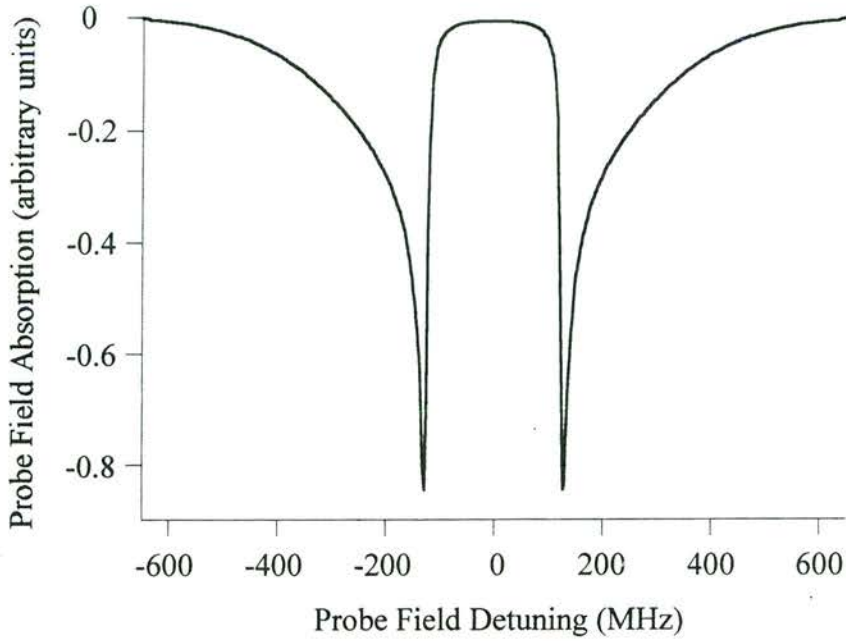


Figure 4.6: Profile of probe field absorption (ρ_{12}^i in arbitrary units) as a function of probe field detuning produced by density matrix analysis of the Cascade scheme ($\lambda_c = 400\text{nm}$, and $\lambda_p = 800\text{nm}$).

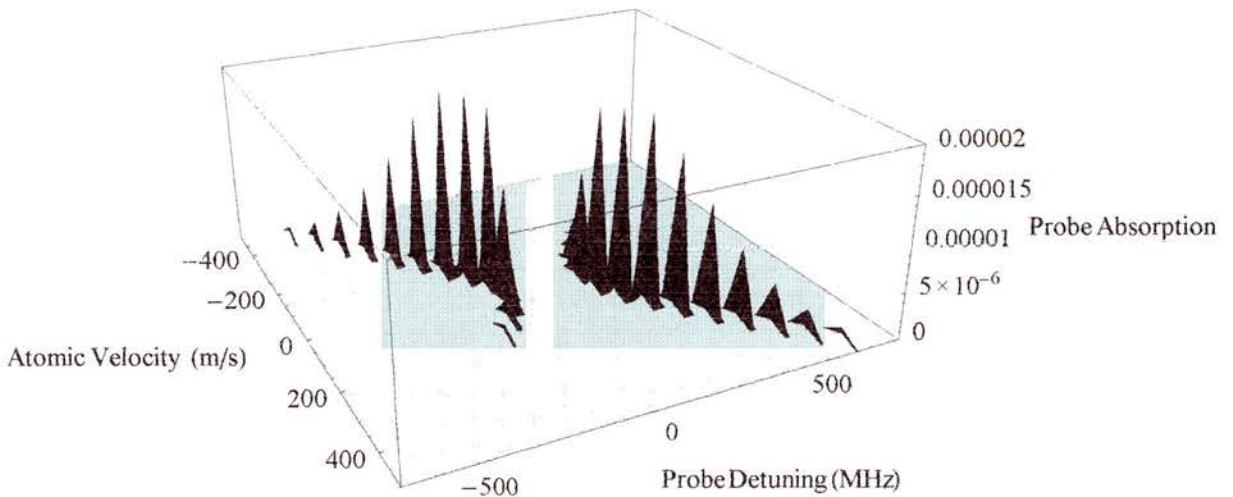


Figure 4.7: Three-dimensional profile of probe field absorption (ρ_{12}^i in arbitrary units) as a function of probe field detuning and atomic velocity for several discrete velocities, produced by density matrix analysis of the Cascade scheme ($\lambda_c = 400\text{nm}$, and $\lambda_p = 800\text{nm}$).

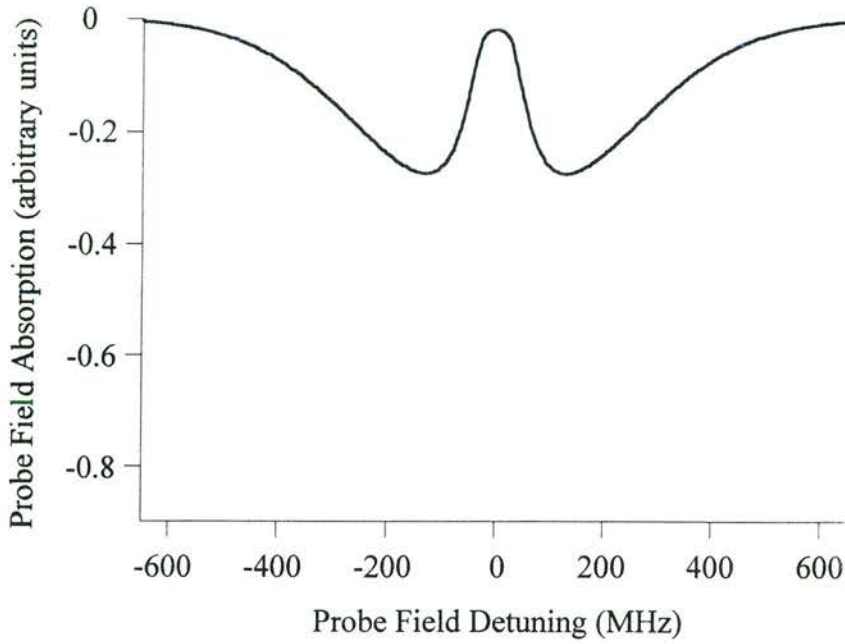


Figure 4.8: Profile of probe field absorption (ρ^i_{12} in arbitrary units) as a function of probe field detuning produced by density matrix analysis of the Cascade scheme ($\lambda_c = 800\text{nm}$, and $\lambda_p = 800\text{nm}$).

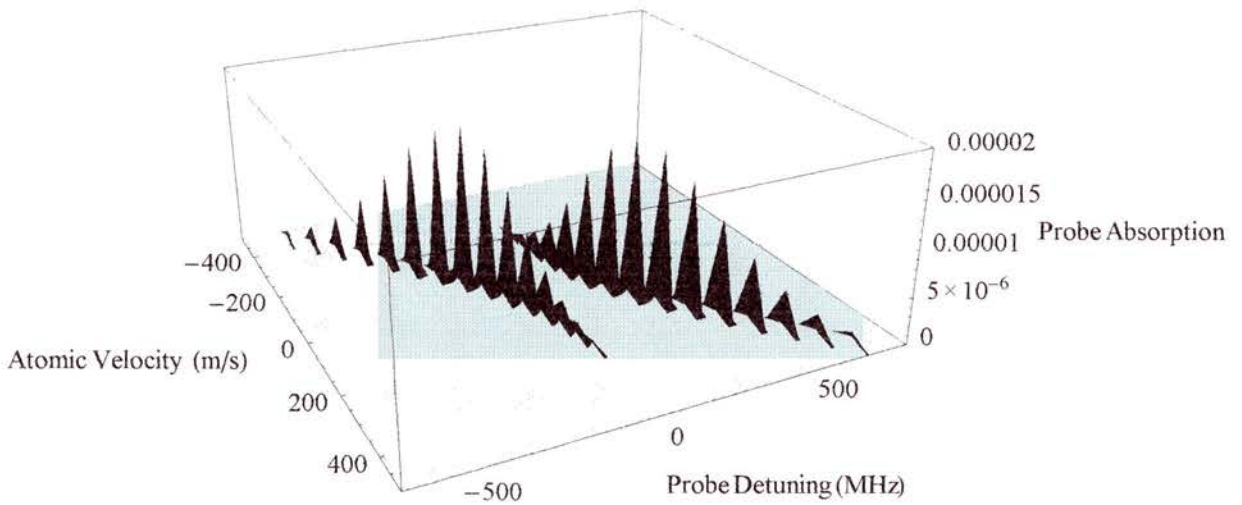


Figure 4.9: Three-dimensional profile of probe field absorption (ρ^i_{12} in arbitrary units) as a function of probe field detuning and atomic velocity for several discrete velocities, produced by density matrix analysis of the Cascade scheme ($\lambda_c = 800\text{nm}$, and $\lambda_p = 800\text{nm}$).

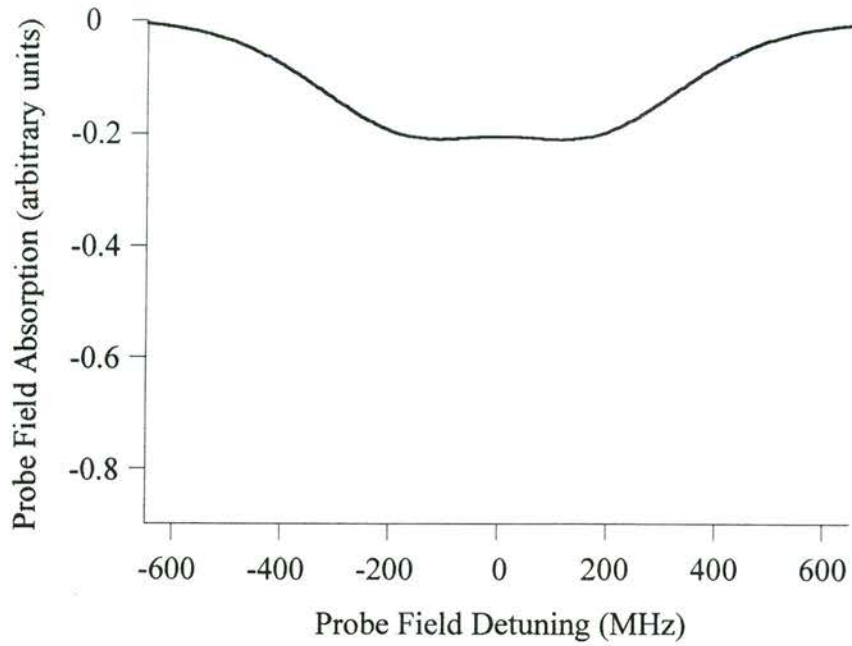


Figure 4.10: Profile of probe field absorption (ρ_{12}^i in arbitrary units) as a function of probe field detuning produced by density matrix analysis of the Cascade scheme ($\lambda_c = 1600\text{nm}$, and $\lambda_p = 800\text{nm}$).

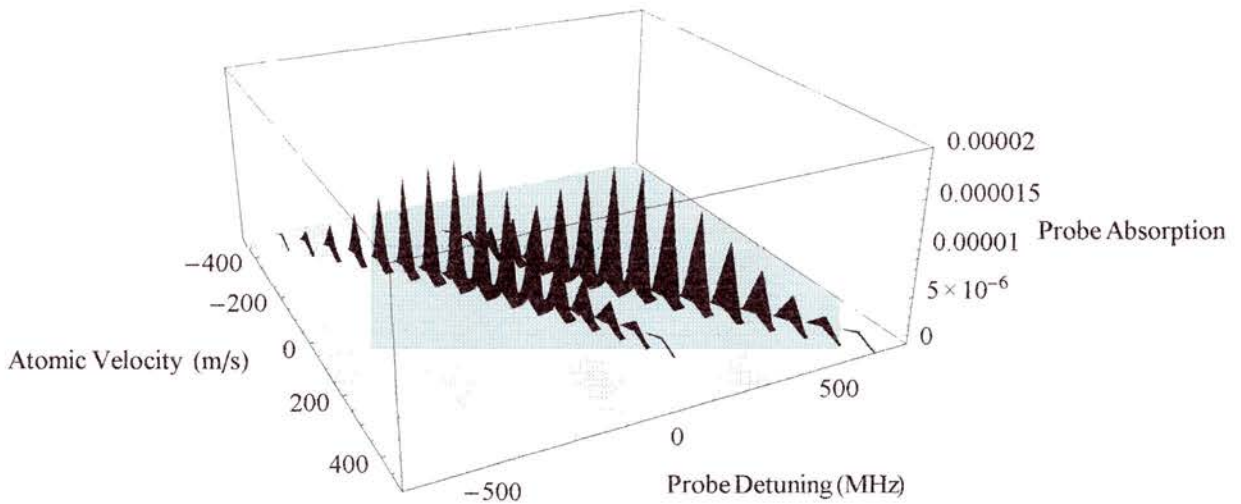


Figure 4.11: Three-dimensional profile of probe field absorption (ρ_{12}^i in arbitrary units) as a function of probe field detuning and atomic velocity for several discrete velocities, produced by density matrix analysis of the Cascade scheme ($\lambda_c = 1600\text{nm}$, and $\lambda_p = 800\text{nm}$).

4.4.2 The Lambda Scheme

4.4.2.a Mismatched wavelengths ($\lambda_c < \lambda_p$)

In this wavelength regime the coupling frequency is twice that of the probe field. Figure 4.12 shows the probe field absorption as a function of linear probe field detuning. A significant transparency window is observed at line centre. Figure 4.13 depicts the absorption as a function of both velocity and detuning for a discrete number of velocities.

4.4.2.b Matched wavelengths ($\lambda_c = \lambda_p$)

In this wavelength regime the coupling frequency is exactly equal to that of the probe field. Figure 4.14 shows the probe field absorption as a function of linear probe field detuning. A significant transparency window is observed at line centre that is narrower than the one predicted for the mismatched ($\lambda_c < \lambda_p$) case. Figure 4.15 depicts the absorption as a function of both velocity and detuning for a discrete number of velocities.

4.4.2.c Mismatched wavelengths ($\lambda_c > \lambda_p$)

In this wavelength regime the probe frequency is twice that of the coupling field. Figure 4.16 shows the probe field absorption as a function of linear probe field detuning. No transparency window is observed at line centre. Figure 4.17 depicts the absorption as a function of both velocity and detuning for a discrete number of velocities.

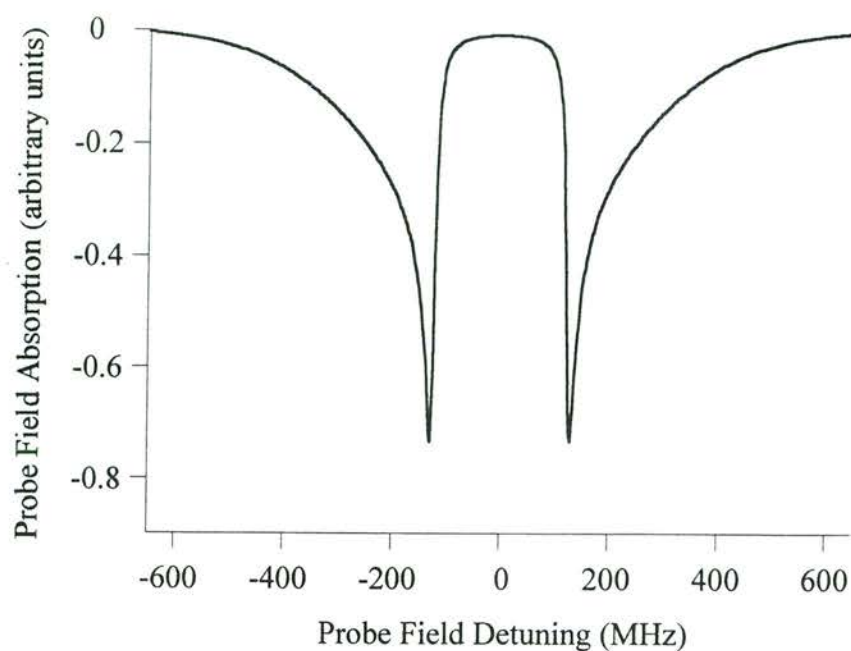


Figure 4.12: Profile of probe field absorption (ρ_{13}^i in arbitrary units) as a function of probe field detuning produced by density matrix analysis of the Lambda scheme ($\lambda_c = 400\text{nm}$, and $\lambda_p = 800\text{nm}$).

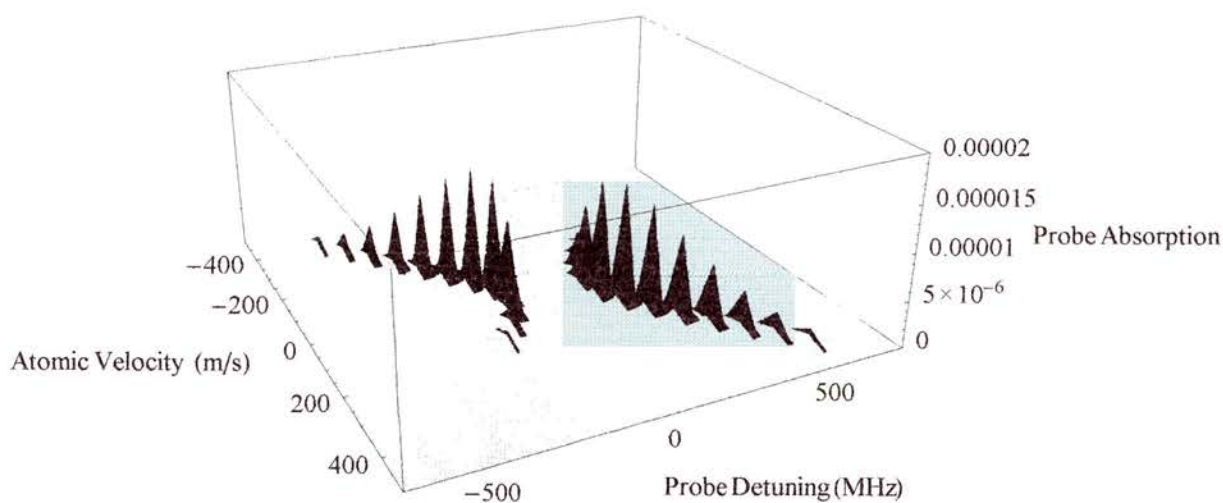


Figure 4.13: Three-dimensional profile of probe field absorption (ρ_{13}^i in arbitrary units) as a function of probe field detuning and atomic velocity for several discrete velocities, produced by density matrix analysis of the Lambda scheme ($\lambda_c = 400\text{nm}$, and $\lambda_p = 800\text{nm}$).

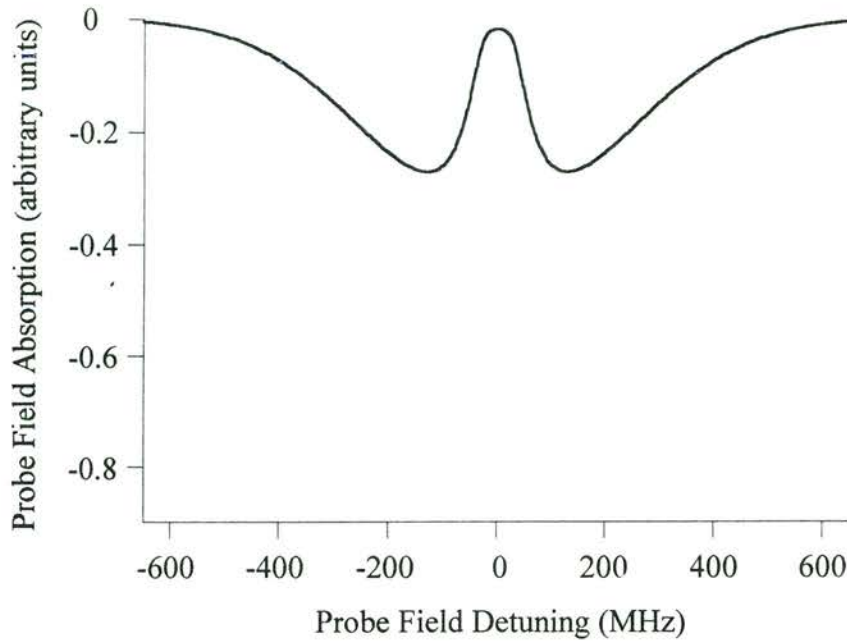


Figure 4.14: Profile of probe field absorption (ρ_{13}^i in arbitrary units) as a function of probe field detuning produced by density matrix analysis of the Lambda scheme ($\lambda_c = 800\text{nm}$, and $\lambda_p = 800\text{nm}$).

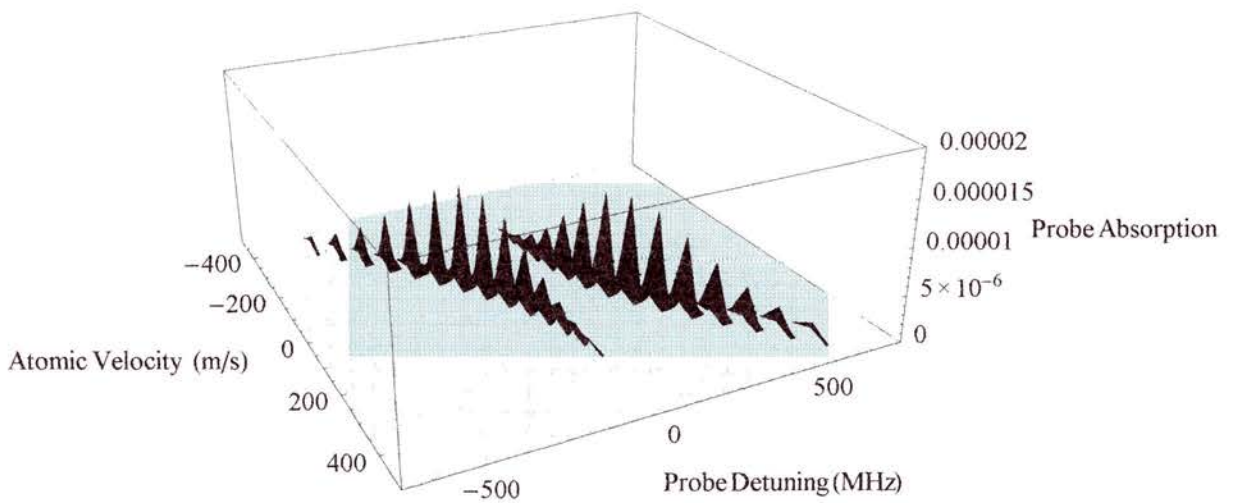


Figure 4.15: Three-dimensional profile of probe field absorption (ρ_{13}^i in arbitrary units) as a function of probe field detuning and atomic velocity for several discrete velocities, produced by density matrix analysis of the Lambda scheme ($\lambda_c = 800\text{nm}$, and $\lambda_p = 800\text{nm}$).

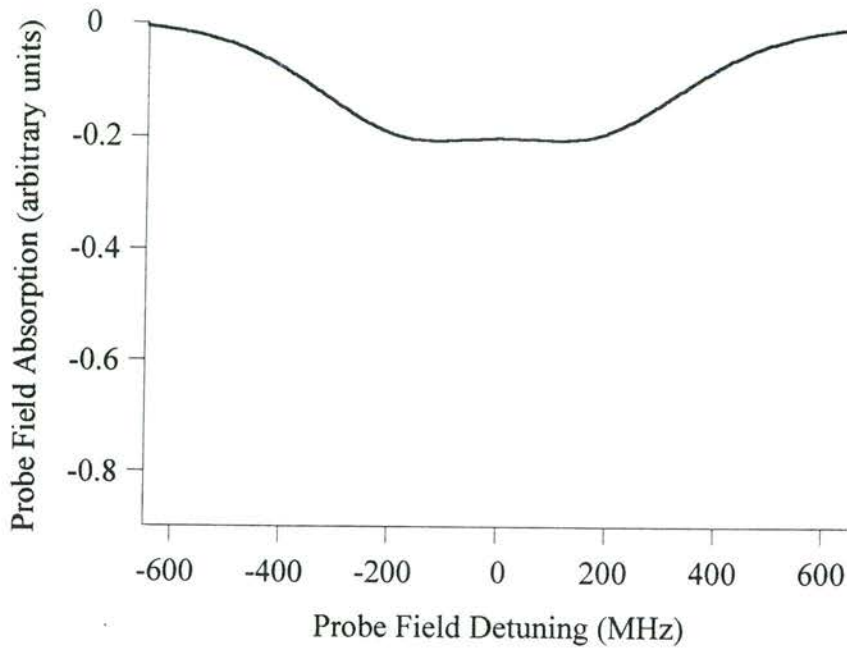


Figure 4.16: Profile of probe field absorption (ρ^i_{13} in arbitrary units) as a function of probe field detuning produced by density matrix analysis of the Lambda scheme ($\lambda_c = 1600\text{nm}$, and $\lambda_p = 800\text{nm}$).

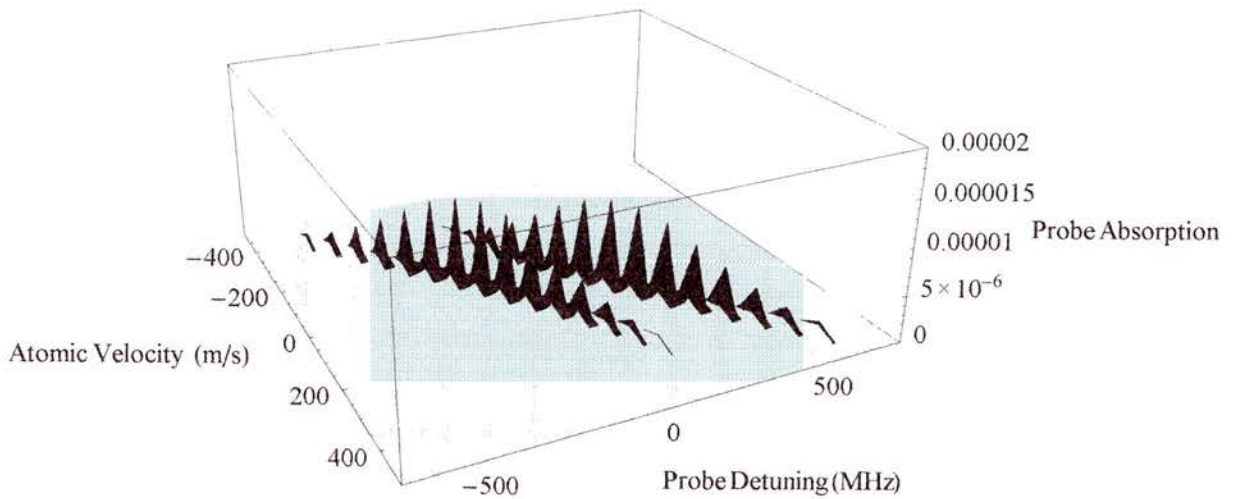


Figure 4.17: Three-dimensional profile of probe field absorption (ρ^i_{13} in arbitrary units) as a function of probe field detuning and atomic velocity for several discrete velocities, produced by density matrix analysis of the Lambda scheme ($\lambda_c = 1600\text{nm}$, and $\lambda_p = 800\text{nm}$).

4.4.3 The Vee Scheme

4.4.3.a Mismatched wavelengths ($\lambda_c < \lambda_p$)

In this wavelength regime the coupling frequency is twice that of the probe field. Figure 4.18 shows the probe field absorption as a function of linear probe field detuning. A very significant transparency window is observed at line centre. Figure 4.19 depicts the absorption as a function of both velocity and detuning for a discrete number of velocities.

4.4.3.b Matched wavelengths ($\lambda_c = \lambda_p$)

In this regime the coupling and probe wavelengths are equal. Figure 4.20 shows the probe field absorption as a function of linear probe field detuning. A significant transparency window is observed at line centre. Figure 4.21 depicts the absorption as a function of both velocity and detuning for a discrete number of velocities.

4.4.3.c Mismatched wavelengths ($\lambda_c > \lambda_p$)

In this wavelength regime the probe frequency is twice that of the coupling field. Figure 4.22 shows the probe field absorption as a function of linear probe field detuning. Importantly, a transparency window is still observed at line centre. Figure 4.23 depicts the absorption as a function of both velocity and detuning for a discrete number of velocities.

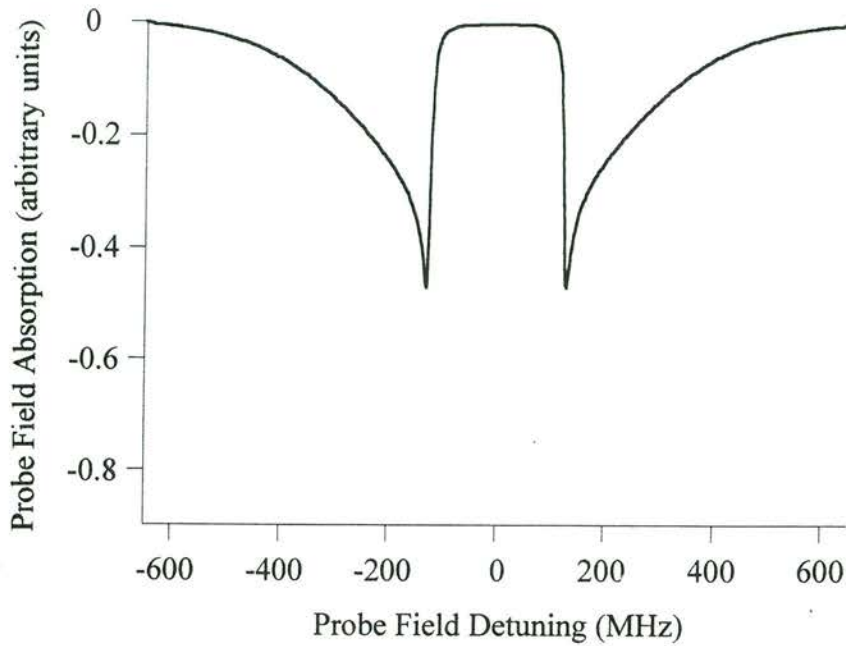


Figure 4.18: Profile of probe field absorption (ρ_{13}^i in arbitrary units) as a function of probe field detuning produced by density matrix analysis of the Vee-type scheme ($\lambda_c = 400\text{nm}$, and $\lambda_p = 800\text{nm}$).

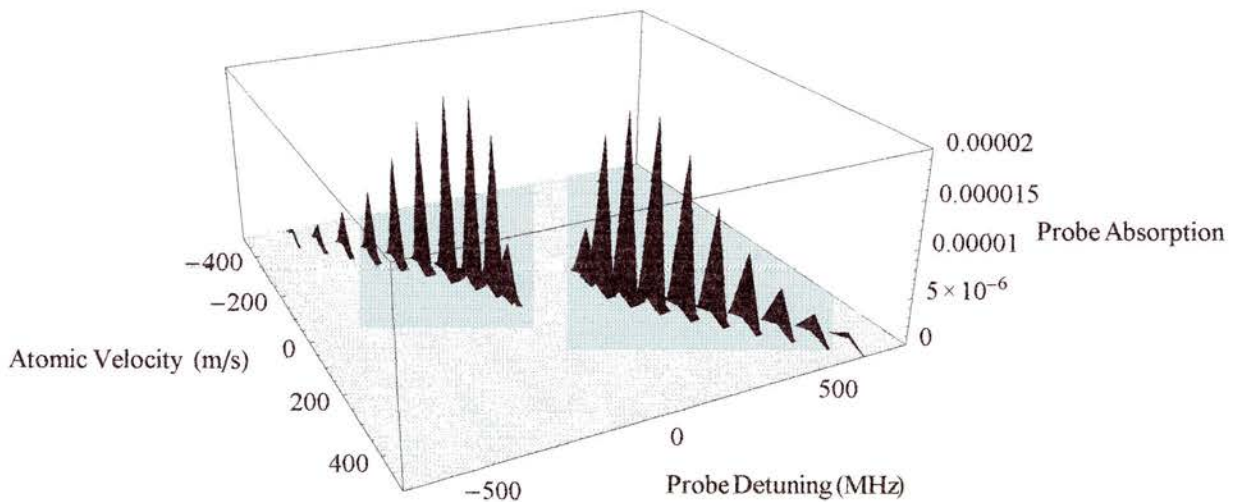


Figure 4.19: Three-dimensional profile of probe field absorption (ρ_{13}^i in arbitrary units) as a function of probe field detuning and atomic velocity for several discrete velocities, produced by density matrix analysis of the Vee-type scheme ($\lambda_c = 400\text{nm}$, and $\lambda_p = 800\text{nm}$).

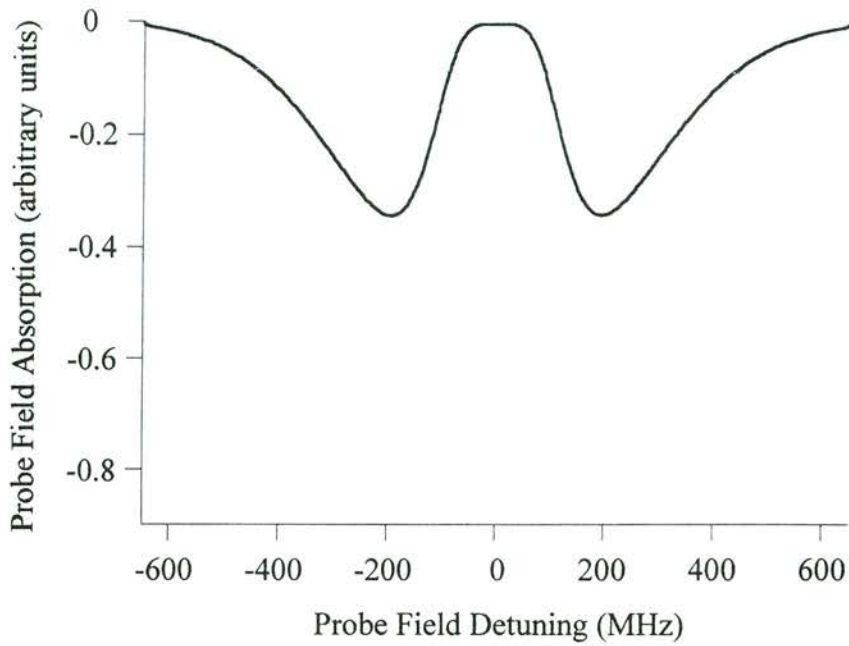


Figure 4.20: Profile of probe field absorption (ρ_{13}^i in arbitrary units) as a function of probe field detuning produced by density matrix analysis of the Vee-type scheme ($\lambda_c = 800\text{nm}$, and $\lambda_p = 800\text{nm}$).

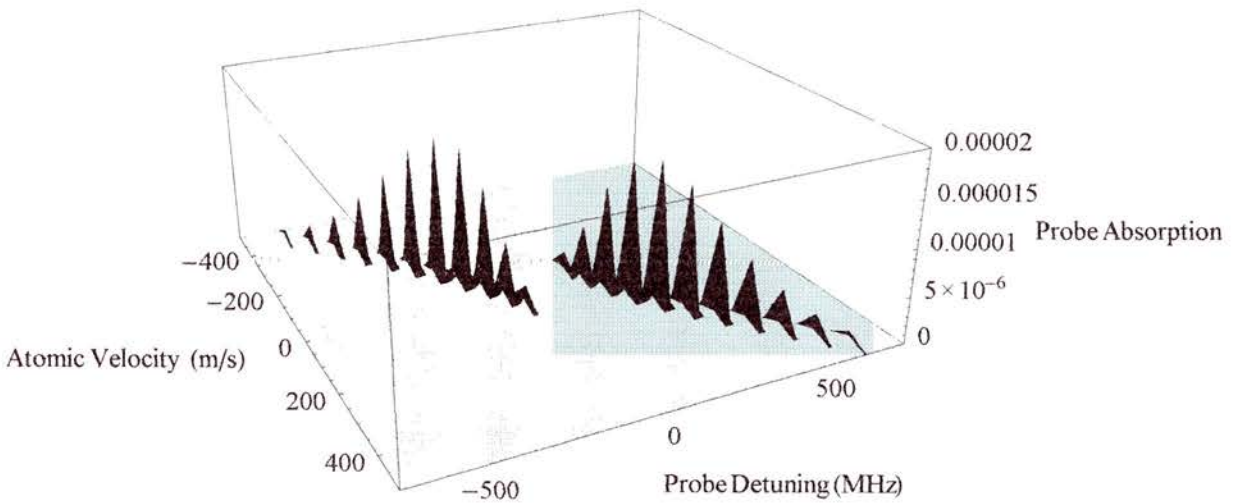


Figure 4.21: Three-dimensional profile of probe field absorption (ρ_{13}^i in arbitrary units) as a function of probe field detuning and atomic velocity for several discrete velocities, produced by density matrix analysis of the Vee-type scheme ($\lambda_c = 800\text{nm}$, and $\lambda_p = 800\text{nm}$).

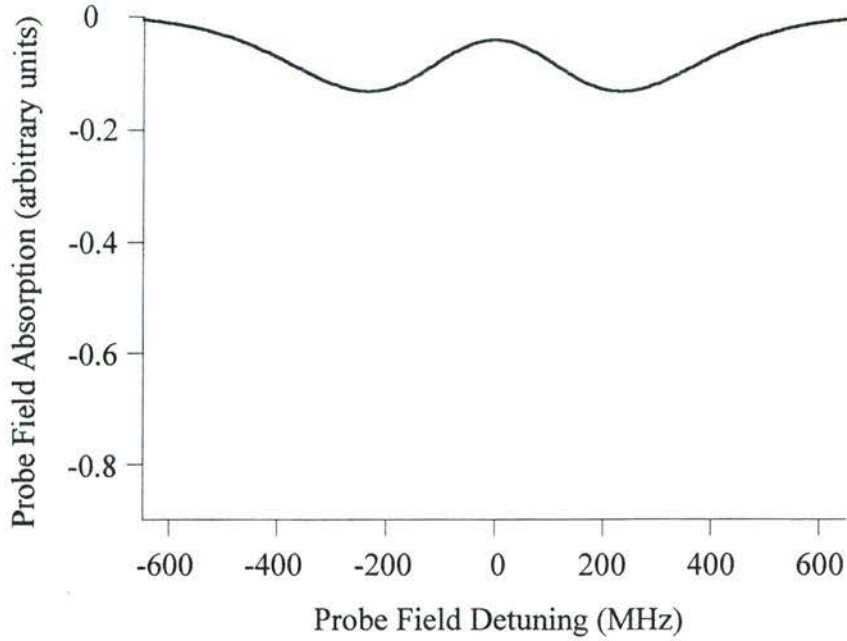


Figure 4.22: Profile of probe field absorption (ρ_{13}^i in arbitrary units) as a function of probe field detuning produced by density matrix analysis of the Vee-type scheme ($\lambda_c = 1600\text{nm}$, and $\lambda_p = 800\text{nm}$).

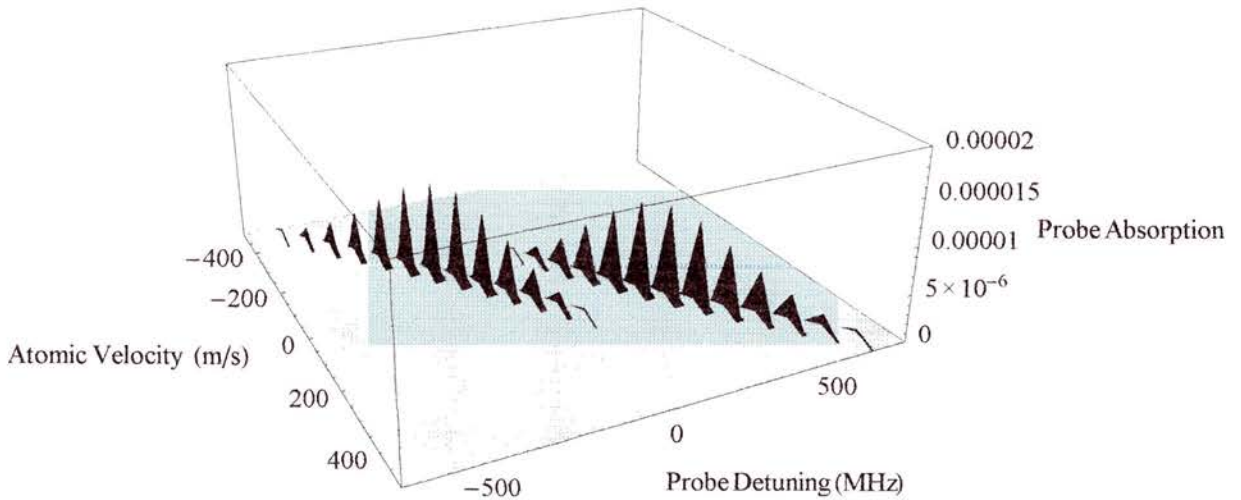


Figure 4.23: Three-dimensional profile of probe field absorption (ρ_{13}^i in arbitrary units) as a function of probe field detuning and atomic velocity for several discrete velocities, produced by density matrix analysis of the Vee-type scheme ($\lambda_c = 1600\text{nm}$, and $\lambda_p = 800\text{nm}$).

These results are now collated with the Autler-Townes and absorption resonance information discussed in Section 4.3. The Autler-Townes components, along with the single and two-photon absorption resonance positions, are re-plotted as a function of probe field detuning and atomic velocity, with the addition of an indication of the magnitude of the Autler-Townes components at certain discrete velocities. The latter is taken directly from the three-dimensional plots displayed in this section. The magnitude of the absorption associated with each Autler-Townes component is indicated by the length of a line drawn, parallel to the x axis, for the selected atomic velocity. The length of these lines is proportional to the absorption coefficient. Table 4.I contains the scaled line lengths in millimetres for all nine systems. The predicted absorption profiles are also collated in Fig. 4.28 so that we have all the information necessary to explain the presence or lack of a transparency in each considered system.

| Velocity (m/s) | Cascade ($\lambda_c < \lambda_p$) | Cascade ($\lambda_c = \lambda_p$) | Cascade ($\lambda_c > \lambda_p$) | Lambda ($\lambda_c < \lambda_p$) | Lambda ($\lambda_c = \lambda_p$) | Lambda ($\lambda_c > \lambda_p$) | Vee ($\lambda_c < \lambda_p$) | Vee ($\lambda_c = \lambda_p$) | Vee ($\lambda_c > \lambda_p$) |
|-------------------|--|--|--|---------------------------------------|---------------------------------------|---------------------------------------|------------------------------------|------------------------------------|------------------------------------|
| -450 | 0.87 | 0.69 | 0.24 | | | | 0.78 | 0.6 | 0.18 |
| -400 | 2.55 | 2.4 | 1.59 | 0.87 | 0.78 | 0.51 | 2.46 | 1.74 | 1.77 |
| -350 | 5.46 | 5.07 | 3.84 | 2.61 | 2.07 | 1.83 | 5.43 | 4.95 | 3.66 |
| -300 | 9.99 | 8.67 | 6.72 | 4.68 | 4.32 | 3.48 | 9.81 | 8.64 | 4.47 |
| -250 | 16.26 | 13.38 | 9.99 | 7.65 | 7.11 | 6.06 | 15.63 | 13.29 | 7.53 |
| -200 | 22.59 | 18.54 | 13.8 | 11.52 | 10.26 | 8.49 | 22.47 | 18.21 | 11.67 |
| -150 | 27.81 | 22.35 | 16.89 | 15 | 12.78 | 10.8 | 27.54 | 21.18 | 13.2 |
| -100 | 29.61 | 22.98 | 18.21 | 17.19 | 14.52 | 12.33 | 27.24 | 19.83 | 12.66 |
| -50 | 27.09 | 20.4 | 17.55 | 16.38 | 13.71 | 12.45 | 22.53 | 14.46 | 10.26 |
| 0 | 14.64 | 15.21 | 15.21 | 11.16 | 11.25 | 11.64 | 7.32 | 6.99 | 7.02 |
| 50 | 6.18 | 10.14 | 12.03 | 4.92 | 8.07 | 9.24 | | 1.8 | 3.84 |
| 100 | 2.34 | 5.52 | 8.97 | 2.58 | 4.74 | 7.11 | | | 1.5 |
| 150 | 0.54 | 2.82 | 5.46 | 0.54 | 2.4 | 4.29 | | | 0.3 |
| 200 | | 1.14 | 2.97 | | 1.14 | 2.52 | | | |
| 250 | | 0.27 | 1.44 | | 0.21 | 1.11 | | | |
| 300 | | | 0.36 | | | 0.15 | | | |
| 350 | | | | | | | | | |
| 400 | | | | | | | | | |
| 450 | | | | | | | | | |

Table 4.1: Scaled heights of individual absorptions peaks for the velocities indicated in each of the nine systems. The heights of one set of Autler-

Townes components is given. The corresponding set have exactly the same height for a velocity of equal magnitude and opposite sign.

By way of example, Fig. 4.24 (a) shows the single photon position and the magnitude of absorption along with (b) the straightforward absorption profile of a simple two level atom interacting with a single resonant field. In the absence of a strong applied field there is no Autler-Townes splitting, and we see a single absorption component which exactly follows the single photon resonance position. Because we are modelling a Doppler-broadened system the single photon resonance has a linear dependence on atomic velocity.

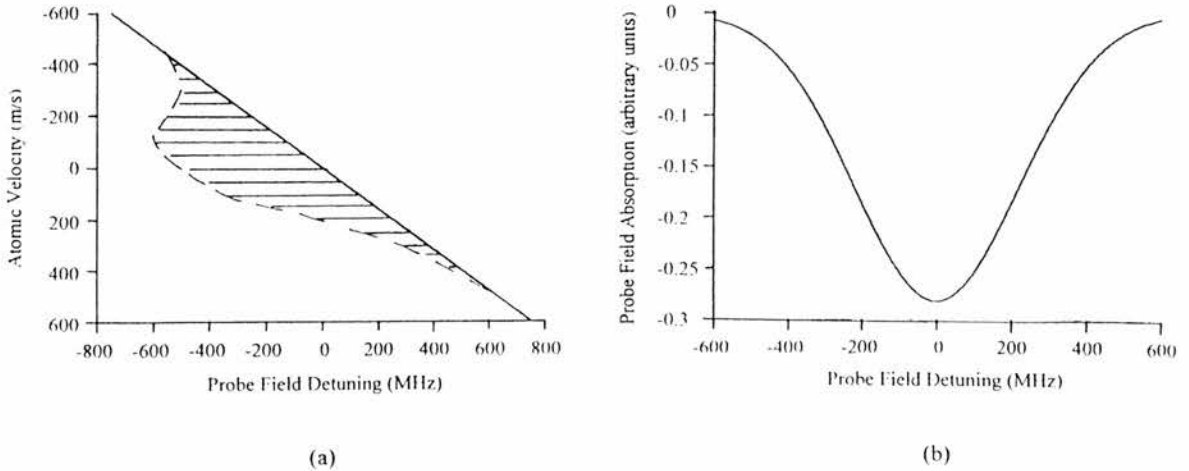


Figure 4.24: *Two-dimensional plot of the single photon absorption component as a function of atomic velocity and probe field detuning, in the absence of the coupling laser. The magnitude of the absorption components is indicated by the length of a line drawn parallel to the x axis for selected velocities. The length of these lines is proportional to the absorption coefficient for the atomic velocity specified.*

In both the analysis presented in Section 4.3 and the density matrix models we have assumed co-propagating beams in the Lambda and Vee-type schemes and counter-propagating beams in the Cascade system. Differences in the nature of the energy level configurations are counterbalanced by selecting these beam geometries so that the Autler-Townes components and absorption resonances occur in the same positions for all three schemes, for a given set of probe and coupling wavelengths, in the limiting case of zero manual detuning of the coupling field (i.e. $\Delta_{\text{coupling}} = 0$). Significant differences are manifested in the magnitudes of the Autler-Townes components for the different configurations. Figures 4.25, 4.26, and 4.27 show the results for all three EIT schemes.

The absorption profiles are also shown in Fig. 4.28 with the three wavelength regimes overlaid for each energy level configuration. To avoid repetition the caption for Figs. 4.25, 4.26, and 4.27 is given here for all three figures:

Figure 4.25, 4.26, and 4.27: *Plots of the Autler-Townes and absorption resonance positions as a function of atomic velocity and probe field detuning for the indicated scheme. Three wavelength regimes are considered: (a) $\lambda_c < \lambda_p$, (b) $\lambda_c = \lambda_p$, and (c) $\lambda_c > \lambda_p$. The magnitude of the Autler-Townes components is indicated, in each plot, by the length of a line drawn parallel to the x axis for selected velocities. The length of these lines is proportional to the absorption coefficient for the atomic velocity specified. The positions of the Autler-Townes components are shown by solid lines, the single photon resonance by a dashed line, and the two-photon resonance by a dotted line.*

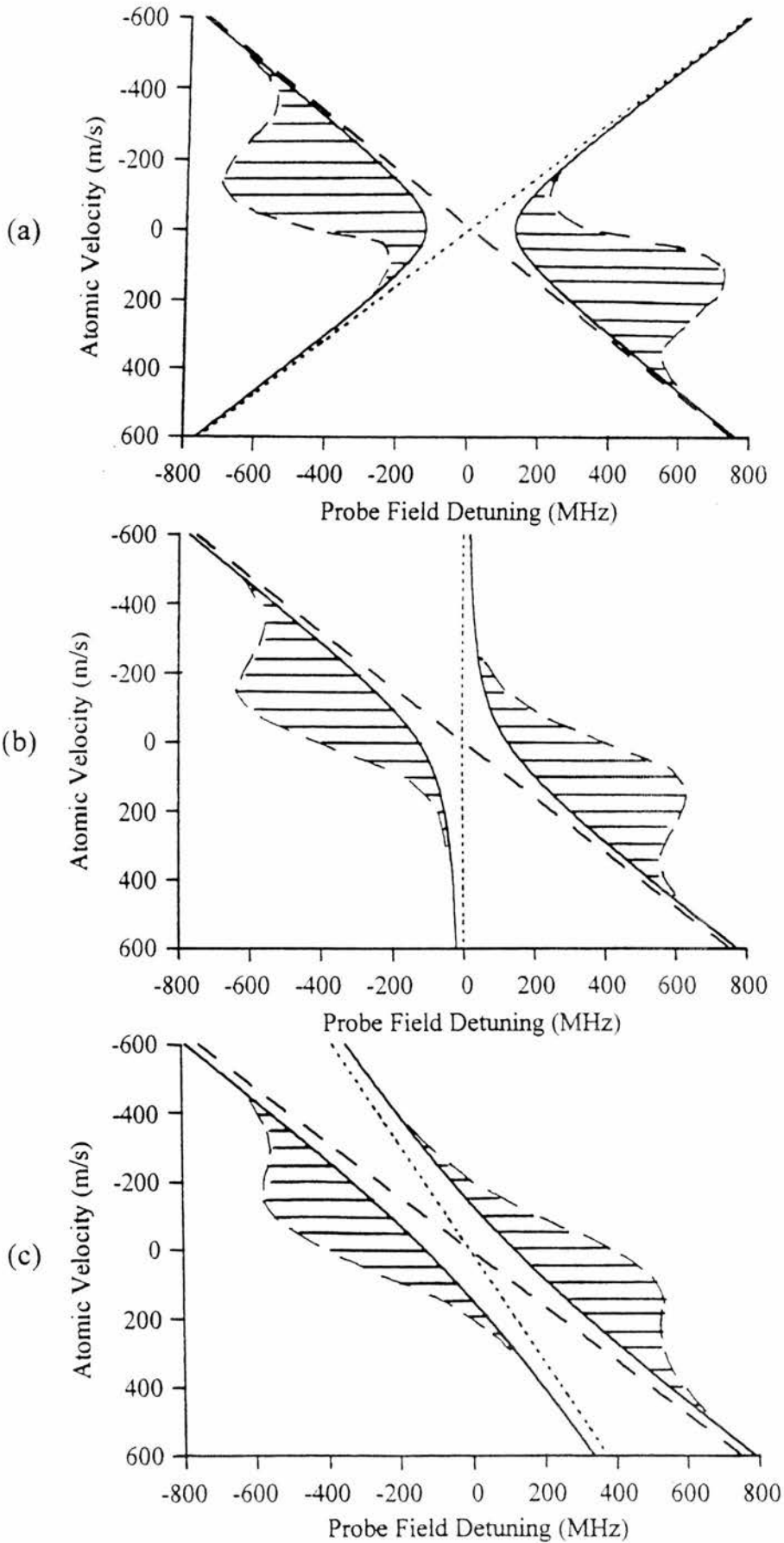


Figure 4.25: *The Cascade scheme.*

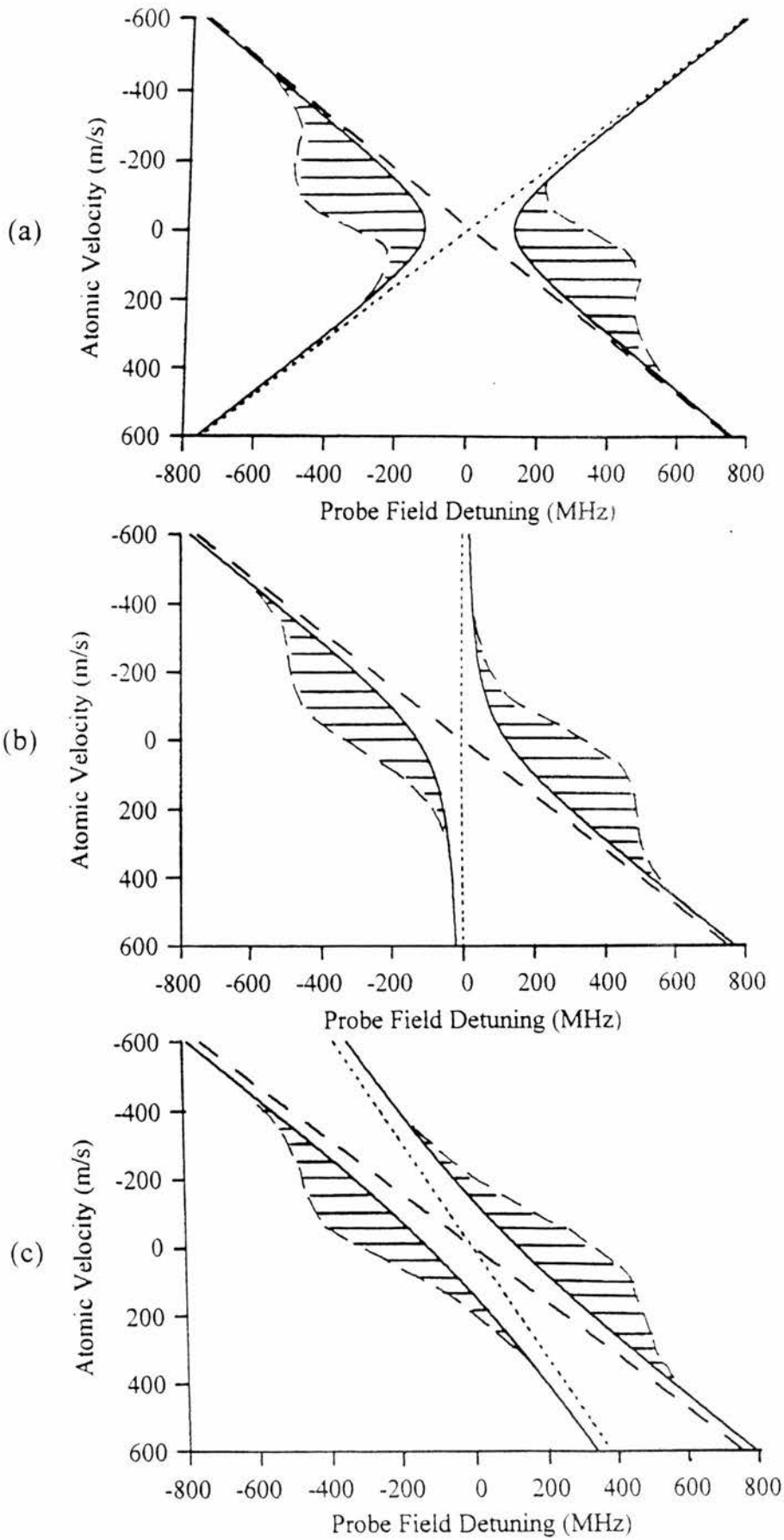


Figure 4.26: *The Lambda scheme.*

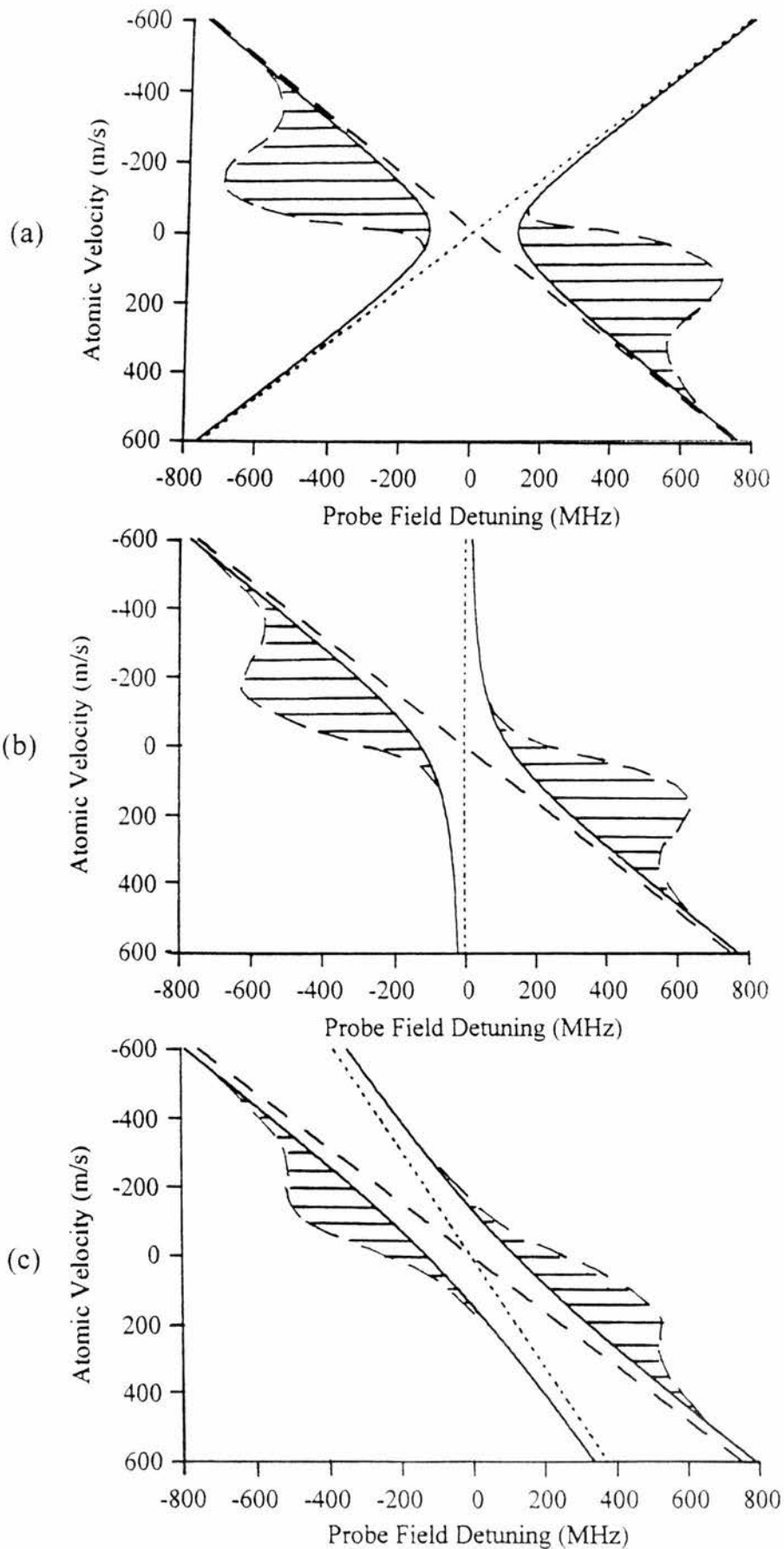


Figure 4.27: *The Vee-type scheme.*

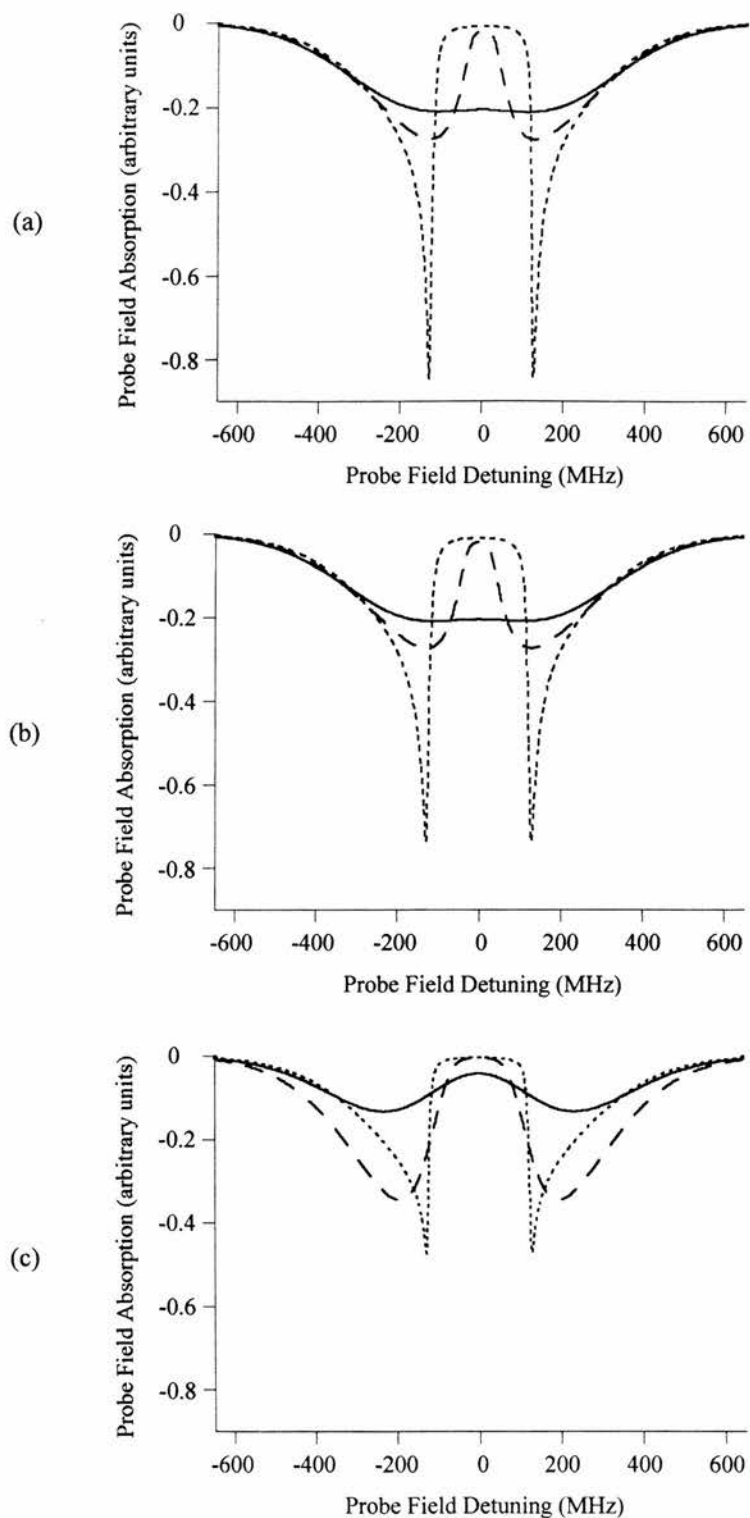


Figure 4.28: Probe field absorption (appropriate off-diagonal element in arbitrary units) as a function of probe field detuning for (a) the Cascade, (b) the Lambda, and (c) the Vee-type schemes. In each case the three wavelength regimes are considered: $\lambda_c < \lambda_p$ (dotted line), $\lambda_c = \lambda_p$ (dashed line), and $\lambda_c > \lambda_p$ (solid line). For ease of comparison the same vertical scale is used in (a), (b), and (c).

4.5 Discussion

From Fig. 4.28 we see that the matched wavelength regime does not provide the best transparency in any of the energy level schemes. In fact, the highest level of transparency is consistently induced in the mismatched wavelength regime for which the coupling frequency is higher than the probe frequency ($\lambda_c < \lambda_p$). We can think of EIT occurring due to the interference of two pathways to absorption in the bare state picture [6,23]. For example, in the Vee scheme absorption may occur due to a single probe photon exciting an atom from state $|1\rangle$ to state $|3\rangle$, or as a result of two photons - one from each field - stimulating the atom from state $|2\rangle$ to state $|1\rangle$ and then to state $|3\rangle$ as shown previously in Fig. 1.8. By considering the positions of the single and two-photon absorption resonances in Figs. 4.25, 4.26, and 4.27, we see that the two pathways to absorption are only coincident, for all schemes regardless of the probe and coupling field wavelengths, for zero atomic velocity. However, the absorption processes associated with a particular velocity group are not confined to a single discrete frequency but extend over a range of frequencies that is the homogeneously broadened lineshape function centred on the positions indicated in Figs. 4.25, 4.26, and 4.27. Interference, and hence EIT, may therefore occur at any point for which the single and two-photon resonance lineshapes overlap. For the case in which the magnitudes of the absorption routes are equal, for a specific frequency, full cancellation may take place. When the magnitudes of the absorptions at a specific frequency are unequal, a partial reduction in absorption occurs. If, on the other hand, the absorption resonances for a given velocity are separated by much more than one homogeneous linewidth, EIT cannot take place and it becomes important to ensure that these absorption components do not obscure the transparency that is created on resonance for other velocity groups.

The best transparency occurs when the coupling frequency is higher than the probe frequency because of the Doppler shifted contribution to the coupling field detuning, referred to here as the Doppler detuning. The Doppler shift in the frequency of the coupling field is proportional to the frequency of the coupling field itself and will therefore increase in magnitude when we decrease the coupling field wavelength. Consequently, the Autler-Townes splitting, which is dependent on detuning, will also increase as the coupling wavelength decreases. In the $\lambda_c < \lambda_p$ regime, the Autler-Townes components for the non-

zero velocity atoms are split further apart and therefore further away from resonance. Thus, EIT created at line centre for the zero velocity group is better preserved in this mismatched wavelength regime because the secondary Autler-Townes components of the non-zero velocity atoms are Doppler detuned away from resonance, and they do not overlap with the transparency. Part (a) of Figs. 4.25, 4.26, and 4.27 clearly show the Autler-Townes splitting increasing with the modulus of the velocity so that coincidence of the single and two-photon resonances (the point for which maximum EIT occurs) at line centre is unobscured.

As we increase the coupling wavelength relative to the probe wavelength, the magnitude of the Doppler detuning decreases relative to the Doppler width of the absorption profile, which is fixed by the probe wavelength. The Autler-Townes splitting for the non-zero velocity atoms will tend towards the zero velocity value, and the associated Autler-Townes absorptions will start to overlap with the line centre transparency. The matched wavelength regime represents the special case when the Doppler shifts of the probe and coupling fields are equal and exactly cancel, ensuring that the two-photon resonance position is fixed for all velocity groups. The result is that the non-zero velocity, secondary, Autler-Townes absorptions only partially obscure the on-resonance transparency. The extent to which the transparency can be maintained in this regime depends largely on the dephasing. If dephasing is increased, the linewidth of the Autler-Townes absorption components close to resonance will increase and further encroach on the transparency window.

In the $\lambda_c > \lambda_p$ regime, Figures 4.25, 4.26, and 4.27 (c) show that the Autler-Townes components overlap completely with line centre. We would reasonably expect the transparency to be destroyed and this is exactly what happens in the Lambda and Cascade systems. However, in the Vee-type scheme the transparency window is maintained. This result can be explained by considering the magnitude of the Autler-Townes components close to resonance. Careful inspection of the traces depicted in Figure 4.25, 4.26, and 4.27 reveals that while the positions of the Autler-Townes components are the same in each energy level scheme, for a given set of wavelengths, the magnitudes are different. In Section 4.3 we defined two types of Autler-Townes components. For high, positive and negative, velocities these primary and secondary Autler-Townes components separate and closely

follow the single and two-photon resonance positions. In this regime the magnitude of each component is determined exclusively by the particular absorption resonance associated with it. The single photon absorption defines the magnitude of the primary Autler-Townes components and the two-photon absorption determines the magnitude of the secondary components. It is the secondary Autler-Townes components that overlap with the on-resonance transparency in the $\lambda_c > \lambda_p$ regime. In a Vee-type system the magnitude of these secondary components falls off very rapidly as velocity increases. Consequently, the transparency window is not destroyed as it is in the Cascade and Lambda schemes.

In all three schemes it is also apparent that the magnitude of these secondary Autler-Townes components falls off more rapidly with increasing velocity when the coupling wavelength is lower. This trend occurs because the Doppler shifted contribution to the coupling field detuning, for a given velocity, is greater for a higher coupling field frequency. Consequently, the relatively large coupling field detuning moves the two-photon resonance further from the intermediate level (states $|1\rangle$, $|2\rangle$, and $|3\rangle$ in the Vee, Cascade, and Lambda schemes respectively) as the coupling wavelength is decreased. Since the magnitude of the secondary Autler-Townes components is dependent on the strength of the two-photon process it reduces as the two-photon resonance moves away from the intermediate state. This diminution of the secondary Autler-Townes components always occurs as velocity increases in a given system. Importantly, it occurs more rapidly when the coupling wavelength is lower and the Doppler shift, $-k_2 V_z$, is consequently greater for a given velocity.

The preceding argument applies to all three schemes, but the Vee configuration exhibits a more sudden reduction in the magnitude of the secondary Autler-Townes components. The explanation for this lies in the nature of the two-photon process. In a Vee scheme the two-photon absorption route begins in the upper level of the coupling transition and therefore relies on that level being significantly populated. When the coupling field is detuned by the Doppler shift associated with non-zero velocity atoms, the population excited into the upper level of the coupling transition rapidly falls off. Consequently, the magnitude of the two-photon absorption reduces even more rapidly in a Vee scheme as the atomic velocity increases and the secondary Autler-Townes components

that overlap with line centre are of such a low magnitude that the transparency may still be observed.

To demonstrate the difference in the nature of the two-photon process in each scheme we consider the situation for which the coupling laser is scanned in frequency away from resonance with the $|1\rangle - |2\rangle$ transition. Figure 4.29 shows a series of traces, for each energy level scheme, in which the coupling field is manually detuned. EIT diminishes as the manual detuning of the coupling laser is increased because the two-photon and single photon resonances no longer coincide at line centre. Gradually, the two-photon process is resolved as a distinct absorption peak. In all cases, for detunings $> 0.75\text{GHz}$, the Doppler-broadened single photon absorption is resolved at line centre. However, the isolated two-photon absorption peak quickly disappears with increasing detuning in the Vee scheme while it persists for the Lambda and Cascade systems.

Returning to the case in which the coupling field is not manually detuned, we conclude that the two-photon process in a Vee scheme is strong for the zero velocity atoms because the coupling field is on resonance and significantly populates level $|2\rangle$. Furthermore, when the coupling field is Doppler shifted from resonance the two-photon effect diminishes because significant population is no longer excited into level $|2\rangle$. Consequently, the two-photon absorption is present for atomic velocities close to zero for which the two routes to absorption interfere and we have EIT, whereas it is absent for higher velocity atoms when it would otherwise overlap and mask the transparency at line centre.

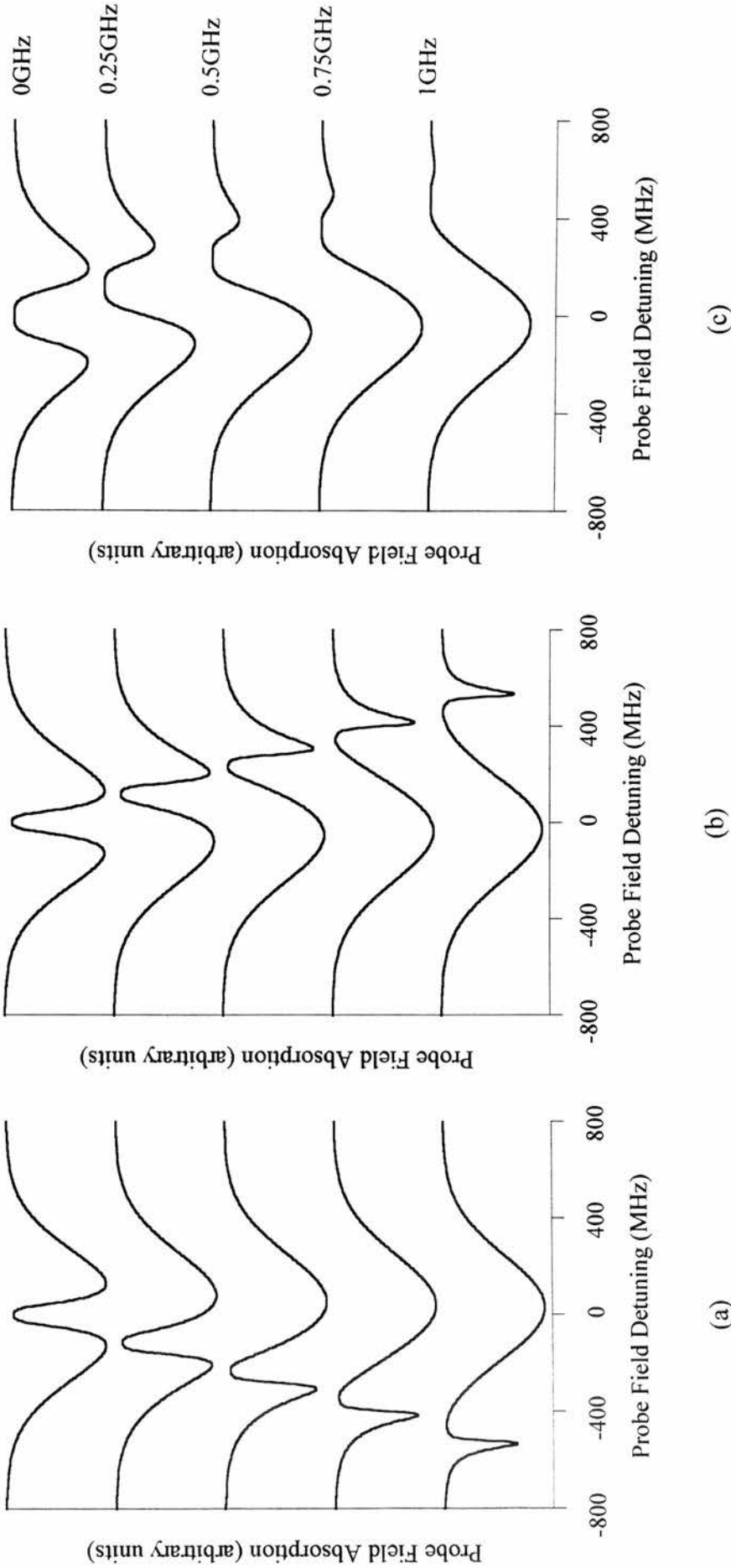


Figure 4.29: A series of absorption profiles showing manual detuning of the coupling field in (a) the Cascade, (b) the Lambda, and (c) the Vee-type systems. The coupling field detuning associated with each trace is indicated to the right of the figure. The topmost trace shows single and two-photon routes interfering to create EIT, and the bottom trace shows the resolved profiles of single and two-photon processes.

Due to the fortuitous nature of the two-photon process in a Vee scheme, the transparency induced therein is better than in a Cascade or Lambda scheme for each wavelength regime. Indeed, comparison of the transparency induced in the mismatched ($\lambda_c > \lambda_p$) Vee scheme and the matched ($\lambda_c = \lambda_p$) Cascade and Lambda systems indicates that while the transparency is slightly deeper in the latter case it is broader in the former. Figure 4.30 shows an overlay of the absorption profiles for matched Lambda and Cascade schemes with the mismatched ($\lambda_c > \lambda_p$) Vee scheme.

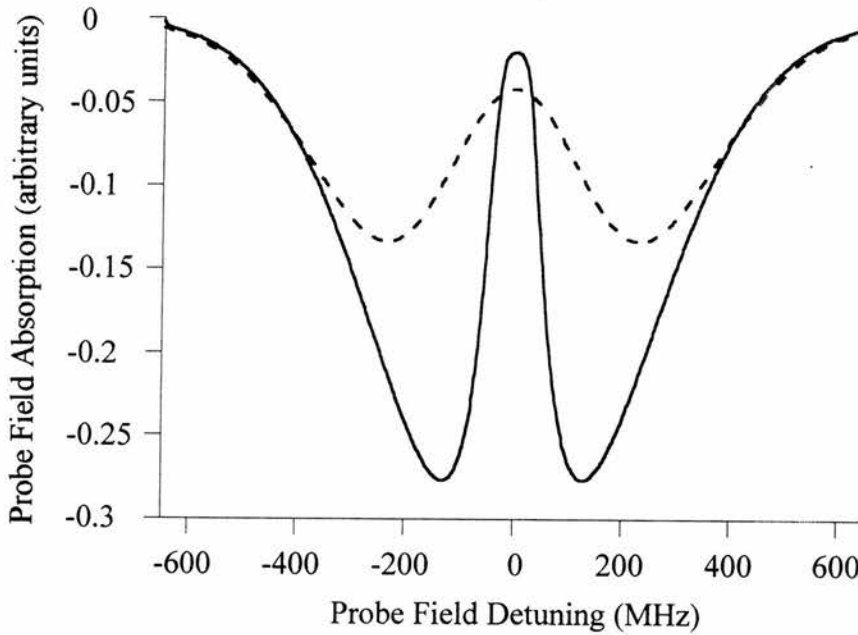


Figure 4.30: The probe field absorption (ρ^i_{12} and ρ^i_{13} in arbitrary units) is plotted as a function of probe field detuning for the mismatched ($\lambda_c > \lambda_p$) Vee scheme and the matched ($\lambda_c = \lambda_p$) Cascade and Lambda systems. The Cascade and Lambda systems have an identical absorption profile for this wavelength regime, indicated with a solid line. The Vee scheme's absorption profile is marked with a dashed line.

Direct comparison of the absorption profiles in the mismatched, $\lambda_c > \lambda_p$, regime for all schemes shows that transparency is present in the Vee scheme while completely destroyed in the Cascade and Lambda systems for our selected coupling field Rabi frequency, as shown in Figure 4.31. This result is generalised in Figure 4.32 which

indicates the on-resonance absorption as a function of coupling field Rabi frequency. Transparency is possible in the Cascade and Lambda schemes if we employ a coupling field Rabi frequency large enough to split the overlapping Autler-Townes components away from line centre by more than the Doppler width, as expected. However, importantly, transparency is achieved in the Vee scheme for a coupling field Rabi frequency much lower than the Doppler width (approximately 500MHz).

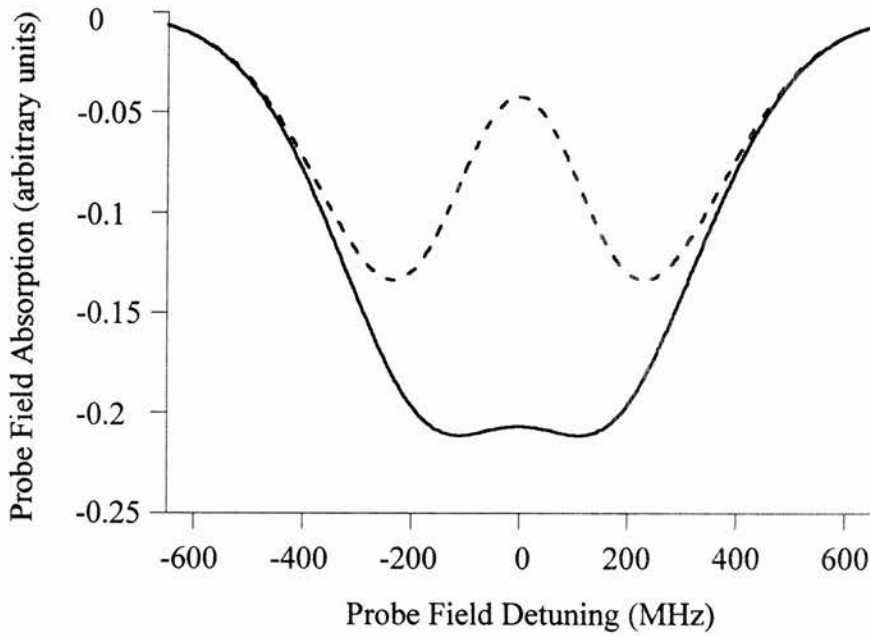


Figure 4.31: Probe field absorption (ρ_{12}^i and ρ_{13}^i in arbitrary units) is plotted as a function of probe field detuning for the mismatched ($\lambda_c > \lambda_p$) Cascade, Lambda and Vee-type systems. The Cascade and Lambda systems have an identical absorption profile for this wavelength regime, indicated with a solid line. The Vee scheme's absorption profile is marked with a dashed line.

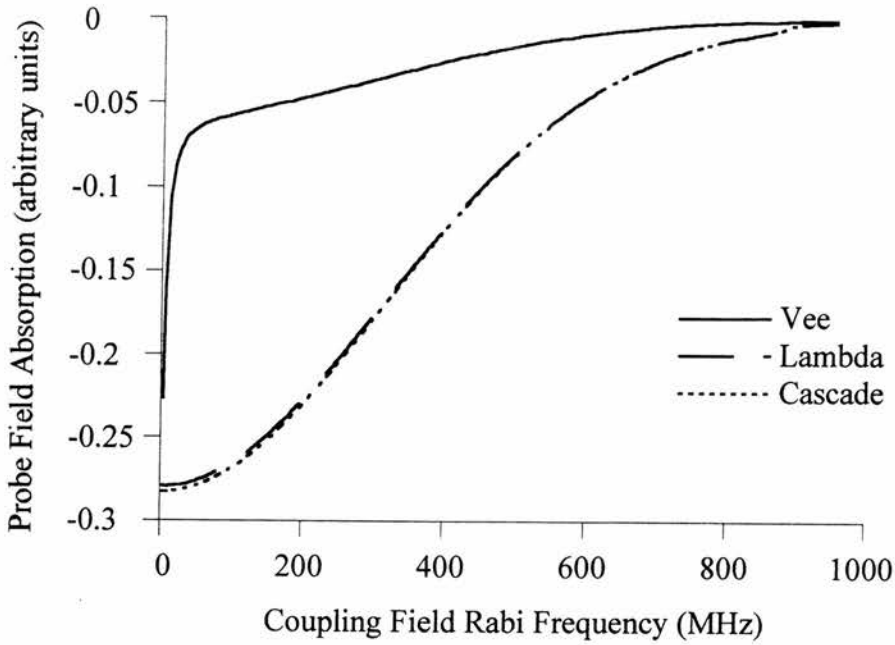


Figure 4.32: *The on-resonance transparency (ρ_{12}^i and ρ_{13}^i in arbitrary units) is plotted as a function of linear coupling field Rabi frequency for all three EIT schemes. The Vee-type scheme is depicted by a solid line and the Cascade and Lambda systems are indicated by dotted and dashed lines respectively.*

The results discussed here can be broadly applied to any mismatched Doppler-broadened system. We have chosen to mismatch the wavelengths by varying the coupling field frequency while that of the probe is constant. In a real experimental scheme it would be more likely that the coupling field remained in the visible region of the spectrum while a higher frequency was sought on the probe transition. Although we have not addressed this case specifically the results presented in this chapter are applicable to it. The level of transparency achievable in a system is the same for a given ratio of both wavelength mismatch and driving Rabi frequency to Doppler width. One further caveat is that the transition decay rates will also affect the level of observed transparency.

For the Vee scheme, we have seen that in the $\lambda_c > \lambda_p$ regime significant transparency is predicted for a driving Rabi frequency that is half the Doppler width. In this system, the ratio of coupling and probe wavelengths is 2:1. We can therefore expect that a 200nm coupling transition driving a 100nm probe transition will induce the same level of

transparency if the coupling field Rabi frequency is adjusted to be half the new Doppler-width and the transition decay rates remain unchanged.

In conclusion, we have shown that significant transparency is possible in a mismatched ($\lambda_c > \lambda_p$) Vee scheme with a wavelength ratio of 2:1 for a sub-Doppler width driving Rabi frequency, subject to the value of the transition decay rates. In the next chapter we will investigate such a system experimentally. Note that the dependence of atomic interference effects on relaxation rates will be considered in Chapter 7.

4.5.1 Further Theoretical Considerations

The main results of the presented analysis have been discussed. We now consider some further points of interest that arise from the theoretical model. Firstly, in Figs. 4.25, 4.26, and 4.27 we see that as the coupling wavelength increases so does the range over which absorption may be observed in all three schemes. This increase in bandwidth occurs because the two-photon process persists for higher velocity atoms due to the reduction in the magnitude of the Doppler shift for a given atomic velocity. There is a corresponding reduction in the peak predicted absorption because the total number of absorbing atoms remains constant. The total integrated absorption is always the same regardless of the choice of probe and coupling wavelengths. Figure 4.33 shows the height of one set of Autler-Townes components plotted as a function of atomic velocity for the three wavelength regimes in the Cascade system. While the maximum height changes so does the range over which absorption occurs so that the total absorption remains unaltered.

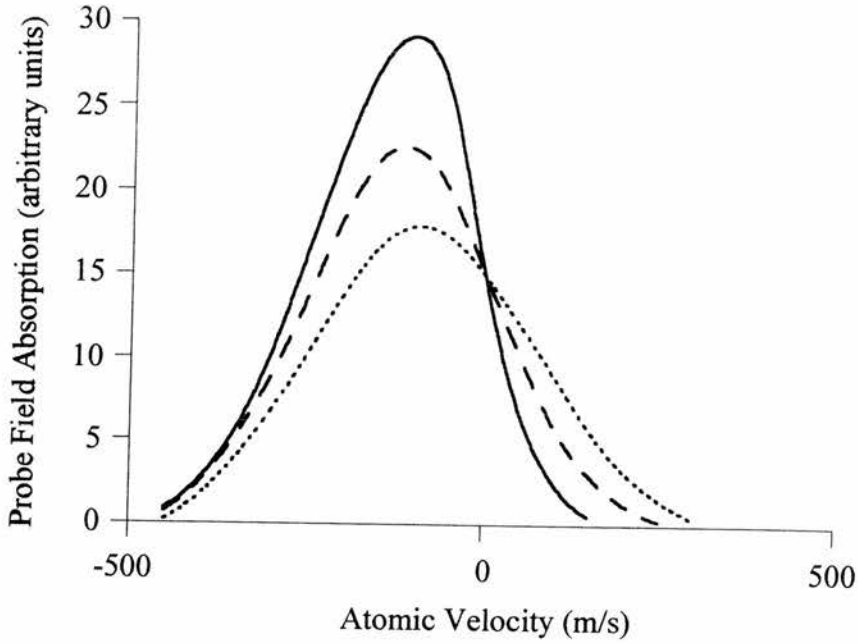


Figure 4.33: *The height of individual Autler-Townes components as a function of atomic velocity in the Cascade scheme for $\lambda_c < \lambda_p$ (solid line), $\lambda_c = \lambda_p$ (dashed line), and $\lambda_c > \lambda_p$ (dotted line).*

Secondly, if we compare the magnitudes of the Autler-Townes components of the Cascade and Lambda schemes we notice that while the absorption profiles for a particular wavelength regime may be identical, the Autler-Townes absorptions are of a lower magnitude in the Lambda scheme. This apparent discrepancy is due to linewidth effects. Referring back to Fig. 4.1 we see that for the Lambda scheme both the decay rates, Γ_{31} and Γ_{32} , describe population movement out of the upper level of the probe transition. The total decay from this level in the Lambda scheme, which determines the linewidth, is therefore twice the value for the Cascade and Vee-type systems. Consequently, the absorption profile of each individual Autler-Townes component is spread out in wavelength and reduced in peak magnitude, with no change in the total absorption. For example, when we integrate over all atomic velocities we get the same ‘net’ absorption profile in the Cascade and Lambda schemes for the matched wavelength case, even though the peak absorptions are lower in the latter case.

So far, we have failed to account for the effect of coupling field saturation. The cynic may claim that the difference in the three energy level schemes is a result of this dissipative effect rather than EIT. It is true to say that coupling field saturation plays its part in reducing the absorption as it does in any system based on a Vee scheme, but it is not the presence of this effect which allows us to observe transparency in the second mismatched regime ($\lambda_c > \lambda_p$), rather the absence of it.

Coupling field saturation occurs in a Vee scheme because the coupling field is connected to the ground state and therefore excites a fraction of the population from that state into the upper level of the coupling field transition. The exact proportion of the population excited in this way will depend upon the strength of the coupling field. There is of course an upper limit that occurs when the coupling field transition is saturated and the populations in the upper and lower levels are equalised. In a Doppler-broadened system this process is velocity selective. While the velocity group of atoms for which the coupling field is on-resonance will quickly become saturated, other velocity groups for which the coupling field is detuned will not. In the latter case, the effects of coupling field saturation are minimal.

Coupling field saturation is inextricably linked to EIT since the latter relies on the interference of single and two-photon absorption, and the magnitude of the two-photon absorption is dependent on the population in the upper level of the coupling transition. If we consider Figs. 4.25, 4.26, and 4.27 we see that the lack of a reduction in absorption in the Cascade and Lambda schemes is not due to a lack of induced transparency for the zero velocity group at line centre. In fact, EIT still takes place for atoms at rest, but it is masked by the secondary Autler-Townes absorptions of the higher velocity groups. In the Vee scheme, we still observe the transparency that is induced at line centre in the normal way, because the secondary Autler-Townes components that overlap with line centre are very small in magnitude. As discussed earlier, these Autler-Townes components are reduced in magnitude because the two-photon process is greatly diminished when the coupling field is detuned from resonance, i.e. when the coupling field saturation effect is negligible. It is therefore the lack of coupling field saturation for high velocity atoms that allows us to observe transparency in the Vee-type scheme for probe frequencies higher than the coupling field frequency. It is of course the case that absorption at line centre is

halved by the coupling field saturation of the zero velocity group atoms, but EIT effects reduce absorption well beyond this limit.

4.6 The Role of Coherence

Theoretical modelling was carried out to investigate the role of coherence in the mismatched ($\lambda_c > \lambda_p$) Vee scheme. Previous work concerned with the wavelength dependence of electromagnetically induced transparency raised the issue that the nature of the observed transparency window was dictated by the interplay of EIT and Autler-Townes splitting [18]. It was postulated that the overlap of Autler-Townes components from different velocity groups controlled the width of the transparency while the depth of the window was set by the level of EIT. This rule applies for the limiting case in which the Autler-Townes components of the non-zero velocity groups do not occur within one homogeneous linewidth of the zero velocity resonance point (i.e. for systems in which $\lambda_c \leq \lambda_p$). If the Autler-Townes absorption components of the non-zero velocity groups *do* overlap with the transparency window created at line centre, the Autler-Townes components will also affect the depth of the transparency window (this occurs for $\lambda_c > \lambda_p$).

In either case, it is important to establish the extent to which the reduction in absorption is due to the quantum coherence effect of EIT, rather than straightforward Autler-Townes splitting. This relationship is of particular interest in the regime for which the common level is Autler-Townes split beyond the Doppler-width. The theory presented in this section explores the role of coherence over a range of coupling field Rabi frequencies for a Vee-type energy level configuration. We choose to base the theoretical model on a real atomic scheme in rubidium vapour. The probe transition is $5S_{1/2} - 6P_{1/2}$ at approximately 422nm and the coupling transition is $5S_{1/2} - 5P_{3/2}$ at approximately 780nm. We assume a closed three level system in which the hyperfine structure of the $5S_{1/2}$ ground state is ignored. The decay rates are $40 \times 10^6 \text{ s}^{-1}$ (Γ_{32}) and $9 \times 10^6 \text{ s}^{-1}$ (Γ_{31}). Appendix C contains the energy level diagram and the density matrix rate equations that describe this system.

Electromagnetically induced transparency in the Vee scheme is driven by the coherence, ρ_{23} , on the unlinked transition, $6P_{1/2} - 5P_{3/2}$, which has both real and imaginary components. The dependence of the probe field on the ρ_{23} coherence is expressed analytically in the density matrix equation describing the imaginary part of the off-diagonal density matrix element ρ_{13}^i , Eq. (C.1e) in Appendix C. Transparency is driven by the

coherence on the unlinked transition in all three EIT schemes. Figure 4.34 shows the unlinked transition for each of the three EIT energy level configurations.

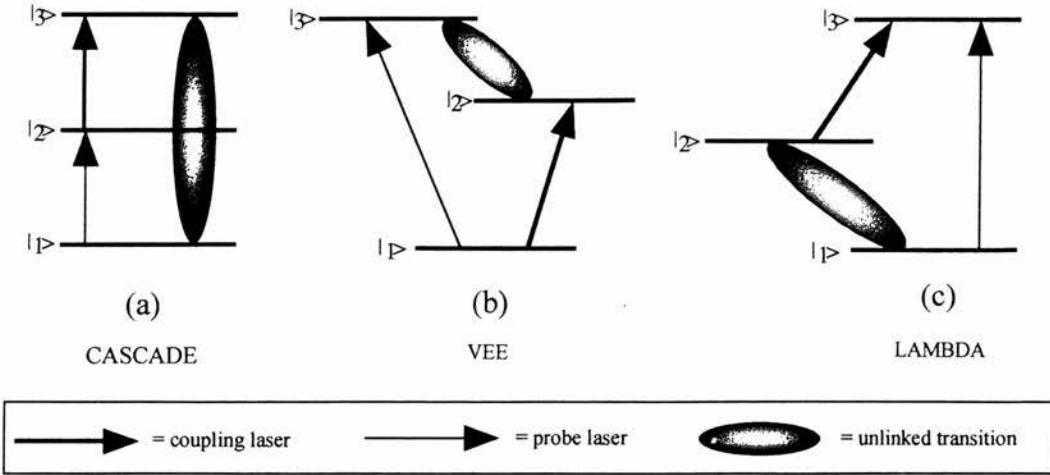


Figure 4.34: *The three schemes for EIT are depicted here with the unlinked transition clearly marked. The coherence set up on this transition drives the transparency created at the frequency of the probe field.*

An ideal coherence exists which results in the maximum possible transparency. The nature of this ‘ideal’ coherence is easiest to understand in the Cascade scheme. In this system, the ideal coherence occurs when the state amplitudes feeding into the upper level of the probe transition exactly balance to yield zero amplitude in that level. Figure 4.35 shows a Cascade scheme with the state amplitudes feeding in from levels $|1\rangle$ and $|3\rangle$ to level $|2\rangle$.

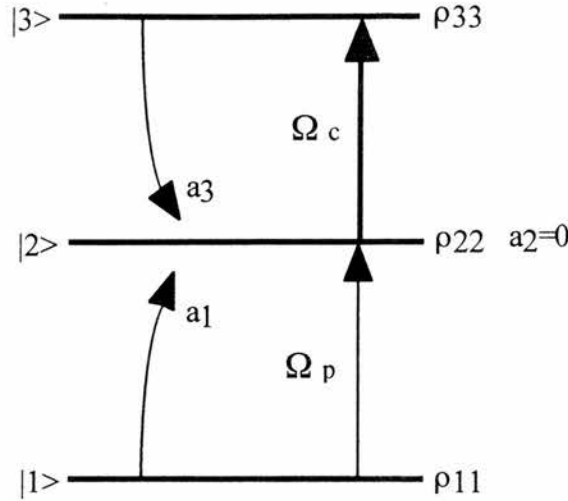


Figure 4.35: *The ideal coherence in a Cascade scheme occurs when the ratio of the state amplitudes feeding into the upper level of the probe transition is equal to the inverse of the ratio of the field Rabi frequencies Eq. (4.14). When this occurs the state amplitude of level |2> will be zero.*

This description of EIT leads to the definition of an ideal coherence. We start by taking the EIT conditions derived in Section 1.3.3 using the state amplitude model, Eqs. (1.7) and (1.6):

$$|a_3| \Omega_c = |a_1| \Omega_p \tag{4.13a}$$

$$|a_2| = 0 \tag{4.13b}$$

Rearranging Eq. (4.13a) we write the state amplitude of level |3> in terms of that of level |1> and the ratio of the Rabi frequencies:

$$|a_3| = |a_1| \frac{\Omega_p}{\Omega_c} \tag{4.14}$$

By definition, the off-diagonal density matrix element is given by the following ensemble average of the state amplitudes:

$$\bar{\rho}_{13} = \overline{a_1 a_3^*} \tag{4.15}$$

This equation can be expanded in the following manner:

$$\begin{aligned}\bar{\rho}_{13} &= (|a_1| \exp^{i\phi_1}) (|a_3| \exp^{-i\phi_3}) \\ &= |a_1| |a_3| \exp^{i(\phi_1 - \phi_3)}\end{aligned}\quad (4.16)$$

Substituting Eq. (4.14) for the state amplitude of level $|3\rangle$ and taking the phase difference for EIT, $\phi_1 - \phi_3$, to be equal to π , we have:

$$\bar{\rho}_{13} = |a_1| |a_3| \frac{\Omega_p}{\Omega_c} \exp^{i\pi} \quad (4.17)$$

Then using Eq. (4.15), for the diagonal density matrix element, we define the ideal driving coherence for EIT in a Cascade scheme:

$$[\rho_{13}]_{\text{ideal}} = -\rho_{11} \frac{\Omega_p}{\Omega_c} \quad (4.18)$$

The principal difference in a Vee scheme is that the two atomic levels of the unlinked transition have a relative phase of 2π instead of π . The ideal coherence in a Vee scheme is therefore defined as:

$$[\rho_{23}]_{\text{ideal}} = \rho_{11} \frac{\Omega_p}{\Omega_c} \quad (4.19)$$

We may also derive an analytical expression directly from the density matrix equations. To emulate an ‘ideal’ coherence the dephasing and decay terms are set to zero. Thus, from Eq. (C.1e) in Appendix C we have:

$$\dot{\tilde{\rho}}_{13} = i\Omega_p (\rho_{33} - \rho_{11}) + i\Omega_c \tilde{\rho}_{23} \quad (4.20)$$

Invoking steady state conditions we set the left hand side of this equation to zero and then rearrange to solve for ρ_{23} . Assuming, with a weak probe field, that the population in level $|3\rangle$ (ρ_{33}) is zero, we arrive at an ideal coherence given by:

$$[\rho_{23}]_{\text{ideal}} = \rho_{11} \frac{\Omega_p}{\Omega_c} \quad (4.21)$$

Equations (4.19) and (4.21) are identical. Having thus obtained an expression for the ideal coherence it is necessary to define a normalised coherence. The level of induced transparency is not proportional to the magnitude of the coherence, and we find there is a specific, ideal coherence for which maximum transparency is produced. Any departure from this ideal value, whether it is an increase or decrease in the driving coherence, will

cause a reduction in the observed transparency. We define the normalised coherence in the following way:

$$\frac{[\rho_{23}]}{[\rho_{23}]_{\text{ideal}}} = \text{Normalised coherence} \quad (4.22)$$

When the real part of the unlinked coherence is equal to its ideal value, the normalised coherence equals one. In order to assess the role of coherence in a Vee scheme the normalised coherence is plotted as a function of the dephasing, γ_{23} , on resonance. Figure 4.36 shows both the real part of the normalised coherence falling away from the 'ideal' value as dephasing is increased, as well as an exactly corresponding reduction in the transparency level. The imaginary part of the normalised coherence is fixed at zero while the probe field is on resonance. Consequently, it is the real part of the driving coherence that dictates the transparency level in this case. Importantly, the model shows that the driving coherence is the sole factor controlling the level of induced transparency, irrespective of the Rabi frequency on the coupling field transition. This result is substantiated by the linear relationship predicted between the real part of the normalised coherence and the induced transparency, for the range of coupling field powers shown in Fig. 4.37.

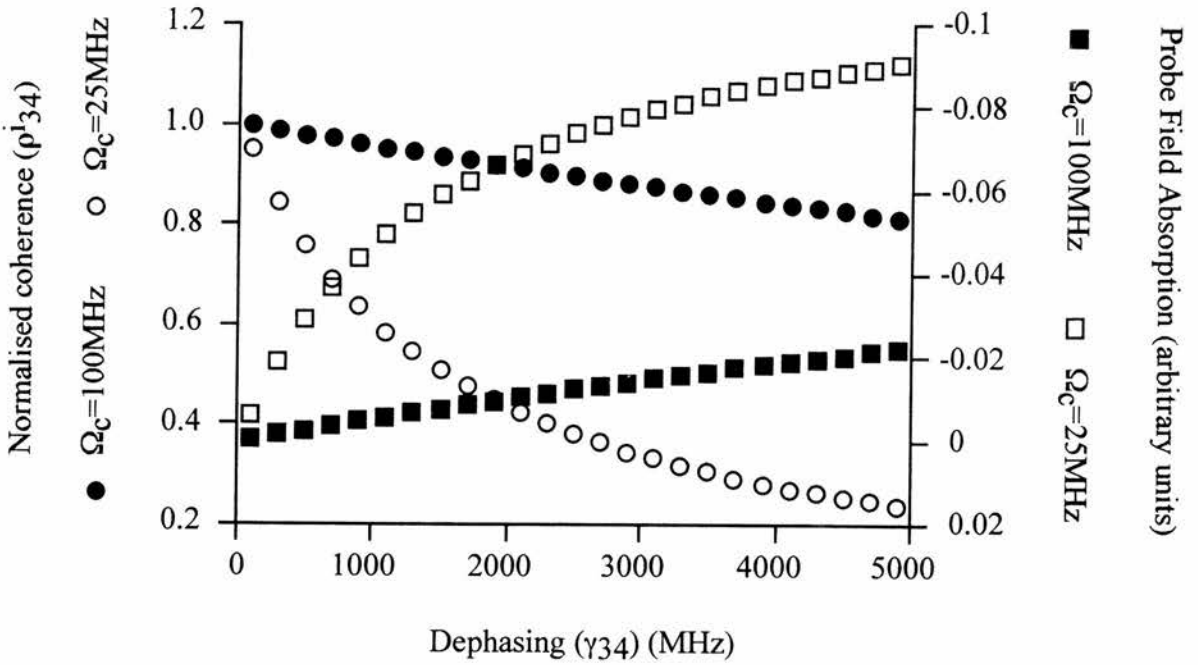


Figure 4.36: The ‘on-resonance’ absorption (ρ_{13}^i in arbitrary units) and normalised coherence plotted as a function of dephasing for high and low coupling field Rabi frequencies. The absorption is denoted by squares and the coherence by circles. These symbols are opaque for the higher Rabi frequency of 100 MHz, and they are transparent for the Rabi frequency of 25MHz.

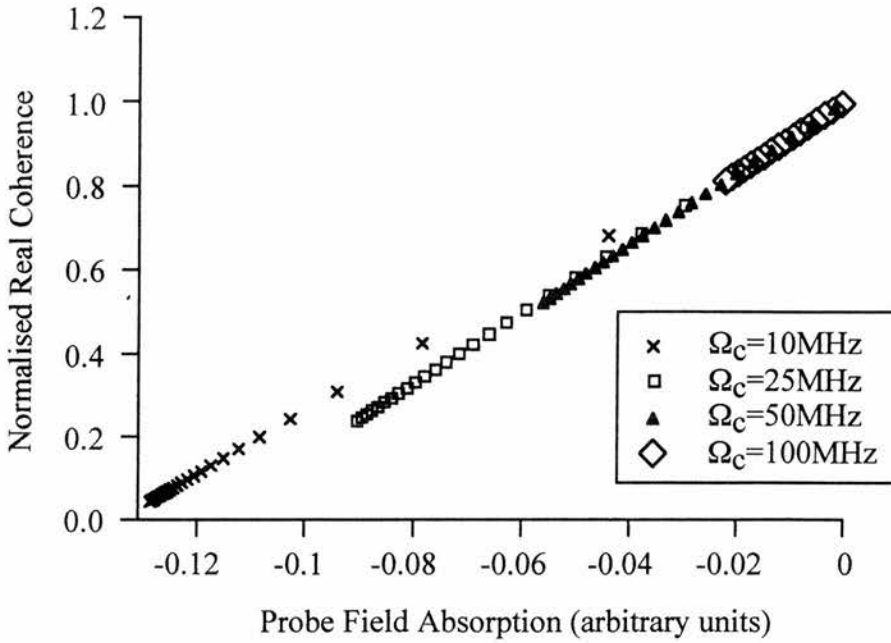


Figure 4.37: The ‘on-resonance’ absorption (ρ_{13}^i in arbitrary units) as a function of the normalised coherence on the unlinked transition for a range of coupling field Rabi frequencies.

Theoretical analysis has shown that, in general, to observe EIT in a mismatched ($\lambda_c > \lambda_p$) regime it is necessary to employ a driving field Rabi frequency that is equal to or greater than the probe Doppler width. Figure 4.36 shows that the normalised coherence stays closer to its ideal value, as dephasing is increased, for higher values of Rabi frequency. This result occurs because the overlapping Autler-Townes components are split further away from resonance, and they are consequently less of a detriment to the transparency window. Importantly, the presented analysis indicates that the driving coherence is still the principal determining factor for the level of transparency regardless of the magnitude of the associated Autler-Townes splitting.

In Chapter 5 we will consider the experimental verification of such a transparency in a mismatched Vee scheme. In addition we will explore the regime for which EIT is predicted in the Vee scheme for driving Rabi frequencies less than the Doppler width.

4.7 Conclusion

The result that EIT is strongest for the mismatched $\lambda_c < \lambda_p$ wavelength regime in a Cascade scheme [18] has been extended to all three energy level configurations. We have also demonstrated the robust nature of the Vee-type system that results from the unique form of the two-photon process. While the induced transparency is more pronounced when the coupling field frequency is higher than that of the probe, it is still realisable for high frequency probe systems if the employed coupling field Rabi frequency exceeds the Doppler width in all schemes. Furthermore, theory predicts that in a Vee-type system transparency may be induced in a probe field of higher frequency than the coupling field for driving Rabi frequencies lower than the Doppler width. Indeed, the transparency induced in the mismatched Vee scheme ($\lambda_c > \lambda_p$) compares favourably with that induced in the matched Cascade and Lambda systems. These conclusions imply that quantum coherence effects are not confined to matched wavelength systems in Doppler-broadened media, and that the Vee scheme provides the best potential level of transparency in a system subject to Doppler effects, particularly for configurations in which the probe frequency is in excess of the coupling field frequency. These results may also have wider implications for other inhomogeneously broadened media such as quantum wells.

It has been theoretically predicted here, and elsewhere [15] that mismatched EIT is possible in a Doppler-broadened medium if we Autler-Townes split beyond the probe Doppler width with a strong driving field. The analysis of Section 4.6 indicates that coherence still underpins the reduction in absorption in the regime for which the coupling field Rabi frequency exceeds the Doppler width. Furthermore, the theoretical results presented in this chapter identify a clear advantage in the Vee scheme for which transparency is predicted for sub-Doppler width driving Rabi frequencies. The following chapter presents the results of the first cw mismatched ($\lambda_c > \lambda_p$) EIT experiment in a Doppler-broadened system. This experiment employs a Vee-type configuration in rubidium vapour and tests the theoretical predictions reported thus far.

References

- [1] J. Gao *et al*, Opt. Comm. **93**, 323-327, (1992).
- [2] A. Nottleman, C. Peters, and W. Lange, Phys. Rev. Lett. **70**, 12, 1783, (1993).
- [3] W. E. van der Veer *et al*, Phys. Rev. Lett. **70**, 21, 3243, (1993).
- [4] E. S. Fry *et al*, Phys. Rev. Lett. **70**, 21, 3235, (1993).
- [5] J. A. Kleinfeld, and A. D. Streater, Phys. Rev. A. **49**, 6, R4301, (1994).
- [6] A. S. Zibrov *et al*, Laser Phys. **5**, 3, 553-555, (1995).
- [7] Y. Zhu, and J. Lin, Phys. Rev. A. **53**, 3, 1767, (1996).
- [8] C. Fort *et al*, Opt. Comm. **139**, 31-34, (1997).
- [9] A. V. Durrant *et al*, Opt. Comm. **151**, 136-146, (1998).
- [10] A. S. Zibrov *et al*, Phys. Rev. Lett. **75**, 1499, (1995).
- [11] C. Peters, and W. Lange, App. Phys. B. **62**, 221-225, (1996).
- [12] G. G. Padmabandu *et al*, Phys. Rev. Lett. **76**, 12, 2053, (1996).
- [13] P. B. Sellin *et al*, Phys. Rev. A. **54**, 3, 2402, (1996).
- [14] F. B. de Jong *et al*, Phys. Rev. A. **57**, 6, 4869, (1998).
- [15] M. D. Lukin *et al*, Laser Phys. **6**, 436-447, (1996).

- [16] B. Lu, W. H. Burkett, and M. Xiao, *Opt. Comm.* **141**, 269-272, (1997).
- [17] G. Vemuri, and G. S. Argarwal, *Phys. Rev. A.* **53**, 1060, (1996).
- [18] S. Shepherd, D. J. Fulton, and M. H. Dunn, *Phys. Rev. A.* **54**, 5394, (1996).
- [19] D. J. Fulton, S. Shepherd, R. R. Moseley, B. D. Sinclair, and M. H. Dunn, *Phys. Rev. A.* **52**, 2302, (1995).
- [20] J. Vanier, *Basic theory of Lasers and Masers*, (Gordon and Breach, London, (1971)).
- [21] S. H. Autler, and C. H. Townes, *Phys. Rev.* **100**, 703, (1955).
- [22] D-Z. Wang, and J-Y. Gao, *Phys. Rev. A.* **52**, 4, 3201, (1995).
- [23] R. Moseley, and M. H. Dunn, *Phys. World.* January, (1995).

CHAPTER 5

Experimental Observation of Electromagnetically Induced Transparency on a Blue Probe in a Doppler- broadened Mismatched Vee-type System

“A fool... is a man who never tried an experiment in his
life.”

Erasmus Darwin
(Charles Darwin's grandfather)



5.1 Introduction

The experimental work presented in this chapter provides practical evidence to support the prediction that EIT is realisable in mismatched schemes even in the presence of Doppler-broadening. Furthermore, a Vee-type system was chosen in which the mismatch of wavelengths was such that the probe frequency was approximately twice that of the coupling field. The interaction of Autler-Townes splitting and EIT in a Vee scheme acts to create a viable method for inversionless lasing in mismatched Doppler-broadened systems. We have seen that Doppler-broadening can be counter-acted by matching the wavelengths of the probe and coupling beams while selecting the appropriate geometry so that the Doppler shifts in each case exactly cancel. This method has been widely employed in the study of EIT [1-4] and in the realisation of the first cw inversionless laser [5]. However, for inversionless systems to be practically useful they must utilise mismatched wavelengths. Having accepted this point, we must decide on the type of medium in which these systems are to be created. Initial work in quantum coherence concentrated on gaseous media that are inherently subject to Doppler effects. Continuous wave research has since moved away from Doppler-broadening in the quest for mismatched systems because it is generally thought that EIT cannot be resolved in a Doppler-broadened absorption profile unless very high powers are employed (powers beyond the capabilities of cw laser sources) [6]. Work has taken place in other media, like atomic beams [7,8] and magneto-optic traps [9-11], which provide a virtually Doppler-free environment. The experiment presented in this chapter reflects the alternative approach of exploring the absolute limits of EIT within gaseous Doppler-broadened systems. The results show that the limitations imposed by Doppler-broadening are not as restrictive as previously supposed.

Initial work on the wavelength dependence of EIT demonstrated that it was possible to resolve quantum coherence effects in a Doppler-broadened Cascade scheme for which the coupling frequency was higher than the probe frequency. Moreover, the strength of EIT would be greater in this mismatched regime than for matched wavelengths. In the previous chapter, this work was extended to all three EIT systems. We saw that while it is possible to observe EIT when the probe frequency is higher than the coupling frequency by employing a coupling field Rabi frequency comparable to or greater than the

probe Doppler width in all schemes, a distinct advantage can be gained by using a Vee-type configuration. Figure 5.1 shows the on-resonance transparency predicted in a Vee scheme for a range of coupling field wavelengths, where the probe wavelength is approximately 422nm.

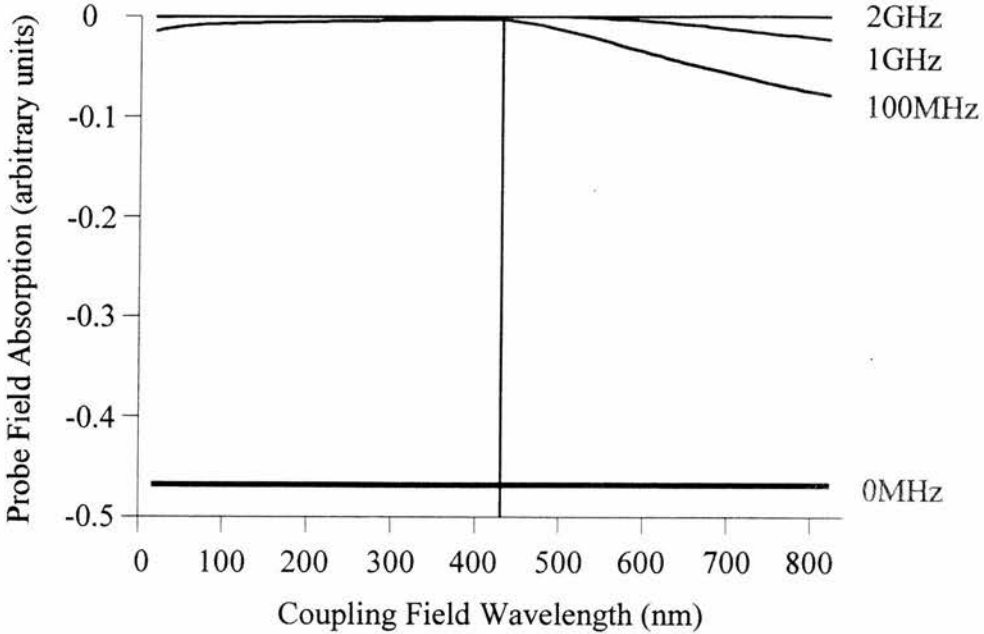


Figure 5.1: The ‘on-resonance’ probe field absorption (ρ_{13}^i in arbitrary units) as a function of coupling field wavelength in a Vee scheme. The probe wavelength is kept constant at approximately 422nm. The absorption is calculated for coupling field Rabi frequencies of 2GHz, 1GHz and 100MHz, as well as in the absence of the coupling field. The solid vertical line represents the case of matched wavelengths.

In this chapter we experimentally test two hypotheses:

- (I) That cw EIT can be realised in the regime for which the probe frequency exceeds that of the coupling field when the driving Rabi frequency is comparable to, or greater than the Doppler width on the probe transition.
- (II) That in a Vee scheme, transparency may even be observed in this wavelength regime for Rabi frequencies less than the probe Doppler width.

Note that in the experimental system we anticipate several problems that have not been considered in the context of the pure model adopted in Chapter 4. These factors may obscure EIT:

- (a) Optical pumping
- (b) Collisional dephasing
- (c) The variation of Rabi frequency throughout the cell
- (d) Coupling field absorption.

The roles of these effects will be quantified in light of the experimental results. Before considering these results we develop the theoretical model of Chapter 4 to incorporate optical pumping, mixing of the hyperfine states, and collisional dephasing of the atomic coherences. The origins of optical pumping will then be discussed along with possible methods of obviating this problem. Finally, the experimental results will be presented and conclusions will be drawn in relation to the hypotheses stated above. The reader might find it useful to refer to the schematic map in Fig. 5.2 which describes the logical structure of this chapter.

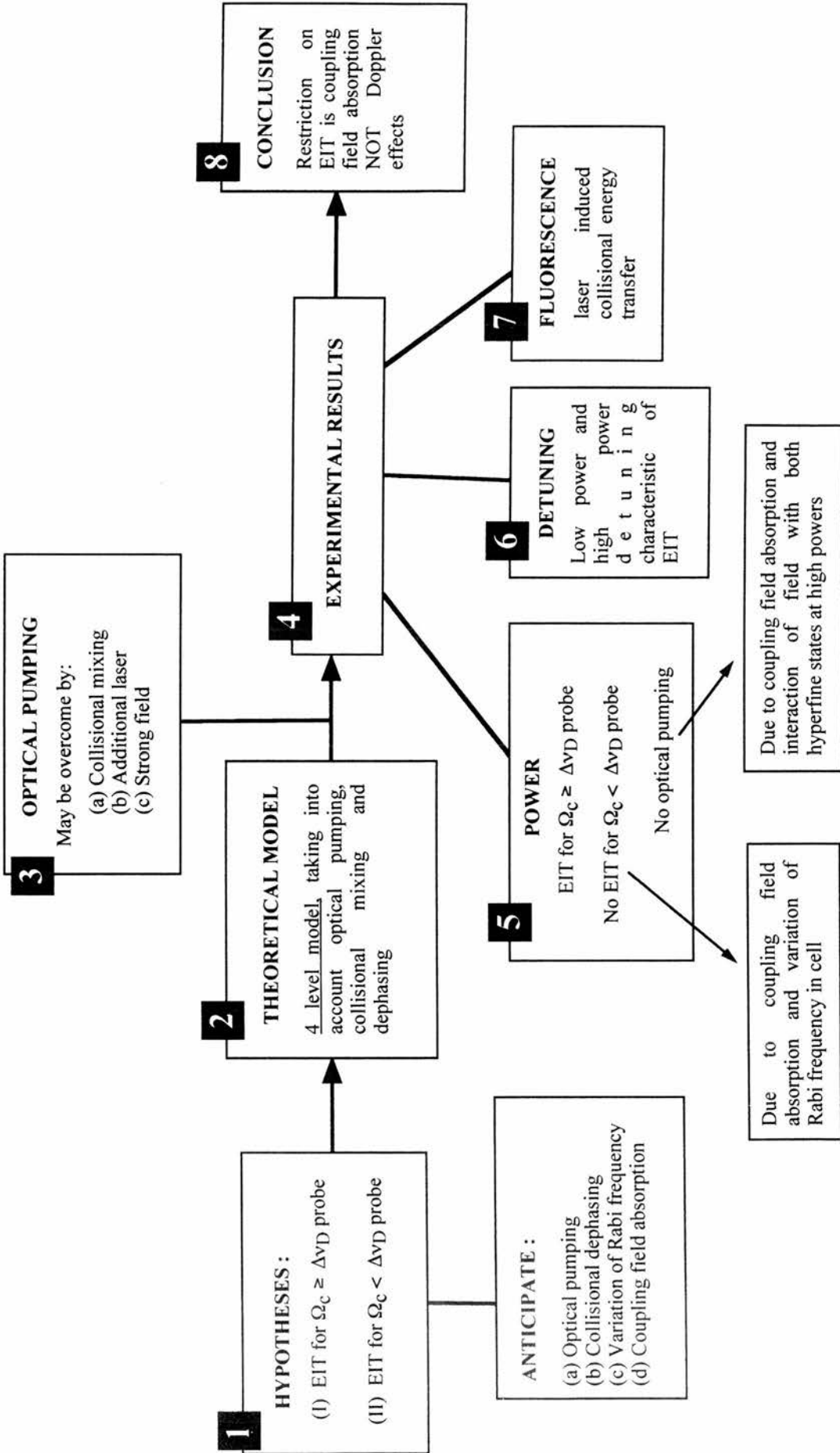


Figure 5.2: A schematic map depicting the work presented in this chapter.

5.2 Theoretical Analysis

We now extend our analysis of a three level Vee scheme to model the experimental system. The relevant energy level structure of atomic rubidium is shown in Fig. 5.3. A fourth level is included so that we can theoretically model the effects of optical pumping by calculating the relative populations in the hyperfine split ground state sub-levels. The parameter Π_T represents the collisional mixing of these hyperfine ground states, and may be varied in the model. In addition, the dephasing terms that describe the relaxation of atomic coherences include a contribution based on the collisional mixing parameter. We are thus able to include both the effects of optical pumping and collisional dephasing in our theoretical analysis.

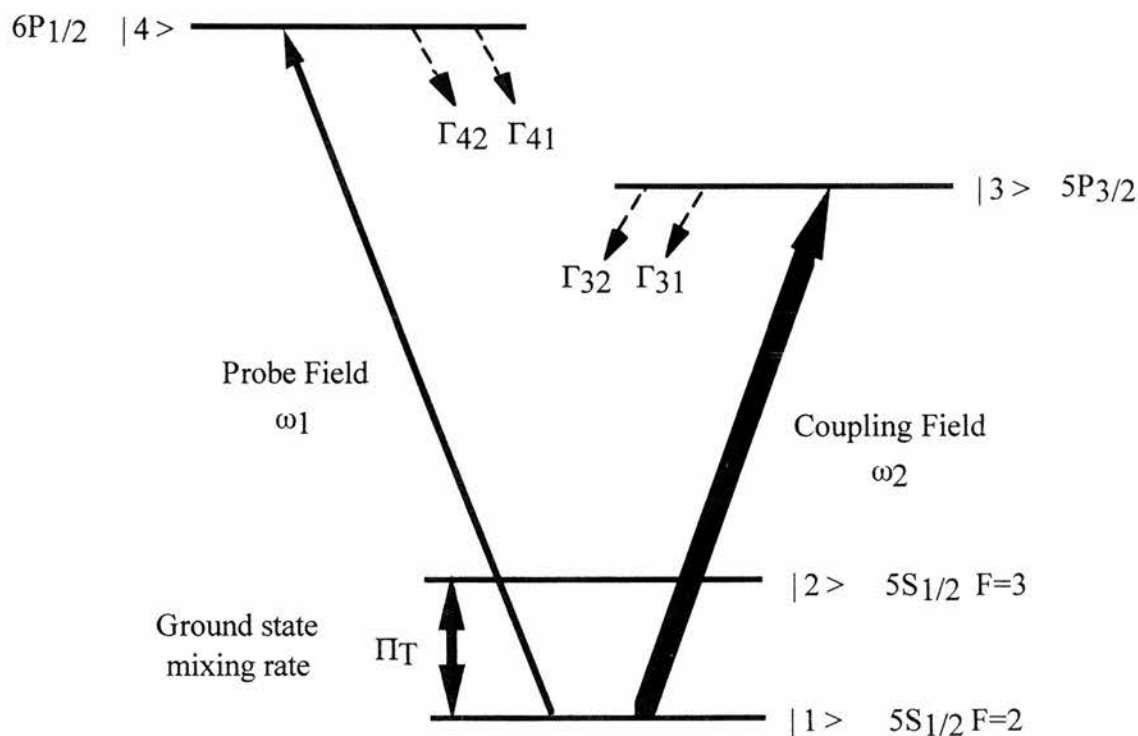


Figure 5.3: Energy level picture of the Vee scheme employed in rubidium vapour, including hyperfine splitting of the $5S_{1/2}$ ground state. The probe is applied to the $5S_{1/2} - 6P_{1/2}$ transition, and the coupling field is applied to the $5S_{1/2} - 5P_{3/2}$ transition. ω_2 and ω_1 are the coupling and probe frequencies respectively, and Π_T is the ground state collisional mixing rate.

Theoretical modelling was carried out utilising the standard density matrix analysis for a three level Vee scheme, as described in Section 2.5 [2], with appropriate modifications to take into account the hyperfine splitting of the ground state. The equations for the slowly varying density matrix components, in a closed system, are [12,13]:

$$\dot{\rho}_{11} = i\Omega_c(\tilde{\rho}_{31} - \tilde{\rho}_{13}) + i\Omega_p(\tilde{\rho}_{41} - \tilde{\rho}_{14}) + \Gamma_{41}\rho_{44} + \Gamma_{31}\rho_{33} + \frac{5}{12}\Pi_T\rho_{22} - \frac{7}{12}\Pi_T\rho_{11} \quad (5.1a)$$

$$\dot{\rho}_{22} = \Gamma_{42}\rho_{44} + \Gamma_{32}\rho_{33} + \frac{7}{12}\Pi_T\rho_{11} - \frac{5}{12}\Pi_T\rho_{22} \quad (5.1b)$$

$$\dot{\rho}_{33} = i\Omega_c(\tilde{\rho}_{13} - \tilde{\rho}_{31}) - \Gamma_{31}\rho_{33} - \Gamma_{32}\rho_{33} \quad (5.1c)$$

$$\dot{\rho}_{44} = i\Omega_p(\tilde{\rho}_{14} - \tilde{\rho}_{41}) - \Gamma_{41}\rho_{44} - \Gamma_{42}\rho_{44} \quad (5.1d)$$

$$\dot{\rho}_{12} = i(\Delta_{12} + i\gamma_{12})\rho_{12} + i\Omega_c\rho_{32} + i\Omega_p\rho_{42} \quad (5.1e)$$

$$\dot{\tilde{\rho}}_{13} = -i(\Delta_{13} - i\gamma_{13})\tilde{\rho}_{13} + i\Omega_c(\rho_{33} - \rho_{11}) + i\Omega_p\tilde{\rho}_{43} \quad (5.1f)$$

$$\dot{\tilde{\rho}}_{14} = -i(\Delta_{14} - i\gamma_{14})\tilde{\rho}_{14} + i\Omega_p(\rho_{44} - \rho_{11}) + i\Omega_c\tilde{\rho}_{34} \quad (5.1g)$$

$$\dot{\rho}_{23} = -i(\Delta_{13} + \Delta_{12} - i\gamma_{23})\rho_{23} - i\Omega_c\rho_{21} \quad (5.1h)$$

$$\dot{\rho}_{24} = -i(\Delta_{14} + \Delta_{12} - i\gamma_{24})\rho_{24} - i\Omega_p\rho_{21} \quad (5.1i)$$

$$\dot{\tilde{\rho}}_{34} = -i(\Delta_{14} + \Delta_{13} - i\gamma_{34})\tilde{\rho}_{34} + i\Omega_c\tilde{\rho}_{14} - i\Omega_p\tilde{\rho}_{31} \quad (5.1j)$$

where subscripts refer to the four levels numbered from the lowest to the highest energy state. In this model it is assumed that the coherent fields only interact with the transitions connected to level $|1\rangle$; therefore, all the off-diagonal coherences linked with level $|2\rangle$ are zero, which is consistent with the above equations. The mixing term, Π_T , is included to allow for thermalisation of the hyperfine split ground state (mixing of the atomic populations in levels $|1\rangle$ and $|2\rangle$). The detunings are defined as:

$$\Delta_{14} = \omega_1 - \omega_{14} - k_1 V_Z \quad (5.2a)$$

$$\Delta_{13} = \omega_2 - \omega_{13} - k_2 V_Z \quad (5.2b)$$

$$\Delta_{12} = -3\text{GHz}(\times 2\pi) \quad (5.2c)$$

where ω_1 and ω_2 denote the angular frequencies of the applied optical fields; V_Z is the atomic velocity along the cell length; k_1 and k_2 are the wavevectors of the applied optical fields, defined by $k_i = 2n\pi/\lambda_i$; and ω_{14} and ω_{13} relate to the frequency separations of the appropriate levels. The Rabi frequencies are defined, in angular terms, as:

$$\Omega_p = \frac{\mu_{14}E_1}{2\hbar} \quad (5.3a)$$

$$\Omega_c = \frac{\mu_{13}E_2}{2\hbar} \quad (5.3b)$$

where E_1 and E_2 are the electric-field strengths of the applied probe and coupling fields respectively, and μ_{14} and μ_{13} are the dipole matrix elements for the transitions. The population decay rates (Γ_{ij}) were set to $\Gamma_{41}=4\times 10^6\text{s}^{-1}$, $\Gamma_{42}=4\times 10^6\text{s}^{-1}$, $\Gamma_{31}=20\times 10^6\text{s}^{-1}$, and $\Gamma_{32}=20\times 10^6\text{s}^{-1}$; and the coherence decay rates (γ_{ij}) according to:

$$\gamma_{12} = \frac{\Pi_T}{2} \quad (5.4a)$$

$$\gamma_{13} = \frac{\Gamma_{32}}{2} + \frac{\Gamma_{31}}{2} + \left(\frac{7}{12} \times \frac{\Pi_T}{2}\right) \quad (5.4b)$$

$$\gamma_{14} = \frac{\Gamma_{41}}{2} + \frac{\Gamma_{42}}{2} + \left(\frac{7}{12} \times \frac{\Pi_T}{2}\right) \quad (5.4c)$$

$$\gamma_{34} = \frac{\Gamma_{41}}{2} + \frac{\Gamma_{42}}{2} + \frac{\Gamma_{31}}{2} + \frac{\Gamma_{32}}{2} \quad (5.4d)$$

$$\gamma_{23} = \frac{\Gamma_{32}}{2} + \frac{\Gamma_{31}}{2} + \left(\frac{5}{12} \times \frac{\Pi_T}{2}\right) \quad (5.4e)$$

$$\gamma_{24} = \frac{\Gamma_{41}}{2} + \frac{\Gamma_{42}}{2} + \left(\frac{5}{12} \times \frac{\Pi_T}{2}\right) \quad (5.4f)$$

Since collisional mixing is taken to occur for atoms in the ground state, we must also assume that all atoms are subject to the appropriate dephasing rate due to collisions, whether or not population transfer occurs. The term Π_T is therefore included in Eqs. (5.4a)-(5.4f).

The density matrix equations are solved by invoking steady-state conditions (appropriate due to the employment of single-frequency cw lasers), i.e. setting all time derivatives equal to zero. Equations (5.1a)-(5.1j) can then be split into sixteen real simultaneous equations, using properties of the density matrix, and solved by using normal linear algebra routines as described in Chapter 2. The solutions yield values for the real and imaginary parts of the coherence on each transition that can be related to the refractive index and the absorption or gain respectively, as well as the proportion of the atomic population in each of the energy levels. Doppler-broadening is taken into account by

integrating over the velocity distribution, thus providing a comprehensive modelling of the system.

5.3 Optical Pumping

The well known effect of optical pumping [14] is undesirable in the context of observing EIT. Optical pumping acts to reduce the absorption by dissipative movement of the atomic population from the lower level of the probe transition. It therefore obscures any coherent effect that may take place. Fortunately, the dissipative nature of this effect makes it easy to distinguish from EIT. The fundamental difference between these phenomena is that optical pumping moves the population out of the lower level, reducing absorption by virtue of the fact that there are less relaxed atoms to absorb the probe. EIT, on the other hand, traps the population in the lower level so that the balance of atomic coherence acts to destroy the process of absorption. In optical pumping the population removed from the ground state is driven into another low lying state and the absorption on transitions connected to this recipient state is increased. This increase in absorption can be detected, and since there is no similar feature in EIT it is used to distinguish between the two effects.

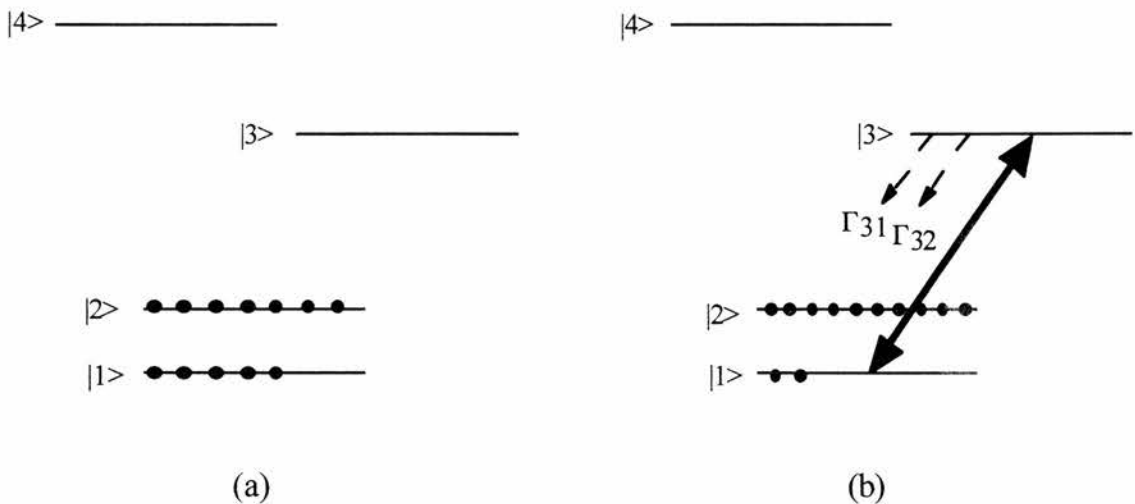


Figure 5.4: The relative hyperfine state populations are shown (a) for the thermal equilibrium case, and (b) with a strong applied field on the coupling transition. The decay rates, Γ_{31} and Γ_{32} , are equal.

Under normal conditions optical pumping effects would be expected to occur due to the strong coupling field depopulating the lower of the hyperfine ground state sub-levels, and driving a significant fraction of the population into the upper hyperfine level, as shown

schematically in Fig 5.4 (b). However, there are several possible processes that may reduce the observed optical pumping. The hyperfine levels in the rubidium ground state are close enough together for collisions to cause mixing of the population between these hyperfine sub-levels because the kinetic energy of the atoms, based on a cell temperature of 130°C, exceeds the energy separation of the states labelled $|1\rangle$ and $|2\rangle$ in Fig. 5.3. Figure 5.5 depicts the relative populations in states $|1\rangle$ and $|2\rangle$ for a coupling field Rabi frequency of 2GHz as a function of the collisional mixing rate. The theoretical model shows that a mixing rate of $200 \times 10^6 \text{ s}^{-1}$ returns the ground state populations to within 10% of their thermal equilibrium values. The dashed lines in Fig. 5.5 represent the thermal equilibrium populations.

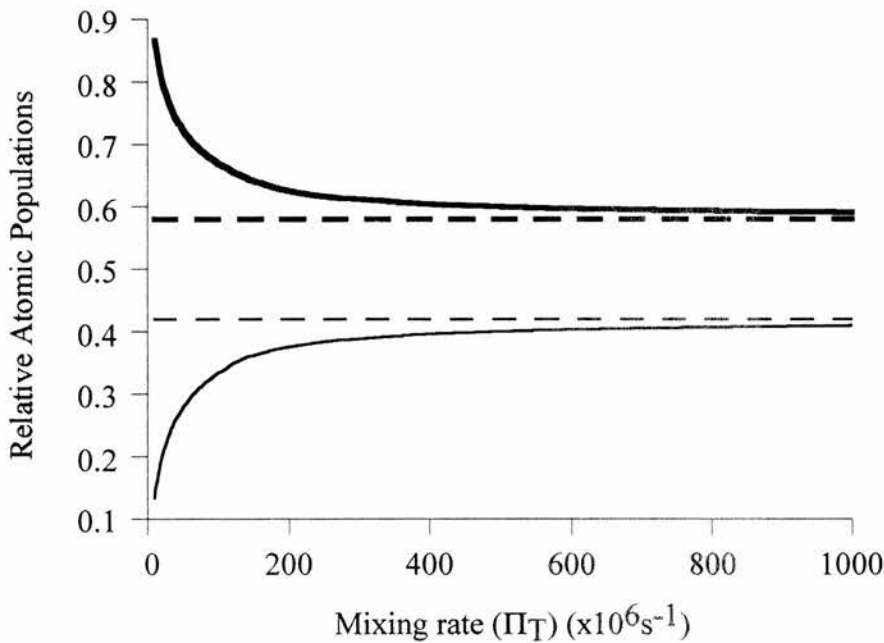


Figure 5.5: *The relative population in the hyperfine ground states, level $|1\rangle$ is represented by a faint line and level $|2\rangle$ by a bold line. The thermal equilibrium values are indicated by dashed lines.*

The ground state collisional mixing rate can be calculated using the formula, $\Pi_T = \sigma v N$, where σ is the collision cross-section, v is the average atom velocity, and N is the atomic particle density. Substitution of appropriate figures (the collision cross-section for rubidium vapour was obtained from Cohen-Tannoudji and Kastler [15]) yields the value,

$\Pi_T = 50 \times 10^3 \text{ s}^{-1}$ under present experimental conditions. This value is far lower than that required to return the hyperfine populations to their thermal equilibrium values.

Alternatively, optical pumping may be destroyed by the method employed in the Zibrov scheme [5]. An additional laser source pumps population out of the level in which it builds up due to the action of the coupling field, and the population is redistributed between the hyperfine states. Figure 5.6 depicts this method in our energy level scheme. It is necessary in this context to make the additional pump source incoherent, which is achieved by increasing the laser linewidth beyond the linewidth of the transition, as described in Section 3.5.1.

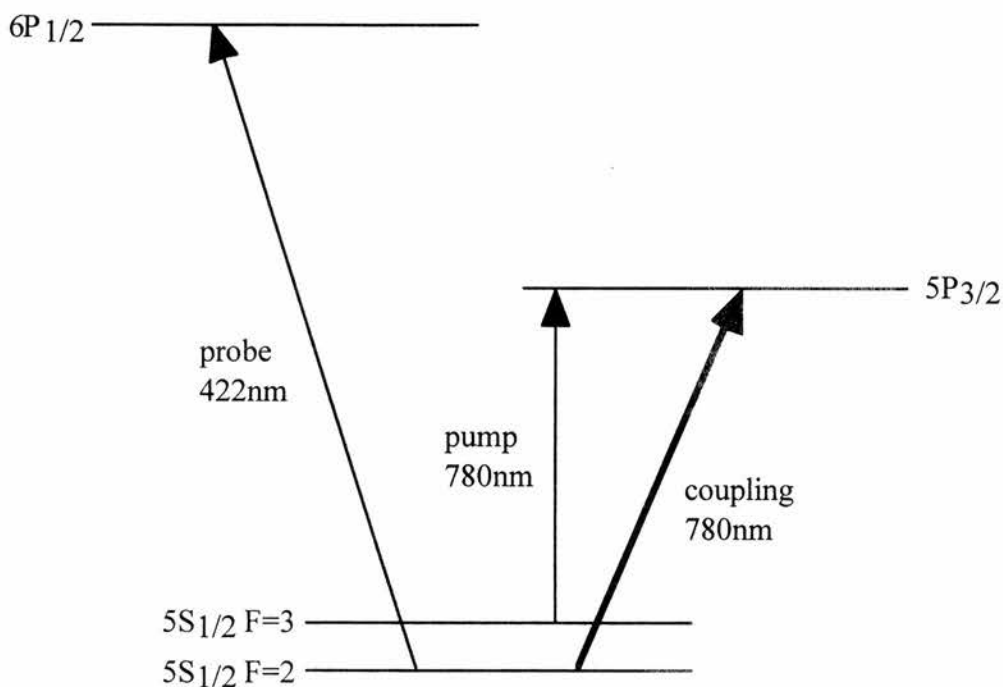


Figure 5.6: Schematic of configuration employed to overcome the effects of optical pumping. Three laser sources are employed, including a pump to redistribute the ground state hyperfine populations.

Importantly, an additional process needs to be considered in relation to optical pumping. For high coupling field Rabi frequencies we may no longer assume that the driving field interacts solely with the $5S_{1/2} (F=2) - 5P_{3/2}$ transition. Interaction may also

take place between the upper hyperfine sub-level $5S_{1/2}$ ($F=3$) and the excited $5P_{3/2}$ state. Shore derived an expression, $\Delta_n \leq 2\Omega_0$, which defines the limit within which a field of Rabi frequency Ω_0 may interact and excite population into a state n detuned by Δ_n from the resonant frequency of the field [16]. The separation of the hyperfine states in ^{85}Rb is approximately 3GHz. Therefore, for coupling field Rabi frequencies less than 1.5GHz the driving field will not interact significantly with the detuned hyperfine transition. However, for coupling field Rabi frequencies exceeding this limit strong interactions will take place on both transitions with implications for the reduction of optical pumping.

In conclusion, experimental results that are taken in the absence of an additional pump field are expected to exhibit the effects of optical pumping for coupling field Rabi frequencies below the limit prescribed by Shore [16]. Optical pumping will be manifested by a reduction in probe field absorption for the resonant hyperfine component accompanied by an increase in absorption on the transition to the other hyperfine ground state.

Note that this argument assumes the coupling field is resonant with the $F=2$ hyperfine state. Results were also taken with the coupling field resonant with the $5S_{1/2}$ ($F=3$) - $5P_{3/2}$ transition. In this case the above arguments still apply except that the population will be optically pumped in the opposite direction, i.e. into the $5S_{1/2}$ ($F=2$) state.

5.4 Experimental Results

We now consider the experimental results obtained for the Vee scheme described in Section 5.2. Initial observations of EIT were very weak, but they clearly showed all the hallmarks of a quantum coherence effect in terms of the response to coupling field powers and detuning. The low magnitude of the transparency was found to be due to poor focusing of the probe and coupling beams along the length of the cell. The results presented here have been carefully optimised to ensure that the probe beam remains within the coupling beam cross-section and that for a given coupling field power the highest possible Rabi frequency is maintained throughout the cell. The coupling and probe beam waists were approximately $110\mu\text{m}$ and $40\mu\text{m}$ respectively. The 2cm rubidium cell was at a temperature of approximately 130°C . Results are given first as a function of coupling field power and then, for a constant power, as a function of coupling field detuning; examples of which are shown in Figs. 5.7 and 5.8.

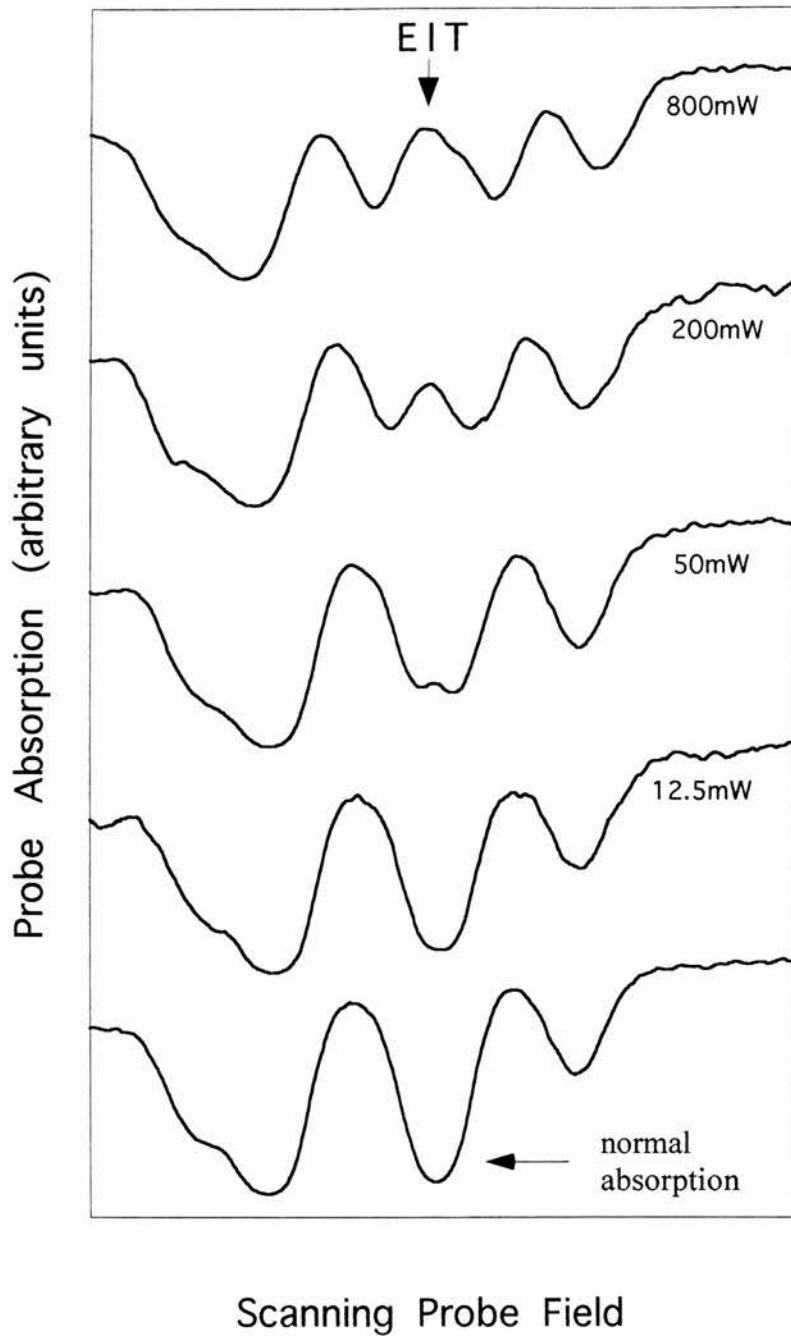


Figure 5.7: Probe absorption as a function of probe field detuning for a variety of coupling field powers. EIT is observed on peak 3 associated with the $5S_{1/2} (F=2) - 5S_{3/2}$ transition in ^{85}Rb .

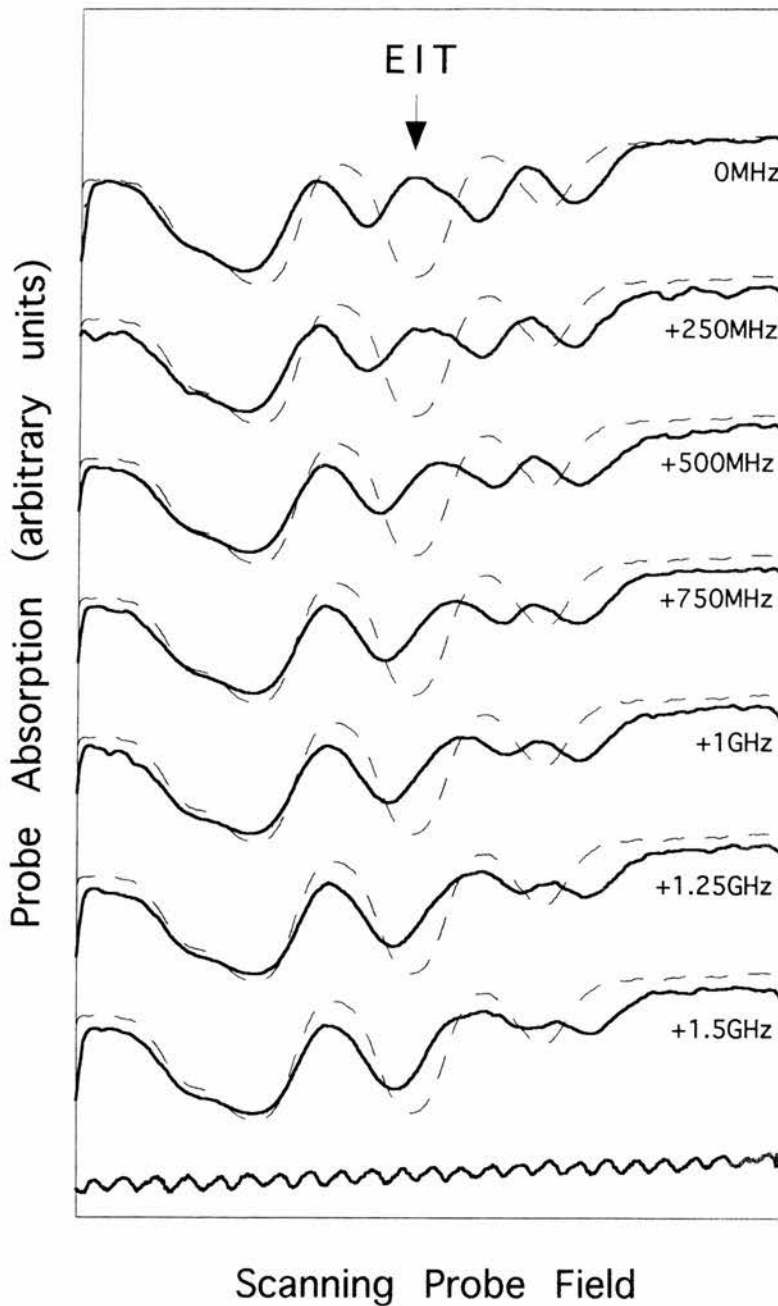


Figure 5.8: For a coupling field power of 800mW the probe absorption is shown as a function of probe field detuning. The top trace shows EIT on peak 3 and successive traces show the coupling field detuned by steps of 250MHz. Each trace (solid line) is superimposed over the absorption in the absence of the coupling laser (dashed line).

5.4.1 Power

The measured absorption exhibits the hyperfine structure of the two rubidium isotopes, ^{85}Rb and ^{87}Rb . Figure 5.9 shows a scan across all four resulting absorption peaks in both the absence (faint line) and presence (bold line) of the coupling laser, which is resonant with the transition corresponding to peak 3 ($5S_{1/2} (F=2) - 5P_{3/2}$ in ^{85}Rb) at a power of 800mW.

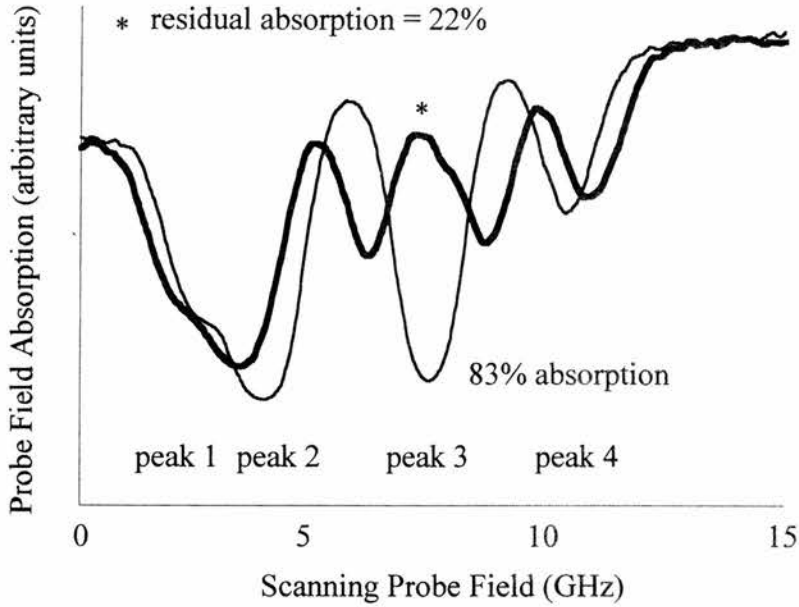


Figure 5.9: Experimental trace of the probe absorption as a function of probe field detuning in the presence (bold line) and absence (faint line) of the coupling laser. The coupling field power equals 800mW. The lower states corresponding to the four absorption peaks, from left to right, are (^{87}Rb , $F=2$), (^{85}Rb , $F=3$), (^{85}Rb , $F=2$), and (^{87}Rb , $F=1$). The maximum absorption on peak 3 (^{85}Rb , $F=2$) is 83%. The induced transparency removes 73% of the absorption.

This experimental trace demonstrates the magnitude of the induced transparency that removes approximately 73% of the absorption. The linear Doppler width is measured to be approximately 1.3GHz. The absence of optical pumping effects is indicated by the lack of a corresponding increase in the absorption of peak 2 (^{85}Rb , $F=3$), which would accompany the observed reduction in absorption if it was due to optical pumping.

Figures 5.10 and 5.11 show absorption profiles obtained in the absence of the coupling laser and for coupling field powers of 50, 200, and 800mW. All four peaks are depicted corresponding to the two hyperfine ground states in each of the rubidium isotopes. In Fig. 5.10 the coupling laser is on-resonance with the transition, $5S_{1/2} (F=3) - 5P_{3/2}$ in ^{85}Rb , corresponding to peak 2. However, since peaks 1 and 2 overlap due to Doppler-broadening, it is difficult to identify where the absorption associated with peak 2 ends and where that associated with peak 1 begins. Moreover, the transparency window corresponding to the coupling field power of 200mW does not line up with the other traces. This misalignment indicates that the coupling laser mode hopped during the course of the experiment, detuning the coupling field slightly from resonance.

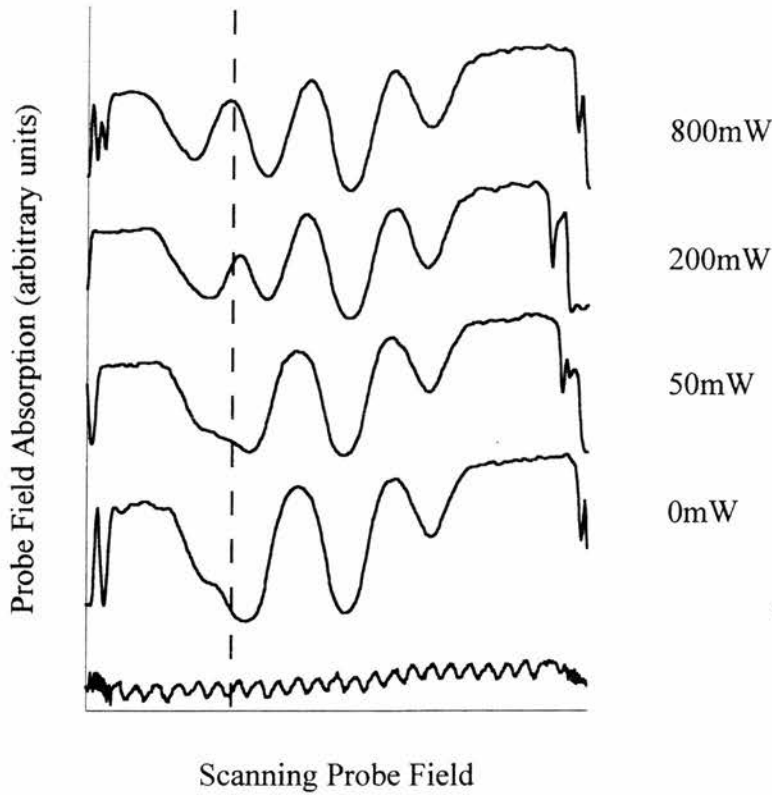


Figure 5.10: *Experimental traces of probe field absorption as a function of probe detuning for a range of coupling field powers. The coupling laser is on-resonance with the $5S_{1/2}$ ($F=3$) - $5P_{3/2}$ transition corresponding to peak 2. The top trace was obtained with a coupling field power of 800mW, the lower traces were obtained with 200mW, 50mW and in the absence of the coupling field. The bottom trace is the confocal marker, in which each cycle corresponds to approximately 600MHz. The vertical dashed line marks the position of EIT.*

Figure 5.11 shows a much clearer set of traces for which the coupling field was on-resonance with the $5S_{1/2}$ ($F=2$) - $5P_{3/2}$ transition in ^{85}Rb , corresponding to peak 3. These experimental results constitute an unambiguous observation of EIT. The transparency window in the centre of peak 3 is enhanced with increasing coupling field power as we would expect from previous experiments [2]. The additional trace in both Fig. 5.10 and Fig. 5.11 is the confocal marker, described in Section 3.3.1, which is used as a frequency reference.

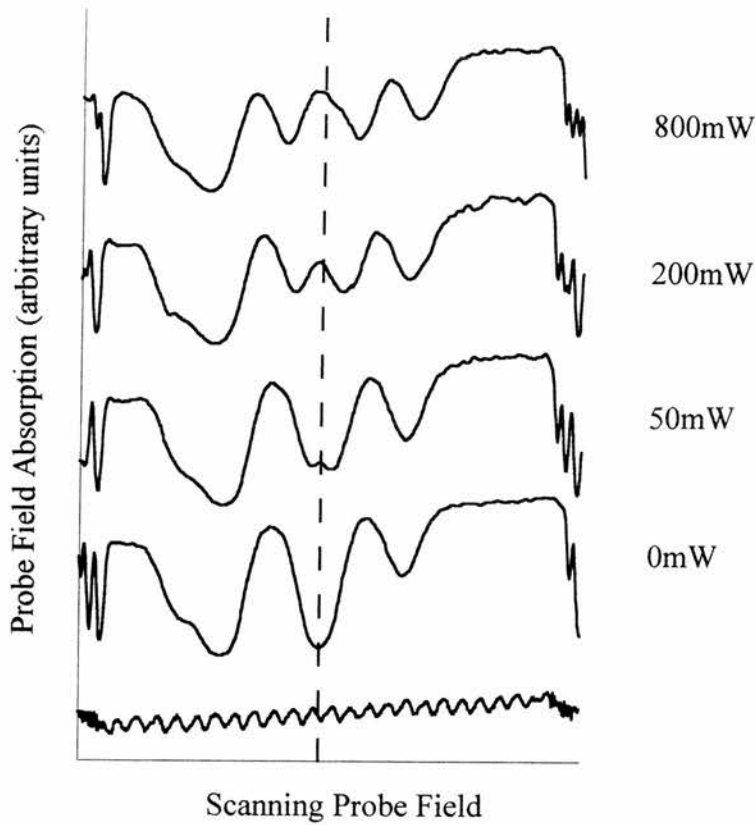


Figure 5.11: *Experimental traces of probe field absorption as a function of probe detuning for a range of coupling field powers. The coupling laser is on-resonance with the $5S_{1/2} (F=2) - 5P_{3/2}$ transition corresponding to peak 3. The top trace was obtained with a coupling field power of 800mW, the lower traces were obtained with 200mW, 50mW and in the absence of the coupling field. The bottom trace is the confocal marker, in which each cycle corresponds to approximately 600MHz. The vertical dashed line marks the position of EIT.*

A comparison is now made between experiment and theory based on the results for peak 3. Figure 5.12 depicts (a) the experimental traces for peak 3 at the coupling field powers of 800mW, 200mW, 50mW, and 0mW; (b) theoretical traces dephased by radiative decay alone; and (c) theoretical traces with $1 \times 10^9 \text{ s}^{-1}$ mixing of the hyperfine ground states. In the latter case, the mixing introduced to the ground state also dephases the atomic coherences in the system, as described in Section 5.2.

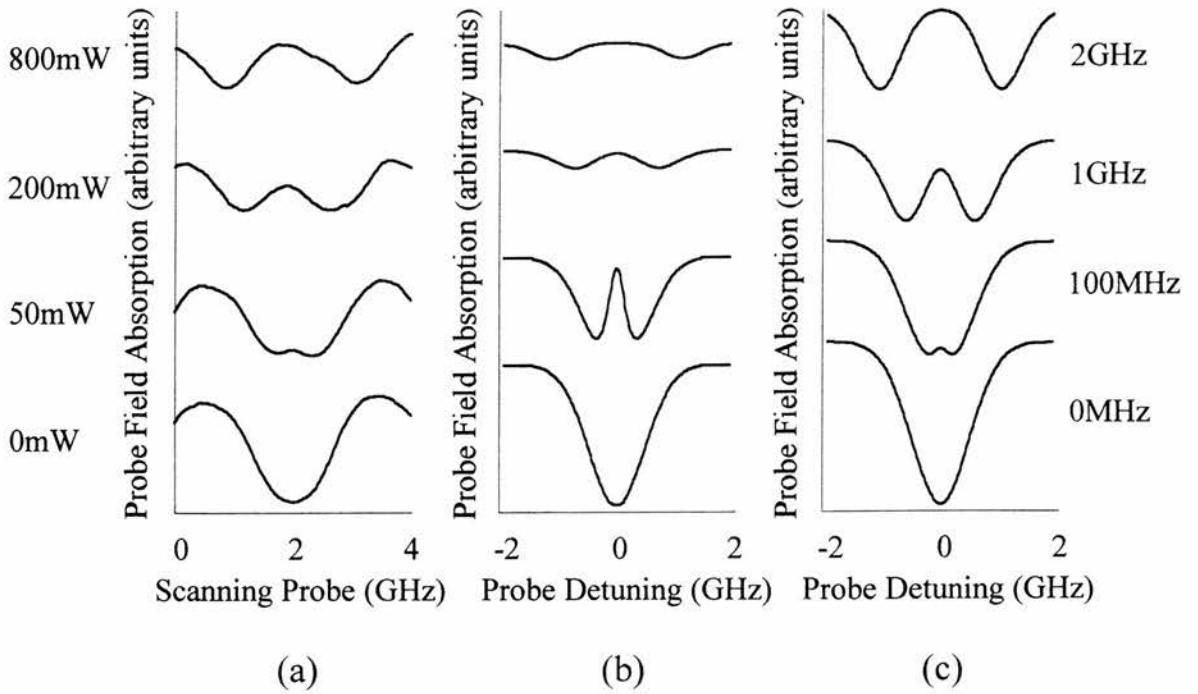


Figure 5.12: Three sets of traces of the probe field absorption as a function of detuning (a) obtained by experiment with coupling field powers, from the top, of 800, 200, 50, and 0mW; (b) obtained by density matrix theory with linear coupling field Rabi frequencies, from the top, of 2GHz, 1GHz, 100MHz, and 0MHz; and (c) obtained by density matrix theory with $1 \times 10^9 \text{ s}^{-1}$ of collisional mixing and Rabi frequencies as before.

There are two surprising aspects of these experimental results. Firstly, there is no evidence of optical pumping in any of the experimental traces; and secondly, the transparency predicted for low coupling field Rabi frequencies is not observed experimentally. Before attempting to explain these observations we consider the matching of experimental traces to theory.

In Fig. 5.12 (b), we see that the observed Autler-Townes splitting is larger, in each case, than the driving coupling field Rabi frequency. The Autler-Townes splitting for atoms at rest will equal the driving coupling field Rabi frequency. However, for a non-zero atomic velocity, the observed splitting will be dictated by the detuning as well as the Rabi frequency (see Eq. (4.1) in Section 4.3). The splitting observed in the Doppler-broadened absorption profile, of the experimental scheme, may not be determined by the zero velocity

group but rather by the primary - single photon - absorption components of two separate non-zero velocity groups either side of resonance. The difference between the observed splitting and the driving Rabi frequency is more pronounced for lower Rabi frequencies because the Doppler-detuning (which is determined by velocity and wavelength) will have a greater impact on the Autler-Townes splitting. Figure 5.13 shows the fractional difference between the observed splitting, Ω_{obs} , and the coupling field Rabi frequency, Ω_c , plotted as a function of the Rabi frequency. The Autler-Townes splitting converges with the driving Rabi frequency as the latter value increases.

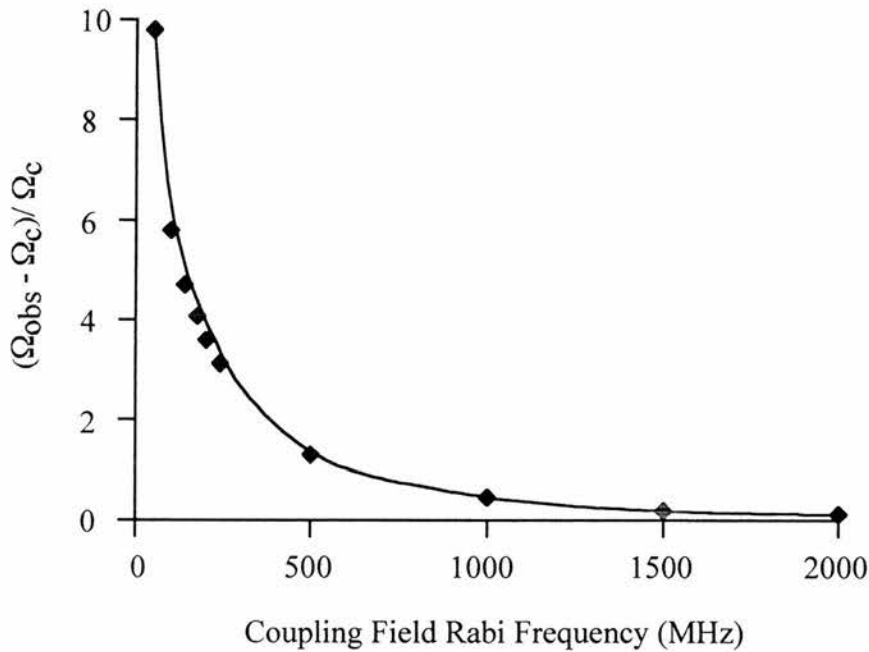


Figure 5.13: *The difference between the coupling field Rabi frequency and the observed Autler-Townes splitting as a fraction of the Rabi frequency is plotted as a function of the coupling field Rabi frequency.*

The coupling field Rabi frequencies employed to create the theoretical traces in Figs. 5.12 (b) and (c) have been carefully chosen to match the theoretically predicted Autler-Townes splitting at the lower dephasing with that observed in the experimental traces.

Figure 5.12 (b) depicts theoretical traces of absorption utilising the model described in Section 5.2 with the collisional mixing rate set to zero. Optical pumping therefore occurs in this four level model, and the dephasing of the coherences is due solely to the natural

level lifetime effects in the atomic system. Optical pumping is velocity selective and will occur for a narrow range of frequencies about line centre at low coupling field powers. This frequency range will increase due to power broadening as higher coupling field strengths are considered. In the high Rabi frequency traces of Fig. 5.12 (b) we clearly see the absorption reducing across the entire lineshape due to optical pumping effects.

In the low power traces of Fig. 5.12 (b) transparency is predicted for a coupling field Rabi frequency that is an order of magnitude less than the Doppler width of approximately 1GHz. The transparency observed on-resonance for low coupling field Rabi frequencies occurs for two reasons. First, the dephasing is low and the coherence is consequently closer to its ideal value for EIT; and second, the absorption at line centre is reduced due to the presence of optical pumping effects. To quantify the extent to which the reduction in absorption is due to EIT, we consider a three level model for which optical pumping is absent.

The three level model is based on the density matrix previously used in Section 2.5.3, and it is identical to the four level model employed here except that the hyperfine ground states are treated as a single level. Figure 5.14 shows a comparison of the three and four level models for a coupling field Rabi frequency of 100MHz. In both these models the dephasing rates are based solely on the radiative decay of the atomic states. The four level model, Fig. 5.14 (a), exhibits a large reduction in absorption due to both EIT and optical pumping. The absorption, in the absence of the coupling laser, is reduced by approximately 89% for a coupling field Rabi frequency of 100MHz in this case. The three level model, Fig. 5.14 (b), shows a smaller reduction in absorption that is due to EIT alone. The absorption, in the absence of the coupling laser, is reduced by approximately 72% for the same coupling field Rabi frequency as before. This comparison indicates that in theory a transparency of 72% can be observed in the four level system if optical pumping is removed by some other means [5,11]. 80% of the reduction in absorption predicted by the four level model can be realised by EIT alone.

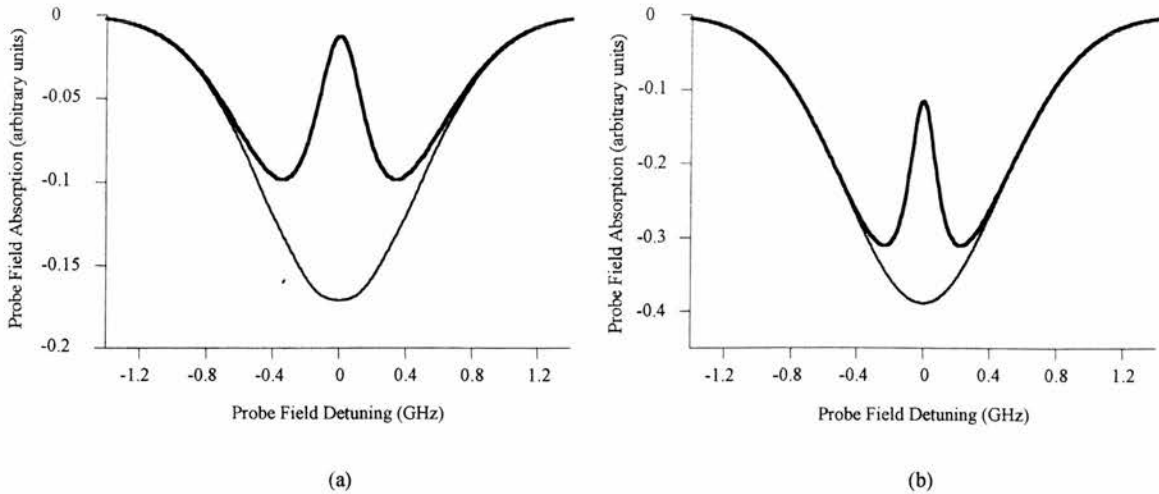


Figure 5.14: *Probe absorption as a function of probe field detuning in the presence (bold line) and absence (faint line) of the coupling laser, for a Rabi frequency of 100MHz in (a) the four level model, and (b) the three level model.*

This analysis demonstrates that even in the absence of optical pumping the theoretical model predicts a significant reduction in absorption due to EIT alone, for low coupling field Rabi frequencies. The lack of observed transparency and optical pumping at low Rabi frequencies has not yet been explained. We saw in Figure 5.5 of Section 5.3 that collisional mixing of the hyperfine states can lead to the destruction of optical pumping and we know that such collisions would also dephase the atomic coherences and diminish the effect of EIT. Figure 5.12 (c) shows a set of theoretical traces calculated for a collisional mixing rate of $1 \times 10^9 \text{ s}^{-1}$. In this instance the optical pumping is destroyed as predicted theoretically and as evidenced by the higher power absorption traces only being reduced in magnitude on-resonance. Furthermore, the transparency that was previously predicted for a coupling field Rabi frequency of 100MHz is not observed. These traces agree more accurately with the experimental plots in Fig. 5.12 (a). However, the calculated collision rate for the experimental system of $50 \times 10^3 \text{ s}^{-1}$ (see Section 5.3) is nearly three orders of magnitude less than that required to explain the discrepancies between experiment and theory. While it is true that the cross-section for dephasing collisions will be greater than that for exchange collisions upon which the calculation of the collisional rate was based, the difference in these parameters is not sufficient to explain a rate of $1 \times 10^9 \text{ s}^{-1}$. It is possible

that mixing in the cell is increased by cell impurities, partial loss of vacuum pressure or fierce temperature gradients in the cell. However, there is no direct evidence to support this explanation of the experimental results. Note that it is problematic to estimate the dephasing in the experiment as the associated change in the broadening of the absorption lineshape is negligible. The linewidth would remain unchanged because the broadening is limited by the Maxwellian distribution of atoms with respect to velocity: there are so few atoms at higher velocities that the broadening of the absorption associated with them has little impact on the overall absorption profile.

We now consider the variation of coupling field Rabi frequency in the vapour cell. The theoretical calculations are based on a single pure driving Rabi frequency; whereas, the experimental scheme exhibits a range of Rabi frequencies along the length and cross-section of the vapour cell due to variations in the coupling laser's intensity in this region. Assuming the best case scenario, in which the focusing is arranged to fit the confocal parameter, the beam waist of the coupling field will double at the edge of the cell relative to the centre. Doubling the beam waist equates to halving the Rabi frequency on-axis. If we move off-axis we can expect the Rabi frequency to reduce further. The experimental traces are therefore made up of a combination of a range of coupling Rabi frequencies. Therefore, we can reasonably expect an experimental trace to exhibit a lower level of transparency than a theoretical model based on the Rabi frequency achieved on-axis at the focus of the coupling laser beam.

Figure 5.15 shows the transparency induced for three coupling field Rabi frequencies with a collisional mixing rate of $200 \times 10^6 \text{ s}^{-1}$ which is sufficient to obviate optical pumping. The intention here is that the coupling field Rabi frequency of 100MHz represents the value in the centre of the vapour cell, on-axis; the lower value of 50MHz represents the value at the edge of the cell, on-axis; and the Rabi frequency of 25MHz represents some point off-axis. Figure 5.15 gives us a qualitative idea of how the variation of coupling field Rabi frequency throughout the cell will affect the overall absorption profile. Although this process will contribute to the discrepancies between theory and experiment it is not sufficient to explain the observations in this case.

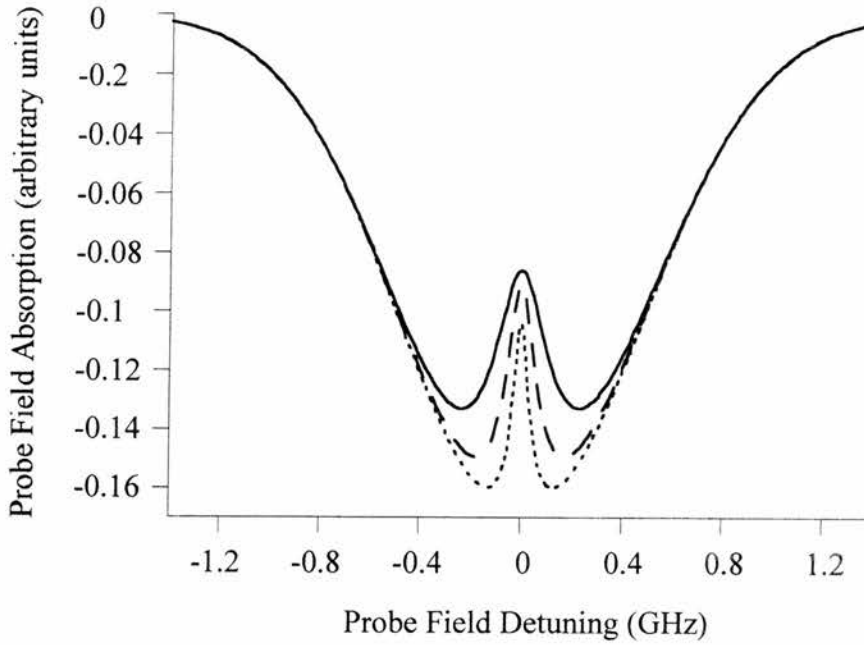


Figure 5.15: Probe field absorption (ρ_{14}^i in arbitrary units) as a function of probe field detuning for the coupling field Rabi frequencies 100MHz (solid line), 50MHz (dashed line), and 25MHz (dotted line). This four level model includes $200 \times 10^6 s^{-1}$ collisional dephasing which destroys optical mixing and reduces the level of transparency predicted due to EIT.

In a recent review, Harris explained that one of the reasons we cannot use EIT to see through walls is that in order to render the wall transparent the coupling field must interact with its entire thickness. To achieve this situation with a laser it would be necessary to employ a power that would inevitably cause the wall structural damage. This explanation is the key to the current experiment. The theoretical model assumes that the strength of interaction with the coupling field is equal for all the atoms along the entire length of the cell. However, in the experiment the coupling field is absorbed as it propagates through the cell, resulting in a reduction in the intensity of the field and therefore also in the strength of interaction.

To understand why the coupling field is absorbed we must consider the relevant experimental conditions. For reasons that will become clear in Chapter 7, the chosen configuration exhibits a coupling transition decay rate that exceeds that of the probe transition. According to the Wigner-Weisskopf expression [16], in general, the rate of

spontaneous decay increases as the cube of the transition frequency. However, in the considered mismatched scheme the probe transition has a decay rate that is significantly lower than that of the coupling transition. This ratio of decay rates occurs because the probe transition has a comparatively weak dipole matrix element. Stimulated processes on the probe transition will be much weaker than on the coupling field transition in this case. In order to ensure a high signal to noise ratio for probe absorption measurements it is therefore necessary to increase the particle density in the vapour cell by raising the temperature. Since the coupling transition decay rate is high, this increase in particle density may lead to absorption of the coupling field even in the strong signal regime.

We would normally expect that on a strongly driven transition the population would flop between the upper and lower states at the Rabi frequency. As the population moves upwards in energy, light is absorbed; and as it moves downwards, light is emitted. The time averaged change in the transmitted light is therefore zero. However, the process of spontaneous emission provides an alternative route for the relaxation of excited state population which does not contribute to the transmitted light amplitude. Consequently, net absorption of the coupling field may occur when the spontaneous emission process rivals that of stimulated emission.

If we accept that the coupling field is absorbed then the resulting reduction in the driving Rabi frequency with distance into the cell would have a profound impact on the probe absorption profile and the level of induced transparency. While significant transparency may be induced at the start of the vapour cell this would be masked by the absorption of the probe as a result of interaction with atoms towards the end of the cell where the coupling strength would be substantially reduced. Having identified this potential cause for the lack of low power EIT, measurements were made of the coupling field absorption for a range of powers and temperatures. These results are presented in Fig. 5.16. Since temperature gradients may be present in the experimental system the absorption of the probe at 422nm was also measured (in the absence of the coupling field) to verify the temperature that corresponded to that employed in the original experiment. A probe absorption equal to that obtained in the experiment was found to occur for a cell temperature of approximately 125°C. Figure 5.16 demonstrates that a finite coupling field absorption occurs at this temperature with a dependence on the incident laser power. Note

that these results were optimised for focusing in the vapour cell. It was found that less coupling field absorption occurs if the beam is focused towards the front of the cell rather than the centre, because this prevents significant absorption in the first half of the cell. For the low power results (50mW) taken in the experiment, Fig. 5.16 shows that approximately 80% of the coupling field is absorbed in the 2cm vapour cell. Consequently, it is understandable that a transparency window is not observed at line centre.

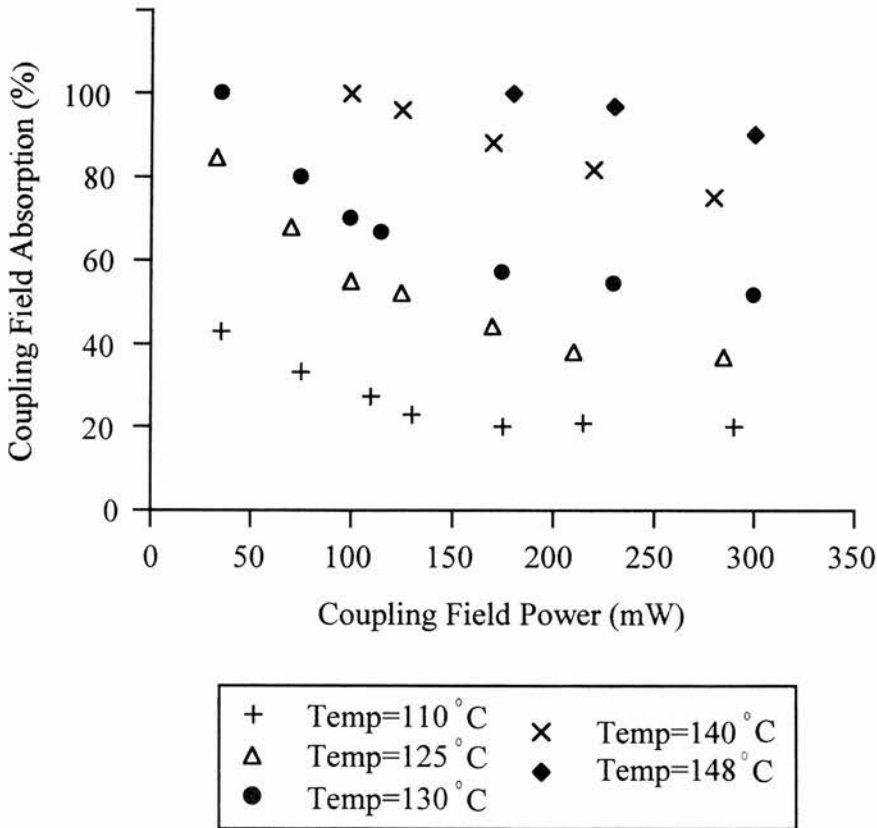


Figure 5.16: Experimentally measured coupling field absorption as a function of the incident coupling field power at cell temperatures of 110, 125, 130, 140 and 148°C.

The presence of coupling field absorption in the vapour cell explains the discrepancies between the presented experimental and theoretical results. The presence of this process will also reduce the effects of optical pumping since this is driven by the interaction of the coupling field.

However, we still have to explain why, at high coupling field powers, EIT is observed and optical pumping is absent. The latter is evidenced by the lack of an increase

in absorption on the detuned hyperfine transition. We are able to observe EIT in the high power regime because the reduced interaction strength at the far end of the vapour cell is still sufficient to create a significant transparency. Furthermore, optical pumping is obviated because we have moved beyond the limit prescribed by Shore that was discussed in Section 5.3. The coupling field is of sufficient strength to interact with both hyperfine transitions and optical pumping is thus destroyed.

In conclusion, the comparison of theory and experiment indicates that coupling field absorption destroys EIT and optical pumping for low coupling field powers. The absorption of the coupling field has been measured directly for a range of incident powers and cell temperatures. In addition, to a lesser extent, the variation of the coupling field intensity across the beam profile and as the beam is focused, contributes to the discrepancies between theory and experiment. For high coupling field Rabi frequencies ($>1.5\text{GHz}$) optical pumping is not observed because the coupling field interacts with the transitions to both hyperfine levels of the ground state. In this regime a significant reduction in absorption is observed due to EIT alone.

Importantly, the problem of coupling field absorption will occur in any mismatched system and is in no way linked to the phenomenon of Doppler-broadening. Indeed, in our experimental scheme the power at which EIT may be observed is limited by this process rather than Doppler effects. In this respect, there is no advantage to be gained by moving to a Doppler free geometry. We can hypothesise that EIT may be observed in a mismatched ($\lambda_c > \lambda_p$) wavelength system for coupling field Rabi frequencies significantly lower than the Doppler width if a particle density is selected in which negligible coupling field absorption occurs. In such a system, we would expect to observe optical pumping and this would have to be dealt with by some other means. A possible method by which the latter may be achieved was described in Section 3.5 [5,11]. However, due to the limitation on particle density the use of such a scheme to achieve inversionless gain will be restricted. The need to increase the particle density in this experiment originated from the choice of transition decay rates which is also restricted in an inversionless gain scheme. The limitation imposed by coupling field absorption on mismatched gain will be discussed in Section 7.6.

5.4.2 Detuning

The effect of detuning the coupling field was considered for low and high coupling field powers. The first set of results was taken for the relatively low coupling laser power of 200mW while the second set was taken for a coupling field power of 800mW. We consider the low power detuning results first as these are less complex and give us a clearer picture of what happens to the transparency window as we detune the coupling laser from resonance.

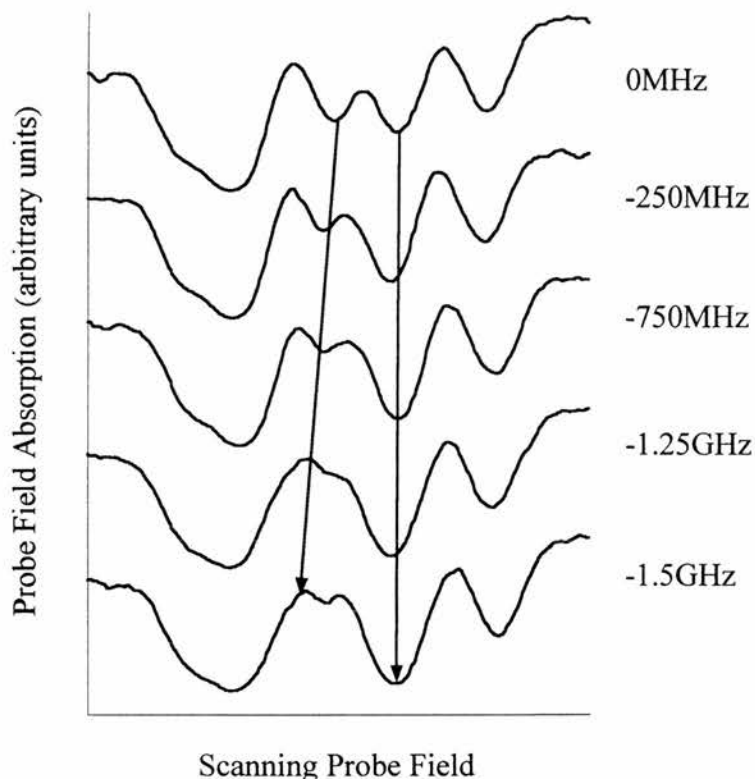


Figure 5.17: *Experimental traces of the probe field absorption as a function of probe field detuning for successive detunings of the coupling laser. The coupling field begins on resonance with peak 3 (^{85}Rb , $F=2$), and the detunings thereafter are given on the right hand side of the appropriate trace. The coupling field power equals 200mW for all these traces. The solid arrowed lines mark the Autler-Townes absorptions of the $F=2$ ground state in ^{85}Rb .*

Figure 5.17 shows the probe field absorption on all four peaks in rubidium vapour for successive detunings of the coupling laser. The top trace depicts the case in which the coupling laser is on resonance with peak 3, corresponding to the $5S_{1/2}$ ($F=2$) - $5P_{3/2}$

transition in ^{85}Rb . This trace exhibits a large transparency window in the third absorption peak. The lower traces show the evolution of this transparency as the coupling laser is detuned from peak 3 by the frequencies indicated to the right of each trace. As the detuning is increased, the transparency window shifts away from resonance. This movement can be mapped by observing the changing positions and magnitudes of the two Autler-Townes peaks associated with the transparency indicated in Fig. 5.17 by solid arrowed lines. The separation of these Autler-Townes components increases as the detuning increases according to Eq. (4.1). We have already discussed the velocity dependent detuning of the Doppler effect in Chapter 4. Here, an additional detuning is imposed in the lab frame that affects all the velocity groups simultaneously, and it has a great impact on the trace observed. Figure 5.18 shows plots of the positions of Autler-Townes components and the single and two-photon resonances in terms of the probe field detuning, for the coupling field detunings that correspond to the experimental traces in Fig. 5.17.

We see from Fig 5.18 that the probe frequency at which the two-photon and single photon resonances are coincident is shifted as the coupling field is detuned. Consequently, the transparency also shifts from line centre when the coupling laser is manually detuned from resonance. The Doppler-broadened absorption peaks that are observed either side of the transparency window become unequal in magnitude as the coupling field is detuned. The peak closest to line centre is enhanced because of the distribution of atoms with respect to velocity. Conversely, as the other absorption peak is pulled further from line centre it reduces in magnitude. When the coupling laser is significantly detuned beyond one homogeneous linewidth from line centre it no longer interacts with the single photon transition and a straightforward single photon absorption profile is resolved at line centre. The homogenous linewidth associated with the coupling laser is power broadened, and it will be approximately equal to the coupling field Rabi frequency, which is 1GHz in this case.

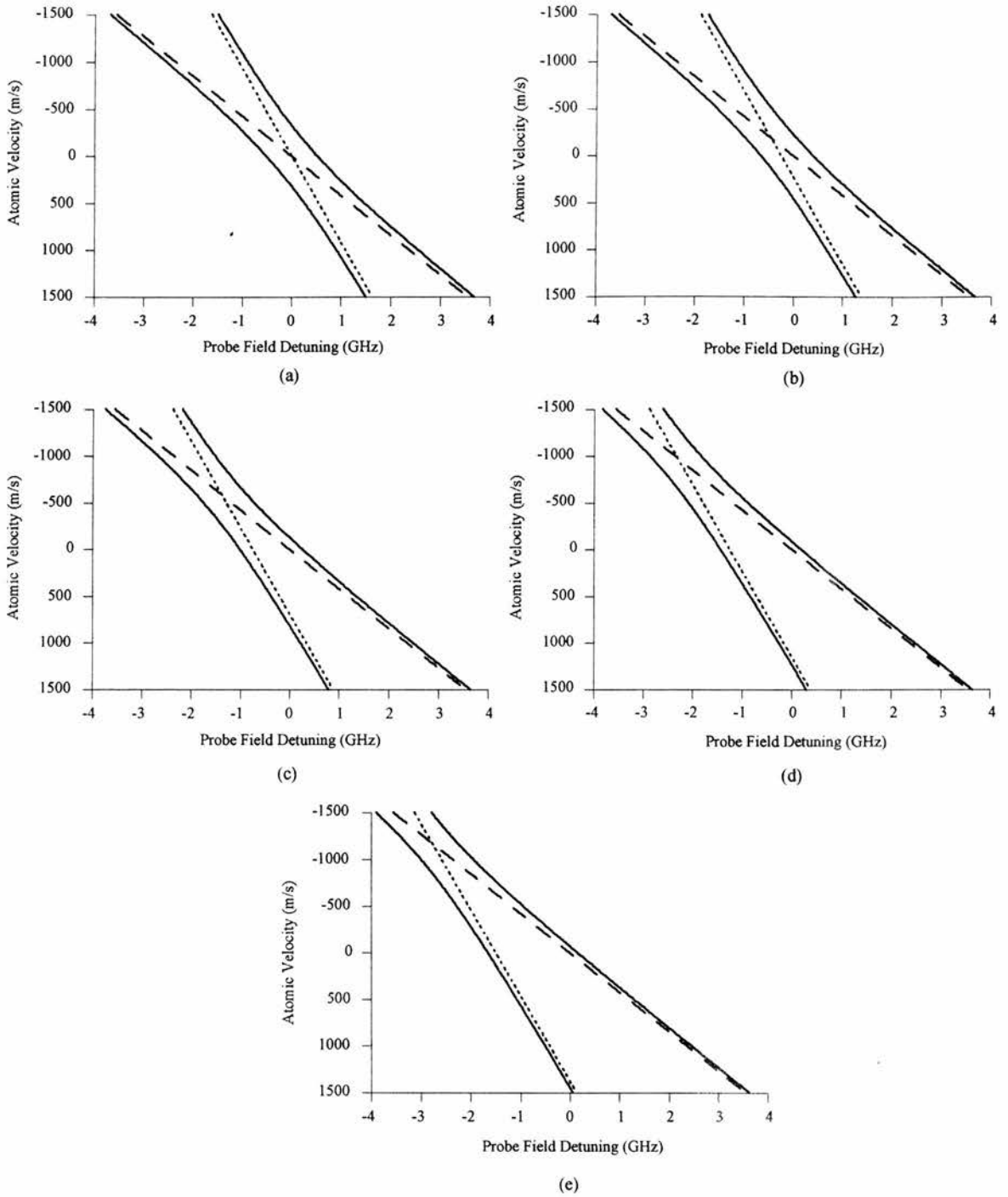


Figure 5.18: *Autler-Townes and absorption resonance positions as a function of probe field detuning and atomic velocity. The Autler-Townes components are indicated by solid lines, the single photon resonances by dashed lines, and the two-photon resonances by dotted lines. Coupling field detunings are (a) 0MHz, (b) -250MHz, (c) -750MHz, (d) -1.25GHz, and (e) -1.5GHz from resonance with the $5S_{1/2} (F=2) - 5P_{3/2}$ transition in ^{85}Rb (peak 3).*

Figure 5.19 shows a comparison between the experimentally observed detuning from peak 3 and the theoretical traces produced by detuning the coupling field in the four level model. The coupling field power is 200mW; the Rabi frequency employed in the theoretical model is 1GHz; and $1 \times 10^9 \text{ s}^{-1}$ collisional dephasing is included to accurately simulate experimental conditions.

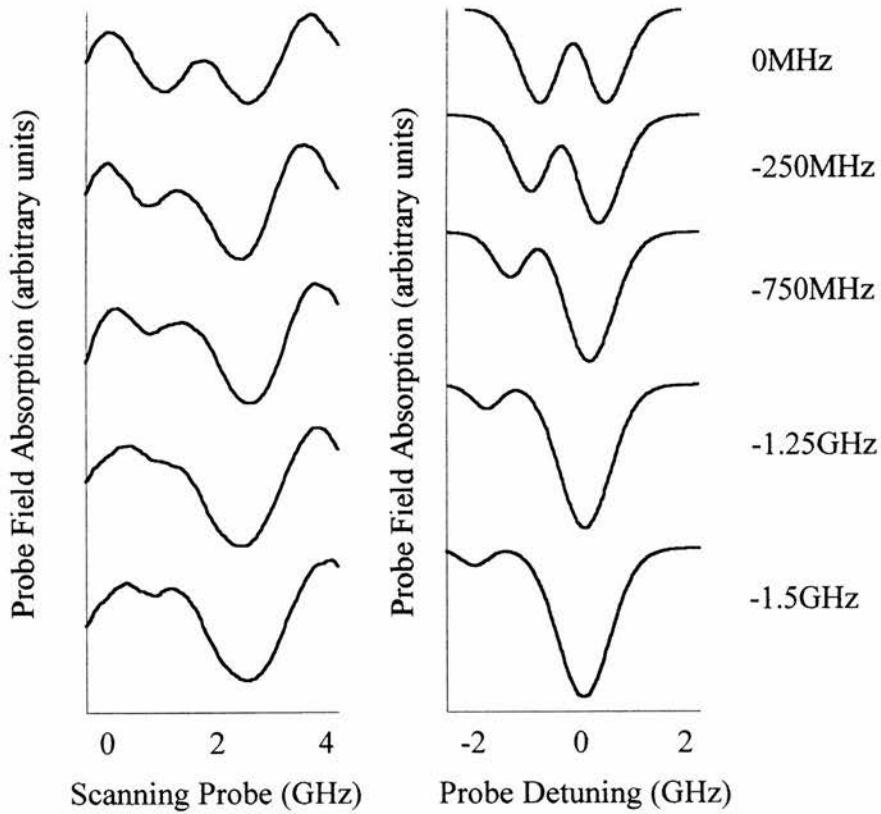


Figure 5.19: (a) Experimental and (b) theoretical traces of the probe field absorption as a function of probe field detuning for various coupling field detunings from peak 3 (^{85}Rb , $F=2$).

Bearing in mind the variation of coupling field Rabi frequency in the vapour cell, Fig. 5.19 shows good agreement between experiment and theory. One significant difference between the experimental and theoretical traces is that the coupling field begins to interact with the next transition (corresponding to peak 2) in the former case. The small absorption peak observed in the final trace of Fig. 5.19 (a), for a coupling field detuning of -1.5GHz, is actually a component of peak 2 rather than peak 3. In our theoretical model the field is only allowed to interact with the prescribed transition; however, this is not the case in reality. As the coupling laser is detuned away from peak 3 it begins to interact with the

transition, $5S_{1/2} (F=3) - 5P_{3/2}$, associated with peak 2. Indeed, Fig 5.20 shows a continuation of the absorption traces shown previously in Fig 5.17 in which the coupling laser tunes onto resonance with peak 2. The detunings indicated to the right of each trace are still referenced to peak 3. This detuning was continued, and Fig 5.21 shows the coupling field moving off resonance with peak 2 so that EIT completely vanishes.

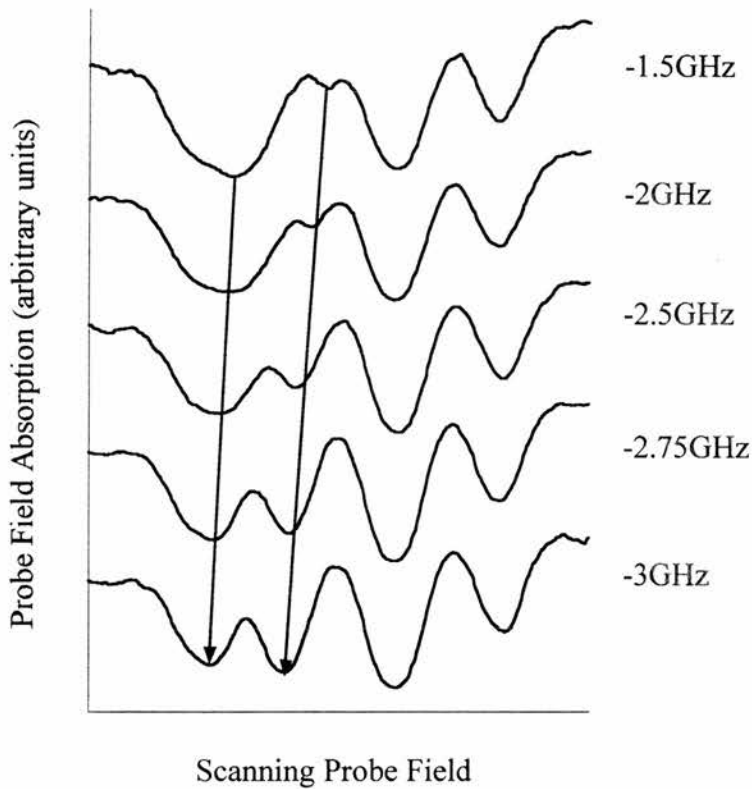


Figure 5.20: *Experimental traces of the probe field absorption as a function of probe field detuning for successive detunings of the coupling laser. The coupling field begins, having been detuned from resonance with peak 3 (^{85}Rb , $F=2$), and the detunings thereafter are given on the right hand side of the appropriate trace. The coupling field power equals 200mW for all these traces. The solid arrowed lines mark the positions of the Autler-Townes absorptions of the $F=3$ ground state in ^{85}Rb .*

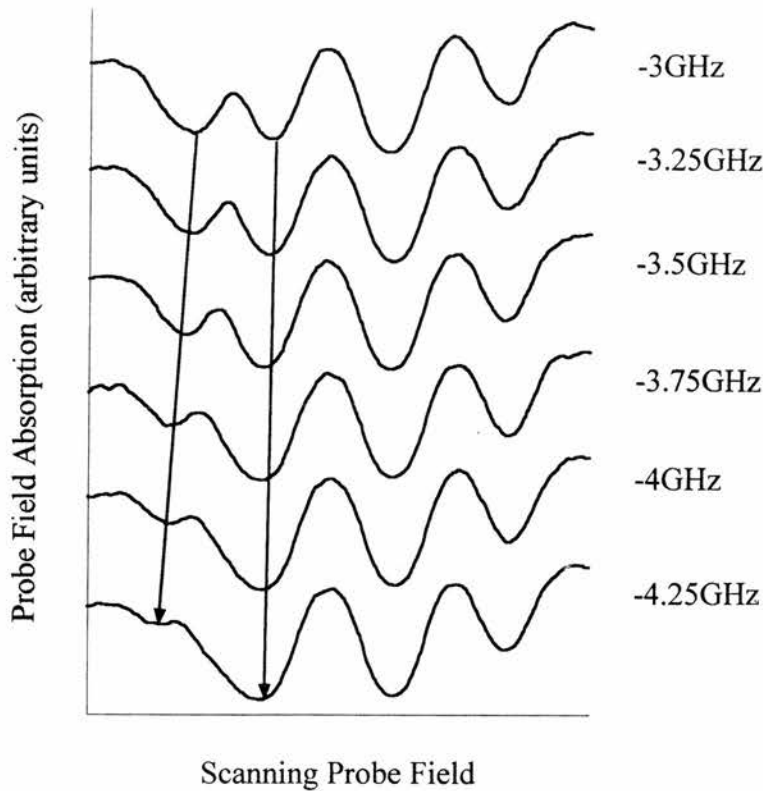


Figure 5.21: *Experimental traces of the probe field absorption as a function of probe field detuning for successive detunings of the coupling laser. The coupling field begins on resonance with peak 2 (^{85}Rb , $F=3$), and the detunings thereafter are given on the right hand side of the appropriate trace. The coupling field power equals 200mW for all these traces. The solid arrowed lines mark the positions of the Autler-Townes absorptions of the $F=3$ ground state in ^{85}Rb .*

It is noted that the detuning required to move the coupling field from resonance with peak 3 to peak 2, 3GHz, corresponds to the separation of the hyperfine levels quoted in atomic data tables [18]. We now consider the case for which the coupling laser is detuned while at the higher power of 800mW. Figure 5.22 shows the interesting observation of ‘double EIT’ that results from the increase in power. The coupling laser now interacts with both peaks 2 and 3, due to power broadening, so that EIT may be observed for both hyperfine transitions in one absorption trace.

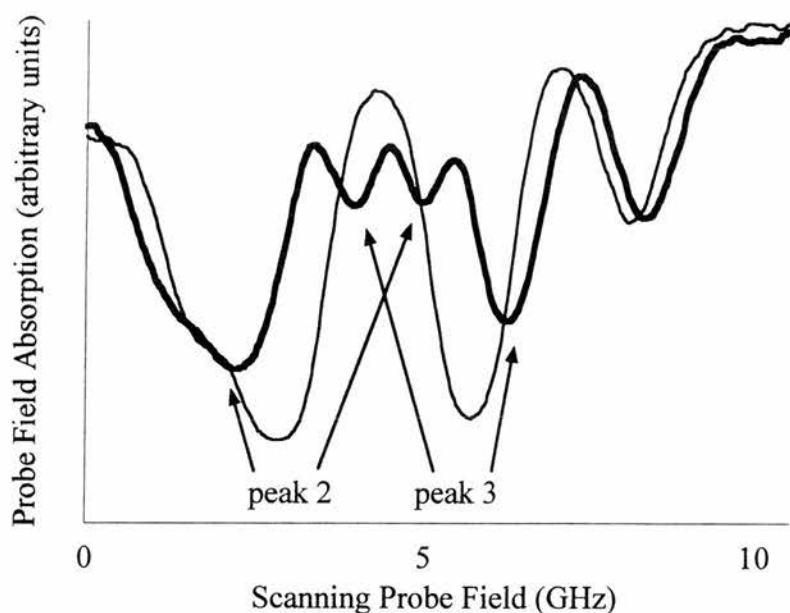


Figure 5.22: *Experimental traces of probe field absorption as a function of probe field detuning in the absence (faint line) and presence (bold line) of the coupling laser at a power of 800mW. The coupling field was detuned by -1.25GHz from resonance with peak 3.*

The effects of detuning for a high coupling field power are shown in Fig. 5.23. The top trace was obtained with the coupling laser on resonance with peak 3 (^{85}Rb , $F=2$) and the lower traces for the coupling field detunings as indicated. The traces shown here are more complicated, the position of the two Autler-Townes peaks associated with peak 3 are marked with solid vertical lines. These lines can be seen to diverge as the magnitude of Autler-Townes splitting increases as a result of the increased detuning from peak 3 (^{85}Rb , $F=2$).

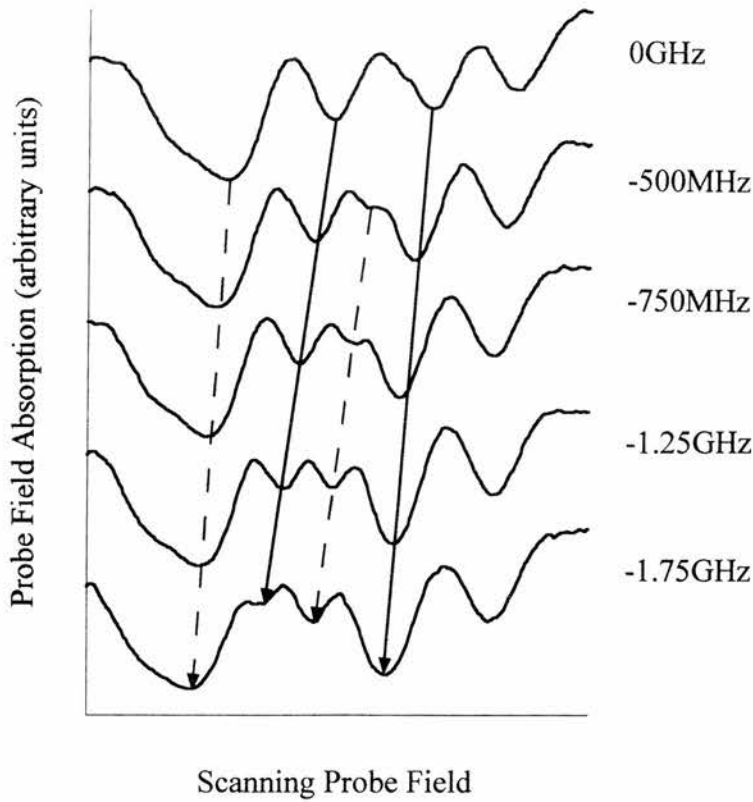


Figure 5.23: *Experimental traces of probe field absorption as a function of probe field detuning for coupling laser detunings from resonance with peak 3 (^{85}Rb , $F=2$), of -500MHz to -1.75GHz in steps of 250MHz. The coupling field power is 800mW.*

In addition to the splitting observed on peak 3 (^{85}Rb , $F=2$), coherently induced transparency is simultaneously observed on peak 2 (^{85}Rb , $F=3$). This concomitant interaction occurs as a result of the high coupling field strength and dipole matrix element of the $5S_{1/2} - 5P_{3/2}$ transition. The Autler-Townes components associated with this additional transparency are shown by the dashed vertical lines in Fig. 5.23. These lines converge because the detuning from the transition linking the upper level of the probe transition to the $F=3$ hyperfine level of the ground state in ^{85}Rb decreases as the coupling laser frequency moves away from resonance with peak 3 and towards peak 2.

Figure 5.24 depicts the analysis of a specific detuning of -1.75GHz from resonance with peak 3 (^{85}Rb , $F=2$) using Eq. (5.5):

$$\Omega_{\text{obs}} = \sqrt{\Omega_c^2 + \Delta_c^2} \quad (5.5)$$

where Ω_{obs} is the magnitude of the observed Autler-Townes splitting and Ω_c and Δ_c are the relevant, on-resonance, Rabi frequency and detuning. This value of detuning should include the contribution of the Doppler shift. Since this contribution is different for each velocity group it is hard to quantify the observed splitting. This dilemma is compounded by the fact that the Rabi frequency in the cell varies across its length and radial cross-section. However, we can approximate the experimental Rabi frequency to be that observed in the absence of any imposed coupling field detuning. The validity of this approach rests on the fact that the Doppler shifted contribution has a lesser impact on the observed splitting when the induced Rabi frequency is relatively large, as it is in this ‘high power’ detuned case. Surprisingly, Fig 5.24 demonstrates fairly good agreement between theoretical analysis and the experimentally observed trace. This analysis can be extended to predict all of the traces observed in Fig 5.23 as a function of detuning.

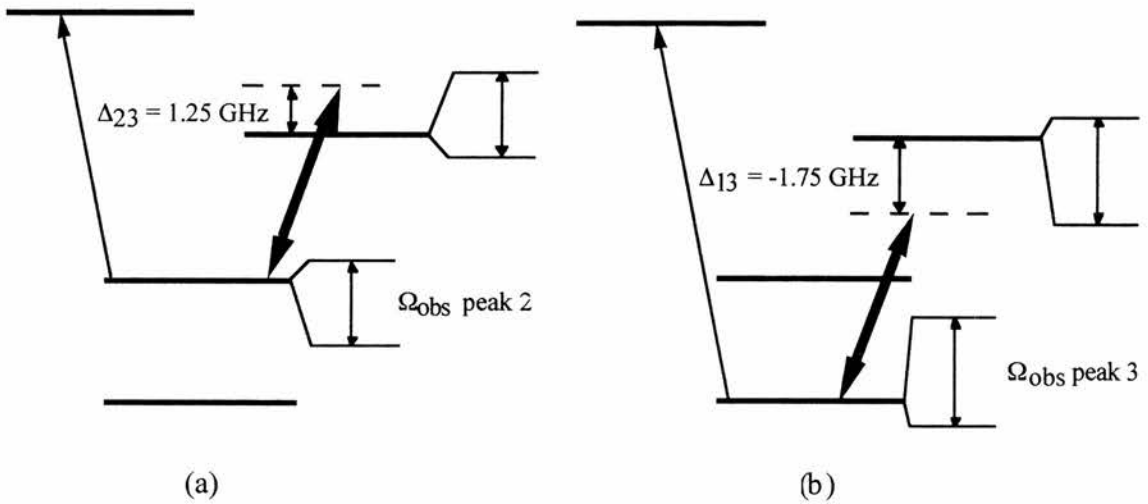


Figure 5.24: Energy level diagrams explaining the last experimental trace of Fig. 5.23. The coupling laser is detuned from peak 3 by -1.75GHz . Part (a) shows the coupling laser, at a power of 800mW , applied to the $5S_{1/2} (F=3) - 5P_{3/2}$ transition in ^{85}Rb with an effective detuning of 1.25GHz . Part (b) shows the coupling laser, at a power of 800mW , applied to the $5S_{1/2} (F=2) - 5P_{3/2}$ transition in ^{85}Rb with a detuning of -1.75GHz .

5.4.3 Fluorescence

Further to the experimental results discussed thus far we observed that in the absence of the probe laser the coupling field produces a blue fluorescence in the rubidium vapour cell. Although this does not play an important role in the experiment, its existence requires some explanation. The fluorescence occurs at four detunings of the coupling laser around 780nm, which correspond to the hyperfine split ground states of the two rubidium isotopes present. Two-photon effects fail to account for this phenomenon as the closest two-photon transition is detuned by 4nm or approximately 2000GHz. The formation of rubidium dimer, due to the high cell temperature, was considered as a possible cause of spontaneous radiative relaxation. However, observation of the fluorescence with a monochromator resolved two spectral lines (in addition to a 780nm peak corresponding to single photon radiative decay from the $5P_{3/2}$ level) at approximately 420nm and 422nm. These spectral lines correspond exactly to the hyperfine split $6P_{1/2}$ level, and therefore indicate an atomic rather than a molecular process. Furthermore, work in rubidium dimers [19] has shown a violet band system, with its maximum intensity centred on 430nm, that only begins to appear at 350 °C, more than twice the cell temperature employed in this experiment.

A possible explanation comes in the form of laser-induced collisional energy transfer [20,21]. By considering the general equation below, (Eq. 5.6) [20] we postulate a collision between an excited rubidium atom and a relaxed one occurring at the instant the relaxed atom accepts energy from an incident photon.



where A and B are atoms, ions or molecules and an asterisk denotes an excited state. By this mechanism the 4nm detuning from the $5D_{5/2}$ level can be seen as an energy deficit that is cancelled by kinetic energy transferred from the initially excited rubidium atom. Quantitatively we require that $h\nu \leq kT$ where $h\nu$ corresponds to the energy deficit, and kT is the kinetic energy of the excited atom. Applying the experimental operating temperature to Eq. (5.6) satisfies the equality; therefore, it is possible that a detuned case of laser-induced collisional energy transfer is responsible for the fluorescence observed in the rubidium vapour cell. This observation differs from other reported experiments in that we

observe this effect to occur within one type of atom, rather than in a gaseous mixture of two atomic vapours [20]. Figure 5.25 shows a schematic energy level diagram of the collisional energy transfer process that is thought to occur.

A second collisional process is also likely to occur in the vapour cell. If we imagine that the atom that emits fluorescence is initially excited and a collision occurs, then an incident photon may stimulate the atom from the $5P_{3/2}$ excited state into the higher energy $5D_{1/2}$ level, with the detuning being taken up by the kinetic energy of the colliding atom. This case differs from that of laser induced collisional energy transfer because the atom that is excited into the $5D_{1/2}$ level begins in $5P_{3/2}$ rather than the ground state. Therefore, no energy, other than the kinetic energy, is transferred from the colliding atom.

The combination of these effects causes the observed fluorescence. Importantly, both of these processes are weak, because of the large detuning, and do not significantly affect the probe field absorption.

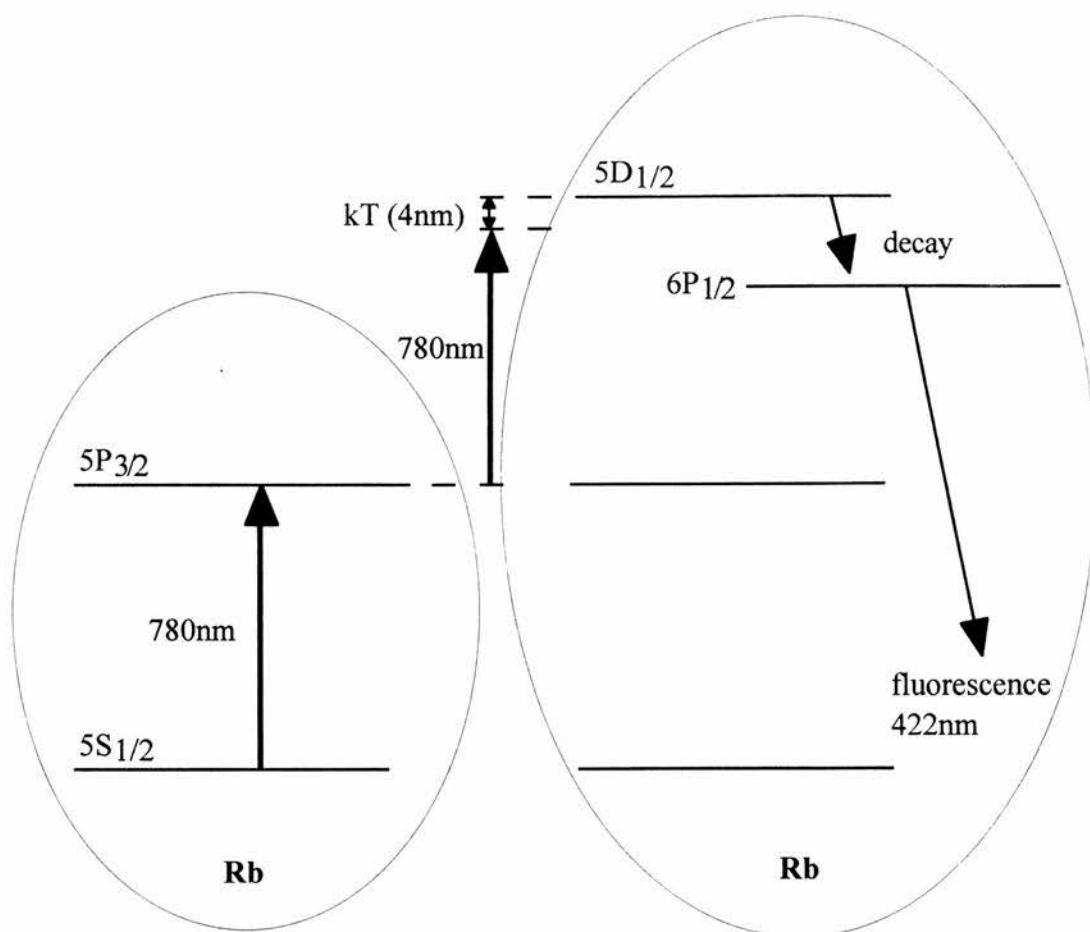


Figure 5.25: Schematic of the specific detuned case of laser induced collisional energy transfer that is believed to have been observed experimentally. The atomic energy level structure of each of the colliding atoms is circled for clarity.

5.5 Discussion

The presented results constitute the first experimental observation of electromagnetically induced transparency in a Doppler-broadened Vee-type system employing mismatched ($\lambda_c > \lambda_p$) wavelengths. This result has been achieved with cw laser sources in the absence of optical pumping effects. In the introduction to this chapter we proposed two hypotheses. Firstly, that EIT could be realised in the frequency up-conversion regime ($\lambda_c > \lambda_p$) for Rabi frequencies equal to or greater than the Doppler width on the probe transition; and secondly, that EIT would still be realisable for this regime in a Vee scheme at coupling Rabi frequencies less than the probe Doppler width.

The experimental results presented in this chapter substantiate the first hypothesis by demonstrating mismatched ($\lambda_c > \lambda_p$) EIT in a Vee scheme for coupling field Rabi splittings comparable to the Doppler width. Although we have not experimentally verified the second hypothesis, analysis has shown that EIT was not observed for sub-Doppler width powers because of coupling field absorption in the vapour cell. Theory predicts that in the absence of coupling field absorption, a transparency of 72% may be induced for a coupling field power of 50mW (equating to a Rabi frequency of approximately 100MHz) if optical pumping is eliminated by some other means, as discussed in Section 3.5 [5,11].

Coupling field absorption can be compensated by reducing the particle density. This approach is sufficient to achieve transparency but becomes an undesirable restriction if we wish to observe gain and lasing at the probe frequency. However, this limitation is applicable to any mismatched scheme regardless of the line broadening mechanism. Analysis of the presented experimental results shows that the limiting factor in our system is coupling field absorption rather than Doppler effects. Absorption of the driving field with increasing particle density is therefore the most significant hurdle to be overcome in the realisation of a mismatched LWI scheme.

The lack of optical pumping is manifested experimentally by the reduction of absorption on one hyperfine transition without an accompanying increase on the other. Fortunately, this undesirable effect is obviated by a combination of coupling field absorption and, at high powers, the interaction of the coupling field with both hyperfine transitions.

In the following chapter we consider the experimental lasing and gain systems that have been realised to date, in the absence of a population inversion. In all of these systems the wavelengths of the employed fields are closely matched. These experiments demonstrate the principle of inversionless lasing based on atomic interference and coherence but avoid the issues related to mismatched wavelengths. In Chapter 7 we will consider theoretical analysis of mismatched inversionless gain in a Doppler-broadened scheme. The effects of coupling field absorption will be ignored in order to isolate the impact of Doppler broadening on amplification without inversion.

The experimental results presented in this chapter have demonstrated all the expected characteristics of EIT, particularly in the case of the high power detuning which can only be explained in terms of EIT. The presented results highlight the potential of the Doppler-broadened Vee scheme as a robust system for mismatched EIT, specifically in the regime for which the probe field frequency exceeds that of the coupling field.

References

- [1] T. Gantsog *et al*, Opt. Com. **124**, 579-594, (1996).
- [2] D. J. Fulton *et al*, Phys. Rev. A. **52**, 3, 2302, (1995).
- [3] Y-q. Li *et al*, Phys. Rev. A. **51**, R1754, (1995).
- [4] Y-q. Li, and M. Xiao, Phys. Rev. A. **51**, 4, R2703, (1995).
- [5] A. S. Zibrov *et al*, Phys. Rev. Lett. **75**, 8, (1995).
- [6] M. D. Lukin *et al*, Laser Phys. **6**, 3, 436-447, (1996).
- [7] G. G. Padmabandu *et al*, Phys. Rev. Lett. **76**, 12, 2053, (1996).
- [8] E. A. Korsunsky *et al*, **56**, 5, 3908, (1997).
- [9] S. A. Hopkins *et al*, Opt. Com. **138**, 184-192, (1997).
- [10] T. Van der Veldt *et al*, Opt. Com. **137**, 420-426, (1997).
- [11] J. Kitching, and L. Hollberg, *Electromagnetically induced transparency in cold atoms*, (presented IQEC, (1998)).
- [12] R. R. Moseley, S. Shepherd, D. J. Fulton, B. D. Sinclair, and M. H. Dunn, Phys. Rev. A. **50**, 4339, (1994).
- [13] R. R. Moseley, Ph.D. thesis, University of St Andrews, 1994 (unpublished).
- [14] A. Corney, *Atomic and Laser Spectroscopy*, (Clarendon Press, Oxford, (1977)).

- [15] C. Cohen-Tannoudji, and A. Kastler, *Progress in Optics*. **V**, 3, (1966).
- [16] B. W. Shore, *The Theory of Coherent Atomic Excitation*, (Wiley, New York, (1990)).
- [17] S. F. Yellin, *Phys. Rev. A*. **57**, 5, 3858, (1998).
- [18] C. E. Moore, *Atomic Energy Levels - As derived From the Analyses of Optical Spectra*, (Circular of the National Bureau of Standards 467, (1952)).
- [19] Ny Tsi - Ze, and Tsien San - Tsiang, *Phys. Rev.* **52**, 91, (1937).
- [20] B. Cheron, H. Kucal, and D. Hennecart, *J. Phys. B: At. Mol. Opt. Phys.* **23**, 4281, (1990).
- [21] R. W. Falcone, W. R. Green, J. C. White, J. F. Young and S. E. Harris, *Phys. Rev. A*. **15**, 1333, (1977).

CHAPTER 6

Review of Inversionless Lasing and Gain Experiments Carried Out to Date

“It is a capital mistake to theorise before you have all the
evidence. It biases the judgement.”

Sir Arthur Conan Doyle

6.1 Introduction

The concept of lasing without inversion (LWI) [1] has been around for almost as long as the concept of the laser itself [2]. Schawlow and Townes proposed the laser in 1958 as an extension of the maser principle [3], and two years later Maiman built the first practical system [4]. It is accepted that conventional laser technology relies on the principle that a population inversion must first be created in the active medium in order that gain will exceed loss, and energy may be extracted from that medium to facilitate lasing [5]. Since the invention of the laser there have been various suggestions for circumventing this requirement. Indeed, as early as 1963 Marcuse proposed a method by which a laser could be created in the absence of a population inversion [1]. It has also recently been suggested that inversionless 'masing' takes place in interstellar space [6], and had been doing so long before the concepts of the laser and maser, both with and without inversion, were invented.

A laser is an amplifier of light and the requirement for a population inversion stems directly from the fundamental need for gain to exceed loss in order to achieve amplification. The mechanism for amplification is the process of stimulated emission. For gain to be greater than loss, this process must dominate that of stimulated absorption [5]. According to Einstein [7], the rate at which both these processes occur is dependent on the same parameter: the Einstein B coefficient. Therefore, if one atom exists in each of the upper and lower states of a transition then a resonant field interacting with the system is equally likely to stimulate either emission or absorption. It follows that the requirement for laser action is to ensure that more atoms exist in the upper than the lower state of the lasing transition, i.e. to invert the population.

Researchers are intrigued by the concept of LWI for the purely scientific reason that it defies conventional thought, and more practically because it may provide access to new regions of the electromagnetic spectrum. Conventional laser technology is limited by the requirement of a population inversion. As the wavelength of a transition decreases (frequency increases), the spontaneous emission rate from the upper level grows as the cube of the transition frequency. Consequently, it becomes more difficult to create and maintain a population inversion on a higher frequency transition because the population decays from the upper level so rapidly. The primary motivation of LWI research is

therefore to access high frequency (short wavelength) regions of the spectrum by removing the requirement to invert the population on the lasing transition.

This chapter reviews the experimental work achieved to date that employs quantum coherence to produce amplification and lasing without inversion (AWI and LWI). Before considering these experiments in detail, we trace the historical development of this field and place it in context with other methods that may be employed to obtain inversionless lasing. For a more detailed treatment of theoretical work on AWI and LWI the reader is directed towards earlier reviews of this topic [8-14].

6.2 Historical Development

In 1963 Marcuse pointed out that the energies of emission and absorption could be displaced by recoil, and that resonant absorption from the lower state could thus be eliminated [1]. The removal of absorption in this manner would obviate the need for a population inversion. However, this method does not provide access to high frequency transitions because the Doppler width is dependent on the recoil energy and makes the excitation requirement for sufficient gain very high. Ironically, this is precisely the problem that prevents conventional laser technology from reaching higher frequencies.

Earlier still, in 1961, Rautian and Sobel'man predicted amplification without inversion (AWI) in two level atoms driven by a strong resonant field [15]. This effect became apparent when the atom was treated quantum mechanically [16]. Amplification was possible when the Rabi frequency induced by the resonant field exceeded the line broadening. In this case, gain without inversion would be present in sidebands placed symmetrically about line centre. This effect was verified experimentally [17] and interpreted theoretically [18,19] by various research groups. Indeed, laser action in the absence of inversion has been observed by this method [20-23]. However, a device based on this approach should not be interpreted as a laser in the strictest sense because the energy necessary to create the output light field is not obtained from the medium; instead, it is transferred from one coherent field to the other with the medium acting merely as an intermediary. Furthermore, this method implies pumping by a coherent field that is resonant with the same transition on which the amplification is produced. It is therefore not possible to access new high frequency transitions by this approach.

In order to obtain frequency up-conversion it is necessary to employ an atomic system with three or more energy levels. Raman lasers satisfy this criteria and they provide both down and up-conversion of frequency based on Stokes and anti-Stokes scattering respectively. The quantum theory of the stimulated Raman process dates back to the early 1930's [24] and the effect is well known. In the case of Stokes scattering, a laser field coherently pumps the medium, in which a population inversion is not required, and lasing may be observed on another transition at a lower frequency. The Raman Stokes system is similar to the two-level atoms described previously, in that energy is not removed from the medium but it is passed from one coherent field to another. In a Raman

anti-Stokes laser, energy is extracted from the medium; however, although a population inversion is not required on the lasing transition it is necessary to invert the population on the connected two-photon transition. Although substantial research has taken place utilising anti-Stokes Raman scattering to achieve frequency up-conversion [25-27], we concentrate here on systems that rely on an underlying quantum coherence to reduce the absorption on a specific transition. Amplification can then be achieved by incoherently pumping the medium so that some population is excited into the upper level of the active transition. Importantly, the upper level of the transition is depleted in order to achieve gain and in this way energy is extracted from the medium as with a conventional laser. However, we must carefully ensure in such a scheme that the proportion of population in the upper energy state never exceeds that in the lower energy state. Lasing without inversion can only be achieved in this way by virtue of the underlying quantum coherence effect. The distinction between Raman processes and atomic interference has also been discussed elsewhere [28].

In addition to these more familiar approaches, LWI has been predicted [29] and observed [30] in microcavity lasers. In these systems the contribution of spontaneous emission to the lasing mode optical output is no longer negligible, to the extent that the lasing threshold can be reduced such that lasing can be observed without population inversion. LWI has also been investigated in Free-Electron lasers [31] which work on the basic principle that an accelerating electron must absorb energy and a decelerating electron must radiate it [32]. Finally, LWI has recently been demonstrated by Faist *et al* [33] in a Quantum Cascade Laser.

6.2.1 Gain and Lasing Without Inversion by Quantum Coherence

We will now focus on the development of LWI based on the quantum coherence effects of Fano interference, coherent population trapping (CPT), and electromagnetically induced transparency (EIT). While there are features that distinguish these effects they all describe a specific case (or cases) of the same basic phenomenon. However, as Mandel stated in his review of this topic [12]: "...most workers disagree on the precise definition of what they mean by LWI or AWI." This disparity is due to the fact that the development of this field was pioneered independently by several different research groups.

Following the discovery of Fano interference [34] in the early 1960s (see Section 1.2) Arkhipkin and Heller presented analysis showing that this effect could be harnessed to amplify radiation in the absence of a population inversion [35]. In their paper a discrete level embedded in the continuum exhibits a Fano interference between direct photoionisation to the continuum and the indirect excitation via the discrete level. Importantly, there was shown to be no reciprocal interference in the emission cross-section of this system. Harris extended this work to the interference of lifetime broadened resonances in 1989 [36], and he coined the term EIT shortly afterwards to describe a generalised form of Fano interference in which the coherence could be supplied by an additional 'coupling' or 'driving' laser field rather than the presence of an autoionising state in the continuum [37]. Independently, Kocharovskaya and Khanin described a theoretical scheme in which amplification of an ultrashort pulse could be achieved in the absence of a population inversion [38]. Their theory was based on the early experiments involving coherent population trapping that were discussed in Section 1.2 [39,40]. In 1989, shortly after Harris' initial paper, Scully and co-workers proposed a scheme for inversionless lasing called the 'degenerate quantum-beat laser' [41]. Collectively these papers [35,36,38,41] represent the initial theory of AWI and LWI that has now led to the successful realisation of both these phenomena in real atomic systems.

The significant link between Fano interference and coherent population trapping was made by Coleman and Knight in 1982 [42]. It is important given the subtleties of each effect that they continue to be considered as distinct phenomena, but it is helpful to keep in mind that they involve the same central process. As Harris pointed out in a recent review of electromagnetically induced transparency [43]: "the physical effect that is the essence of EIT is called coherent population trapping". Finally, we note the words of Scully and Fleischhauer in their review of LWI [8]. Having highlighted the differences between the origin of gain in specific systems, the authors state that "in all cases, however, atomic coherence and interference explains the physics, and we emphasise the utility and generality of this approach."

We will now consider the experimental AWI systems that have been realised to date, where the definition of AWI follows that of Mandel [12] with some slight modification and addition: AWI is "a mechanism that will lead to the amplification of a

weak probe field by transfer of energy from a strong and coherent driving field (if any) and by extraction of energy from the material (specifically by depleting the upper level of the lasing transition) without the prerequisite of a population inversion between the lasing levels." Importantly, this amplification is made possible by the reduction of absorption on the active transition which is achieved in the presence of atomic coherence and interference.

6.3 Experimental Amplification Without Inversion

We now consider, in chronological order, the nine schemes in which AWI has been realised experimentally. The subsequent section will concern LWI schemes after which the future of this field will be assessed, particularly in the context of LWI with frequency up-conversion. The distinction between AWI and LWI is simply that in the latter case the active medium has been placed inside an appropriate cavity that acts to feedback the gain achieved in the former case and hence produce an output laser beam.

6.3.1 Gao *et al*, June 1992 [44]

The first experimental observation of AWI was made by Gao and co-workers in Changchun, China [44]. The authors utilised a system previously proposed by Narducci *et al* [45] in which a nearly degenerate pair of ground state levels is coupled to a high lying state by a coherent field. The off-resonance interaction of the ground state levels with the excited state creates a coherent superposition between the ground state levels. These levels are also coupled to another excited state upon which the attenuation or amplification of a weak probe field is monitored. In the presence of an external incoherent pumping mechanism, which excites a small proportion of the atomic population into the upper level of the probe transition, amplification is predicted on the probe field [45].

Gao *et al* employed such a scheme in sodium vapour as shown in Fig. 6.1. The ground state levels are the $F=2$ and $F=1$ hyperfine components of the sodium $3S_{1/2}$ ground state. These levels are coupled, by an intense pulsed laser field at 589.6nm, to the $3P_{1/2}$ excited state. This laser field drives the coherence in the system, and it is provided by a tuneable Dye laser with a linewidth of 8GHz and a pulse duration of 8ns. The probe transition is formed between the hyperfine split ground state levels and the $3P_{3/2}$ excited state. The weak probe field is supplied by a continuous wave ring cavity Dye laser operating at 589.0nm with a linewidth of 1MHz. Incoherent pumping is provided by a dc discharge of 53V.

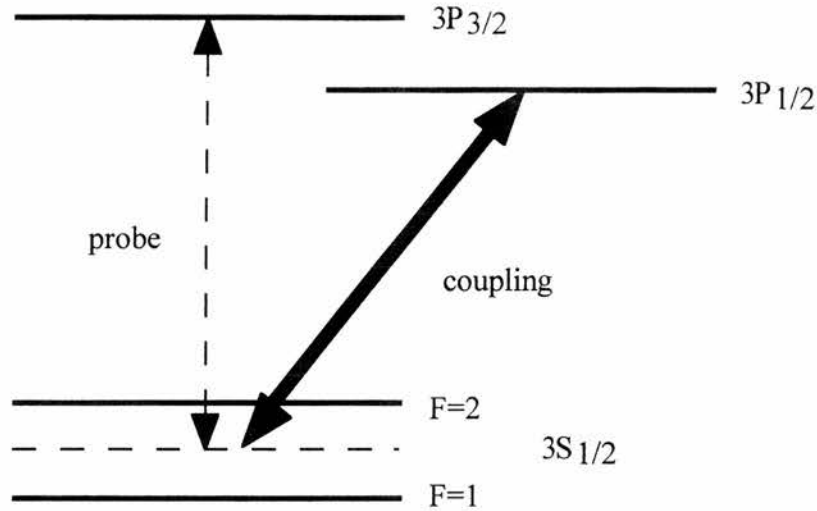


Figure 6.1: Schematic energy level diagram of the levels employed in sodium vapour. $F=1$ and $F=2$ are the hyperfine components of the $3S_{1/2}$ ground state. The dashed line indicates the mid-point between these hyperfine states.

The active region of the sodium cell is 3mm long. The transmitted probe field is monitored with a photomultiplier tube and processed by a box car integrator that is carefully synchronised with the coherent driving pulse. Results obtained in this fashion show straightforward Doppler-broadened absorption in the absence of the coherent driving field, and gain in Rabi-like sidebands evenly spaced about line centre when the driving laser pulse is applied. The presented results [44] show reasonable qualitative agreement with the previous theory [45], particularly when bearing in mind the following mitigating factors. The theory developed by Narducci *et al* was based on steady state conditions; whereas, the experiment conducted at Changchun employed a driving laser field with a pulse duration significantly shorter than the atomic lifetimes of both excited states. In addition, the theoretical analysis did not account for Doppler effects or the underlying degeneracy of the hyperfine ground state levels that would have affected the experimental results.

In light of this fact Doss *et al* carried forward the theoretical analysis in 1993 by modelling the same system in the transient regime [46]. Good experimental agreement was

obtained, particularly by showing that the separation of the Rabi sidebands scaled with the driving field intensity, and the effect of detuning the driving field on the relative magnitudes of these sidebands. Narrow spectral features at line centre were predicted by the theory. The fact that these were not observed experimentally was explained by the omission of Doppler-broadening in the theoretical model.

In 1994 Meyer *et al* published analysis of this experiment that included the effects of the magnetic sub-levels of the $F=2$ and $F=1$ hyperfine ground states [47]. This treatment concluded that since Gao and co-workers had utilised linearly polarised light, no coherence could have been established between the ground states. Indeed, controversy over this first observation of AWI already existed due to the fact that the presence or lack of a population inversion had not been verified by any means in the original experiment. To redress the balance Gao *et al* published a second set of results in 1994 [48]. In this follow up experiment a long laser pulse was used as the driving field with a duration in excess of the atomic lifetimes of the employed excited states. Amplification was also demonstrated on both the 589.0nm and 589.6nm transition by exchanging the probe and driving fields. The authors attempted to verify the absence of inversion by demonstrating that no gain was observed when the driving field was absent and the discharge present, or vice versa. In addition, the population distributions in the excited states were calculated from experimental measurements of absorption and spontaneous emission. However, the controversy surrounding these early experiments still remains. The first concrete evidence of AWI was supplied by Nottlemann *et al* [49].

6.3.2 Nottlemann *et al*, March 1993 [49]

Nottlemann *et al* presented clearer evidence of AWI in 1993 [49]. Their system was based on a Lambda type scheme driven by a short pulse, in which coherence is established between two low lying states [38,50]. The experiment was carried out in samarium vapour in the presence of a static magnetic field which controlled the Zeeman splitting between the low-lying states. The energy level diagram of this system is shown in Fig. 6.2. Contrary to the typical Lambda scheme, the employed configuration included a third lower level which facilitated the excitation of population into state $|4\rangle$ without disturbing the Zeeman coherence set up between the low lying $|1\rangle$ and $|3\rangle$ states.

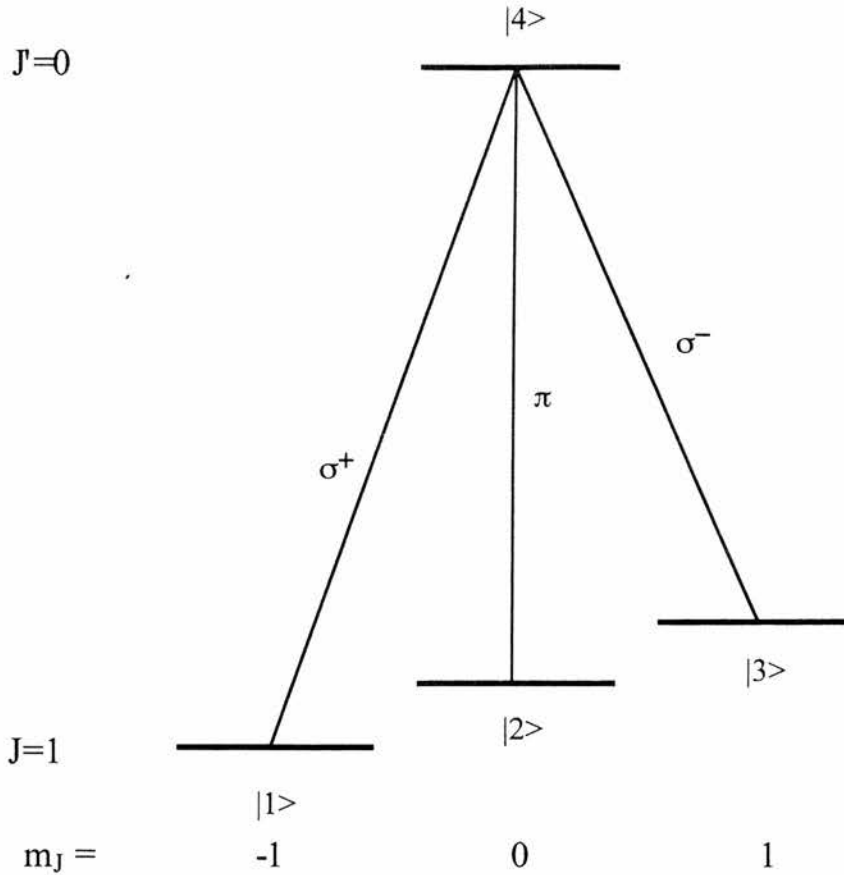


Figure 6.2: Energy level scheme for the $J=1 - J'=0$ transition in samarium vapour.

An equidistant train of picosecond pulses is applied to the $J=1 - J'=0$ transition at 570.68nm. The linear polarisation of the pulse train is arranged perpendicular to the magnetic field so that only the σ^+ and σ^- transitions are driven. This action establishes the necessary coherence between states $|1\rangle$ and $|3\rangle$. The pulse train has an RF period T_p , and each pulse causes the Zeeman coherence to oscillate with the double Larmor frequency (2Ω). Discrete values of the magnetic field are chosen such that the coherence oscillation period is RF resonant with the pulse train:

$$\frac{\pi}{\Omega} = \frac{T_p}{n} \quad \text{where } n=1, 2, \text{ or } 4 \quad (6.1)$$

A test picosecond pulse of similar polarisation follows the last pulse of the train with a delay time of $T_p/4$. By altering the discrete value of the magnetic field (i.e. n) the test pulse will arrive at different phases of the oscillating Zeeman coherence. If $n=1$ the real part of the coherence is zero, and the test pulse is attenuated; if $n=2$ the coherence has

a maximum positive value, and the attenuation is increased; finally, if $n=4$ the real part of the coherence is negative, and inversionless amplification can be achieved.

During the delay time $T_p/4$ the optical coherences (but not the Zeeman coherences) relax almost completely, as does the upper state population established by the driving pulse train. In order to provide some population in state $|4\rangle$, without creating an inversion, an orthogonally polarised pump pulse is applied to the medium 175ps before the test pulse arrives. Due to the polarisation of the pump pulse it drives the π transition, re-establishing a modest upper state population, without disturbing the σ^+ and σ^- transitions.

AWI was observed by this method, employing a synchronously pumped Dye laser to provide the driving test and pump pulses. The lack of an inversion is carefully ensured by limiting the area of the employed picosecond pulses, such that at no time is an inversion present in the system. The absence of inversion is also demonstrated experimentally by the fact that no gain is observed when $n=1$. Indeed, the presented results clearly show amplification without inversion (when $n=4$) in good agreement with the accompanying theory. Note that the maximum gain achieved of 7% was limited in this system by dispersion which affects the pulse propagation; consequently, the experiment was restricted to an optically thin sample (5mm).

Further analysis of these results was provided by the same group in a subsequent paper which also demonstrated that the same set-up could be used to achieve 'inversion without amplification' [51].

6.3.3 van der Veer *et al*, May 1993 [52]

In May 1993 experimental papers were published by van der Veer *et al* [52] and Fry *et al* [53] which showed AWI. The former demonstrated experimentally both amplification and the absence of inversion. Amplification without inversion was facilitated by establishing a coherence between magnetic sub-states as in the Nottlemann experiment [49]. The principle difference between these schemes is that van der Veer and co-workers utilised separate transitions for the coupling and probe laser pulses. The energy level scheme employed in cadmium vapour is shown in Fig. 6.3.

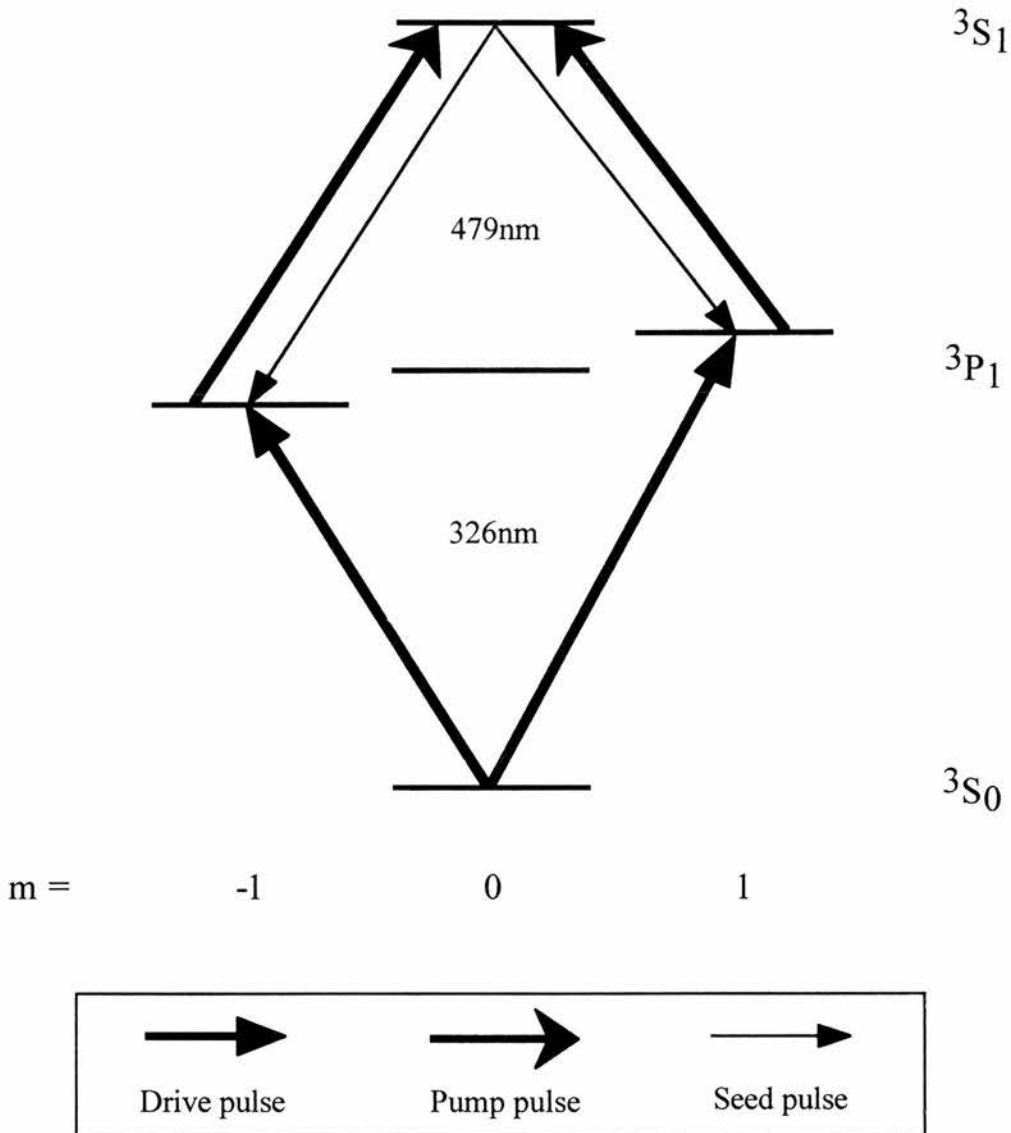


Figure 6.3: Energy level scheme utilised in cadmium vapour in which the drive pulse coherently populates the $m=-1$ and $m=1$ levels of the $3P_1$ state.

A Q-switched Nd:YAG laser pumped two pulsed Dye lasers. The first was frequency doubled by KDP to 326nm and the second operated at 479nm, resonant with the $5s2\ ^1S_0 - 5s5p\ ^3P_1$ and $5s5p\ ^3P_1 - 5s6s\ ^3S_1$ transitions in cadmium respectively. A linearly polarised light pulse, provided by the first laser, excites population into the $3P_1$ state, and it creates a coherent superposition of the $m=1$ and $m=-1$ magnetic sub-states in the presence of a static magnetic field. The coherence thus prepared, oscillates with a

frequency dependent on the splitting of the magnetic sub-states that is determined by the strength of the magnetic field. A subsequent pulse arrives, provided by the second dye laser, resonant with the $^3P_1 - ^3S_1$ transition. This 'pump' pulse excites a fraction of the population into the high energy 3S_1 state. The polarisation of this light pulse is perpendicular to the first pulse to ensure that the maximum excitation of population will occur when the applied magnetic field is zero. A small portion of the light from the second laser is delayed and reduced in intensity to form a seed or 'test' pulse. The magnetic field is supplied, parallel to the pump and seed beams, by a set of magnetic field coils. Varying the current through these coils controls the strength of the field, the splitting of the magnetic sub-levels, and hence the oscillation frequency of the coherence that has been established between them.

The fluorescence from the upper 3S_1 state and the amplification of the seed pulse are monitored as a function of the magnetic field strength. The former provides an indication of the population in the excited 3S_1 state. Results showed that both these parameters varied with respect to the field strength and both reached a maximum when the field was zero. The key question is whether the population at this point is inverted on the amplified $^3P_1 - ^3S_1$ transition. Van der Veer *et al* addressed this point by repeating the experiment with no delay between the first and second laser pulses. Consequently, the upper state population was no longer dependent on the magnetic field strength. As the magnetic field strength is increased, the oscillation frequency of the coherence becomes short compared with the duration of the driving laser pulse. In this instance, atoms within the vapour will be excited at different times and therefore with different phase. Therefore, increasing the magnetic field strength will dephase the coherence between the magnetic sub-levels. Experimental results demonstrated that this increase in field strength caused the gain to diminish, which proves that the amplification obtained in this system was inversionless. A gain factor of 4.3 (defined as the integral of the amplified pulse divided by the integral of the seed pulse) is obtained for a cell volume of 3cm^3 at a temperature of 220°C .

6.3.4 Fry *et al*, May 1993 [53]

The Fry experiment demonstrates amplification, in the absence of a population inversion, of a pair of laser beams that are also responsible for preparing the necessary

atomic coherence [53]. This novel scheme allows the authors to make a clear experimental demonstration of the presence of coherence between the sub-levels of the hyperfine split ground state in sodium. The D_1 line in sodium is used, as it was in the Gao experiment [44], and the energy level structure is shown in Fig. 6.4. Figure 6.4 (b) shows the detailed structure including magnetic sub-states while Fig. 6.4 (a) shows the simple four level scheme that can be used to explain the underlying physics.

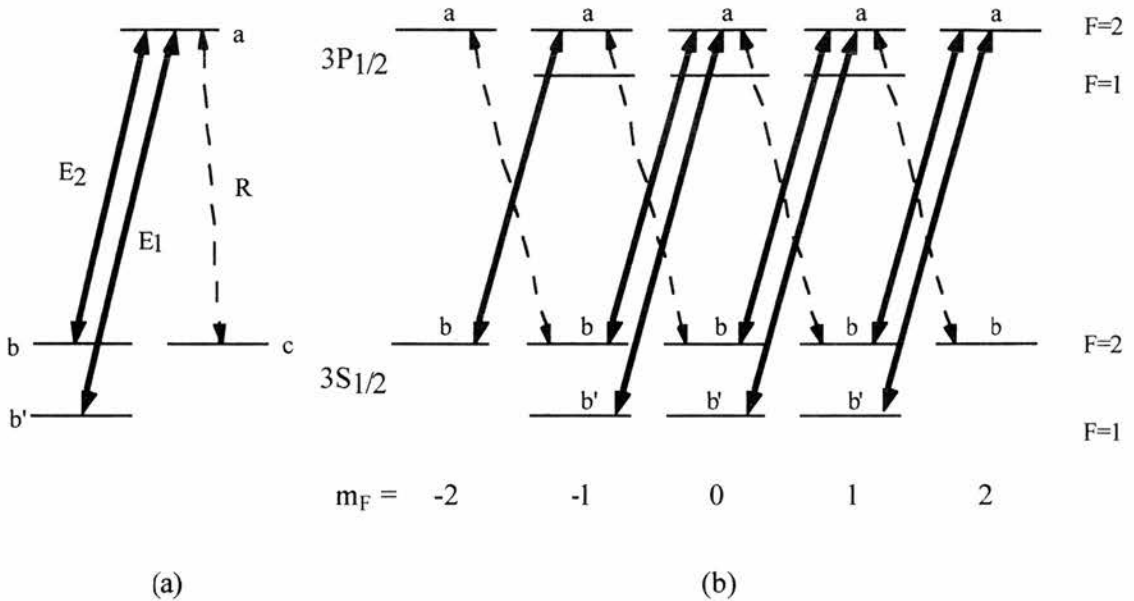


Figure 6.4: Energy level scheme in sodium vapour with driving fields E_1 and E_2 , and pumping field R . (a) Generic four level system. (b) Detailed energy level structure including hyperfine and magnetic sub-levels.

A frequency doubled continuous wave Dye laser is resonant with the $3S_{1/2}$ ($F=2$) - $3P_{1/2}$ ($F=2$) transition (E_2). The same beam passes through an acousto-optic modulator, and it is frequency shifted by 1.77GHz to be resonant with the $3S_{1/2}$ ($F=1$) - $3P_{1/2}$ ($F=2$) component of the D_1 line (E_1). Both beams are right circularly polarised, and as mentioned previously, Meyer *et al* have shown, by taking the hyperfine structure of sodium into account, that circularly polarised beams are necessary to establish coherence in the sodium ground state sub-levels [47]. The Fry experiment consisted of three phases: the first demonstrated the existence of coherence between the hyperfine split levels of the ground

state ($3S_{1/2}$ ($F=2$) and $3S_{1/2}$ ($F=1$)), the second demonstrated amplification of the laser fields, and the third verified the lack of inversion between the $3P_{1/2}$ and $3S_{1/2}$ levels.

'Coherence switching' was employed to indicate the presence of a trapped coherent state. By considering the energy levels in Fig. 6.4 (b) we see that in the absence of any coherent effect, the population would be optically pumped by the two applied fields into the b state for which $m_F = 2$. However, the coherence established between the pairs of b and b' ground state sub-levels traps a fraction of the atomic population in these states [39,40]. To verify this hypothesis experimentally one of the two driving fields is turned off. In the event that population was coherently trapped in the b and b' states, this population would be released and the remaining field would begin to absorb. Therefore, as the coherence is switched off, so too is the transmission of the remaining optical field. Indeed, this outcome was clearly demonstrated in the experiment.

To produce AWI, a fraction of the Dye laser beam is left circularly polarised and directed into the cell. This geometry causes excitation of a fraction of the ground state population into level $3P_{1/2}$ (as shown by the dotted lines in Fig. 6.4 (a) and (b)). Amplification of the E_1 field is observed, but it diminishes after a few radiative lifetimes because the population of atoms that can be excited is depleted and the population in the b' state accumulates in excess of the trapping fraction. Nevertheless, amplification is demonstrated of up to 10% with a 40mm cell length at a temperature in the range of 150 to 200°C.

To verify the lack of inversion between the $3S_{1/2}$ ground state and the $3P_{1/2}$ excited state the experiment was repeated but as the left circularly polarised pump field arrived the E_2 field was switched off. Since the latter action destroys the coherence, the presence of amplification in this instance would indicate that an inversion was present in the system. However, it was experimentally shown that only absorption of the E_1 field occurred in this regime; therefore, the amplification demonstrated with both fields present was inversionless.

This experiment has been considered in detail, by various authors, in an issue of Quantum Optics dedicated to Willis Lamb [47,54,55]. In addition, Graf and Arimondo have explored the effects of atomic collisions and Doppler-broadening in this system [56].

We now consider the first demonstration of steady state gain that was made by Kleinfeld and Streater [57].

6.3.5 Kleinfeld and Streater, June 1994 [57]

Kleinfeld and Streater used the system described originally by Narducci *et al* [45] to obtain the first observation of steady state AWI [57]. The basic scheme was described previously in Section 6.3.1. The specific energy level structure utilised in potassium by Kleinfeld and Streater is depicted in Fig. 6.5. The authors of this experiment pointed out that both the ρ_{12} and ρ_{34} coherences were responsible for the observation of amplification in the absence of inversion, and that the relative contributions of these coherences would depend on the exact parameters of the system and the conditions of the experiment. In addition, Kleinfeld and Streater noted that the coherence between the low-lying sub-levels was dependent on both the ground state relaxation (mixing) rate being small compared to the relaxation rate of state $|4\rangle$, as well as the separation of the ground state sub-levels being small compared to the Rabi frequency induced by the driving field.

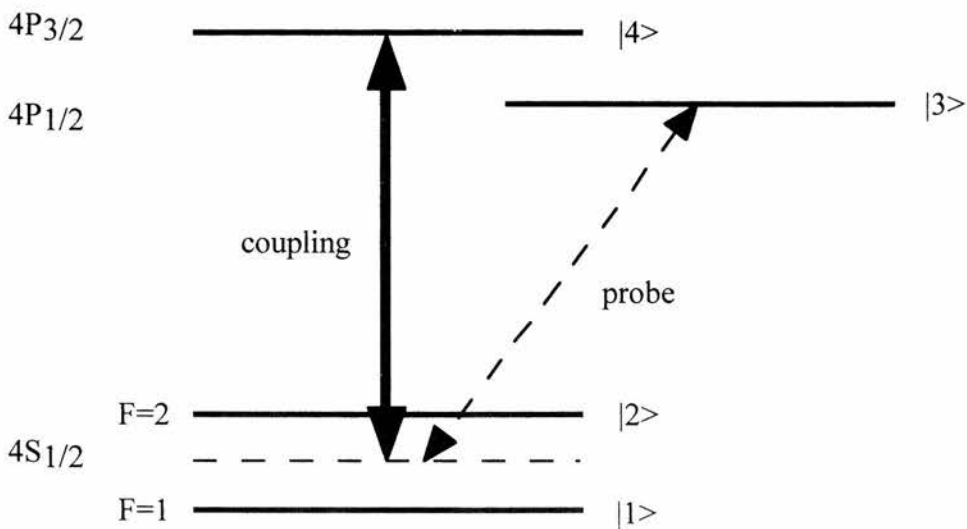


Figure 6.5: Energy level scheme in Potassium vapour. The dashed line corresponds to the mid-point between the $F=2$ and $F=1$ hyperfine components of the $4S_{1/2}$ state.

The driving field resonant with the $4S_{1/2} - 4P_{3/2}$ transition (D_1 line) was supplied by a Kr^+ pumped single mode continuous wave (cw) Dye laser. A single mode cw Ti:sapphire laser was utilised for the probe beam and both lasers co-propagated through the potassium cell. A buffer gas was introduced into the cell in order to populate the upper level of the probe transition by collisional transfer from level $|4\rangle$. Helium was used since this minimised the dephasing of coherence that would also result from collisional processes [58,59].

Experimental results demonstrated good agreement with the theoretical model described in the same paper [57]. Gain was observed, which reached a maximum when the probe laser was detuned from resonance. In the latter case a distinct spectral feature exhibiting gain was resolved from the absorption profile. The authors speculate that this feature could also be achieved with a three level scheme, i.e. without the ground state ρ_{12} coherence. They concluded that gain in this regime was driven by the coherence between levels $|3\rangle$ and $|4\rangle$. Indeed, this feature is a demonstration of gain for the two-photon process associated with the probe transition, and it is made possible by the presence of the driving field. Kleinfeld and Streater repeated the experiment with the probe and coupling transitions reversed, observing no gain due to the unequal collisional transfer rates between the excited states of the transitions concerned.

By altering the pressure of the helium buffer gas, further results were obtained. It was shown that for a low buffer gas pressure, gain could not be observed on either the D_1 or the D_2 line in potassium because the transit relaxations increased while the collisional transfer of population between excited states reduced. Conversely, if the buffer gas pressure is raised, gain can be achieved on resonance, and experimental curves in good agreement with Narducci *et al's* original theory were obtained for the splitting of the gain profile as a function of driving field power [45].

While no direct measurements were taken to confirm the lack of inversion in their original experiment Kleinfeld and Streater showed that no inversion existed in their theoretical model by a large margin, and that this model demonstrated good agreement with experimental results. Subsequent to their first experimental paper, Kleinfeld and Streater published further analysis of this experiment which included observation of coherence effects on the violet $4S_{1/2} - 5P_{3/2}$ transition in Potassium (no gain was observed) and a

discussion of the problems associated with making direct measurements of the atomic state populations [60]. In 1996 a further study was presented that examined the impact of coherence dephasing and most importantly provided measurements of the relative populations that indicated that the $4P_{1/2} - 4S_{1/2}$ transition was not inverted in the original experiment [61].

Note that in Chapter 4 we saw that the two-photon process in a Vee scheme diminishes as detuning is increased. Contrary to this prediction, Kleinfeld and Streater observe a strong two-photon effect for large detunings of the coupling field. The two-photon process remains strong in their scheme because the detunings employed are of the same order of magnitude as the Rabi frequency induced by the driving field; consequently, the upper level of the coupling field transition remains populated.

6.3.6 Zibrov *et al*, May-June 1995 [62]

Zibrov and co-workers showed AWI in a four level system very similar to that of Kleinfeld and Streater [57] and Gao *et al* [44], except that the driving field was resonant with one specific ground state sub-level rather than detuned between them [62]. Consequently, Zibrov's system does not rely on any low level ρ_{12} coherence, but rather the coherence induced between the upper states labelled a and c in Fig. 6.6. The coherence thus obtained was explained in terms of quantum interference between multiple pathways to absorption on the probe transition, as described in Section 1.3.2 of this thesis.

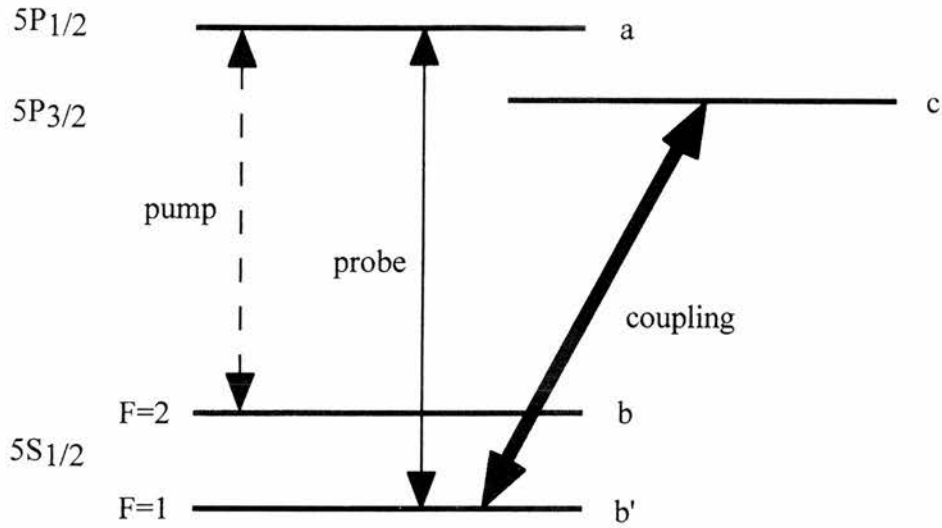


Figure 6.6: Simplified energy level scheme in ^{87}Rb .

The probe and driving fields were provided by cw tuneable extended cavity diode lasers resonant with the D_1 ($5S_{1/2} - 5P_{1/2}$) and D_2 ($5S_{1/2} - 5P_{3/2}$) lines of ^{87}Rb respectively. With both these fields tuned to the $F=1$ ground state sub-level, optical pumping would occur due to the driving field, and the absorption would be significantly reduced on the probe transition. A pump source is provided by an unstabilised diode laser with a linewidth greater than the radiative decay of the transition. This laser therefore acts as an incoherent pump replacing the population optical pumped out of state b' . At the same time a modest population is established in the upper level of the probe transition. Note that a weak magnetic field is required to destroy the Zeeman coherence established in the magnetic sub-levels of the $F=2$ ground state by the incoherent pump.

Experimental results show the Doppler-broadened absorption profile in the absence and presence of the incoherent pump field. Initially, a reduction in absorption is observed due to the presence of the driving field in the absence of incoherent pumping. However, since the pump field is also used to destroy optical pumping, the latter is still present in these results. The transmission peaks in the absorption spectrum can therefore be attributed to optical pumping of velocity groups associated with the $5S_{1/2}$ ($F=1$) - $5P_{3/2}$ ($F=2$), the $5S_{1/2}$ ($F=1$) - $5P_{3/2}$ ($F=1$), and the $5S_{1/2}$ ($F=1$) - $5P_{3/2}$ ($F=0$) transitions by the drive field. When the incoherent field is introduced a narrow amplification feature is

observed, and the rest of the absorption profile increases in magnitude. The former effect is facilitated by the underlying quantum interference, and the latter observation is caused by the destruction of optical pumping. Gains of 10 to 16% were observed for a 4cm cell at 50°C [62].

The lack of inversion is verified in this experiment by increasing the linewidth of the probe laser. This broadening of the linewidth can be achieved by modulating the driving current of the laser diode. In the regime where the laser linewidth greatly exceeds the decay rate of the probe transition the probe field can no longer coherently interact with the rubidium atoms. Therefore, we would only expect to observe gain if a population inversion was present on the probe transition. Zibrov *et al* found that the amplification rapidly diminished when the probe linewidth was increased, proving that amplification was in fact achieved in the absence of inversion. Indeed, as we shall see in Section 6.4.1 inversionless lasing was subsequently achieved in this system [63].

6.3.7 Zhu and Lin, March 1996 [64]

The reported experiment describes the observation of sub-Doppler AWI in rubidium vapour [64]. Despite the Doppler-broadening present in the experimental system, the authors observe a spectrally narrow gain feature for a coupling field Rabi frequency much lower than the Doppler width. This observation is made possible by matching the wavelengths of the probe and coupling fields, as described in Chapter 4, and resolving the single and two-photon absorption processes by detuning the coupling field from resonance. A Lambda scheme is employed for this work, following the theoretical study of Imamoglu *et al* [65] as shown in Fig. 6.7. This experiment demonstrates a similar observation of AWI to that made by Kleinfeld and Streater [57]. Both systems exhibit gain in the resolved two-photon process. The principal difference is the choice of energy level configuration which was a Vee scheme in the earlier experiment and a Lambda scheme in the current system.

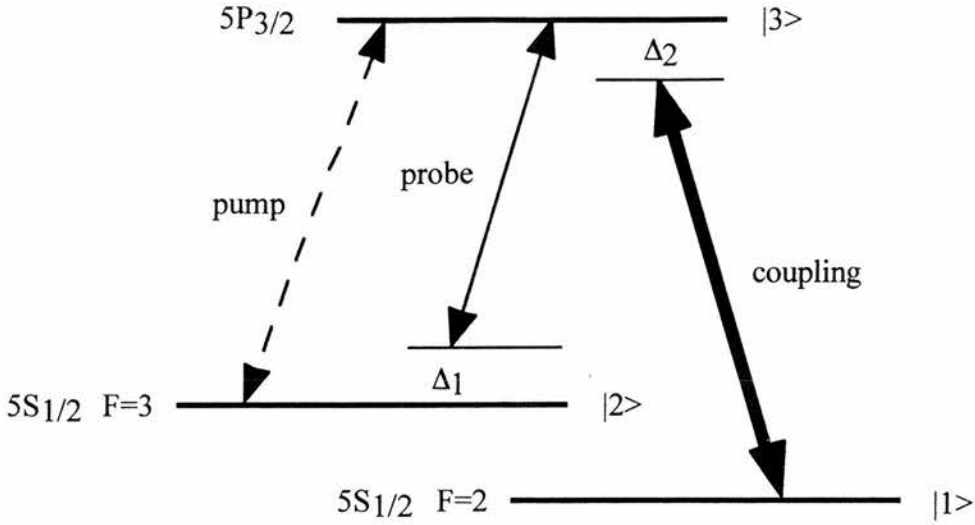


Figure 6.7: Energy level scheme for ^{85}Rb . In ^{87}Rb the ground states are $5S_{1/2}$ ($F=2$) and $5S_{1/2}$ ($F=1$).

The levels labelled $|1\rangle$ and $|2\rangle$ in Fig. 6.7 are the hyperfine split ground states of rubidium. Both naturally occurring isotopes, ^{85}Rb and ^{87}Rb , are present in this experiment. The ground state sub-levels of Fig. 6.7 are labelled according to the ^{85}Rb isotope for which level $|1\rangle$ is $5S_{1/2}$ ($F=2$), level $|2\rangle$ is $5S_{1/2}$ ($F=3$), and the splitting between them is approximately 3GHz. For the ^{87}Rb isotope level $|1\rangle$ is $5S_{1/2}$ ($F=1$), level $|2\rangle$ is $5S_{1/2}$ ($F=2$), and the splitting is approximately 6GHz (for a fuller treatment of rubidium's atomic structure refer to Section 3.6). The coupling field drives the transition between the lower of the two hyperfine ground states ($5S_{1/2}$ ($F=2$) for ^{85}Rb and $5S_{1/2}$ ($F=1$) for ^{87}Rb) and the $5P_{3/2}$ excited state. The probe laser is tuned to the transition between the higher of the hyperfine ground states ($5S_{1/2}$ ($F=3$) for ^{85}Rb and $5S_{1/2}$ ($F=2$) for ^{87}Rb) and the $5P_{3/2}$ excited state. The pump laser is resonant with the same transition as the probe. The coupling, probe and pump lasers are provided by a cw Ti:sapphire, a cw external cavity diode, and a cw temperature-stabilised diode respectively. While the coupling and probe beams co-propagate to achieve cancellation of the Doppler shifts, the pump propagates in the opposite direction through the cell. Importantly, the linewidth of

Gain is observed in both rubidium isotopes when the coupling laser detuning is approximately equal to the probe field detuning, i.e. when the zero velocity group of atoms is in two-photon resonance. Experimental results are only reported for the regime in which the coupling field detuning is greater than zero. 10% gain is recorded for ^{85}Rb (relative abundance of 72%) for a 7.5cm cell length at 60°C. The authors provide theoretical analysis of this system from both the density matrix and dressed state perspective [64]. The origin of gain in this scheme is a hidden inversion in the dressed state basis which is manifested as the ρ_{12} low level coherence in the bare state picture. Although no direct measurement of the populations was made, the authors point out that the dominance of absorption at line centre indicates a lack of inversion in the bare states.

The authors also note that the difference between their system and a similar Raman lasing scheme [66] is the requirement for some population in the upper level of the probe transition. Having said that, it is arguable that the gain observed in both the Kleinfeld and Streater [57], and Zhu and Lin [64] experiments is not due to atomic interference (in the former case this comment refers only to the gain achieved with significant coupling field detunings). The cancellation of absorption that can be achieved in such a scheme is realised when the single and two-photon resonances are coincident; whereas, these demonstrations of AWI operate in the opposite regime. Although gain may be observed without population inversion on the probe transition, it is the two-photon process that is clearly giving rise to this gain in much the same way as a Raman laser. The origin of the gain reported in these experiments is not identical to that achieved in a purely Raman based system, nor is it identical to that found in a scheme for which the single and two-photon processes interfere to provide the underlying reduction in absorption that makes AWI possible. In fairness to the authors they do not claim that the origin of gain in their system is quantum interference [62] rather that inversionless amplification is possible due to a hidden inversion in the dressed states. These last two experiments [62,64] highlight the distinction between these two mechanisms for AWI.

6.3.8 Fort *et al*, June 1997 [67]

AWI is demonstrated for a Vee-type scheme in caesium vapour [67]. As with previous experiments [53,57,62,64] the use of closely matched probe and coupling

wavelengths allows observation of a narrow gain feature in a Doppler-broadened medium. One interesting aspect of this experiment is that the hyperfine structure of atomic caesium is resolvable even in the Doppler limit. The smallest hyperfine splitting on the caesium D_1 line is 1168MHz [68], which is significantly greater than the Doppler width at room temperature (380MHz). This property of caesium allows the authors to make a comparison of the transparency and gain achievable with different hyperfine states.

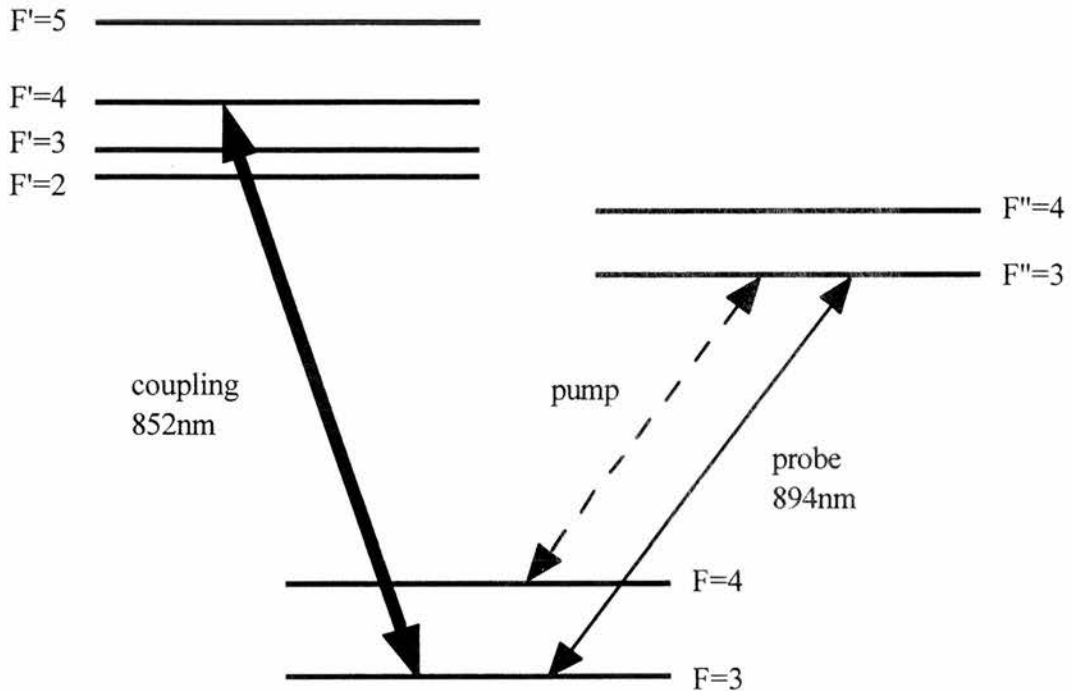


Figure 6.8: Energy level scheme for caesium vapour, including the hyperfine levels. The laser fields are in the configuration that provides maximum gain.

The energy level structure employed in this experiment is shown in Fig. 6.8. The coupling field is provided by a diode laser resonant with one of the hyperfine components of the D_2 line (852nm), the frequency of which is controlled by injection locking. An extended cavity diode laser probes the D_1 line (894nm) while a third diode laser beam, also resonant with the D_1 line, provides a small upper state population and destroys optical pumping. Note that the latter 'pump' laser has its linewidth artificially broadened by injecting noise into the drive current.

Experimental results demonstrate both transparency (in the absence of the pump) and gain (in the presence of the pump). The authors note that better transparency and subsequent amplification are achieved for hyperfine states with lower F numbers. In addition, they found that a small magnetic field applied perpendicular to the incoherent pump polarisation increased gain by reducing the Zeeman alignment in the ground state. The absence of a population inversion was indicated by the fact that the main effect of the pump field, off resonance, was to increase the absorption of the probe field. The same observation was made by Zibrov *et al* [62] and it is a consequence of the pump field destroying optical pumping. A maximum gain of 2.5% was observed in a 4cm cell at 40°C when the probe was resonant with the $F=3 - F''=3$ component of the D_1 line and the coupling field was resonant with the $F=3 - F'=4$ component of the D_2 line. The authors suggest a future scheme in which the probe has a shorter wavelength of 386nm on the $6S_{1/2} - 8S_{1/2}$ transition.

6.3.9 Durrant *et al*, May 1998 [69]

The final AWI experiment to be considered exhibits inversionless gain in a sample of cold rubidium atoms [69]. This observation is achieved by placing rubidium in a magneto-optic trap and inducing coherence between the Zeeman sub-states of the $F=1$ component of the $5S_{1/2}$ ground state in ^{87}Rb . AWI is reported as part of a wider investigation into EIT, CPT, and optical pumping in laser-cooled rubidium. The experiments included a study of the effects of different relative beam polarisations on the induced transparency. Such investigation is possible in a magneto-optical trap because Doppler effects are negated and the associated constraints on beam geometries, powers and wavelengths are removed.

A sample of ^{87}Rb atoms is prepared in a conventional magneto-optic trap. The trapping beams are provided by external cavity grating-controlled laser diodes operating at approximately 780nm, and the spherical quadrupole magnetic field has an axial gradient of 12Gcm^{-1} . The trapping beams are tuned close to the $F=2$ to $F'=3$ hyperfine component of the $5S_{1/2} - 5P_{3/2}$ transition to trap approximately 2×10^6 atoms, in the absence of a re-

pumping beam, in the $F=1$ ground level. Sub-mK temperatures can be achieved by this method.

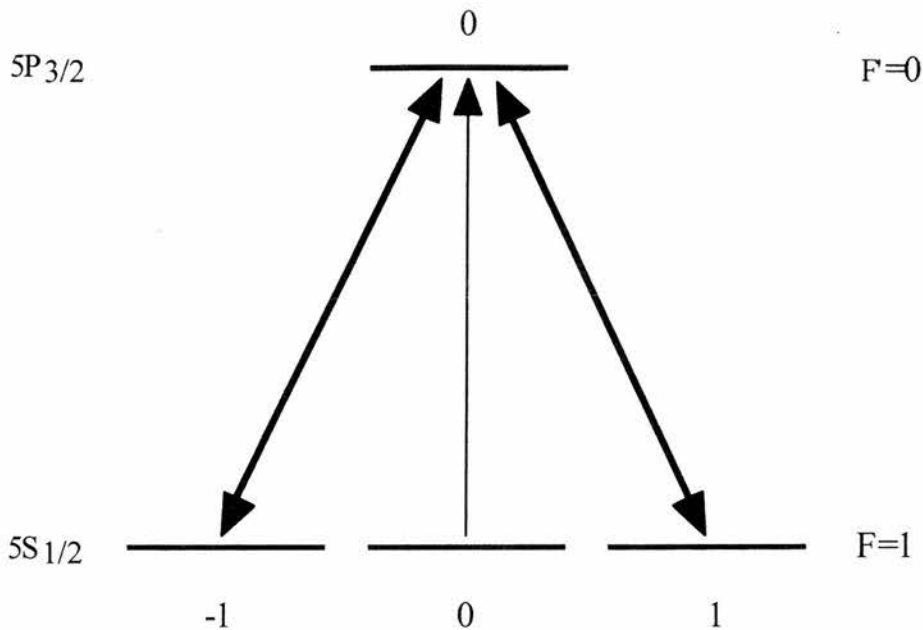


Figure 6.9: Energy level scheme employed in ^{87}Rb to provide inversionless gain. The double headed arrows indicate the driving beams and the single headed arrow represents the probe beam.

Figure 6.9 depicts the Zeeman sub-states for the considered hyperfine component of the $5S_{1/2} - 5P_{3/2}$ transition. The coupling and probe beams are supplied by linewidth narrowed laser diodes, and a similar laser is linewidth broadened to provide incoherent pumping on the probe transition. Linewidth broadening is achieved by means of an acousto-optic modulator driven by RF white noise (as described in Section 3.5). Absorption is reduced on the probe transition via the coherence induced between the Zeeman sub-states $m_F=-1$ and $m_F=1$. In the presence of the pump laser, gain is observed when the coupling field is detuned from resonance. In this case, the single and two-photon absorption processes are resolved for much smaller detunings since the single photon absorption is not Doppler-broadened as in previous experiments [57,64,70]. Furthermore, gain occurs here for significantly smaller coupling field powers than are necessary in a vapour cell. The amplification observed is much the same as that recorded previously by Kleinfeld and Streater [57], and Zhu and Lin [64] except that a respectable 8% gain is

achieved for a coupling field intensity that is approximately two orders of magnitude smaller. By virtue of the homogeneously broadened regime, facilitated by the magneto-optic trap, the theoretical model shows excellent agreement with the experimental results. The authors rely on theoretical calculations of the sub-level populations to establish the lack of inversion on the probe transition.

Note that an additional AWI experiment has been carried out in a magneto-optic trap by Kitching and Hollberg at NIST [71], and it will be published shortly.

6.4 Experimental Lasing Without Inversion

The following section considers experiments in which gain in the absence of inversion was harnessed by way of an optical cavity to produce laser action. Although chronological order is maintained within sections, note that the first demonstrations of LWI preceded the later experiments exhibiting AWI.

6.4.1 Zibrov *et al*, August 1995 [63]

The first demonstration of LWI was made by Zibrov *et al* [63] in the system described in Section 6.3.6. Having achieved AWI in rubidium vapour [62] and experimentally verified the absence of inversion, the authors went on to observe self-generating laser oscillation at the probe wavelength by placing the rubidium cell in a ring cavity.

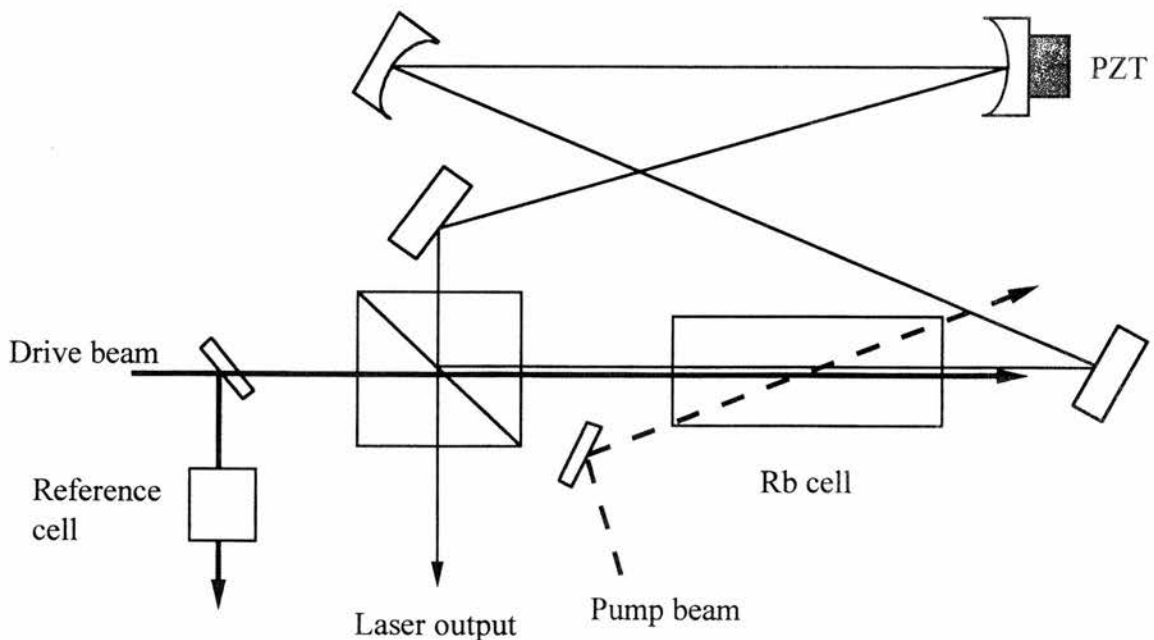


Figure 6.10: Schematic of the ring resonator employed to produce inversionless lasing at 794nm.

Figure 6.10 shows the experimental set-up employed in this work. A polarisation cube forms one of the cavity mirrors to allow substantial transmission of the drive field and high reflectance of the orthogonally polarised lasing field. The resulting laser radiation is selected at the cavity output by a monochromator, and the frequencies of the drive and

pump fields are controlled using additional rubidium reference cells. Lasing was shown in three longitudinal cavity modes at around 794nm when the driving field was on resonance with the $5S_{1/2}$ (F=1) - $5P_{3/2}$ (F=2) transition. The frequency of the laser radiation was verified by making a beat note measurement with an independent laser. Interestingly, the frequency of the laser output, thus determined, was shown to tune with the frequency of the driving field. This tuning behaviour provides further confirmation of the underlying quantum interference effect, and it distinguishes this lasing scheme from those attributed to Raman gain [25-27]. With no probe field initially present, LWI built up from cavity noise and reached $30\mu\text{W}$ at 794nm.

6.4.2 Peters and Lange, 1996 [72]

In this experiment laser action was demonstrated in a commercial HeNe laser for which the cavity loss had been increased such that the threshold condition could not be satisfied by conventional means [72]. The authors dubbed this observation *lasing without threshold inversion* (LWTI), and its demonstration was facilitated by creating Zeeman coherence between low lying states in a modified double Lambda system. The employed energy level structure is shown in Fig. 6.11.

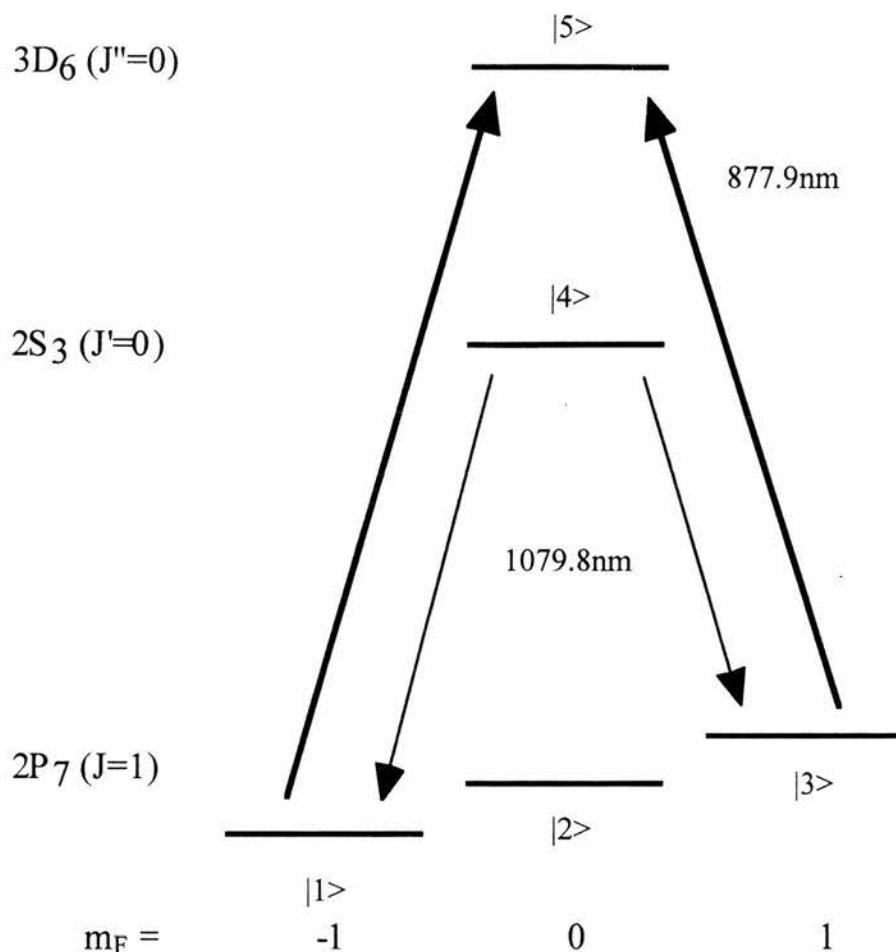


Figure 6.11: Energy level scheme in helium for down converted lasing without threshold inversion.

The driving field (cw single frequency Ti:sapphire laser) couples the magnetic sub-states of the low lying $2P_7$ level to the $3D_6$ excited state. A Zeeman coherence is induced between the sub-states labelled $|1\rangle$ and $|3\rangle$. The probe transition is the HeNe line at 1079.8nm corresponding to the $2P_7 - 2S_3$ transition as shown in Fig. 6.11. A birefringent filter is placed in the HeNe cavity to select the probe wavelength. The upper level of the probe transition is populated by electrical discharge as in a standard HeNe system. A longitudinal magnetic field is applied to the gas by placing the discharge tube in a magnetic coil. The magnetic field is varied to establish the role of coherence in this experiment. In the presence of a magnetic field, the coherence between levels $|1\rangle$ and three $|3\rangle$ will diminish.

When the driving field was introduced into the HeNe cavity, the laser output was enhanced by 10% for a coupling power of 500mW. The output displayed a dependence on the magnetic field strength, reaching a maximum when the field was zero. Cavity losses were increased such that lasing only occurred when the magnetic field was close to zero. This result constitutes LWTI because the change in cavity loss increases the threshold of the laser to create a situation in which laser action would not occur in the absence of the low level coherence. Theoretical analysis verifies that laser action is present due to Zeeman coherence and that the population inversion alone would not be sufficient to maintain laser operation.

In addition, Peters and Lange observe that by rotating the polarisation of the driving beam by 90° , laser action can be suppressed even when the threshold inversion condition is satisfied. The authors also claim to have demonstrated frequency up-conversion by switching laser action on and off at 611.8nm with a driving field at a frequency of 824.9nm. However, no experimental evidence is presented to back up this claim.

6.4.3 Padmabandu *et al*, March 1996 [73]

Laser oscillation was demonstrated in a sodium atomic beam in the absence of a population inversion [73]. A Lambda scheme, based on that of Imamoglu [65], was employed on the sodium D_1 line ($3S_{1/2} - 3P_{1/2}$) as shown in Fig. 6.12. Transparency was first demonstrated due to coherence between the lower levels in the presence of the coherent driving laser. An incoherent pump was added to observe gain, and the lack of inversion predicted by density matrix analysis was confirmed by experimental observation. Finally, the beam was placed in a ring cavity and laser oscillations were recorded.

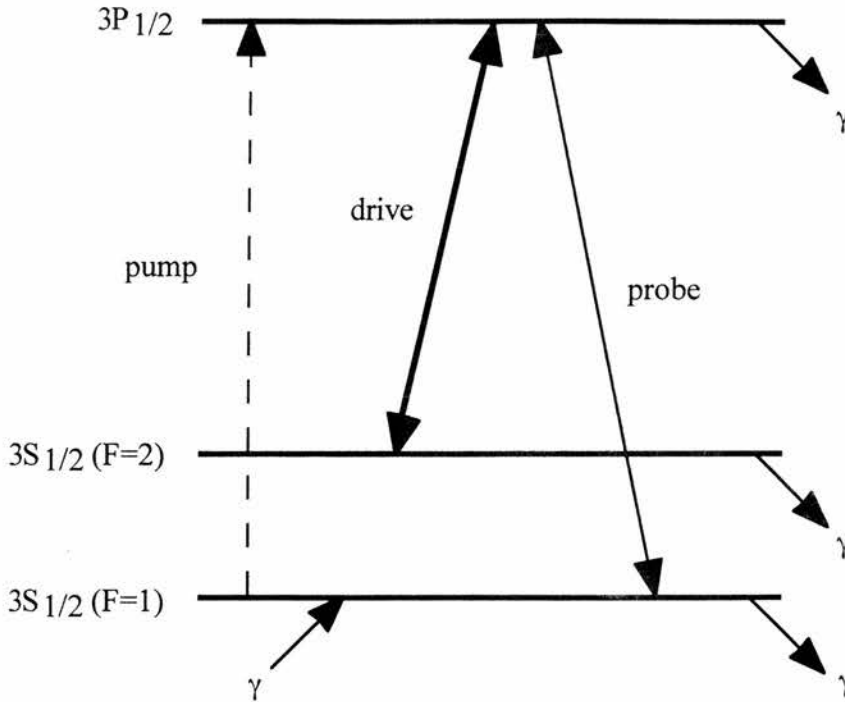


Figure 6.12: *Lambda-type energy level scheme in sodium. The medium is prepared as a beam; consequently, the transit time of atoms in the interaction region must be taken into account. The transit time is included as γ in the figure.*

Analytical forms of the steady state solutions to the density matrix equations showed that inversion was not possible on the probe transition if the incoherent pump rate was less than the decay rate on that transition. In addition, the analysis suggested that this system could not be a Raman laser since two-photon inversion would only occur for very high pumping rates.

The atomic beam was prepared by thermal effusion from an oven at 280 - 320°C. The residual Doppler width in this beam was approximately 60MHz. All of the employed lasers propagated perpendicular to the beam axis. Helmholtz coils were utilised to reduce the magnetic field in the interaction region to <5mG. The drive field was supplied by a cw frequency-stabilised ring cavity Dye laser. A fraction of this beam was separated and frequency shifted by an acousto-optic modulator to provide the probe. The drive beam was tuned to the $3S_{1/2} (F=2) - 3P_{1/2} (F=1)$ transition, and the probe was shifted by

1772MHz to be resonant with the $3S_{1/2} (F=1) - 3P_{1/2} (F=1)$ transition. The probe was scanned by varying the frequency shift introduced by the modulator. The incoherent pump was provided by a second ring Dye laser that passed through an acousto-optic modulator driven by white noise, so that the frequency shift had a bandwidth of 70MHz. The linewidth of the pump laser was therefore sufficiently increased to render it incoherent.

In the presence of the drive laser the probe is nearly 100% transmitted. It is interesting to note that the absorption off-resonance increased due to optical pumping caused by the drive laser that indirectly populates the lower level of the probe transition. Since the population in this state is greater than its thermal equilibrium value, the absorption is increased. When the incoherent pump is introduced, gain is observed on resonance and the absorption off-resonance reduces. Importantly, the action of the incoherent pump, moving population from the lower level into the upper level of the probe transition, only increases the off-resonance absorption by a small amount and the absorption is in fact greater than that observed in the absence of both the drive and pump fields. This observation suggests that no population inversion can be present due to the optical pumping of population into the lower level of the probe transition by the drive laser. A maximum of 10% gain is achieved in the beam which absorbs 16% of the probe in the absence of the driving field.

A ring cavity is installed with a length of 47.5cm and a free spectral range of 630MHz, as shown in Fig. 6.13. With the probe laser blocked, the cavity length is scanned via the PZT mounted high reflector (HR) and laser output is observed at intervals of approximately 600MHz. The observed laser oscillations were unstable due to acoustic vibrations of the cavity length. However, the experiment confirmed the following aspects of LWI in a Lambda scheme: the probe and drive lasers must be equally detuned from line centre, these beams must be orthogonally polarised, the pump must be incoherent, the drive and probe beams must co-propagate, and laser oscillation is only created in the direction coinciding with that of the drive beam.

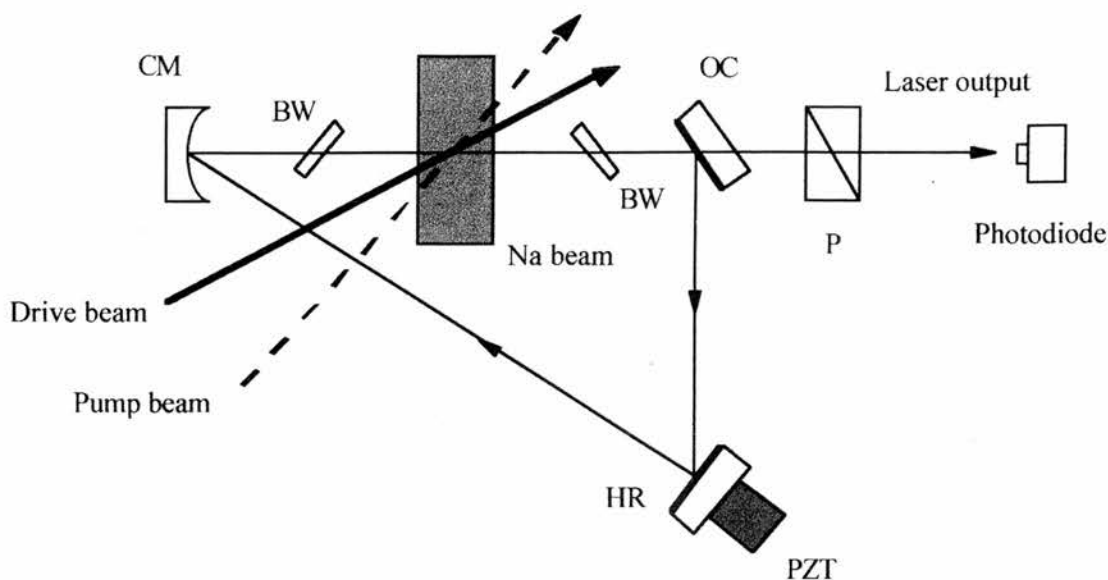


Figure 6.13: Ring cavity laser, with the sodium atomic beam moving perpendicular to the page. CM = curved mirror, OC = output coupler, HR = high reflector, PZT = piezotranslator, and BW = Brewster window.

6.4.4 Sellin *et al*, September 1996 [74]

Although this experiment exhibits laser action, it is not inversionless. Rather, the authors show that in addition to gain without population inversion in a barium atomic beam, it is possible to achieve field assisted lasing [74]. That is, enhanced laser action due to a driving coherent field in the presence of an inversion. Barium is chosen since it provides a near ideal three level system as shown in Fig. 6.14. The predominance of ^{138}Ba which is free of nuclear spin allows the study of a system in which the complications of hyperfine structure are absent.

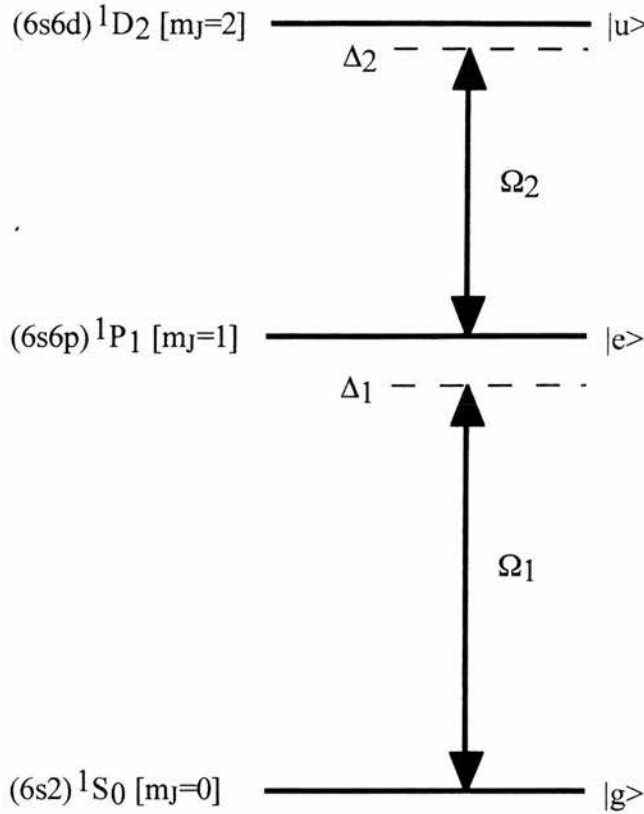


Figure 6.14: Energy level scheme in barium vapour. The three level system is driven by two coherent fields Ω_1 and Ω_2 .

The experimental set-up involves two coherent driving fields coupling the $|e\rangle - |g\rangle$ and $|u\rangle - |e\rangle$ transitions as shown in Fig. 6.14. These fields are supplied by a single mode ring Dye laser (554nm) and a Ti:sapphire laser (821nm) respectively. The barium atoms were prepared in an atomic beam and passed through a confocal optical cavity of length 5cm, producing a maximum estimated beam density of 10^{10} atoms cm^{-3} . The cavity operated at 821nm with a finesse of 530 and the excitation fields intersected the atomic beam (diameter 2mm) in the centre of the cavity. Orthogonal orientation of the beam, cavity axis, and excitation fields provided near Doppler-free conditions.

By piezoelectrically scanning the cavity the authors monitored emission from the $|u\rangle - |e\rangle$ transition. No 'probe' field is added to the system, gain is monitored by observing the amplification of natural atomic fluorescence emitted into the cavity modes. Gain is indicated by a faster than linear increase in cavity output as a function of atomic density.

The particle density is varied by altering the oven temperature in the atomic beam, and a measure of the resulting density is obtained by monitoring fluorescence from the $|e\rangle - |g\rangle$ transition since the population of state $|e\rangle$ is insensitive to the value of Ω_2 . Two regimes are considered: first, the value of Ω_2 is low and, according to theoretical analysis, there is no population inversion on the $|u\rangle - |e\rangle$ transition; and second, the value of Ω_2 is increased and the population on $|u\rangle - |e\rangle$ is inverted.

In the first regime, the cavity output power shows a weak but clearly super-linear growth with atomic density, indicating the presence of inversionless gain. In the second regime, population inversion occurs and laser action is observed since the total emission rate exceeds twice the spontaneous emission rate, i.e. stimulated emission dominates. Theoretical analysis shows that more laser gain is achieved in this field assisted case than would be in an undriven system. A maximum cavity output of $1\mu\text{W}$ is recorded, the magnitude of this value is limited by the number of atoms present in the interaction region and the maximum atomic emission rate of the beam. Despite the lack of LWI in this experiment, the authors do make the important point that quantum coherence may be used to assist laser action in conventional systems in addition to its application in inversionless schemes.

6.4.5 Jong *et al*, June 1998 [75]

Following their demonstration of amplification in cadmium vapour [52] the Amsterdam group have recently demonstrated LWI in the same system [75] by utilising trains of picosecond pulses rather than the single nanosecond pulses of the previous experiment. As the authors point out, there is a distinction between this demonstration of LWI and those made previously by Zibrov *et al* [63] and Padmabandu *et al* [73]. Namely, the former demonstrates lasing without inversion in the atomic state basis, with a hidden inversion in the dressed or coupled and un-coupled states, and the latter experiments demonstrated lasing in the absence of inversion in any state basis.

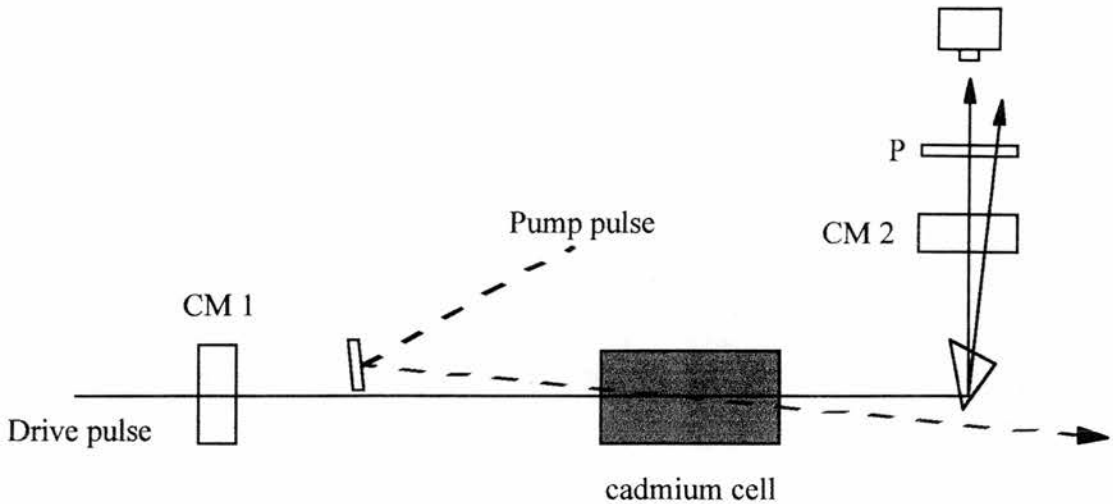


Figure 6.15: *Standing wave laser cavity for lasing without inversion in cadmium.*

In this experiment a 10cm cell of cadmium vapour is used at a temperature of 225°C. The magnetic field that was previously used to verify the role of coherence and the lack of population inversion is not required here as these important observations were made in the original experiment [52]. Having said that, the earlier experiments were repeated before observing laser oscillations (refer to Section 6.3.3). To achieve laser action the probe is blocked and a laser cavity is formed by introducing mirrors CM1 and CM2 as shown schematically in Fig. 6.15. The cavity length is 107cm, matched to the Nd:YAG oscillator and the Dye lasers. The first pump pulse, which establishes coherence, remains unchanged with respect to the previous experiment [52]. The second pulse that provides excitation of population into the upper lasing level is replaced by a pulse train. This train consists of five 35ps pulses. With the correct alignment of cavity mirrors a train of 470nm output pulses was detected from the cavity. Interestingly, the output train of pulses consisted of only four pulses that did not grow exponentially in intensity. This observation suggests that the laser saturates after just a few round trips of the cavity. Theoretical calculations back up this conclusion, and it is used as a basis for estimating a round trip gain of 230 [75].

6.5 Conclusions and a View of the Future

Having discussed all the AWI and LWI experiments that have occurred to date, it is clear that LWI is a practically realisable phenomenon. However, none of the reported experiments address the quintessential issue of inversionless lasing: the production of lasing on a high frequency transition. In the ideal limit, LWI can be realised on a transition far removed in frequency from the driving or coupling field that induces the necessary coherence. To set this work in context, it is interesting to consider the research of Baldwin and Solem [76-78]. LWI is one of many approaches that are currently being pursued in the quest for higher frequency laser technology. Encouragingly, Baldwin and Solem commented in a recent review of proposals for gamma-ray lasers that the "best hope for a successful system may be inversionless lasing" [78].

A wide range of 'proof of principle' experiments has been conducted in this field, and the focus is now shifting to more practical systems in which the lasing transition can be induced at a significantly higher frequency than the coupling field. Two studies have been published that discuss this issue [79,80], the most recent of which states that systems with mismatched drive and lasing transitions "have yet to be addressed both theoretically and experimentally"[80]. This contention emphasises the timeliness of the work presented in this thesis. While we have not attempted to study the regime of laser action, we have both analysed the underlying quantum interference effect that makes LWI possible and identified systems in which mismatched wavelengths may be employed despite Doppler-broadening. As stated in the referenced studies [79,80], Doppler effects are perceived as one of the major hurdles that must be overcome before realising practical mismatched systems. Note that other practical difficulties have been identified [80] that are equally applicable to all mismatched systems regardless of the mechanism or magnitude of line broadening. These obstacles are not considered in this thesis; instead, study is confined to issues relating specifically to Doppler-broadened schemes. With these comments in mind, Chapter 7 draws a theoretical comparison of matched and mismatched AWI in Doppler-broadened rubidium vapour. The findings of this study will be related back to the experiments that have been described in this chapter.

References

- [1] D. Marcuse, Proc. Inst. Elec. Electron. Engrs. **51**, 849, (1963).
- [2] J. R. Whinnery (Symposium Chairman), *Lasers - Invention to Application*, (National Academy Press, Washington DC, (1987)).
- [3] A. L. Schawlow, and C. H. Townes, Phys. Rev. **112**, 1940, (1958).
- [4] T. H. Maiman, Phys. Rev. Lett. **4**, 564, (1960).
- [5] A. E. Siegman, *Lasers*, (University Science Books, (1986)).
- [6] H. Liu, and J. Sun, Opt. Comm. **150**, 153-157, (1998).
- [7] A. Einstein, Phys. Zs. **18**, 121, (1917).
- [8] M. Scully, and M. Fleischhauer, Science. **263**, 21 January, (1994).
- [9] B. G. Levi, Phys. Today. September, (1995).
- [10] O. Kocharovskaya, Phys. Rep. **219**, 3-6, 175-190, (1992).
- [11] E. Arimondo, Progress in Optics. **35**, 257, (1996).
- [12] P. Mandel, Contemp. Phys. **34**, 5, 235-246, (1993).
- [13] O. Kocharovskaya, Hyp. Int. **107**, 187-195, (1997).
- [14] M. O. Scully, Phys. Rep. **219**, 191, (1992).

- [15] S. G. Rautian, and I. I. Sobel'man, Soviet Phys. JETP, **14**, 328, (1962).
- [16] R. Loudon, *The Quantum Theory of Light*, (Oxford University press, (1991)).
- [17] F. Y. Wu, S. Ezekiel, M. Ducloy, and B. R. Mollow, Phys. Rev. Lett. **38**, 1077, (1990).
- [18] C. Cohen-Tannoudji, and S. Reynaud, J. Phys. B. **10**, 345, 365, (1977).
- [19] P. L. Knight, and P. W. Milonni, Phys. Rep. **66**, 21, (1980).
- [20] I. S. Zel'nikovich, S. A. Pulkin, and L. S. Gaida, Opt. Spectrosc. **62**, 1401, (1987).
- [21] D. Grandclement, G. Grynberg, and M. Pinard, Phys. Rev. Lett. **59**, 40, (1987).
- [22] G. Khitrova, G. F. Valley, and H. M. Gibbs, Phys. Rev. Lett. **60**, 1126, (1988).
- [23] A. Lezama, Y. Zhu, M. Kanskar, and T. W. Mossberg, Phys. Rev. A. **41**, 1576, (1990).
- [24] M. Goppert-Mayer, Ann. Phys. (Leipz.) **9**, 273, (1931).
- [25] H.-Y. Ling, J. -M. Yuan, L. M. Narducci, J. R. Tredicce, Opt. Comm. **78**, 5, 6, (1990).
- [26] A. Feitisch, D. Schnier, T. Muller, and B. Wellegehausen, IEEE. J. Quant. Elec. QE-**24**, 507, (1988).
- [27] M. Hube, M. Dieckmann, H. Welling, and B. Wellegehausen, J. Opt. Soc. Am. B **6**, 1220, (1989).
- [28] E. Arimondo (Chairman), Phys. Rep. **219**, 3-6, 203-212, (1992).

- [29] Y. Yamamoto, and G. Bjork, Japanese J. Appl. Phys. **30**, 12A, L2039-L2041, (1991).
- [30] B. Zhang *et al*, Solid State Comm. **91**, 9, 699-701, (1994).
- [31] B. Sherman *et al*, Phys. Rev. Lett. **75**, 25, 4602, (1995).
- [32] C. Davis, *Lasers and Electro-Optics - Fundamentals and Engineering*, (Cambridge University Press, (1996)).
- [33] J. Faist *et al*, Phys. Rev. Lett. **76**, 3, 411, (1996).
- [34] U. Fano, Phys. Rev. **124**, 1866, (1961).
- [35] V. G. Arkhipkin, and Y. I. Heller, Phys. Lett. **98A**, 1-2, 12, (1983).
- [36] S. E. Harris, Phys. Rev. Lett. **62**, 9, 1033, (1989).
- [37] S. E. Harris, J. Field, and A. Imamoglu, Phys. Rev. Lett. **64**, 1107, (1990).
- [38] O. Kocharovskaya, and Ya. I. Khanin, JETP Lett. **48**, 630, (1988).
- [39] E. Arimondo, G. Orriols, Lettre Al Nuovo Cimento. **17**, 10, (1976).
- [40] H. R. Gray, R. M. Whitely, and C. R. Stroud, Optics Letters. **3**, 6, (1978).
- [41] M. O. Scully, S-Y. Zhu, and A. Gavrielides, Phys. Rev. Lett. **62**, 24, 2813, (1989).
- [42] P. E. Coleman, and P. Knight, J. Phys. B. **15**, L235, (1982).
- [43] S. E. Harris, Phys. Today. July, (1997).

- [44] J. Gao *et al*, *Opt. Comm.* **93**, 323-327, (1992).
- [45] L. M. Narducci *et al*, *Opt. Comm.* **81**, 6, 379, (1991).
- [46] H. M. Doss *et al*, *Opt. Comm.* **95**, 57-63, (1993).
- [47] G. M. Meyer *et al*, *Quantum Opt.* **6**, 231-243, (1994).
- [48] J-Y. Gao *et al*, *Opt. Comm.* **110**, 590-594, (1994).
- [49] A. Nottleman, C. Peters, and W. Lange, *Phys. Rev. Lett.* **70**, 12, 1783, (1993).
- [50] Y. I. Khanin, and O. Kocharovskaya, *J. Opt. Soc. Am.* **B7**, 2016, (1990).
- [51] W. Lange, A. Nottleman, and C. Peters, *Quantum Opt.* **6**, 273-285, (1994).
- [52] W. E. van der Veer *et al*, *Phys. Rev. Lett.* **70**, 21, 3243, (1993).
- [53] E. S. Fry *et al*, *Phys. Rev. Lett.* **70**, 21, 3235, (1993).
- [54] G. G. Padmabandu *et al*, *Quantum Opt.* **6**, 261-271, (1994).
- [55] D. E. Nikonov *et al*, *Quantum Opt.* **6**, 245-260, (1994).
- [56] M. Graf, and E. Arimondo, *Phys. Rev. A.* **51**, 5, 4030, (1995).
- [57] J. A. Kleinfeld, and A. D. Streater, *Phys. Rev. A.* **49**, 6, R4301, (1994).
- [58] J. Ciurylo, and L. Krausse, *J. Quant. Spectrosc. Radiat. Transfer.* **28**, 457, (1980).

- [59] E. L. Lewis, Phys. Rep. **58**, 1, (1980).
- [60] J. A. Kleinfeld, and A. D. Streater, Laser Phys. **5**, 3, 556-562, (1995).
- [61] J. A. Kleinfeld, and A. D. Streater, Phys. Rev. A. **53**, 3, 1839, (1996).
- [62] A. S. Zibrov *et al*, Laser Phys, **5**, 3, 553-555, (1995).
- [63] A. S. Zibrov *et al*, Phys. Rev. Lett. **75**, 8, (1995).
- [64] Y. Zhu, and J. Lin, Phys. Rev. A. **53**, 3, 1767, (1996).
- [65] A. Imamoglu, J. E. field, and S. E. Harris, Phys. Rev. Lett. **66**, 9, 1154, (1991).
- [66] P. Kumar, and J. Shapiro, Opt. Lett. **10**, 226, (1985).
- [67] C. Fort *et al*, Opt. Comm. **139**, 31-34, (1997).
- [68] S. H. Boss *et al*, Opt. Comm. **120**, 150, (1995).
- [69] A. V. Durrant *et al*, Opt. Comm. **151**, 136-146, (1998).
- [70] R. R. Moseley *et al*, Opt. Comm. **119**, 61, (1995).
- [71] J. Kitching, and L. Hollberg, *Electromagnetically induced transparency in cold atoms*, (presented IQEC, (1998)).
- [72] C. Peters, and W. Lange, App. Phys. B. **62**, 221-225, (1996).
- [73] G. G. Padmabandu *et al*, Phys. Rev. Lett. **76**, 12, 2053, (1996).

[74] P. B. Sellin *et al*, Phys. Rev. A. **54**, 3, 2402, (1996).

[75] F. B. de Jong *et al*, Phys. Rev. A. **57**, 6, 4869, (1998).

[76] G. C. Baldwin, J. C. Solem, and V. I. Gol'danskii, Rev. of Mod. Phys. **53**, 4, 687, (1981).

[77] G. C. Baldwin, and J. C. Solem, Rev. of Mod. Phys. **69**, 4, 1085, (1997).

[78] G. C. Baldwin, and J. C. Solem, Laser Phys. **5**, 2, 231-239, (1995).

[79] M. D. Lukin *et al*, Laser Phys. **6**, 3, 436-447, (1996).

[80] S. F. Yelin *et al*, Phys. Rev. A. **57**, 5, 3858, (1998).

CHAPTER 7

Theoretical Analysis of Mismatched Gain in Doppler-broadened Media

“He who loves practice without theory is like the sailor who boards ship without a rudder and compass and never knows where he may cast.”

Leonardo de Vinci

7.1 Introduction

In Chapters 4 and 5 theoretical and experimental evidence was presented for the realisation of EIT in energy level systems for which the probe and coupling wavelengths differ [1,2]. Most significantly, it was demonstrated that EIT is possible for probe frequencies higher than the employed coupling field frequency in a Vee-type scheme despite the effects of Doppler-broadening. The importance of this discovery has been emphasised in the context of inversionless lasing. Mismatched wavelength systems are necessary for lasing without inversion to provide a means of accessing problematic high frequency transitions. In the previous chapter we considered the experimental inversionless gain and lasing systems that have been realised to date. From a practical perspective, it is important that a realistic device can be facilitated with the minimum of additional apparatus such as vacuum pumps and cooling systems. It would therefore be a great advantage to create the necessary quantum coherence effect without moving outside a Doppler-broadened medium. This advantage is best exploited, for continuous wave systems with probe frequencies in excess of the coupling field frequency, in a Vee-type scheme [2]. In order to assess the importance of the results presented in this thesis, it is necessary to take the prediction and observation of EIT, in such a configuration, one step further to show that an appreciable level of gain is possible.

In this chapter, a theoretical study of gain in matched and mismatched Vee-type systems predicts that a level of gain can be achieved that is comparable to that measured in the experiments reported in the previous chapter. The mismatched Vee scheme therefore offers a viable alternative to Doppler-free or pulsed systems for the production of high frequency inversionless lasers. Note that we consider only the effects of Doppler-broadening and ignore the problems associated with coupling field absorption. This position is justified by the fact that the latter's effect on gain in a mismatched scheme is independent of the mechanism and magnitude of line-broadening. We seek to establish that Doppler-broadening alone does not preclude the production of LWI at high frequencies.

As we have already seen, the Vee scheme presents a unique opportunity to induce transparency in a high frequency probe field without having to rely on high coupling field powers or an artificial reduction in the Doppler width. This chapter presents a theoretical study of the extent to which this fact can be exploited to produce high frequency

inversionless lasers. The work described here does not provide a comprehensive answer to this question, but it tackles the first hurdle on the way to creating an inversionless laser. That is, we consider the ability of the mismatched ($\lambda_c > \lambda_p$) Vee scheme to produce gain in the presence of a modest level of incoherent excitation. If significant gain can be realised without inverting the population on the probe transition, then it is reasonable to be optimistic about the viability of inversionless lasers based on the Doppler-broadened Vee scheme.

To assess the level of gain that is predicted we compare a mismatched ($\lambda_c > \lambda_p$) Vee scheme with a matched ($\lambda_c = \lambda_p$) Vee system. This comparison is useful in that inversionless lasing has already been achieved for matched wavelengths in rubidium atomic vapour [3]. In addition, by calculating the absolute gain from the off-diagonal density matrix element, we can also compare the gain predicted in our system to those realised in the LWI experiments reviewed in Chapter 6.

The mismatched ($\lambda_c > \lambda_p$) Vee system is selected so as to simulate, as closely as possible, the real system in atomic rubidium vapour that was utilised experimentally in Chapter 5. The limitation being that we must not, in so doing, compromise the validity of the comparison between the matched and mismatched schemes. We consider both transparency and gain for a range of coupling field Rabi frequencies realisable with continuous wave laser powers. Significantly, the Rabi frequencies employed are all less than the Doppler width for the chosen schemes.

The density matrix analysis presented demonstrates that the gain produced for a given incoherent pumping rate is greater in the case of matched wavelengths, but it is still significant for the mismatched scheme in which the frequency of the lasing transition is well in excess of the frequency of the coupling transition. We find that a significant transparency window is produced, even for mismatched wavelengths, for coupling field Rabi frequencies greater than the homogenous linewidth but substantially less than the Doppler width. Approximately 8% gain is predicted in a 422nm probe field driven by a 780nm coupling field, with only a modest level of incoherent pumping.

We proceed by considering the basis upon which the comparison between matched and mismatched Vee schemes is made. Detail is then provided concerning the conversion of

the off-diagonal density matrix element (proportional to the absorption coefficient) into an absolute percentage absorption or gain. The results of the comparison are then presented and discussed. Finally, some practical concerns are highlighted that will be important for the experimental realisation of mismatched gain.

7.2 Comparison of Matched and Mismatched Systems

In order to assess the feasibility of producing inversionless gain and subsequent lasing in mismatched Doppler-broadened systems, a theoretical comparison of a matched and a mismatched scheme is presented. In these schemes all parameters are made equal, except the transition wavelengths. The coupling field Rabi frequency is varied and the imaginary part of the off-diagonal density matrix element associated with the probe transition is monitored with respect to probe field detuning, in the presence and absence of incoherent excitation.

Figure 7.1 depicts the schemes utilised in this comparison. The mismatched system, Fig. 7.1 (b), corresponds to the real atomic scheme in rubidium that was employed experimentally (see Section 5.2): the probe transition is $5S_{1/2} - 6P_{1/2}$ and the coupling transition is $5S_{1/2} - 5P_{3/2}$. For the purposes of this study the effects of the ground state hyperfine structure are ignored, within the density matrix model, and we consider a simple three level Vee scheme. The matched system, Fig. 7.1 (a), is also based on rubidium: the probe transition is $5S_{1/2} - 6P_{1/2}$ and the coupling transition is $5S_{1/2} - 6P_{3/2}$. In both configurations the probe transition is identical, to ensure that the level of Doppler-broadening is the same in each system. However, the decay rates associated with the aforementioned coupling field transitions are different. In order to make the systems equal for all parameters other than wavelength, the decay rate from the $6P_{3/2}$ state has been altered from its true value in the matched scheme. Note that replacing the decay rate in the matched system with the real value, for the $6P_{3/2}$ level, actually reduces the level of predicted gain. The effect of the decay rates on the predicted gain will be considered further in Section 7.5.

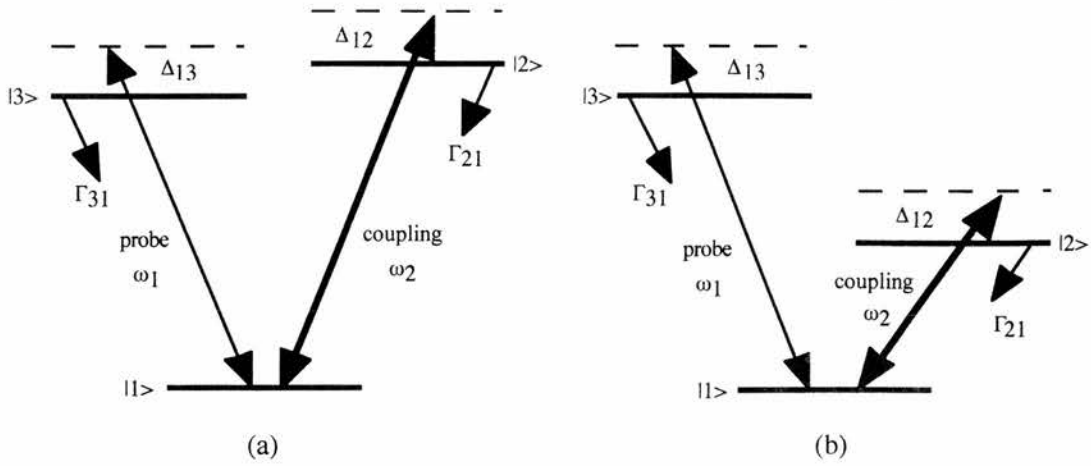


Figure 7.1: Schematic energy level diagrams for (a) the matched and (b) the mismatched Vee schemes.

For the purposes of this comparison, the temperature of the cell in which the interaction takes place is taken to be 130 °C, which corresponds to an experimentally measured absorption of approximately 80% on the employed probe transition ($5S_{1/2}$ ($F=3$) - $6P_{1/2}$).

Theoretical modelling of these schemes was carried out utilising standard density matrix analysis for a three level Vee scheme [4], as described in Section 2.5.3. The equations for the slowly varying density matrix components, in a closed system, are [5,6] given below. They correspond to Matrix 2.4 previously quoted in Section 2.5.3 with the addition of the incoherent pumping term R_{13} :

$$\dot{\rho}_{11} = i\Omega_c(\tilde{\rho}_{21} - \tilde{\rho}_{12}) + i\Omega_p(\tilde{\rho}_{31} - \tilde{\rho}_{13}) + R_{13}(\rho_{33} - \rho_{11}) + \Gamma_{21}\rho_{22} + \Gamma_{31}\rho_{33} \quad (7.1a)$$

$$\dot{\rho}_{22} = i\Omega_c(\tilde{\rho}_{12} - \tilde{\rho}_{21}) - \Gamma_{21}\rho_{22} \quad (7.1b)$$

$$\dot{\rho}_{33} = i\Omega_p(\tilde{\rho}_{13} - \tilde{\rho}_{31}) - \Gamma_{31}\rho_{33} - R_{13}(\rho_{33} - \rho_{11}) \quad (7.1c)$$

$$\dot{\tilde{\rho}}_{12} = -i(\Delta_{12} - i\gamma_{12})\tilde{\rho}_{12} + i\Omega_c(\rho_{22} - \rho_{11}) - i\Omega_p\tilde{\rho}_{32} \quad (7.1d)$$

$$\dot{\tilde{\rho}}_{13} = -i(\Delta_{13} - i\gamma_{13})\tilde{\rho}_{13} + i\Omega_p(\rho_{33} - \rho_{11}) + i\Omega_c\tilde{\rho}_{23} \quad (7.1e)$$

$$\dot{\tilde{\rho}}_{23} = -i(\Delta_{12} - \Delta_{13} - i\gamma_{23})\tilde{\rho}_{23} + i\Omega_c\tilde{\rho}_{13} - i\tilde{\rho}_{21} \quad (7.1f)$$

where subscripts refer to the three levels as indicated in Fig. 7.1. The pumping term, R_{13} , was included to allow for the excitation of atomic population into the upper level of the

probe transition; this is necessary to achieve gain. The detunings are defined, in both schemes, as:

$$\Delta_{13} = \omega_1 - \omega_{13} - k_1 V_Z \quad (7.2a)$$

$$\Delta_{12} = \omega_2 - \omega_{12} - k_2 V_Z \quad (7.2b)$$

where ω_1 and ω_2 denote the angular frequencies of the applied probe and coupling fields, V_Z is the atomic velocity along the cell length, k_1 and k_2 are the wavevectors of the probe and coupling fields (defined as $k_i=2\pi n/\lambda_i$), ω_{13} and ω_{12} are the angular transition frequencies of the probe and coupling fields, and the $\omega_1 - \omega_{13}$ and $\omega_2 - \omega_{12}$ terms in Eqs. (7.2a) and (7.2.b) correspond to the zero velocity detuning of the probe and coupling fields in the lab frame. Note that the single indices 1 and 2 refer to the coupling and probe fields respectively; in all other cases the indices refer to the atomic levels labelled in Fig. 1.7. The angular Rabi frequencies are defined for the probe and coupling fields as stated previously:

$$\Omega_p = \frac{\mu_{13}E_1}{2\hbar} \quad (7.3a)$$

$$\Omega_c = \frac{\mu_{12}E_2}{2\hbar} \quad (7.3b)$$

where E_1 and E_2 are the electric-field strengths and μ_{13} and μ_{12} are the dipole matrix elements for the probe and coupling transitions. The population decay rates (Γ_{ij}) are set to $\Gamma_{31}=8\times 10^{-6}\text{s}^{-1}$ and $\Gamma_{21}=40\times 10^{-6}\text{s}^{-1}$ in both systems while the coherence decay rates (γ_{ij}), in both schemes are defined according to:

$$\gamma_{12} = \frac{1}{2}(\Gamma_{21} + R_{13}) \quad (7.4a)$$

$$\gamma_{13} = \frac{1}{2}(\Gamma_{31} + 2R_{13}) \quad (7.4b)$$

$$\gamma_{23} = \frac{1}{2}(\Gamma_{31} + \Gamma_{21} + R_{13}) \quad (7.4c)$$

where the pumping term R_{13} contributes to the dephasing of transitions linked to one or other of states $|1\rangle$ and $|3\rangle$. Note that the effects of collisional dephasing have been ignored in this analysis; and in this sense we assume an ideal system, dephased solely by the natural population decays and the imposed incoherent excitation. Equations (7.1a)-(7.1f) are solved as previously described in Section 5.2 and more fully in Chapter 2.

7.3 Absorption and Gain Measurements

Density matrix analysis does not provide an absolute measurement of absorption or gain. Moreover, this information is necessary to assess the potential of a system as an inversionless laser. Previous work has been concerned simply with the relative magnitudes of absorption and transparency, for which the density matrix is sufficient. An experimenter is at liberty to adjust the magnitude of absorption or gain by simply altering the particle density of the active medium. However, as particle density is limited by the apparatus, the physical amount of the substance available, collisional dephasing, absorption of the driving field, and the temperature at which the medium begins to form molecules, it is necessary to have a clear picture of the amount of gain expected for a given set of experimental conditions. Calculating absolute absorption is also important in the design of an atomic beam, where the residual Doppler width is traded off against particle density [7].

A method was first devised to calculate absorption so that the theory could be compared to experimental measurements in rubidium vapour. This study concentrated on the 422nm ($5S_{1/2} - 6P_{1/2}$) transition. Two methods were employed to calculate the absorption. The first describes the interaction of radiation and the atom in terms of transition probabilities [8], taking a measure of absorption from the Einstein A coefficient and accounting for inhomogeneous Doppler-broadening by including a lineshape function based on a linear Doppler width [9]. The second converts the imaginary part of the off-diagonal density matrix element, ρ_{13}^i , into an absorption coefficient by utilising the relationship between susceptibility and the density matrix element, Eq. (2.10) [9-11].

Care was taken to select values for particle density and transition decay rates to ensure that reasonable agreement was achieved between the two theories and experimental data. As we saw in Section 3.6.3 and 3.6.4, published values of the aforementioned parameters vary considerably.

7.3.1 Simple Two Level Theory

The most straightforward way to calculate the absorption experienced by a light field interacting with an atomic transition is to use a formula for the absorption coefficient based on the atomic population, the lifetime of the upper state, and the transition lineshape

function. Since we are employing a narrowband laser field, we can neglect its spectral width. A two level atom will absorb incident light as long as the proportion of the atomic population in the lower energy state is greater than that in the upper state. This condition will be generally true in a medium that is not subject to any form of excitation. However, if the majority of the population is excited into the upper state, gain will occur and can be calculated by exactly the same equation - the resulting coefficient will simply change sign.

The absorption or gain coefficient allows us to calculate the variation of the intensity of the radiation as it passes through the interaction medium, according to:

$$I_\nu(z) = I_\nu(0) \text{Exp}[\gamma(\nu)z] \quad (7.5)$$

where $I_\nu(0)$ is the intensity of radiation incident on the cell. The absorption or gain coefficient is defined, with respect to a linear frequency, according to Yariv [9]:

$$\gamma(\nu) = (N_2 - N_1) \frac{c^2}{8\pi n^2 \nu^2 t_{\text{spont}}} g(\nu) \quad (7.6a)$$

$$t_{\text{spont}} = \frac{1}{A_{21}} \quad (7.6b)$$

where Eq. (7.6b) represents the spontaneous lifetime of the transition in question, N_i is the atomic population in state i , c is the speed of light, n is the refractive index, ν is the transition frequency, and $g(\nu)$ is the lineshape function of the transition. In the case of a relaxed medium, subject to a single light field that is near resonant with the ground state and an arbitrary excited state, we may assume that all the atomic population begins in the ground state, and Eq. (7.6a) can be reduced to:

$$\gamma(\nu) = N \frac{c^2}{8\pi n^2 \nu^2 t_{\text{spont}}} g(\nu) \quad (7.7)$$

We write this formula in terms of the wavelength rather than the frequency of the transition, and the Einstein A coefficient rather than the lifetime:

$$\gamma(\nu) = \frac{A_{21} N \lambda^2}{8\pi n^2} g(\nu) \quad (7.8)$$

The nature of the lineshape function for a transition will depend on whether the medium is homogeneously or inhomogeneously broadened. Since we are dealing with a gaseous medium, we assume the Doppler effect will be the dominant broadening

mechanism. The lineshape function for an inhomogeneously broadened medium is given by:

$$g(\nu) = \frac{2\sqrt{\ln 2}}{\sqrt{\pi}\Delta\nu_D} e^{-4(\ln 2)(\nu-\nu_0)^2/\Delta\nu_D^2} \quad (7.9)$$

On resonance this equation reduces to:

$$g(\nu) = \frac{2\sqrt{\ln 2}}{\sqrt{\pi}\Delta\nu_D} \quad (7.10)$$

and the Doppler width, $\Delta\nu_D$, is defined as:

$$\Delta\nu_D = 2\nu_0 \sqrt{\frac{2k_B T}{Mc^2} \ln 2} \quad (7.11)$$

where ν_0 is the resonant frequency, k_B is Boltzmann's constant (1.381×10^{-23} J/K), T is the cell temperature in Kelvin, M is the atomic weight, and c is the speed of light. Equations (7.8), (7.10), and (7.11) allow us to calculate the on-resonance absorption in a two level atom subject to a monochromatic radiation field.

7.3.2 Calculation of Absorption Based on Density Matrix Analysis

The density matrix analysis traditionally employed in this work gives us a relative picture of the absorption, transparency or gain experienced by an optical field interacting with the atomic system. This insight is achieved through the imaginary part of the off-diagonal density matrix element for a specific transition, which is directly proportional to the absorption or gain coefficient. The off-diagonal density matrix element is related to the polarisation and thus to the atomic susceptibility in the following way [10]:

$$\chi' - i\chi'' = \frac{N\mu_{ij}\rho_{ij}}{\epsilon_0 E} \quad (7.12)$$

The imaginary part of the susceptibility is directly related to the gain coefficient [9,10]:

$$\gamma(\omega) = \frac{-k\chi''(\omega)}{n^2} \quad (7.13)$$

where the wavevector $k=2\pi n/\lambda$, and the amplitude of the optical field varies exponentially with distance, z , according to $\text{Exp}[(\gamma/2)z]$.

Rearranging and substituting Eq. (7.12) into Eq. (7.13) allows us to define the relationship between the density matrix element and the absolute absorption or gain per unit length:

$$\gamma(\omega) = \frac{3A_{ji} N \lambda^2 \text{Im}(\rho_{ij})}{8\pi n \Omega_{ij}} \quad (7.14)$$

where the Einstein A coefficient is that of the specific transition in question ($A_{ji}=1/\tau$), N is the total atomic population per cubic metre, and the Rabi frequency is defined in angular terms according to Eq. (7.15):

$$\Omega_{ij} = \frac{\mu_{ij} E}{2\hbar} \quad (7.15)$$

In the application of Eq. (7.14), it is essential to take full account of the system's degeneracy. In this case, we are concerned solely with one rubidium isotope and one of the two hyperfine ground state levels. An experimental absorption trace in rubidium vapour consists of four peaks, corresponding to the two hyperfine ground states in each of the two isotopes. Since we are concerned with only one of these peaks we must take this into account when calculating the atomic population, N, and the transition Einstein A coefficient.

Both methods were initially used to calculate absorption as a function of temperature on a well characterised transition in rubidium. This analysis provided a test of the equations' validity via comparison with experimental measurements of absorption. Figure 7.2 demonstrates good agreement between experiment and theory for the $5S_{1/2}$ ($F=3$) - $6P_{1/2}$ transition. The dashed line is based on the simple two level theory while the solid line was calculated by density matrix analysis. The experimental points in Fig. 7.2 were obtained with a cell length of 2cm, as used previously in the experiment reported in Chapter 5.

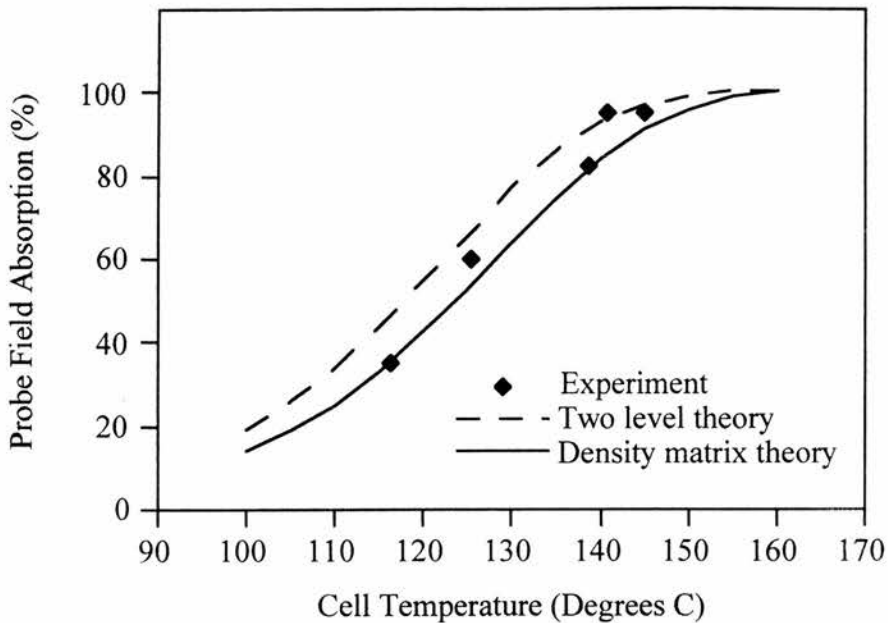


Figure 7.2: *Experimental measurements of absorption, in a 2cm cell, for the $5S_{1/2} (F=3) - 6P_{1/2}$ transition in ^{85}Rb , presented along with theoretical calculations based on the simple two level model (dashed line) and the density matrix analysis (solid line).*

Figures 7.3, 7.4 and 7.5 show absorption measurements taken in cells of length 2cm, 4cm, and 10cm respectively for (a) peak 2 ($5S_{1/2} (F=3) - 6P_{1/2}$ in ^{85}Rb) and (b) peak 3 ($5S_{1/2} (F=2) - 6P_{1/2}$ in ^{85}Rb). In all cases theoretical calculations are presented for the simple two level model (dashed line) and the density matrix analysis (solid line). The experimental measurements confirm the validity of the absorption calculations described in this section.

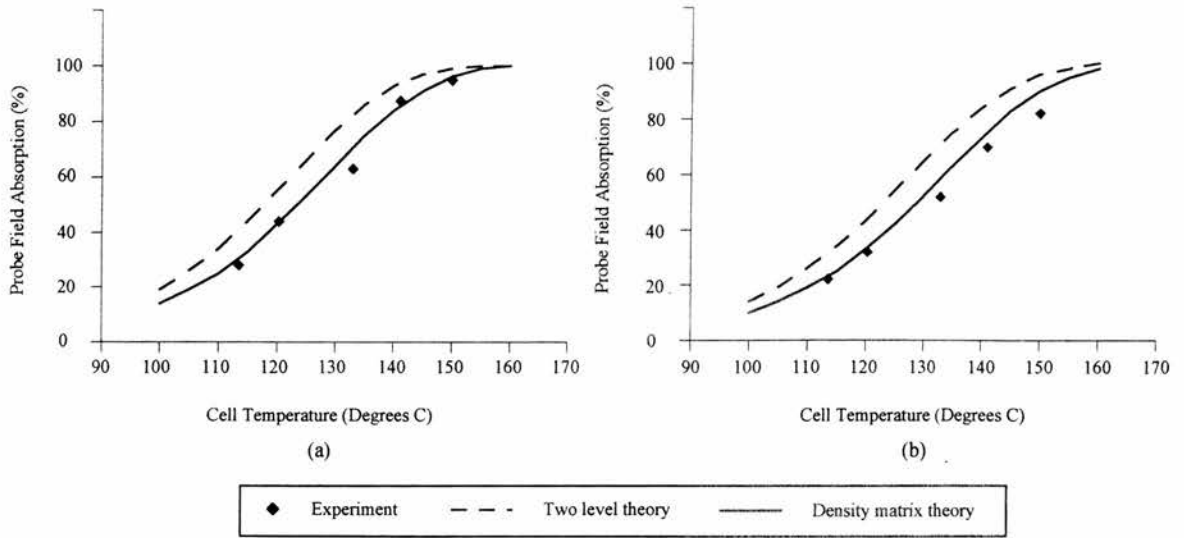


Figure 7.3: Experimental and theoretical absorption measurements in a 2cm cell for (a) the $5S_{1/2} (F=3) - 6P_{1/2}$ transition and (b) the $5S_{1/2} (F=2) - 6P_{1/2}$ transition in ^{85}Rb .

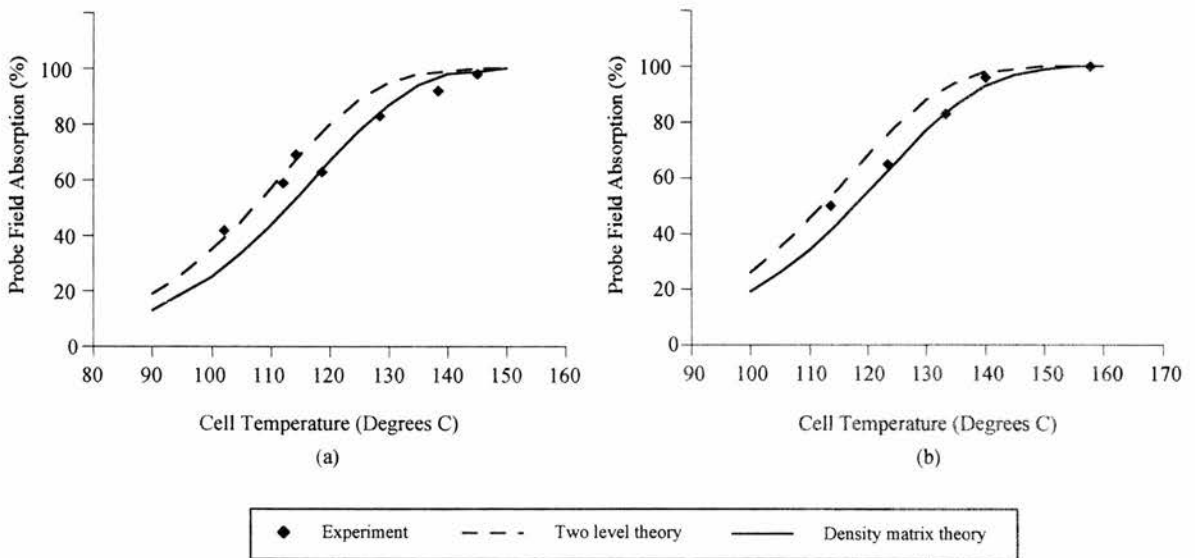


Figure 7.4: Experimental and theoretical absorption measurements in a 4cm cell for (a) the $5S_{1/2} (F=3) - 6P_{1/2}$ transition and (b) the $5S_{1/2} (F=2) - 6P_{1/2}$ transition in ^{85}Rb .

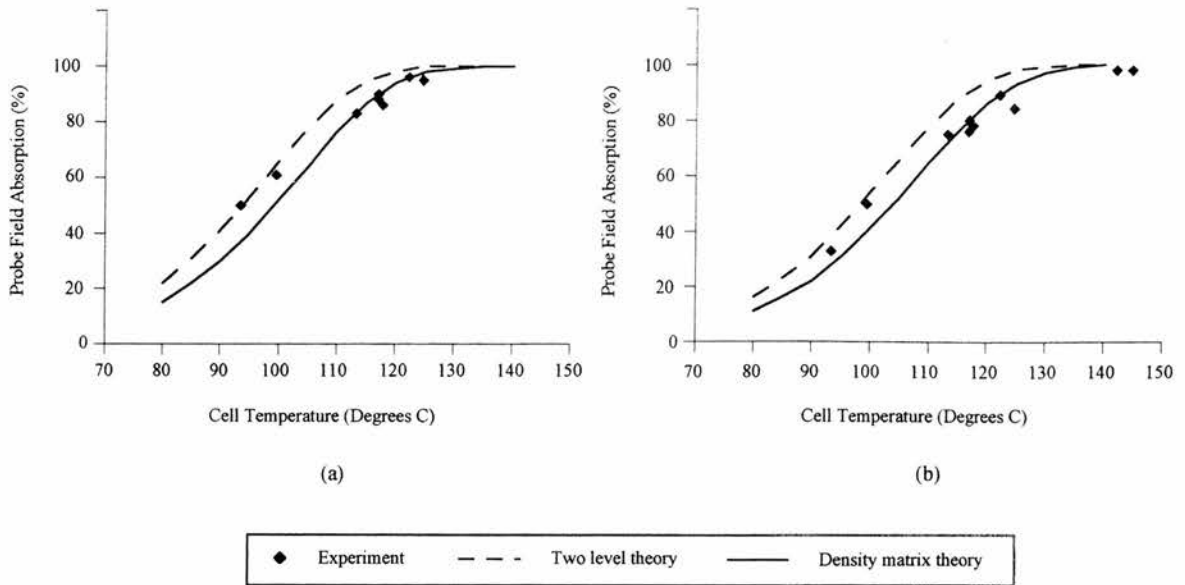


Figure 7.5: *Experimental and theoretical absorption measurements in a 10cm cell for (a) the $5S_{1/2} (F=3) - 6P_{1/2}$ transition and (b) the $5S_{1/2} (F=2) - 6P_{1/2}$ transition in ^{85}Rb .*

The relationship between the off-diagonal density matrix element and the absorption coefficient has also been employed by Scully and co-workers [3,12]. The main source of uncertainty in this calculation comes from the discrepancies in available values of the transition A coefficient and the atomic population. This data was considered in Sections 3.6.3 and 3.6.4. Bearing in mind the errors implied by the wide range of values published for these parameters, the final error in the calculated gain will be large. For the purposes of this work, the population density was calculated according to Thompson and Xu [13] while the Einstein A coefficients were taken from Weise and Martin [14].

The discrepancies between the two theoretical calculations occur because the density matrix method provides a more comprehensive model of a real atomic system. In the simple transition probability approach, line broadening is taken into account with a single lineshape function based solely on Doppler effects. Density matrix analysis incorporates both homogeneous and inhomogeneous broadening, through the damping of the ρ_{ij} elements and the integration of those elements over the velocity range.

If we consider the $5S_{1/2} (F=3) - 6P_{1/2}$ transition in rubidium, we can now calculate the absorption that would be experienced by a probe field of appropriate wavelength (approximately 422nm) by taking the cell temperature to be 130°C and using the other

relevant parameters found in Section 3.6. Equation (7.8) gives an absorption coefficient of 73m^{-1} , which can be converted into a percentage absorption using the following formula:

$$\text{Percentage absorption} = [1 - \text{Exp}(-\gamma L)] \times 100 \quad (7.16)$$

where γ is the absorption coefficient and L is the length of the interaction cell. In this case, 77% of the incident light will be absorbed in a 2cm cell.

For the same conditions the two level density matrix model discussed in Section 2.3 is used in conjunction with Eq. (7.14) to give an absorption coefficient of 52m^{-1} , corresponding to 64% of the incident radiation being absorbed in a 2cm cell.

For the purposes of the theoretical study presented in his chapter, the second method of calculating absolute values of gain, based on density matrix analysis, is employed. The first method provided a useful means of verifying these calculations by comparison with experimental measurements. We will now consider the results of the theoretical study of gain in the Vee-type configuration utilising density matrix analysis and the calculation described in this section.

7.4 Theoretical Results

Figure 7.6 shows the peak ‘on-resonance’ absorption (ρ^i_{13}) as a function of the linear coupling field Rabi frequency, in the absence of incoherent pumping. This graph demonstrates that the transparency achieved in the matched system is deeper than the transparency in the mismatched configuration, for a given coupling field Rabi frequency. However, the graph also shows that approximately 75% of the absorption is removed in the mismatched system for a coupling field Rabi frequency of only 10MHz. The Doppler width for the probe transition is approximately 1.11GHz, and the homogeneous linewidth is 2.55MHz. Thus, significant transparencies are predicted in both schemes for coupling field Rabi frequencies greater than the homogeneous linewidth and substantially less than the Doppler width.

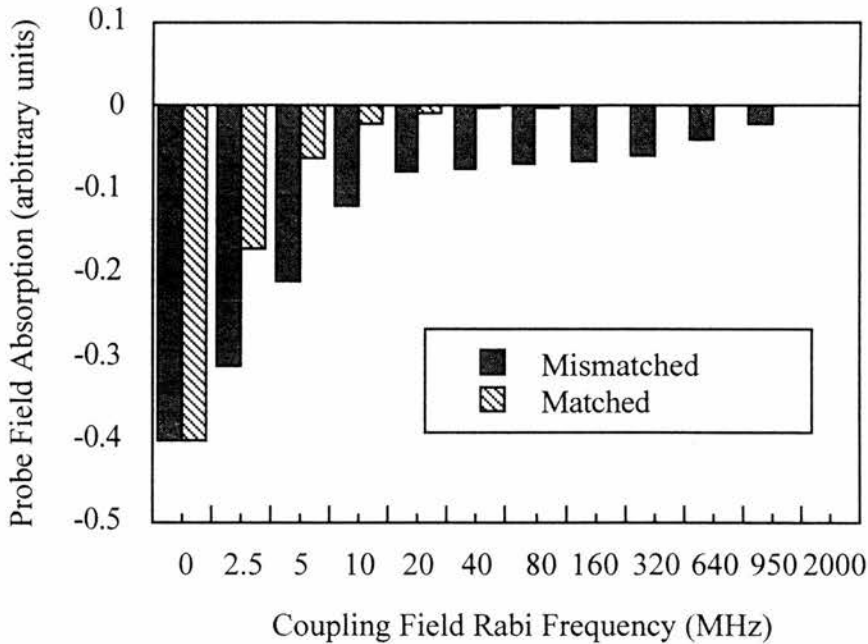


Figure 7.6: Bar chart showing the ‘on-resonance’ absorption (ρ^i_{13} in arbitrary units) in the matched and mismatched systems for a range of coupling field Rabi frequencies.

Tables 7.I and 7.II contain the principal results of a comparison between the matched and mismatched schemes. Values are given for the off-diagonal density matrix element relating to absorption or gain, ρ^i_{13} , and the diagonal matrix elements, ρ_{11} , ρ_{22} , and ρ_{33} , relating to the relative atomic population in states $|1\rangle$, $|2\rangle$, and $|3\rangle$ respectively. The

actual percentage absorption and gain that would be experienced by the probe field in a 2cm cell at 130°C is also given along with the bandwidth over which gain is predicted. Normal absorption is calculated by setting both the coupling field Rabi frequency, Ω_c , and the incoherent pumping rate, R_{13} , to zero. Electromagnetically induced transparency is calculated for coupling field Rabi frequencies of 20MHz, 160MHz, and 950MHz with the pumping rate, R_{13} , retained at zero. Gain is then determined by introducing a non-zero pumping rate for the same range of coupling field Rabi frequencies. The incoherent pumping rate, R_{13} , is $10 \times 10^6 \text{ s}^{-1}$ in both the matched and mismatched systems.

| Matched | Rabi frequency (MHz) | ρ_{13}^i resonance | ρ_{13}^i peak | ρ_{11} | ρ_{22} | ρ_{33} | Absorption % | Gain % | Gain bandwidth (MHz) |
|--------------|----------------------|-------------------------|--------------------|-------------|-------------|-------------|--------------|---------|----------------------|
| Absorption | $\Omega_c=0$ | -0.0004 | -0.0004 | 1 | 0 | 0 | 64 | | |
| Transparency | $\Omega_c=20$ | -0.00002 | -0.00002 | 0.9823 | 0.0177 | 0 | 5 | | |
| Transparency | $\Omega_c=160$ | -0.000001 | -0.000001 | 0.875 | 0.125 | 0 | 0.3 | | |
| Transparency | $\Omega_c=950$ | 0 | 0 | 0.62 | 0.38 | 0 | 0 | | |
| Gain | $\Omega_c=20$ | 0.000082 | 0.000082 | 0.634 | 0.014 | 0.352 | | 24 | 18 |
| Gain | $\Omega_c=160$ | 0.000025 | 0.000102 | 0.58 | 0.099 | 0.321 | | 7 / 30 | 108 |
| Gain | $\Omega_c=950$ | 0.000001 | 0.000033 | 0.451 | 0.299 | 0.25 | | 0.3 / 9 | 648 |

TABLE 7.1: Principal results of theoretical modelling for the matched system. Values are shown for the density matrix elements relating to absorption, gain and the relative atomic populations for various coupling field Rabi frequencies in the absence and presence of incoherent excitation. In the case of gain, the incoherent excitation, R_{13} , equals $10 \times 10^6 \text{ s}^{-1}$. Absolute values of absorption and gain are also provided. In the latter case the numbers before and after the oblique refer to the resonance and peak gain respectively. Conditions: $T=130^\circ\text{C}$, cell length=2cm.

| Mismatched | Rabi frequency (MHz) | ρ_{13}^i resonance | ρ_{13}^i peak | ρ_{11} | ρ_{22} | ρ_{33} | Absorption % | Gain % | Gain bandwidth (MHz) |
|--------------|----------------------|-------------------------|--------------------|-------------|-------------|-------------|--------------|--------|----------------------|
| Absorption | $\Omega_c=0$ | -0.0004 | -0.0004 | 1 | 0 | 0 | 64 | | |
| Transparency | $\Omega_c=20$ | -0.000084 | -0.000084 | 0.968 | 0.032 | 0 | 19 | | |
| Transparency | $\Omega_c=160$ | -0.000062 | -0.000062 | 0.799 | 0.201 | 0 | 15 | | |
| Transparency | $\Omega_c=950$ | -0.00002 | -0.00002 | 0.552 | 0.448 | 0 | 5 | | |
| Gain | $\Omega_c=20$ | 0.000018 | 0.000018 | 0.627 | 0.025 | 0.348 | | 5 | 27 |
| Gain | $\Omega_c=160$ | 0.0000315 | 0.0000315 | 0.541 | 0.159 | 0.3 | | 8 | 108 |
| Gain | $\Omega_c=950$ | 0.000012 | 0.000012 | 0.418 | 0.351 | 0.231 | | 3 | 324 |

TABLE 7.II. Principal results of theoretical modelling for the mismatched system. Values are shown for the density matrix elements relating to absorption, gain and the relative atomic populations for various coupling field Rabi frequencies in the absence and presence of incoherent excitation. In the case of gain, the incoherent excitation, R_{13} , equals $10 \times 10^6 \text{ s}^{-1}$. Absolute values of absorption and gain are also provided. Conditions as in Table 7.I.

The absorption predicted in both systems, in the absence of the coupling field, is identical since the probe transition is exactly the same in each case. The off-diagonal density matrix element is directly proportional to the absorption coefficient; by convention a negative value corresponds to absorption and a positive value indicates gain. In the absence of the coupling laser all the atomic population is in the ground state due to the probe laser being very weak and not significantly exciting population into level $|3\rangle$. The absorption profile of both systems is shown in Fig. 7.7 in the absence of the coupling field.

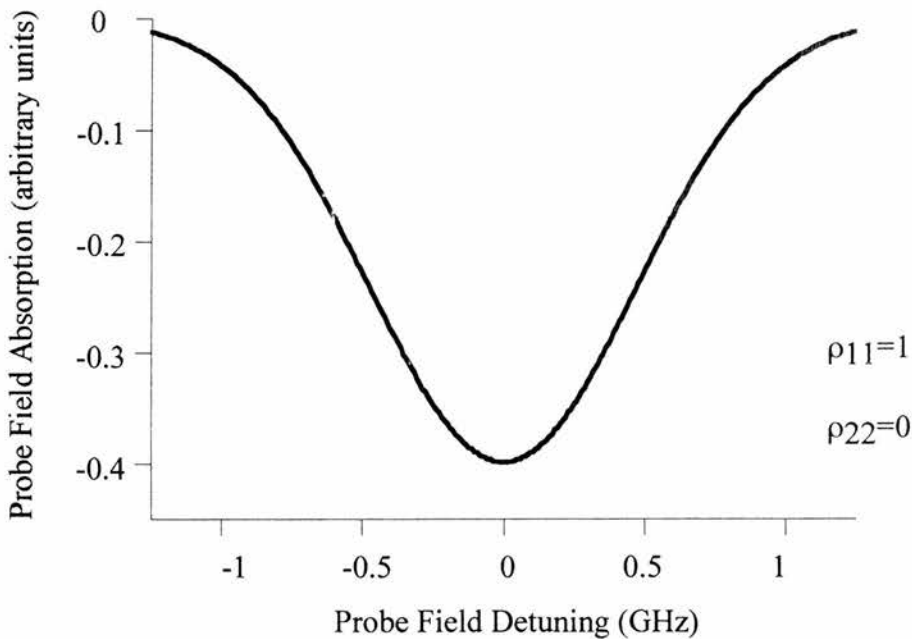


Figure 7.7: Probe field absorption (ρ_{13}^i in arbitrary units) as a function of probe field detuning in the absence of the coupling field. This Doppler-broadened absorption trace is identical for both the matched and mismatched systems. The relative populations in levels $|1\rangle$ (ρ_{11}) and $|2\rangle$ (ρ_{22}) are also indicated.

As the coupling laser is turned on, the absorption is significantly reduced in both schemes. This effect is more pronounced in the case of matched wavelengths, but it is still present in the mismatched system. Figure 7.8 (a) and (b) shows the absorption profiles in the presence of the coupling laser for the Rabi frequencies indicated in the matched and mismatched systems respectively.

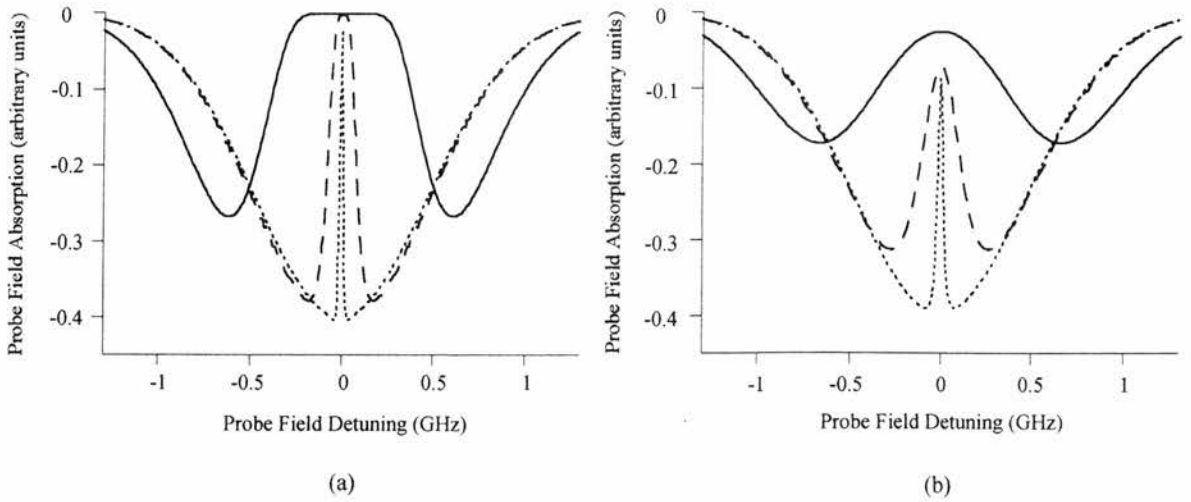


Figure 7.8: Overlaid absorption profiles (ρ_{13}^i in arbitrary units) showing transparency in (a) the matched and (b) the mismatched schemes. Coupling Rabi frequencies are 950MHz (solid lines), 160MHz (dashed lines), and 20MHz (dotted lines).

The coupling field also has the effect of exciting some of the atomic population into the upper level of the coupling transition, and the proportion of the population in level $|2\rangle$ increases as the coupling field Rabi frequency increases. Figure 7.9 shows the relative atomic populations in each state in the presence of the coupling laser for both the matched and mismatched schemes.

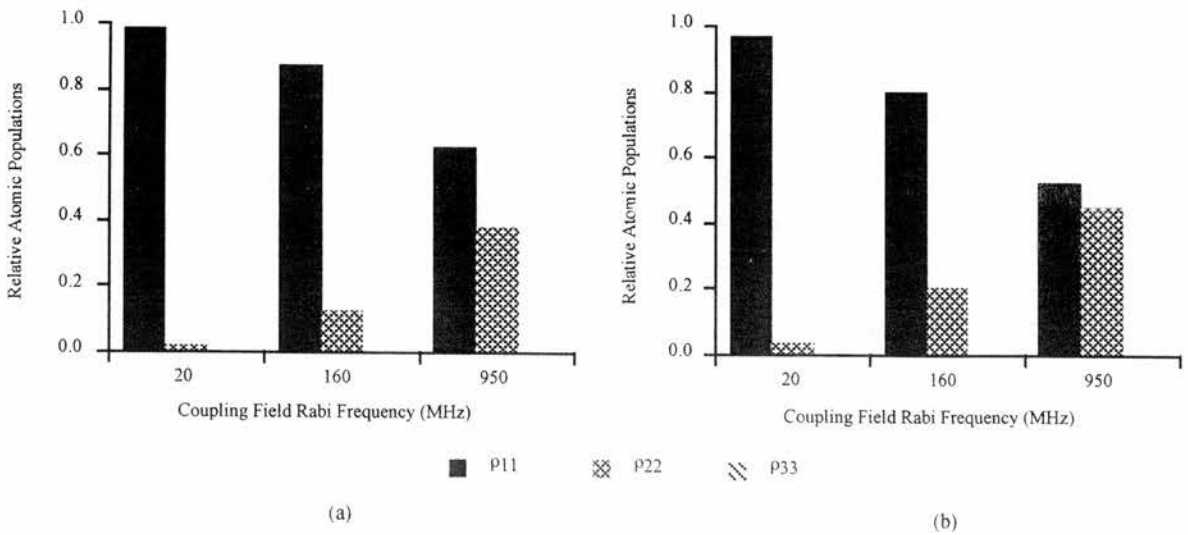


Figure 7.9: The relative atomic populations in (a) the matched and (b) the mismatched systems in the presence of the coupling laser at the coupling field Rabi frequencies indicated.

For a coupling field Rabi frequency of 20MHz, significantly less than the Doppler width, gain is predicted in both configurations. The peak matched gain is nearly five times the mismatched gain, over roughly the same bandwidth. It is surprising, however, that even a modest gain is predicted for such a low Rabi frequency in a mismatched system. Figure 7.10 shows overlaid plots of the absorption or gain as a function of probe field detuning for various coupling Rabi frequencies in the matched and mismatched schemes.

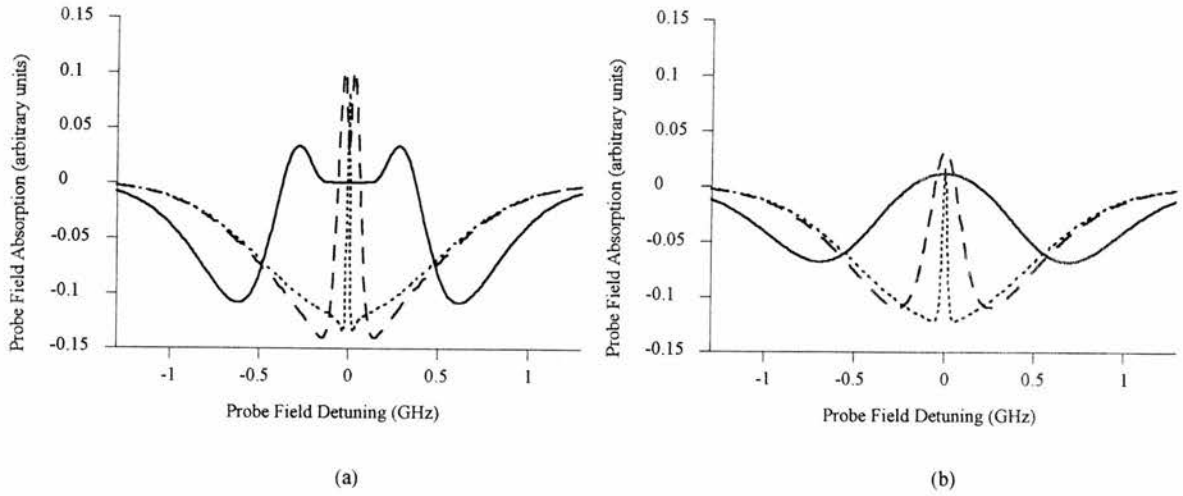


Figure 7.10: Absorption or gain (ρ_{13}^i in arbitrary units) as a function of probe field detuning in (a) the matched and (b) the mismatched system in the presence of the coupling field and a modest level of incoherent pumping. Coupling Rabi frequencies are 950MHz (solid lines), 160MHz (dashed lines), and 20MHz (dotted lines).

As the coupling field Rabi frequency is increased, the total net gain increases along with the bandwidth over which it may be observed. The magnitude of predicted gain reaches a maximum for a certain Rabi frequency because for greater Rabi frequencies the gain bandwidth begins to increase to such an extent that the peak gain is reduced. In Fig. 7.11 we see the evolution of the peak gain and the gain bandwidth as the coupling field Rabi frequency is increased.

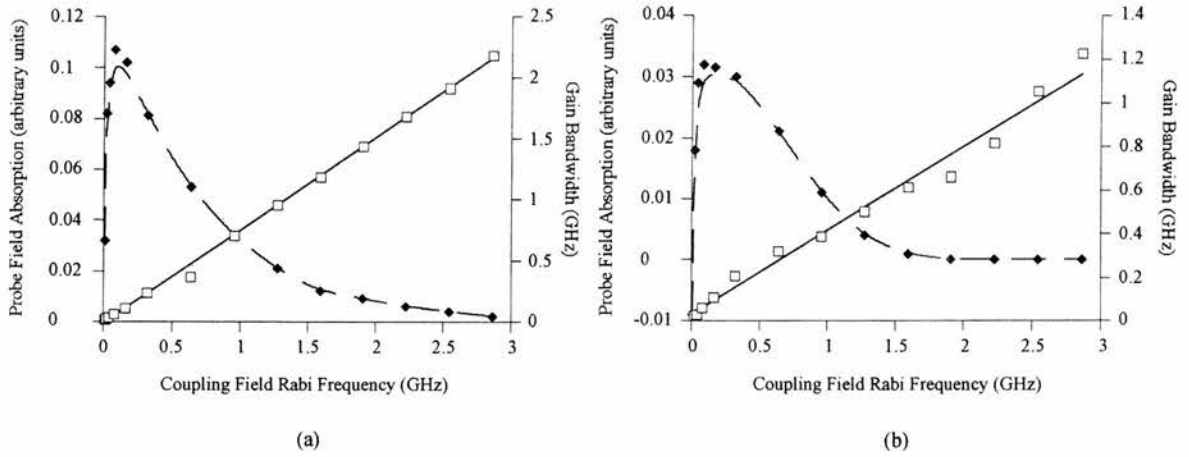


Figure 7.11: The peak gain (dashed line) and the gain bandwidth (solid line) as a function of coupling field Rabi frequency in the presence of a modest level of incoherent pumping for (a) the matched and (b) the mismatched schemes.

Interestingly, for higher coupling field Rabi frequencies splitting is predicted in the gain profile. In this case the peak gain occurs in two Rabi-like side bands equally spaced about line centre, rather than on line centre itself. Such splitting has been predicted previously in a Vee-type scheme [15-18]. Both the peak, as well as the on-resonance, gain were given in Table 7.I. In Figure 7.12 we observe the dependence of the on-resonance and peak gain on the coupling field Rabi frequency for the matched system. Note that no such splitting occurs in the mismatched scheme for the considered driving Rabi frequencies.

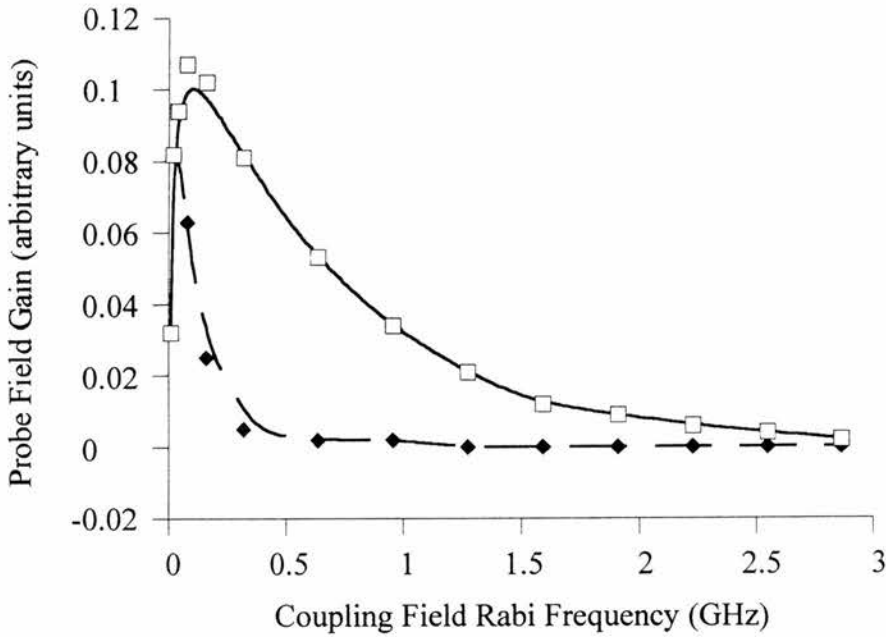


Figure 7.12: The peak (solid line) and on-resonance (dashed line) gain (ρ^i_{13} in arbitrary units) as a function of Rabi frequency for the matched scheme.

From the population data we can see that, over the range of Rabi frequencies considered, both schemes are inversionless in that there is always a greater proportion of the population in the lower level of the probe transition than there is in the upper level. However, for a Rabi frequency of 950MHz both schemes have less than half of the total population in the ground state because a substantial fraction of the population is pumped into the upper level of the coupling field transition. Figures 7.13 (a) and (b) show the relative populations in the matched and mismatched schemes respectively.

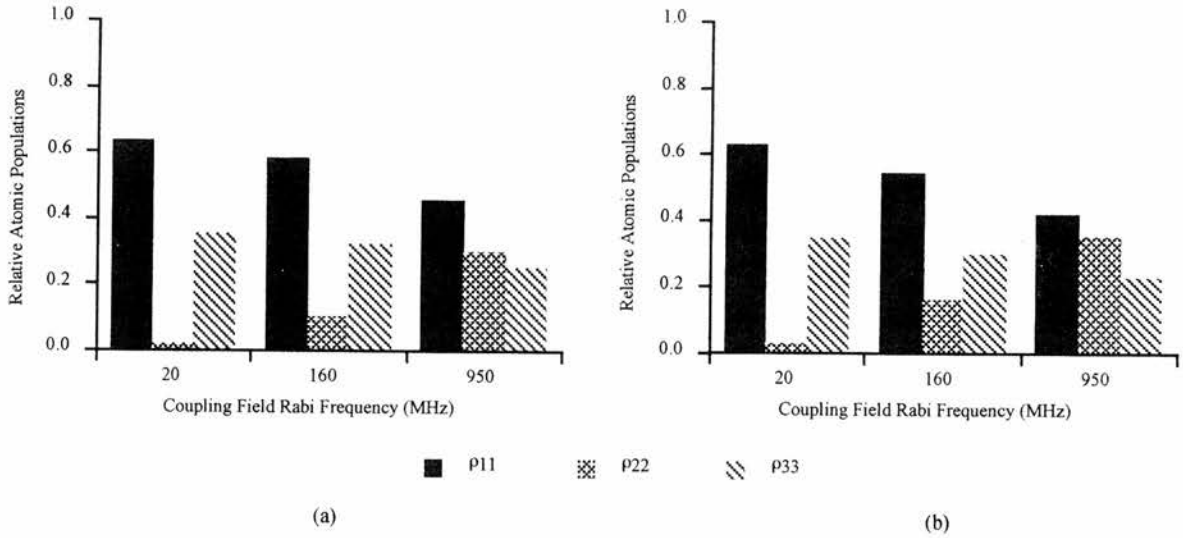


Figure 7.13: *The relative atomic populations for the coupling Rabi frequencies indicated, in the presence of a modest level of incoherent pumping for (a) the matched and (b) the mismatched schemes.*

Finally, Fig. 7.14 shows the transparency and gain as a function of probe field detuning for both schemes, for the coupling field Rabi frequency of 160MHz. This example shows inversionless gain in both the matched and mismatched cases. The nature of the initial transparency determines, to a certain extent, the form of the gain.

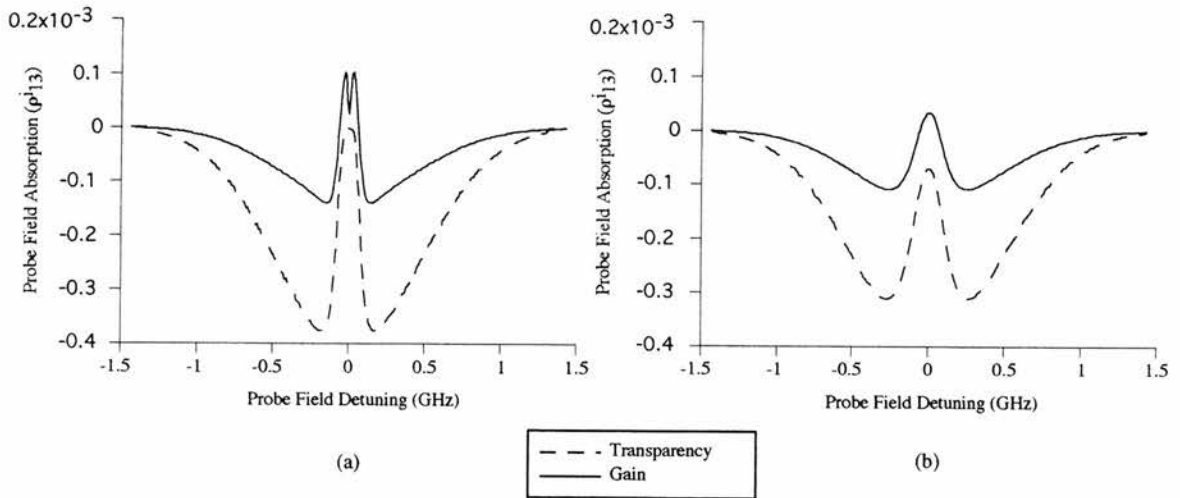


Figure. 7.14: The absorption (ρ_{13}^i in arbitrary units) as a function of probe field detuning in the absence and presence of incoherent excitation for (a) the matched and (b) the mismatched schemes. The coupling field Rabi frequency is 160MHz in both cases. The dashed lines correspond to the transparency induced in the absence of incoherent excitation, and the solid lines represent the gain that may be achieved with an incoherent pumping rate of $10 \times 10^6 \text{ s}^{-1}$.

7.5 Discussion

The significance of these results is that both transparency and inversionless gain are predicted for a probe frequency higher than the employed coupling frequency in a Doppler-broadened medium, and that these coherently induced effects can be realised for coupling field Rabi frequencies far less than the Doppler width of the probe transition. It is generally accepted that transparency and gain can be produced in a Doppler-broadened scheme by Autler-Townes splitting beyond the Doppler width [12]. Continuous wave laser systems are limited in power and this method of achieving transparency and subsequent gain is not generally viable. In addition, as the results presented in Fig. 7.11 showed, the gain does not indefinitely increase for higher coupling field Rabi frequencies. However, the results presented in this chapter show that gain is still observable for the much lower output powers associated with cw lasers without resorting to either wavelength matching or a Doppler free environment.

This prediction can be explained by adopting the approach used in Chapter 4, i.e. by looking at the relative positions and magnitudes of the Autler-Townes components, as well as the positions of the single and two-photon absorption resonances. The positions of the Autler-Townes components in a Vee scheme are given, in terms of the probe field detuning, by Eq. (7.17):

$$\Delta_{\text{probe}} = k_1 V_z + \frac{1}{2} (\Delta_{\text{coupling}} - k_2 V_z) \pm \frac{1}{2} \sqrt{\Omega_c^2 + (\Delta_{\text{coupling}} - k_2 V_z)^2} \quad (7.17)$$

where $\Delta_{\text{probe}} = \omega_1 - \omega_{13}$, $\Delta_{\text{coupling}} = \omega_2 - \omega_{12}$, and the single and two-photon resonance positions are given by Eqs. (7.18a) and (7.18b) respectively:

$$\Delta_{\text{probe}} = k_1 V_z \quad (7.18a)$$

$$\Delta_{\text{probe}} = k_1 V_z - k_2 V_z + \Delta_{\text{coupling}} \quad (7.18b)$$

In a matched wavelength scheme the EIT feature is resolved from the Doppler-broadened absorption profile because the position of the two-photon resonance is fixed, independent of the atomic velocity, and the transparency created at line centre for the zero velocity group remains visible. In our mismatched scheme the two-photon resonance position will be different for each velocity group. Figure 7.15 shows the positions of the Autler-Townes components and absorption resonances for (a) the matched and (b) the

mismatched schemes for a coupling field Rabi frequency of 160MHz. We consider the case for which the coupling laser is not manually detuned, i.e. Δ_{coupling} equals zero. Figure 7.15 (b) clearly shows that the secondary Autler-Townes components of the non-zero velocity groups, associated with two-photon resonance, overlap with the transparency at line centre when the probe field frequency is higher than that of the coupling field.

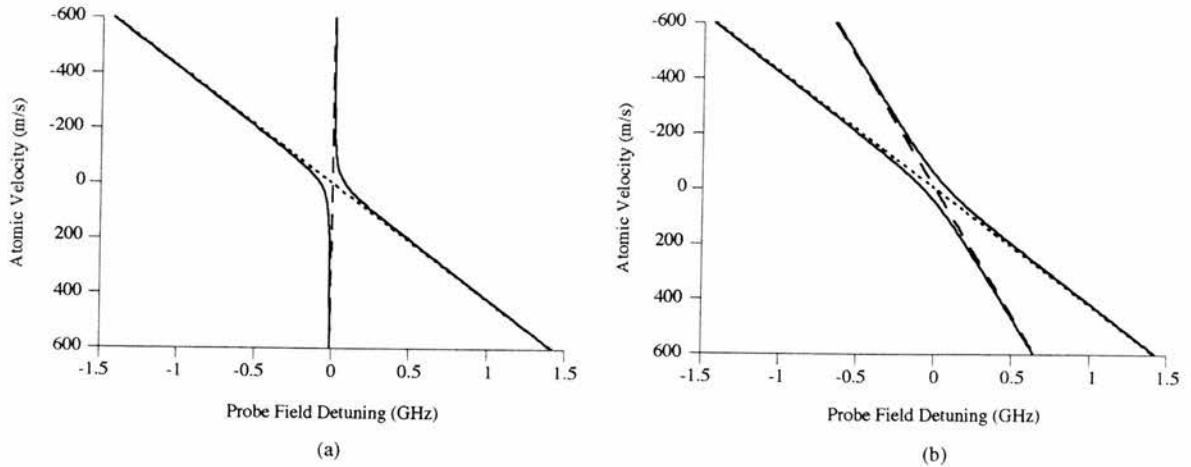
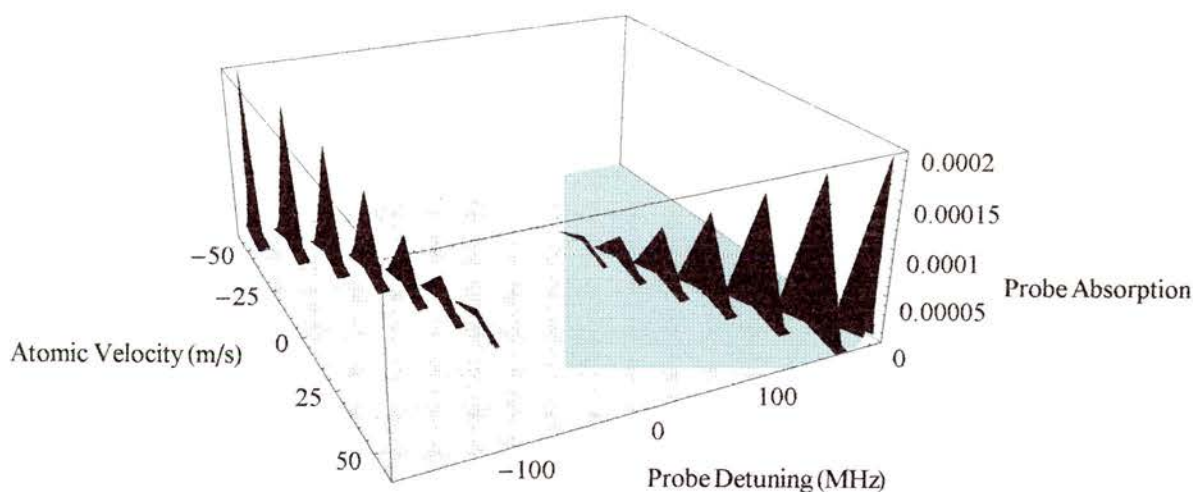


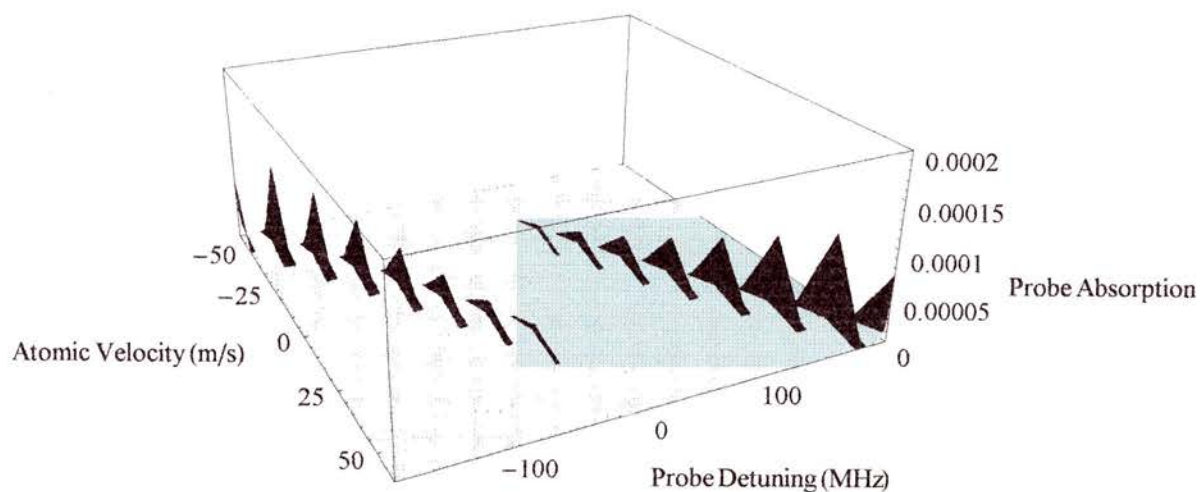
Figure 7.15: *The positions, in terms of probe field detuning, of the Autler-Townes components and single and two-photon resonances for (a) the matched and (b) the mismatched schemes. The solid lines correspond to the Autler-Townes components, the dotted lines to the single photon resonances, and the dashed lines to the two-photon resonances.*

The fundamental difference between the matched and mismatched schemes is that in the former case the secondary Autler-Townes components do not overlap and mask the transparency on resonance. However, despite the differences in the presented theoretical results, transparency is predicted in the mismatched Vee scheme. This result is a consequence of the two-photon process in a Vee scheme ($|2\rangle \rightarrow |1\rangle \rightarrow |3\rangle$) which begins in the upper level of the coupling field transition. For non-zero velocity groups the coupling field is Doppler shifted away from the $|1\rangle \rightarrow |2\rangle$ transition and does not significantly populate state $|2\rangle$. Therefore, as we consider atoms of a higher velocity the magnitude of the two-photon absorption process diminishes, and the secondary Autler-Townes components that overlap with the transparency window are very small in magnitude.

Figure 7.16 shows three-dimensional plots of the absorption as a function of atomic velocity and probe field detuning for (a) the matched and (b) mismatched schemes. The probe absorptions are calculated for a finite number of atomic velocities within the Doppler-broadened profile; only the velocity groups that contribute to the absorption near resonance are considered. In both cases the secondary Autler-Townes components quickly disappear as the atomic velocity increases. Some advantage is still gained by matching wavelengths due to the small two-photon contribution to absorption for atoms with a velocity very close to zero. However, Fig. 7.16 (b) unequivocally shows that, due to the nature of the two-photon process in a Vee scheme, transparency is observable in a mismatched system in which the probe field frequency is well in excess of that of the coupling field.



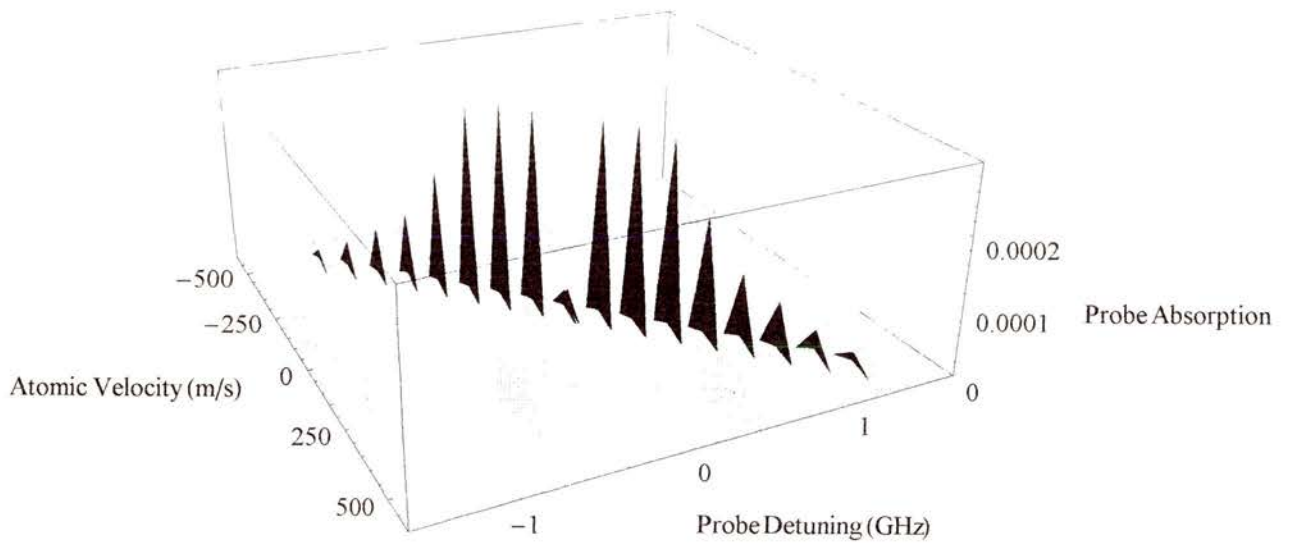
(a)



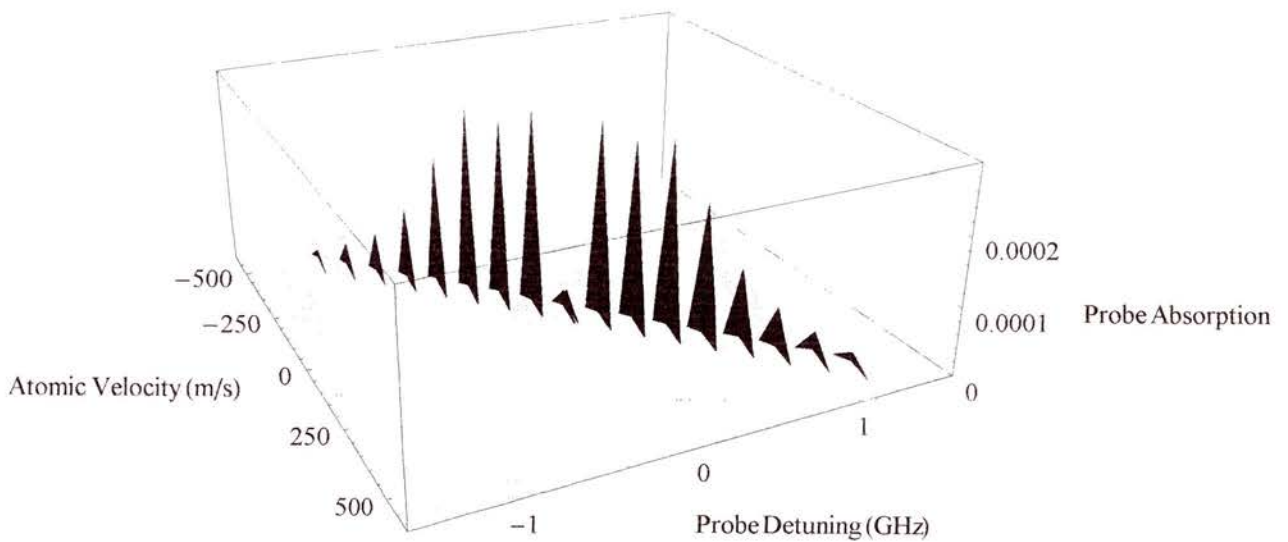
(b)

Figure 7.16: Probe field absorption (ρ_{13}^i in arbitrary units) as a function of probe field detuning and atomic velocity for selected discrete velocities for (a) the matched and (b) the mismatched schemes with a coupling field Rabi frequency of 160MHz. This figure shows a close up of the Autler-Townes components close to resonance for a velocity range of -60 to 60ms^{-1} .

The results presented in this chapter demonstrate that the mismatched transparency can be turned into gain in exactly the same way as in the matched scheme. Indeed, Figure 7.14 showed that the induced transparency predetermines the nature of the gain that is achievable in each system. In the matched scheme the transparency window is a narrow, deep feature; whereas, the mismatched scheme exhibits a wider, shallower transparency. Hence the gain in the mismatched case is broader and of a lower peak magnitude. Importantly, in both schemes the total reduction in absorption, upon the application of the coupling field, is the same, as is the further increase in ρ_{13}^i when incoherent pumping is introduced. We now consider three-dimensional absorption profiles for the three selected Rabi frequencies: 20MHz, 160MHz, and 950MHz in the absence of incoherent pumping. In so doing we assess the effect of varying the coupling field Rabi frequency on the magnitudes of the Autler-Townes components in the matched and mismatched schemes.

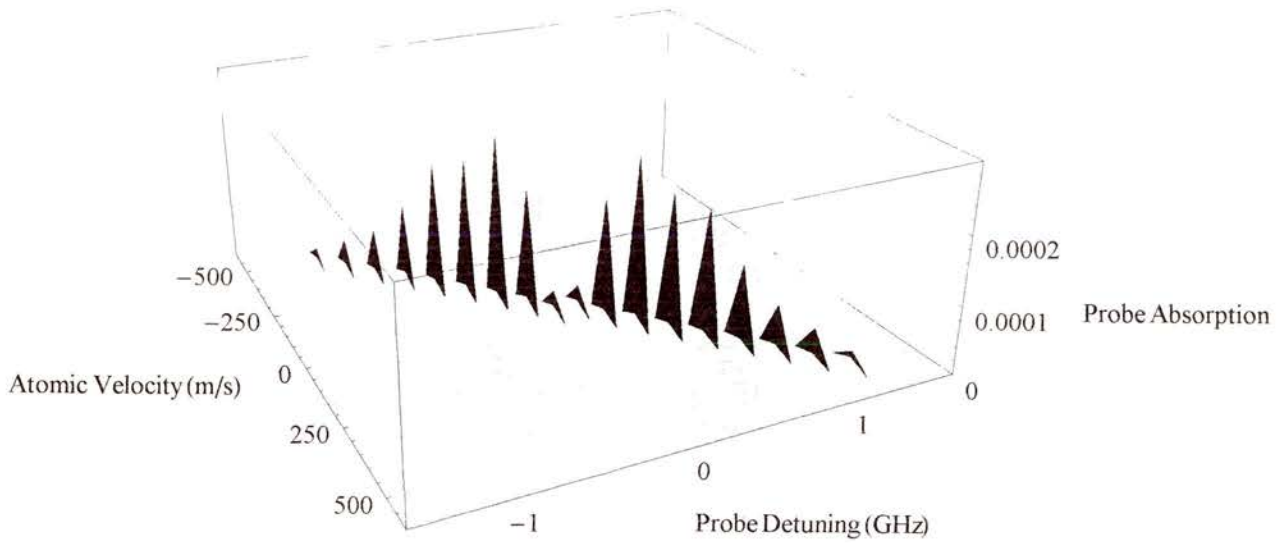


(a)

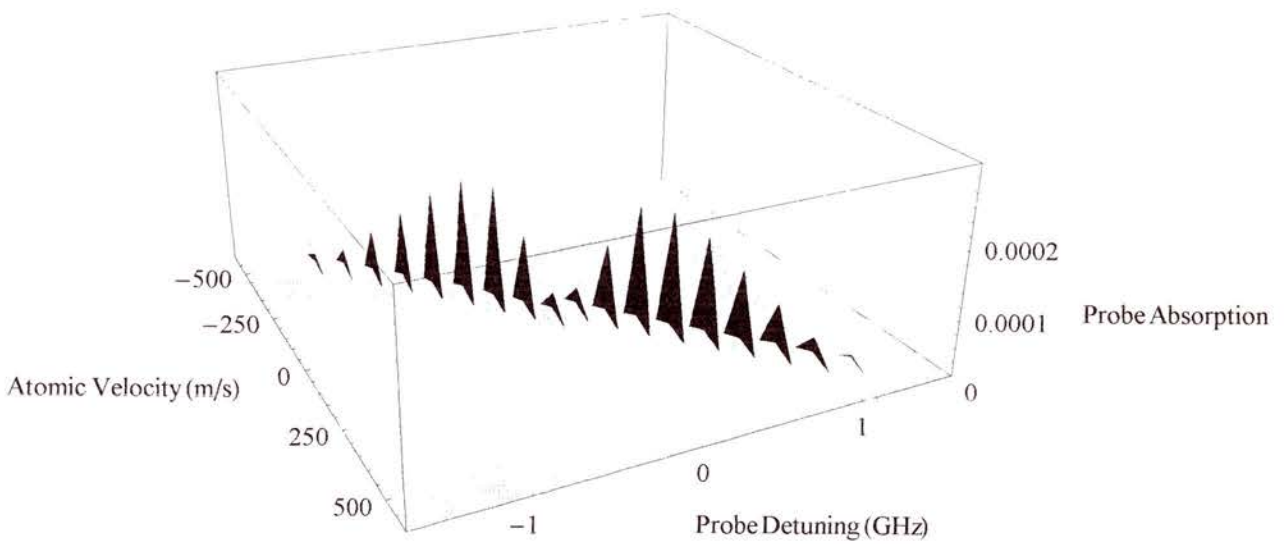


(b)

Figure 7.17: Probe field absorption (ρ_{13}^i in arbitrary units) as a function of probe field detuning and atomic velocity for selected discrete velocities for (a) the matched and (b) the mismatched schemes with a coupling field Rabi frequency of 20MHz. The incoherent pumping rate is zero.

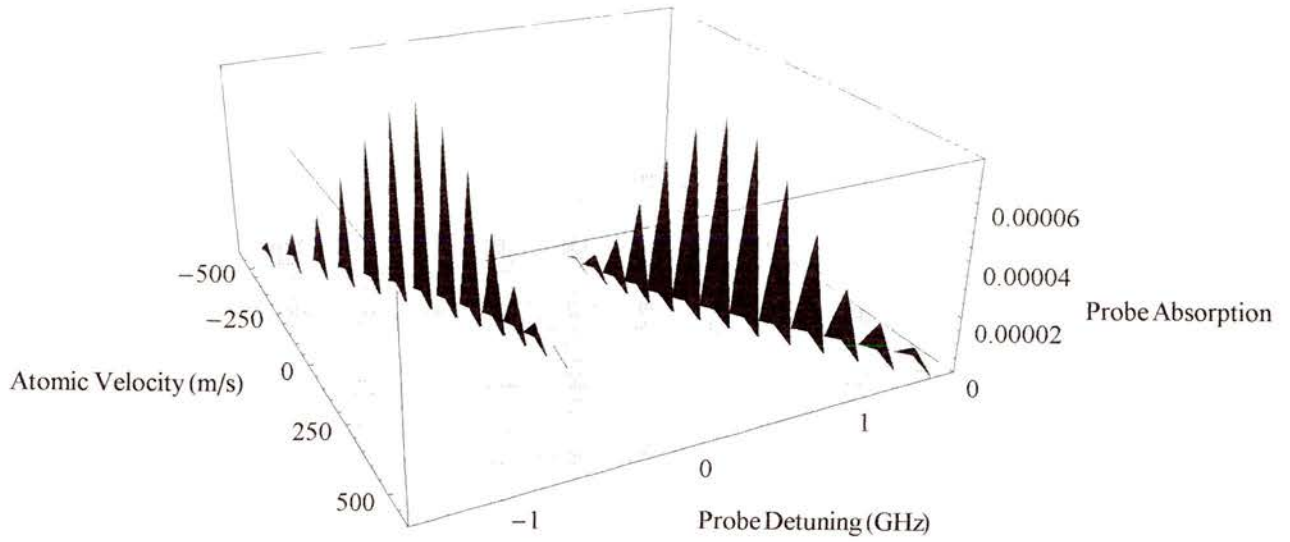


(a)

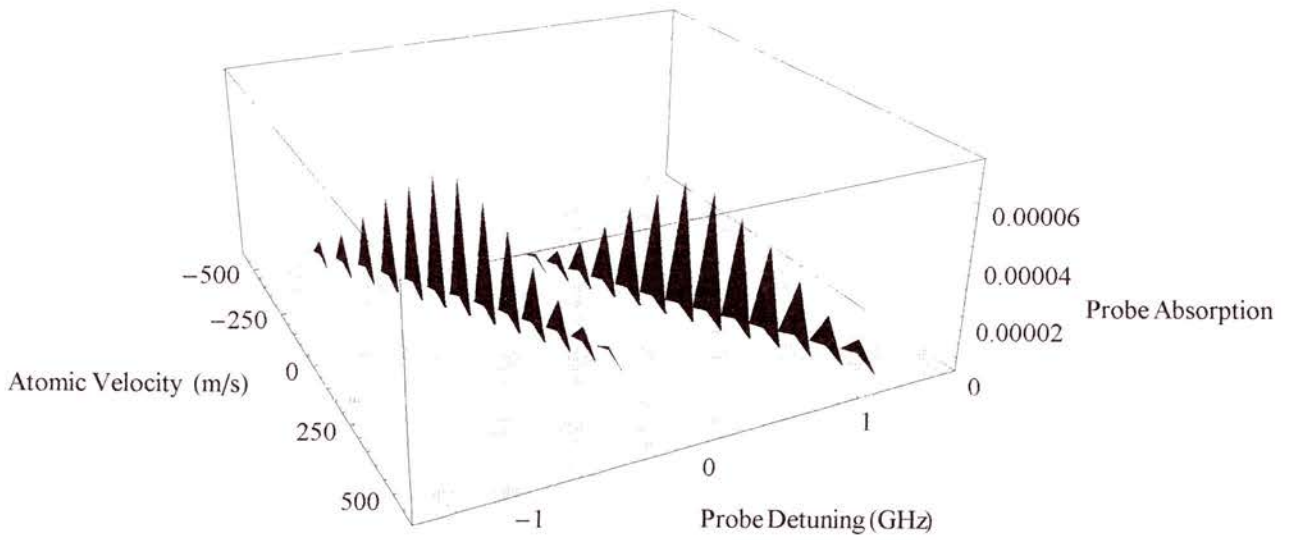


(b)

Figure 7.18: Probe field absorption (ρ_{13}^i in arbitrary units) as a function of probe field detuning and atomic velocity for selected discrete velocities for (a) the matched and (b) the mismatched schemes with a coupling field Rabi frequency of 160MHz. The incoherent pumping rate is zero.



(a)



(b)

Figure 7.19: Probe field absorption (ρ_{13}^i in arbitrary units) as a function of probe field detuning and atomic velocity for selected discrete velocities for (a) the matched and (b) the mismatched schemes with a coupling field Rabi frequency of 950MHz. The incoherent pumping rate is zero.

From the presented series of three-dimensional plots, Figs. 7.17, 7.18, and 7.19, we see that the secondary, two-photon, Autler-Townes components persist for higher velocities when the coupling field Rabi frequency is greater. For higher Rabi frequencies, the two-photon absorption is reduced less dramatically as the coupling field is Doppler detuned from resonance because the stronger field still interacts with the transition and populates the excited state, $|2\rangle$. Fortuitously, as we increase the coupling field Rabi frequency the splitting of the Autler-Townes components from line centre also increases. These effects are compensatory and the transparency window actually widens as the coupling field Rabi frequency is increased.

We also see from Figs. 7.17 to 7.19 that the observed splitting in the Doppler-broadened absorption profile does not equal the zero velocity Autler-Townes splitting. In the Doppler-broadened case the observed splitting is more complex than that implied previously by Eq. (4.1) because the detuning is dependent on atomic velocity. In Fig. 7.17, for a low coupling field Rabi frequency, we see that the splitting of the integrated Doppler-broadened absorption profile is determined not by the zero velocity Autler-Townes components but by the primary Autler-Townes components of the 200 and -200ms^{-1} velocity groups. As the Rabi frequency is increased the observed splitting becomes closer to the zero velocity value because the Doppler shifted detuning is small compared to the Rabi frequency. As previously described in Section 5.4.1 (Fig. 5.13) these values converge as the Rabi frequency increases.

The results presented in this chapter confirm that the transparency predicted in Chapter 4 and experimentally verified in Chapter 5 can be turned into gain without the need for a population inversion. This theoretical prediction raises the question: how far can we mismatch the wavelengths in a Doppler-broadened Vee scheme? Figure 7.20 shows a plot of the 'on-resonance' absorption coefficient as a fraction of the absorption coefficient in the absence of the coupling laser, for different values of the coupling field Rabi frequency. For the purposes of this plot we consider only transparency, for which the incoherent excitation rate is set to zero. The probe field wavelength is varied while the coupling field wavelength is held constant at 780nm. The solid and dashed vertical lines correspond to our matched and mismatched systems respectively. By plotting the logarithm of the absorption we see that in the matched case a coupling field Rabi frequency of less than

1GHz reduces the absorption by more than three orders of magnitude. This plot also shows that, in the mismatched case, a coupling field of 950MHz still reduces the absorption by more than an order of magnitude.

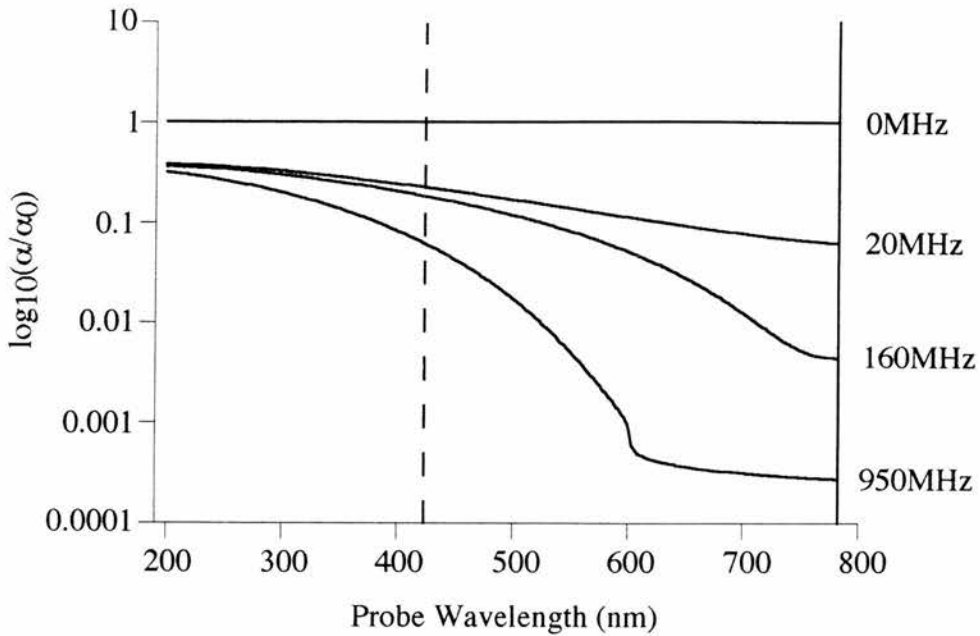


Figure 7.20: *The logarithm of the ratio of the absorption coefficient in the presence and absence of the coupling field ($\log_{10}\alpha/\alpha_0$) is plotted as a function of the probe wavelength. The probe wavelength is varied while the coupling wavelength is held constant at 780nm. The solid vertical line marks the matched scheme and the dashed vertical line marks the mismatched system. The magnitude of the coupling field Rabi frequency is given on the right hand side of each trace.*

A region of almost constant transparency is predicted for a Rabi frequency of 950MHz, when the probe wavelength is greater than 600nm. The level of transparency is constant because the Autler-Townes splitting rivals the Doppler width for this wavelength range. As the wavelength of the probe decreases the level of induced transparency reduces; however, even at the UV wavelength of 200nm, a transparency of approximately 60% is predicted for a coupling field Rabi frequency of 950MHz.

The splitting predicted in the gain profile is worth further consideration and has been predicted previously in the context of traditional gain [18] and inversionless gain [15-

17]. Interestingly, if dephasing is artificially increased the splitting disappears and the on-resonance gain actually increases. The dephasing could be increased, in practice, by introducing a buffer gas, or increasing particle density. Figure 7.21 shows the on-resonance gain as a function of dephasing on the unlinked $|2\rangle - |3\rangle$ transition for a coupling field Rabi frequency of 160MHz in the matched and mismatched schemes.

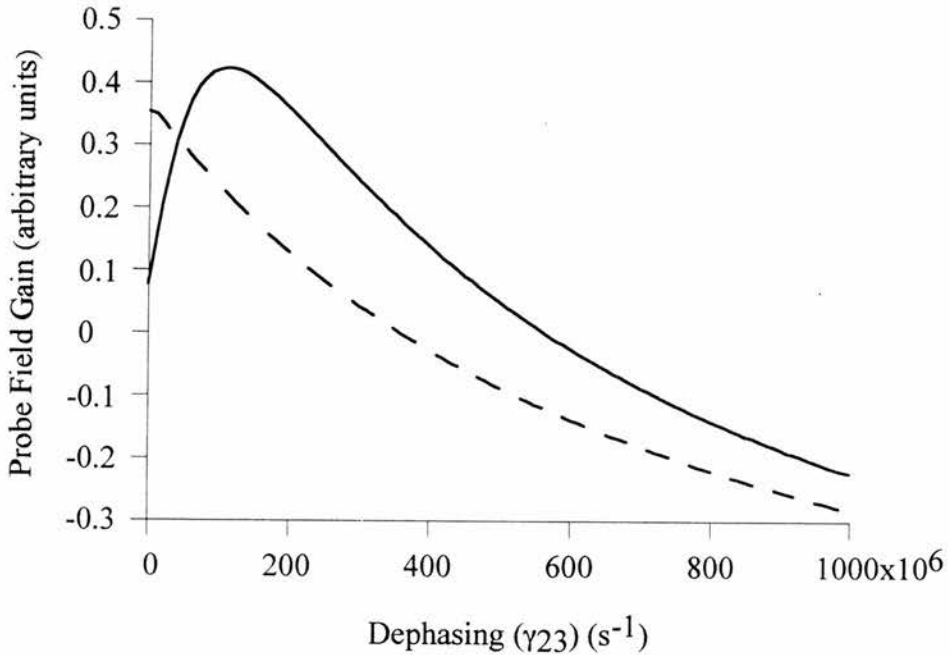


Figure 7.21: On-resonance gain (ρ_{13}^i in arbitrary units) as a function of dephasing on the unlinked transition (γ_{23}) for the matched (solid line) and the mismatched (dashed line) systems. The coupling field Rabi frequency is 160MHz in both cases.

In the mismatched scheme no splitting of the gain profile is predicted for this Rabi frequency, and the gain diminishes as dephasing is increased as we would expect. However, in the matched case the gain initially increases with increasing dephasing. This surprising result occurs as a consequence of the observed splitting. In Fig. 7.22 we see the evolution of the gain profile for values of increasing dephasing. These traces show the peak gain in the Rabi-like sidebands decrease while the gain on-resonance slightly increases. The gain is enhanced on-resonance due to the broadening of the sidebands associated with an increasing dephasing.

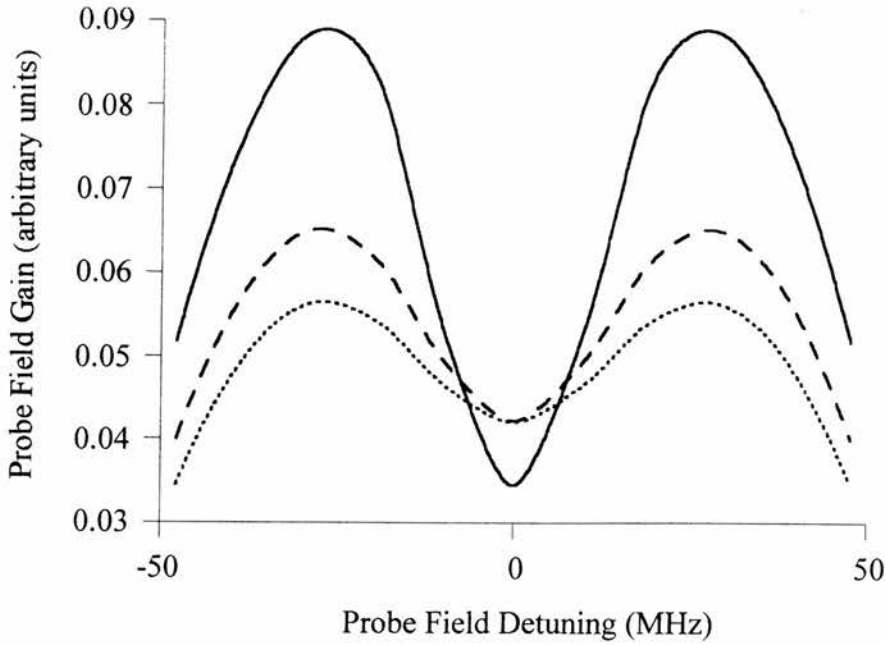


Figure 7.22: Overlaid plots of gain (ρ_{13}^i in arbitrary units) as a function of probe field detuning close to resonance in the matched scheme for a range of dephasings. The considered values of the dephasing on the unlinked transition are $50 \times 10^6 \text{ s}^{-1}$ (solid line), $100 \times 10^6 \text{ s}^{-1}$ (dashed line), and $125 \times 10^6 \text{ s}^{-1}$ (dotted line).

In the comparison made in this chapter and previously in Chapter 4, it was necessary to alter the decay rates artificially in one or all of the systems to ensure the comparison of wavelength dependence was valid. We consider here the effect of changing the decay rates on the gain that may be observed in the matched and mismatched systems. Figure 7.23 depicts the on-resonance gain as a function of the spontaneous decay rates on the coupling (solid line) and probe (dashed line) transitions for (a) the matched and (b) mismatched schemes. An independent increase in the decay rate on the probe and coupling transitions causes the gain to decrease in the former case and increase in the latter. This relationship is true of both systems, but Fig. 7.23 shows that the mismatched scheme is more sensitive to changes in the decay rates. The decay on the coupling transition is particularly important in the mismatched scheme because this decay rate controls the level of population that may be maintained in the upper level of this transition and thereby determines the strength of the two-photon process. Selecting an atomic system with a fast rate of decay on this transition will ensure that the two-photon absorption for high

velocity atoms that overlaps with the transparency at line centre is of a negligible magnitude. Obviously, the mismatched system is more sensitive to this decay rate because the two-photon absorption components have a greater overlap with line centre.

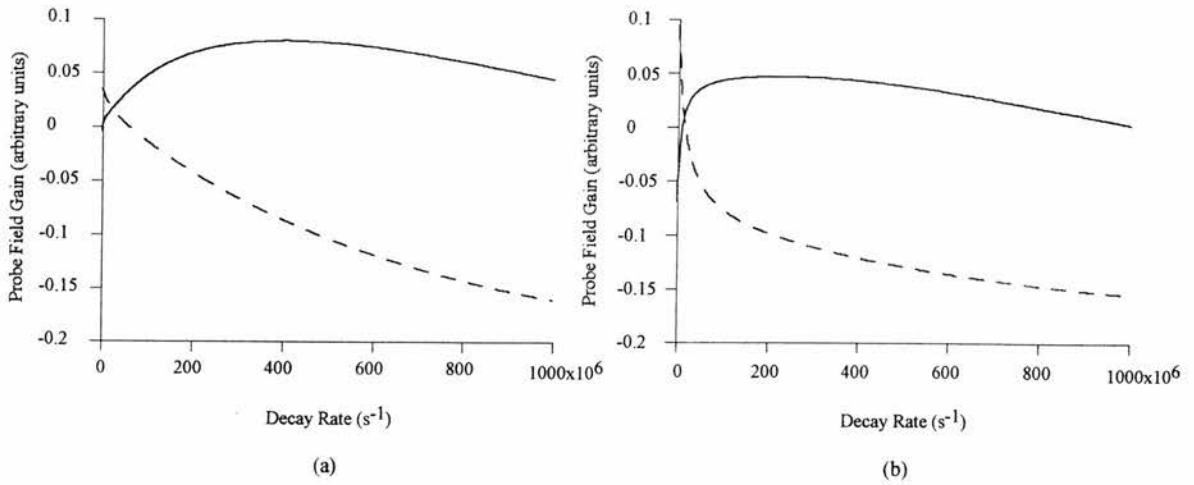


Figure 7.23: On-resonance gain (ρ_{13}^i in arbitrary units) plotted as a function of the coupling (solid line) and probe (dashed line) field decay rates for (a) the matched and (b) the mismatched schemes. The employed coupling field Rabi frequency is 160MHz, and the incoherent pumping rate is $10 \times 10^6 \text{ s}^{-1}$.

A large decay rate on the probe transition is detrimental in an inversionless gain scheme because, for a given incoherent pumping rate, it will result in a smaller upper state population. In addition, the relaxation of population contributes to the dephasing of the coherence. In a Vee scheme the decay rates on the probe and coupling transitions both contribute to the dephasing on the unlinked transition ($|2\rangle - |3\rangle$); consequently, the gain is eventually reduced for high decay rates on either transition.

Note that the dependence of the gain on the relaxation rates predicted in Fig. 7.23 leads to the problem of coupling field absorption in mismatched systems. The requirement of a coupling decay rate equal to or higher than the probe decay rate for inversionless gain has been discussed independently by Yelin *et al* [19]. In Chapter 5 a system was employed in which the coupling transition decay rate exceeded that of the probe transition. This configuration was chosen in order that the condition for inversionless gain, $\Gamma_c \geq \Gamma_p$, could be satisfied. The implications of coupling field absorption will be discussed in the following section.

7.6 Further Practical Considerations

The theoretical study presented in this chapter is intended to give a general insight into the production of inversionless gain in Doppler-broadened, mismatched systems. The theoretical mismatched scheme was based on the experimental system in which mismatched transparency has already been demonstrated in Chapter 5 [1]. The exact experimental conditions in that instance have been used to calculate the values of absolute gain in this chapter. For a 2cm cell length of rubidium and a linear coupling Rabi frequency of 160MHz, we predict a gain of approximately 8% at 130 °C in the absence of coupling field absorption. This calculation is based on the incoherent excitation rate of $10 \times 10^6 \text{ s}^{-1}$, and it involves a coupling field Rabi frequency that can be easily attained with cw laser powers. This level of predicted gain [20] compares favourably with the gains observed in recent inversionless gain and lasing experiments [3,21-28], as shown in Table 7.III.

| | Boon [20] | Nottelmann [21] | Fry [22] | Zibrov [3,23] | Zhu [24] | Fort [25] | Durrant [26] | Peters [27] | Padmabandu [28] |
|--------------------------------|--------------|--------------------|-------------|------------------|-------------|--------------|-----------------|----------------|--------------------|
| laser | ? | NO | NO | YES | NO | NO | NO | YES | YES |
| gain (%) | 8 | 7 | 10 | 8 to 16 | 10 | 2.5 | 8 | 10 | 10 |
| cell length (cm) | 2 | 0.5 | 4 | 4 | 7.5 | 4 | ? | 30 | ? |
| cell temp. (°C) | 130 | 777 | 150-200 | 60 | 60 | 40 | sub-mK | ? | 280-320 |
| probe wavelength (nm) | 422 | 570.68 | 589 | 794 | 780 | 894 | 780 | 878 | 589 |
| coupling wavelength (nm) | 780 | 570.68 | 589 | 780 | 780 | 852 | 780 | 1080 | 589 |
| medium | rubidium | samarium | sodium | rubidium | rubidium | caesium | rubidium | helium | sodium |

Table 7.III: Comparison of absolute gain and conditions employed to achieve it in our theoretical system and eight experimental schemes, indicated by the first author in each case.

However, we have not taken into account the effects of coupling field absorption. The experimental results in Chapter 5 exhibited such effects, and we saw that the level of transparency predicted was not observed experimentally. The absorption of the coupling field causes the driving Rabi frequency to diminish with the field's propagation through the interaction region. Consequently, the level of EIT and subsequent inversionless gain will be reduced. This problem is not specific to our scheme, and it will in fact limit any AWI or LWI system for which the probe frequency exceeds the coupling frequency. Loudon defines the relationship between the Einstein A coefficient and the dipole matrix element as [11]:

$$A_{ij} = \frac{\mu_{ij}^2 \omega_0^3}{3\pi\epsilon_0 \hbar c^3} \quad (7.19)$$

It was shown previously in Fig. 7.23 and independently by Yelin *et al* [19] that it is necessary for the coupling decay rate to equal or exceed that on the probe transition to achieve inversionless gain. Therefore, we do not wish the probe transition decay rate to increase when we move to a mismatched regime. Equation (7.19) indicates that to increase the frequency of the probe transition without affecting the relaxation rate, we must select a transition with a weak dipole matrix element. The absorption or gain on such a transition will therefore be small for a given particle density.

In general, the probe gain will increase with particle density until the coupling field absorption in the vapour cell becomes significant. In the latter case, the driving field is absorbed in the strong signal regime because of the high decay rate on the coupling field transition. Reducing this decay rate will also reduce the level of gain as shown previously in Fig. 7.23. The coupling field absorption can be reduced by increasing the driving Rabi frequency so that even when the intensity of the field is reduced towards the end of the cell it is still sufficient to induce the necessary transparency. Unfortunately, increasing the Rabi frequency spreads the gain out over a wider bandwidth, and as we saw in Fig. 7.11 the level of peak gain will eventually reduce. A maximum obtainable gain therefore exists, for which the coupling Rabi frequency is traded off against the particle density and the level of coupling field absorption in the cell. This limitation on the inversionless gain applies to all mismatched systems. The theoretical analysis presented in this chapter demonstrates that

mismatched inversionless gain in a Doppler-broadened medium is realisable in a Vee scheme subject to the limits of coupling field absorption.

7.7 Conclusion

The results presented in this chapter confirm that it is not necessary to rely on the frequency or wavelength matching effect to achieve a good transparency in a medium subject to the effects of Doppler-broadening. Furthermore, we have seen that it is possible to take this one step further and produce true inversionless gain in mismatched schemes for which the probe wavelength is less than that of the coupling field. EIT has already been demonstrated in such a system, and it was discussed in detail in Chapter 5 [1]. In the absence of coupling field absorption, 8% gain is predicted for this configuration with a modest level of incoherent pumping. This level of gain is comparable to that achieved in existing inversionless laser systems. Although the effects of driving field absorption have not been taken into account, the Rabi frequency for which gain has been calculated is more than an order of magnitude less than the maximum obtainable with a cw Ti:sapphire laser. It is therefore not unreasonable to assume that this level of gain should be realisable in rubidium vapour with careful choice of the experimental conditions. Furthermore, it has been clearly demonstrated that while Doppler-broadening reduces the gain obtainable in the mismatched ($\lambda_c > \lambda_p$) regime, significant gain persists in a Vee-type configuration. The future of this experimental system will be discussed in Chapter 8.

Thus far, the results indicate that there is a promising alternative method to achieving inversionless lasing through Doppler free systems. This alternative approach relies on the Vee scheme, and it is viable because the two-photon absorption of high velocity atoms that masks transparency on-resonance is very weak in the Vee configuration. In particular, the results in this chapter demonstrate that the unique nature of the Vee scheme can be exploited to realise gain or amplification without inversion in a three level system. This is the first step to realising a robust high frequency inversionless laser in a real experimental scheme.

References

- [1] J. R. Boon *et al*, Phys. Rev. A. **57**, 2, 1323-1328, (1998).
- [2] J. R. Boon *et al*, Phys. Rev. A. (submitted June 1998).
- [3] A.S. Zibrov *et al*, Phys. Rev. Lett. **75**, 8, (1995).
- [4] D. J. Fulton, S. Shepherd, R. R. Moseley, B. D. Sinclair, and M. H. Dunn, Phys. Rev. A. **52**, 2303, (1995).
- [5] R. R. Moseley, S. Shepherd, D. J. Fulton, B. D. Sinclair, and M. H. Dunn, Phys. Rev. A. **50**, 4339, (1994).
- [6] R. R. Moseley, Ph.D. thesis, University of St. Andrews, 1994 (unpublished).
- [7] N. F. Ramsey, *Molecular Beams*, (Clarendon Press, Oxford, (1956)).
- [8] A. Einstein, Phys. Zs. **18**, 121, (1917).
- [9] A. Yariv, *Optical Electronics*, (Saunders HBJ, 4th edition, (1971)).
- [10] A. Yariv, *Quantum Electronics*, (Wiley, 3rd edition, (1989)).
- [11] R. Loudon, *The Quantum Theory of Light*, (Oxford University Press, (1991)).
- [12] M. D. Lukin *et al*, Laser Phys. **6**, 3, 436-447, (1996).
- [13] D. C. Thompson, and G-X. Xu, Can. J. of Phys. **60**, 1496, (1982).

- [14] W. L. Wiese, and G. A. Martin, *A Physicist's Desk Reference* (American Institute of Physics, (1989)).
- [15] L. M. Narducci *et al*, Opt. Comm. **81**, 379, (1991).
- [16] W. Tan, W. Lu, and R. G. Harrison, Phys. Rev. A. **46**, R3613, (1992).
- [17] L. M. Narducci *et al*, Opt. Comm. **86**, 324, (1991).
- [18] J. S. Uppal, R. G. Harrison, and J. V. Moloney, Phys. Rev. A. **36**, 4823, (1987).
- [19] S. F. Yelin *et al*, Phys. Rev. A. **57**, 5, 3858, (1998).
- [20] J. R. Boon *et al*, Phys. Rev. A. (to be published September 1998).
- [21] A. Nottleman, C. Peters, and W. Lange, Phys. Rev. Lett. **70**, 12, 1783, (1993).
- [22] E. S. Fry *et al*, Phys. Rev. Lett. **70**, 21, 3235, (1993).
- [23] A. S. Zibrov *et al*, Laser Phys. **5**, 3, 553-555, (1995).
- [24] Y. Zhu, and J. Lin, Phys. Rev. A. **53**, 3, 1767, (1996).
- [25] C. Fort *et al*, Opt. Comm. **139**, 31-34 (1997).
- [26] A. V. Durrant *et al*, Opt. Comm. **151**, 136-146, (1998).
- [27] C. Peters, and W. Lange, Appl. Phys. B, **62**, 221-225, (1996).
- [28] G. G. Padmabandu *et al*, Phys. Rev. Lett. **76**, 12, 2053, (1996).

CHAPTER 8

Conclusions and Future Work

“I would have gotten away with it too if it weren’t for you
meddling kids.”

The bad guys in Scooby Doo

8.1 Conclusions

The work presented in this thesis delimits the effects of mismatching the probe and coupling wavelengths in Doppler-broadened systems. It has been shown that the consequences of Doppler-broadening are not as stringent as was originally assumed. Theoretical analysis has been carried out on the reduction of absorption due to EIT and the creation of inversionless gain. In addition, a mismatched Vee scheme subject to Doppler effects has been studied experimentally. The primary motivation for this work relates to its application to inversionless lasing. Although the concept of lasing without inversion contradicts one of the fundamental axioms of laser theory, it has recently been demonstrated experimentally [1]. The principle of LWI has been tested but for this phenomenon to have a significant impact on future laser technology it must be harnessed to access high frequency regions of the electromagnetic spectrum. Doppler-broadening was quickly identified as one of the major difficulties that must be overcome to achieve this goal [2]. To this end, we have investigated mismatching the probe and coupling wavelengths in Doppler-broadened media. Concentrating on the underlying effect of EIT, we demonstrated the potential for mismatched LWI in a Doppler-broadened medium, by exploiting the advantages of the Vee-type configuration.

In Chapter 4 theoretical study revealed that the best EIT in a Doppler-broadened system is achieved for coupling wavelengths less than the probe wavelength in all three considered schemes. Our model showed, as expected, that matching the wavelengths enabled significant EIT to be observed in all of the systems that were studied. For the wavelength regime in which the probe frequency greatly exceeds the coupling frequency, the presented analysis confirmed that it is necessary, in general, to employ a driving Rabi frequency comparable to or greater than the Doppler width on the probe transition.

Analysis of the role of coherence showed that the coherence on the unlinked transition dictates the level of transparency. Importantly, in the regime for which the Autler-Townes splitting exceeds the Doppler width it was shown that coherence still underpins the reduction in absorption.

Furthermore, an advantage was identified in the Vee scheme where transparency is predicted for Rabi frequencies less than the Doppler width. This surprising discovery was explained by considering the roles of individual velocity groups in a Doppler-broadened

system. It was shown that the two-photon process in a Vee scheme is strong for zero velocity atoms facilitating EIT on-resonance by the interference of alternative pathways to absorption. Fortuitously, the same two-photon process diminishes rapidly as the modulus of the atomic velocity increases and the two photon absorption of the non-zero velocity Autler-Townes components that would be detrimental to the observation of EIT in a mismatched scheme is negligible. This diminution of the two-photon process occurs in the Vee scheme because it originates in the upper level of the coupling transition rather than the ground state and is therefore more seriously reduced in magnitude when the coupling field is Doppler shifted from resonance.

An experimental mismatched Vee scheme was investigated in Chapter 5 for which the probe field frequency was approximately double the coupling field frequency. This system was realised in Doppler-broadened rubidium vapour. The results verified the hypothesis that EIT could be observed in the $\lambda_c > \lambda_p$ wavelength regime for coupling field Rabi frequencies equal to or greater than the Doppler width. A comprehensive study was carried out characterising the behaviour of EIT subject to both variations in the coupling field power and frequency. However, EIT was not observed for sub-Doppler width driving Rabi frequencies. Comparison of experiment and theory clearly showed that the limitation on EIT in the considered system was coupling field absorption rather than Doppler effects. Although anticipated, optical pumping was not present in this system due to a combination of coupling field absorption and the interaction of this field, at high powers, with both the hyperfine transitions of atomic rubidium

A comprehensive review of reported inversionless gain and lasing experiments was presented in Chapter 6. Importantly, the schemes considered to date have all utilised closely matched wavelengths. The principle of LWI has been clearly demonstrated in the described experiments and the hunt is now on for a practical mismatched system [2,3].

Chapter 7 presented a theoretical comparison of matched and mismatched inversionless gain in a Doppler broadened system based on rubidium. Crucially, the mismatched system utilised a probe field frequency greater than that of the coupling field. While the predicted matched gain was higher than that in the mismatched system, gain was still significant in the latter case even when the driving Rabi frequency was less than the probe Doppler width. An 8% gain was predicted for a 2cm cell at 130°C, in the absence of

coupling field absorption. This amplification was achieved theoretically with a modest incoherent pumping rate and a sub-Doppler width Rabi frequency easily obtainable with cw laser powers. The predicted gain compares favourably with the experiments described in Chapter 6.

In conclusion, we have investigated the limit imposed by Doppler-broadening in the mismatched wavelength regime. It has been demonstrated that systems subject to Doppler effects are not confined to matched wavelengths. Furthermore, by employing a Vee-type system inversionless gain is predicted for sub-Doppler width driving Rabi frequencies.

EIT has been observed experimentally in a mismatched Vee scheme for a coupling Rabi frequency comparable to the Doppler width, and we have identified the problem of coupling field absorption. Absorption of the driving field is an important factor that will restrict any mismatched ($\lambda_c > \lambda_p$) system regardless of the line broadening mechanism. The work presented in this thesis demonstrates the potential of creating a mismatched inversionless laser in a Doppler-broadened Vee scheme.

8.2 Future Work

The study of mismatched gain in Chapter 7 ignored the effects of coupling field absorption that were identified in Chapter 5. In that context, it was shown that Doppler-broadening did not preclude the production of AWI in an otherwise ideal system. However, to experimentally verify this theory it is necessary to incorporate all known effects into the theoretical model in order to select the most advantageous experimental conditions. Therefore, the next step is to further quantify the effects of coupling field absorption. It is possible to model the resulting variation of Rabi frequency along the cell length by integrating with respect to the distance propagated through the cell, in much the same way as we integrate over the velocity range to model Doppler-broadening. It will be possible to calculate a particle density in which no coupling field absorption occurs. Theory predicts that mismatched EIT should be observable for a coupling Rabi frequency less than the Doppler width associated with the probe transition in such a system. By this method the second hypothesis stated in Section 5.1 can be experimentally tested.

The experimental conditions best suited for mismatched inversionless gain can then be calculated, based on a trade-off of the particle density with the driving Rabi frequency. We know that both the available probe gain and the coupling field absorption scale with the particle density. However, since coupling field absorption is detrimental to EIT it will also degrade the observable gain. A maximum gain will be reached when the particle density is traded-off against the driving Rabi frequency. Increasing the Rabi frequency will reduce the effects of coupling field absorption; as the gain bandwidth increases the on-resonance gain reaches a maximum and then begins to diminish. These effects will define a maximum interaction length for a given coupling field Rabi frequency and cell temperature. A further increase in the cell length would result in a reduction in gain due to coupling field absorption.

In this respect, the detrimental effects of coupling field absorption are similar to the restriction of phase matching in nonlinear processes. In a nonlinear medium the phase matching condition defines an optimum length of crystal beyond which the nonlinear effect will diminish. This limitation can be tackled by quasi-phase matching. In this case, the medium is periodically poled so that the maximum interaction length can be harnessed many times over. It may be possible to achieve an analogous solution in inversionless

lasers by splitting the coupling beam and driving the interaction medium in stages. For example, the coupling beam could be split into two beams which would propagate through the cell in opposite directions. The strength of interaction would therefore be more evenly spread throughout the cell. However, such a configuration would have implications for the effects of Doppler-broadening since we could no longer assume that the probe and coupling fields were co-propagating.

Having quantified the effects of coupling field absorption and calculated the experimental conditions that would lead to the maximum possible gain in the mismatched rubidium system of Chapter 5, it would be pertinent to investigate this inversionless gain experimentally. If sufficient gain can be achieved in a real system, the final step would be to construct an optical cavity like those employed in Section 6.4. In order to achieve both gain and lasing it will be necessary to incoherently pump the probe transition. This pumping can be achieved by increasing the linewidth of a conventional laser, as described in Section 3.5. We now consider some alternative mismatched schemes that may be employed in future work beyond the blue 422nm system considered in this thesis.

8.2.1 Near Ultra-Violet Scheme

A potential scheme has been considered for optical fields that are further removed in wavelength than the blue and infrared transitions of the experimental system in Chapter 5. Figure 8.1 depicts an energy level scheme for a near ultra-violet (uv) probe field driven by an infrared coupling laser. The probe and coupling transitions correspond to the $5S_{1/2} - 7P_{3/2}$ and $5S_{1/2} - 5P_{3/2}$ energy levels in rubidium vapour. Transparency is possible in this system although it is more problematic to observe due to the requirement of a probe source at the uv wavelength of 358.807nm.

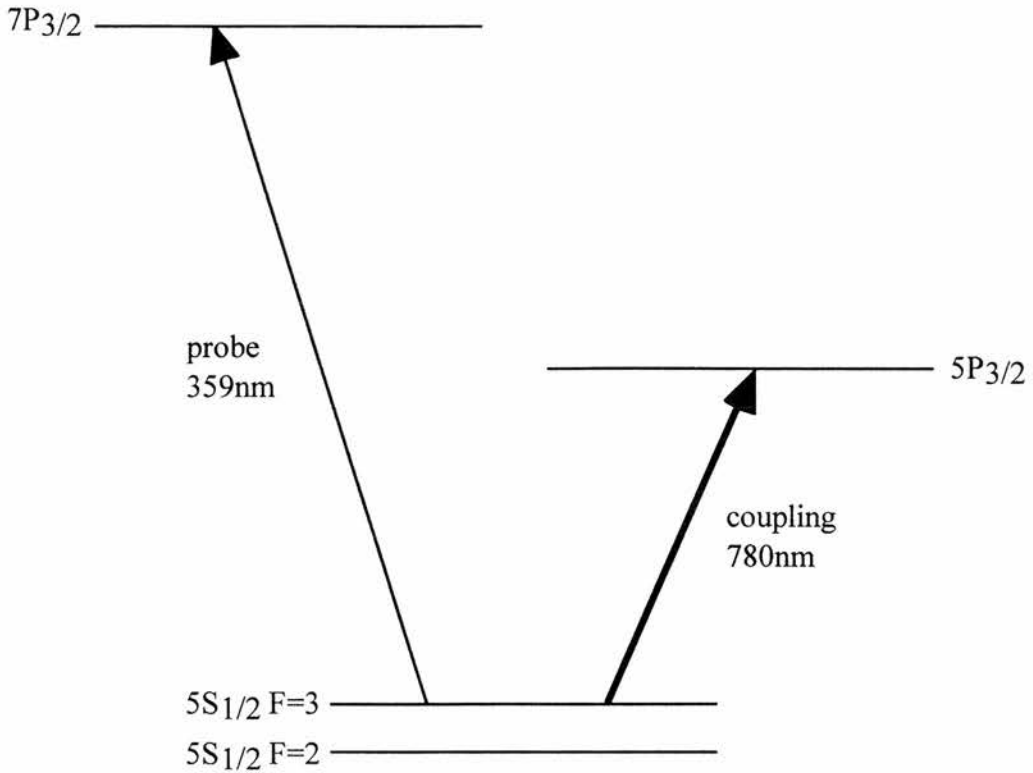


Figure 8.1: Schematic of system employing infrared field to drive a transparency in a near ultra-violet transition.

However, since both this scheme and the blue system can be realised in rubidium we expect to use very similar apparatus to facilitate both configurations. This similarity is important in the context of realising an inversionless laser. In this regime a probe beam is not required since the field will build up from spontaneous emission in the laser cavity as with a conventional laser system. Upon realisation of the blue scheme as an inversionless laser, the uv system could be implemented by altering the incoherent excitation to incorporate the appropriate energy state and by changing the cavity mirrors for the uv wavelength.

By virtue of this approach, it will be possible in the future to examine the more extreme mismatching in the uv system without the need to create a scanning single frequency uv source. Figure 8.2 shows the theoretical transparency predicted by the density matrix model, assuming no optical pumping by approximating the energy level structure to a closed three level system.

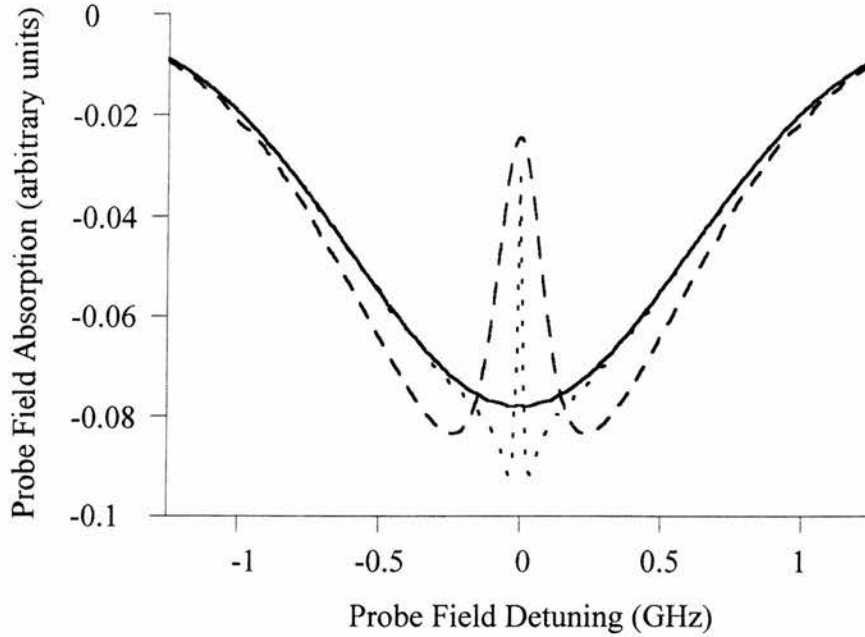


Figure 8.2: Probe field absorption (ρ_{24}^i in arbitrary units) as a function of probe detuning calculated via density matrix analysis of a closed three level system based on a near ultra-violet probe field controlled by an infrared coupling field. The absorption profile is shown for coupling field Rabi frequencies of 100MHz (dashed line), 10MHz (dotted line), and 0MHz (solid line). The Doppler width in this case is approximately 1.4GHz, based on a cell temperature of 200°C. We assume an ideal system in which dephasing results solely from natural level life time effects.

8.2.2 Radio Frequency Scheme

A recent goal of several research groups in this area [3-5] has been to control quantum coherence effects in an optical field with a radio frequency (RF) source. Some interesting conceptual problems arise when quantum coherence effects move into the RF regime. Figure 8.3 shows one possible RF scheme in rubidium vapour. The RF coupling field is applied to the hyperfine split ground state. Consequently, there is no ‘traditional’ means of population decay from the upper level ($5S_{1/2}$, $F=3$) of the coupling transition. Furthermore, this transition’s frequency may well be comparable to the Rabi frequency required to induce a transparency. The hyperfine splitting of the $5S_{1/2}$ ground state is 3GHz. The fact that the transition frequency and the Rabi frequency will be of the same

order of magnitude questions the validity of the rotating wave approximation upon which the density matrix model described in Section 2.2 is based. The removal of this approximation will complicate the theoretical modelling of the system.

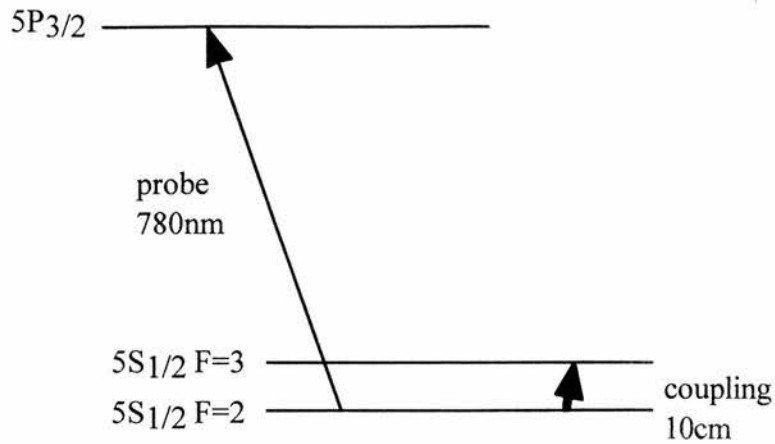


Figure 8.3: Schematic of system employing RF field to drive a transparency in an optical infrared transition.

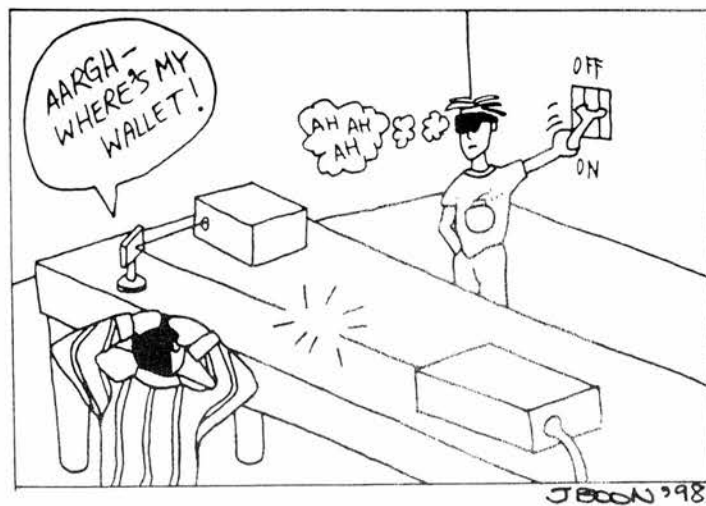
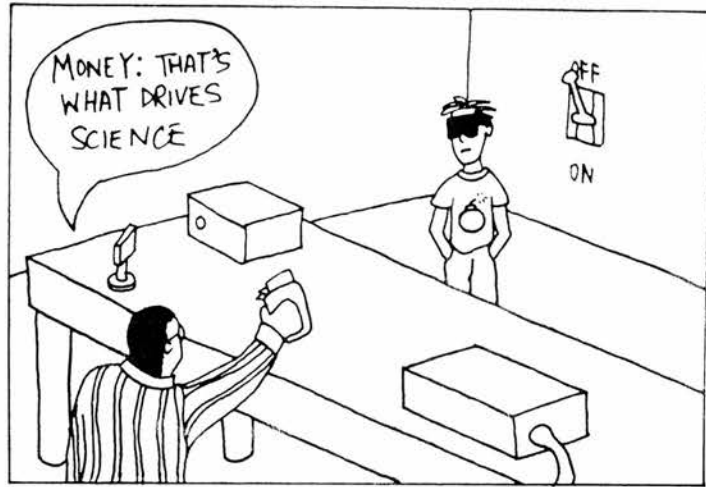
The question of population decay has a more straightforward answer. Collisional mixing of the hyperfine states causes movement of the atomic population and hence decay. In addition, if such an experiment is carried out in an atomic beam, as those recently published [6,7], the transit time of the atoms across the profile of the probe beam acts as the effective decay rate. Transit time may also be considered in a simple cell if the mean free path of the atoms is greater than the beam waists of the employed optical fields.

The RF scheme is an extreme case of a mismatched system in which the coupling wavelength is greater than the probe wavelength. Consequently, the Doppler shifts for non-zero velocity atoms will be very small. In Fig 8.3 the coupling wavelength is approximately 10cm compared to the 780nm probe field. Therefore, the Autler-Townes splitting will not noticeably vary with atomic velocity, and the secondary Autler-Townes components for high velocity atoms will overlap with line centre. In such an RF scheme the advantage of the Vee-type system is negligible and we must rely on splitting the Autler-Townes components beyond the Doppler width in any scheme.

The final hurdle in assessing the feasibility of an RF scheme is ascertaining how much RF power is required to produce a given Rabi frequency. Fortunately, this

relationship has been well characterised in work on rubidium clocks which utilise the same transition in rubidium vapour [8-10]; however, relatively high RF powers are required to produce a modest Rabi frequency. So much so that it is not economically viable to produce quantum coherence effects in a standard gas cell, subject to Doppler-broadening, with an RF field. Alternative approaches are under consideration. It may be possible, for example, to achieve an RF scheme in molecules in which stronger dipole moments exist at the appropriate wavelength range.

Since the emergence of EIT and LWI in the late 1980s the worldwide research effort has not abated. Importantly, the plethora of theoretical studies has been increasingly accompanied by experimental demonstrations of atomic interference and coherence effects. The first inversionless lasers have been realised [1,11,12] and the time is ripe for the study of practical mismatched schemes that are set to revolutionise modern laser technology. The work presented in this thesis signposts a possible avenue of future research in this crucial mismatched regime.



References

- [1] A. S. Zibrov *et al*, Phys. Rev. Lett. **75**, 8, (1995).
- [2] M. D. Lukin *et al*, Laser Phys. **6**, 3, 436-447, (1996).
- [3] S. F. Yelin *et al*, Phys. Rev. A. **57**, 5, 3858, (1998).
- [4] Y. Zhao *et al*, Phys. Rev. Lett. **79**, 4, 641, (1997).
- [5] B. S. Ham, M. S. Shahriar, and P. R. Hemmer, J. Opt. Soc. Am. B. **15**, 5, 1541, (1998).
- [6] G. G. Padmabandu *et al*, Phys. Rev. Lett. **76**, 12, 2053, (1996).
- [7] E. A. Korsunsky *et al*, **56**, 5, 3908, (1997).
- [8] R. P. Frueholz, and J. C. Camparo, J. Appl. Phys. **57**, 3, 704, (1985).
- [9] M. Hashimoto, and M. Ohtsu, J. Opt. Soc. Am. B. **6**, 10, 1777, (1989).
- [10] M. Hashimoto, and M. Ohtsu, IEEE J. Quan. Elec. B. **6**, 10, 446, (1987).
- [11] G. G. Padmabandu *et al*, Phys. Rev. Lett. **76**, 12, 2053, (1996).
- [12] F. B. de Jong *et al*, Phys. Rev. A. **57**, 6, 4869, (1998).

Appendices

“I hear and I forget, I see and I remember, I do and I understand.”

Confucius

A. Solving the Density Matrix with Mathematica

The program described in this Appendix solves the density matrix (Matrix 2.1) derived in Section 2.3. Indented bold text represents the actual Mathematica code, while plain interspersed text explains the code's purpose. The considered density matrix describes a two level atom interacting with a single optical field, the exact parameters used correspond to the $5S_{1/2} - 6P_{1/2}$ transition in atomic rubidium vapour.

The first step is to initialise the values of the relevant constants. These parameters are defined as follows:

```
wtconfact=1.66*10^-27;          weight=85*wtconfact;
  kB=1.381*10^-23;          Γ21=0.008*10^9;
  γ12=Γ21/2;
  k12=(N[2*Pi])/(421.5523*10^-9);
```

where **wtconfact** is the weight conversion factor equal to a single atomic mass unit, **weight** is the mass of rubidium in kilograms, **k_B** is Boltzmann's constant, **Γ₂₁** is the population decay rate from level $|2\rangle$ to level $|1\rangle$, **γ₁₂** is the coherence dephasing rate between levels $|1\rangle$ and $|2\rangle$, and **k₁₂** is the wavevector of the probe field applied to the transition between levels $|1\rangle$ and $|2\rangle$.

The next step is to define the following parameters, which are either variables or may be subject to change depending on the experimental conditions:

```
tc=150;          tK=273+tc;
  v:=v;
thermal=Sqrt[(2*kB*tK)/weight];
exth[v_]=Exp[-((v/thermal)^2)]/(Sqrt[N[Pi]]*thermal);
  Ω12=0.001*10^9;
  del12:= del12;          Δ12:= del12-(k12*v);
```

where **t_c** is the temperature of the rubidium vapour in °C, **t_K** is the temperature of the vapour in Kelvin, **v** is the velocity of the rubidium atoms defined here as a variable,

thermal is the average thermal atomic velocity, **exth[v_]** represents the velocity distribution as a Maxwellian function, taking the velocity, **v**, as an argument (see Eq. (2.24)), Ω_{12} is the angular Rabi frequency for the probe field connecting levels $|1\rangle$ and $|2\rangle$, **del₁₂** is the detuning of the probe field in the lab frame, and Δ_{12} is the total detuning incorporating the Doppler shift. Note that the Rabi frequency given here is half the actual value, as defined in Eq. 2.11.

The matrix elements are inputted as previously derived (Matrix 2.1):

```
A={
  { - $\Gamma_{21}$  , 0 , -2* $\Omega_{12}$  },
  { 0 ,  $\gamma_{12}$  , - $\Delta_{12}$  },
  { -2* $\Omega_{12}$  ,  $\Delta_{12}$  ,  $\gamma_{12}$  }
};
```

and the solution matrix, such that **A . x = b**:

```
b={ {0} , {0} , { - $\Omega_{12}$  } };
```

The matrix is now solved by taking the inverse of A (a standard transform in Mathematica), and multiplying by the solution matrix, so that **x = A⁻¹ . b**:

```
x={ Inverse[A] . b };
```

The matrix **x** contains the values for the density matrix elements which include the homogeneous probe field detuning and the velocity **v**, within the Doppler shifted detuning terms, as variables. Doppler-broadening is taken into account by integrating over the velocity distribution via Simpson's rule:

```
int[v_,del12_]=exth[v]*x[[1,3]];

l1=-400;
u1= 400;
n= 600;
```

```

dvel= (ul-ll)/n;

Do[vel[i]=ll+(i*dvel), {i,0,n,1}];

Do[ $\rho_{12}^i[\mathbf{del}_{12}] = (dvel/3)*$ 
  (int[vel[0],del12]+int[vel[n],del12])
  (+(2*(Sum[int[vel[tt],del12],{tt,2,n-2,2}])))
  (+(4*(Sum[int[vel[qq],del12],{qq,1,n-1,2}])))
),
{del12,-0.8*109,0.8*109,0.005*109}
];

```

The limits of the integration are set from $-v$ to v (**ll to ul**) in small steps (**dvel**). The desired density matrix element is selected from the vector array **x** and Simpson's Rule, Eq. (A.1), is employed to carry out the necessary integration over all group velocities for each specified detuning. In this case, the detuning ranges from $-800 \times 10^6 \text{ s}^{-1}$ to $800 \times 10^6 \text{ s}^{-1}$ in steps of $5 \times 10^6 \text{ s}^{-1}$. In standard mathematical notation the integration given by Simpson's rule is as follows:

$$\int_{ll}^{ul} \frac{ul - ll}{3n} \left(\text{int}[\text{vel}(tt), \text{del}_{12}] + \text{int}[\text{vel}(n), \text{del}_{12}] + 4 \sum_{k=1}^{\frac{1}{2}n} \text{int}[\text{vel}(2k-1), \text{del}_{12}] + 2 \sum_{k=1}^{\frac{1}{2}n-1} \text{int}[\text{vel}(2k), \text{del}_{12}] \right) \quad (\text{A.1})$$

The resulting data can be plotted with respect to detuning by tabulating it in the following manner:

```

 $\rho_{12}^i$ tab=Table[{del12,  $\rho_{12}^i$ [del12]} ,
  ({ del12, -0.8*109, 0.8*109, 0.005*109 } ] );
 $\rho_{12}^i$ flat=Flatten[ $\rho_{12}^i$ tab];
 $\rho_{12}^i$ part=Partition[ $\rho_{12}^i$ flat,2];

```

and plotting the selected element, in this case ρ_{12}^i , with a y axis of the specified limits:

```
ListPlot [ $\rho_{12}^i$ part,      Frame -> True,  
          Axes -> None,  
          PlotRange -> {1*10-3,1*10-2},  
          PlotJoined ->True ] ;
```

B. Coherent Excitation Scheme

We consider the energy level scheme employed to model the effects of coherent excitation in Section 3.5. The energy level structure is based on rubidium vapour wherein the probe and coupling fields are resonant with the $5S_{1/2} - 6P_{1/2}$ and $5S_{1/2} - 5P_{3/2}$ transitions respectively. The coherent pump field is applied to the $5P_{3/2} - 5D_{5/2}$ transition and this facilitates pumping via spontaneous relaxation into the $6P_{1/2}$ state. The hyperfine structure of the ground state is ignored in this model, and it is treated as a single level. The energy level diagram is shown in Fig. B.1, and the density matrix describing this system is given in Matrix B.1.

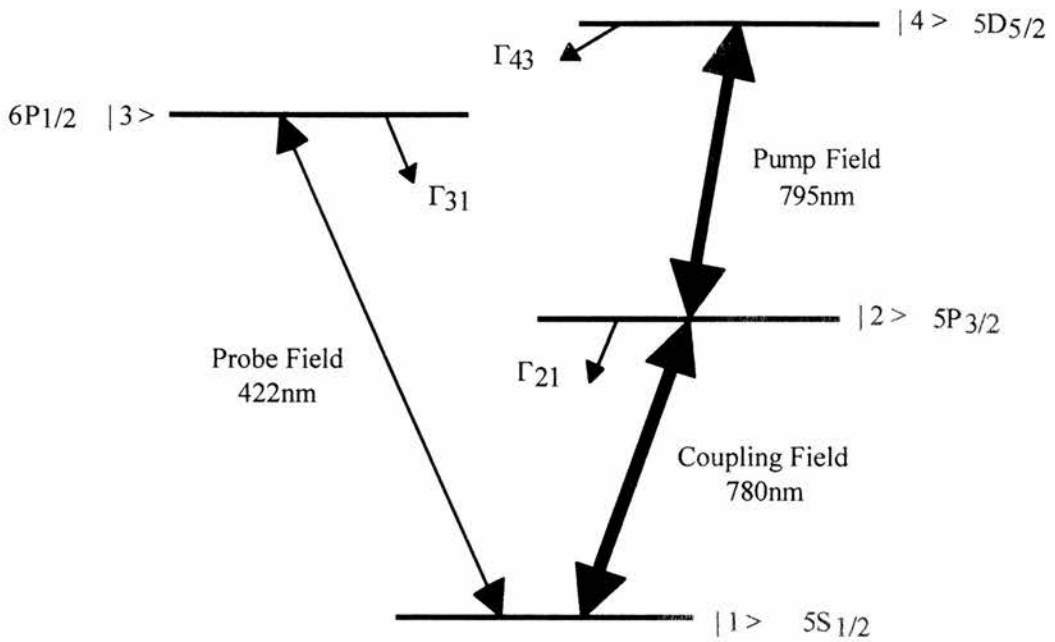


Figure B.1: Energy level structure for coherently pumped inversionless gain scheme in rubidium.

C. Role of Coherence Model

The following equations describe the three level Vee scheme based on the $5S_{1/2} - 6P_{1/2}$ and $5S_{1/2} - 5P_{3/2}$ transitions in rubidium that is employed to model the effects of the coherence ρ_{23} between the $6P_{1/2}$ and $5P_{3/2}$ states in Section 4.6:

$$\dot{\rho}_{11} = i\Omega_c(\tilde{\rho}_{21} - \tilde{\rho}_{12}) + i\Omega_p(\tilde{\rho}_{31} - \tilde{\rho}_{13}) + \Gamma_{21}\rho_{22} + \Gamma_{31}\rho_{33} \quad (C.1a)$$

$$\dot{\rho}_{22} = i\Omega_c(\tilde{\rho}_{12} - \tilde{\rho}_{21}) - \Gamma_{21}\rho_{22} \quad (C.1b)$$

$$\dot{\rho}_{33} = i\Omega_p(\tilde{\rho}_{13} - \tilde{\rho}_{31}) - \Gamma_{31}\rho_{33} \quad (C.1c)$$

$$\dot{\tilde{\rho}}_{12} = -i(\Delta_{12} - i\gamma_{12})\tilde{\rho}_{12} + i\Omega_c(\rho_{22} - \rho_{11}) - i\Omega_p\tilde{\rho}_{32} \quad (C.1d)$$

$$\dot{\tilde{\rho}}_{13} = -i(\Delta_{13} - i\gamma_{13})\tilde{\rho}_{13} + i\Omega_p(\rho_{33} - \rho_{11}) + i\Omega_c\tilde{\rho}_{23} \quad (C.1e)$$

$$\dot{\tilde{\rho}}_{23} = -i(\Delta_{12} - \Delta_{13} - i\gamma_{23})\tilde{\rho}_{23} + i\Omega_c\tilde{\rho}_{13} - i\tilde{\rho}_{21} \quad (C.1f)$$

The energy level structure is shown in Fig. C.1. The hyperfine structure of the $5S_{1/2}$ ground state is ignored.

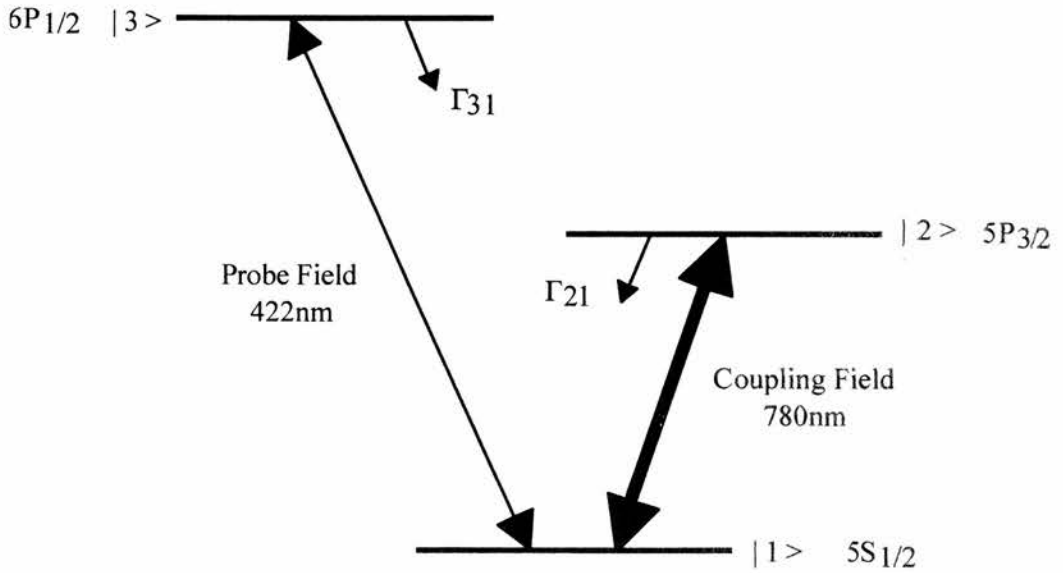


Figure C.1: Energy level structure of atomic system employed in 'role of coherence' model.

D. Publications, Presentations, and Awards

The following is a chronological list of the publications, presentations, and awards that have been made in connection with the work in this thesis.

D.1 Publications

Experimental observation of a coherently induced transparency on a blue probe in a Doppler-broadened mismatched V-type system

James R. Boon, Evangelini Zekou, David J. Fulton, and Malcolm H. Dunn
Physical Review A **57**, 2, 1323-1328, (1998).

Prediction of inversionless gain in a mismatched Doppler-broadened medium

James R. Boon, Evangelini Zekou, David McGloin, and Malcolm H. Dunn
Physical Review A **58**, 3, (1998).

Comparison of wavelength dependence in Cascade, Lambda and Vee-type schemes for electromagnetically induced transparency

James R. Boon, Evangelini Zekou, David McGloin, and Malcolm H. Dunn
Physical Review A, submitted 11/6/98.

D.2 Presentations

Inversionless lasing in the visible spectrum

Evangelini Zekou and James R. Boon

Poster 14 at the Inaugural Meeting of the Scottish Lasers and Electro-Optics Society (LEOS) Chapter, Glasgow, 1996.

Coherently induced transparency and inversionless gain on a blue probe field in a Doppler-broadened V-type medium

David J. Fulton, Sara Shepherd, Evangelini Zekou, James R. Boon, and Malcolm H. Dunn

Quantum Electronics and Laser Science Conference 1997 (QELS 97), Technical Digest Series, Vol. 12, paper QTuE8 (Optical Society of America, Washington DC, 1997).

Turning the world of lasers upside down

James R. Boon

LEOS Scottish Chapter Meeting, St. Andrews, 1997.

Coherently induced transparency and inversionless gain on a blue probe in a Doppler-broadened medium

David J. Fulton, James R. Boon, Evangelini Zekou, Sara Shepherd, and Malcolm H. Dunn
Thirteenth UK National Quantum Electronics Conference (QE-13), Cardiff, 1997.

A study of inversionless gain in mismatched Doppler-broadened systems

James R. Boon, Evangelini Zekou, David McGloin, and Malcolm H. Dunn
International Quantum Electronics Conference (IQEC) 1998, Technical Digest Series, Vol. 7, paper QWK6 (Optical Society of America, Washington DC, 1998).

D.3 Awards

EIT: Turning the world of lasers upside down (without inverting the population)

James R. Boon

The Gray Essay Prize, awarded by the University of St. Andrews 1996.

Quantum Coherence: Turning the world of lasers upside down - without inverting the population

James R. Boon

Second place in the national final of the Institute of Physics NEXUS lecture competition 1997.

“Some scientists tried to make an organised jungle of plastic but it didn’t improve conditions and the scientists left saying, ‘let’s go to the moon instead,’ and as there is nothing on the moon it seemed the best place for them.”

Spike Milligan